

**The Design, Optimisation, and
Characterisation of GaSb/GaAs
Quantum Ring-Based
Vertical-Cavity Devices Emitting
at Telecoms Wavelengths**

Thomas Julian Wilson

MPhys. Hons

This thesis is submitted in partial fulfilment of the requirements for the degree of
Doctor of Philosophy at Lancaster University.

No part of this thesis has been or is being submitted to any other university or
academic institution.

March 2021

**This work is carried out with the support of IQE plc as part of a CASE
studentship.**

The Design, Optimisation, and Characterisation of GaSb/GaAs Quantum Ring-Based Vertical-Cavity Devices Emitting at Telecoms Wavelengths

Thomas Julian Wilson MPhys. (Hons), March 2020

Abstract

The aim of this work is to establish the feasibility of designing and producing telecoms-wavelength vertical-cavity structures using GaSb quantum rings (QRs) embedded in GaAs - $\text{Al}_x\text{Ga}_{1-x}\text{As}$ resonators. Additionally, various methods of characterising the optical and material properties of the produced samples are assessed, to determine the most suitable techniques in terms of accuracy, ease of use, cost, and measurement time. Extensive optical modelling is carried out to design and optimise vertical-cavity surface-emitting lasers (VCSELs), and single-photon light-emitting diodes (SPLEDs). Optical models are used to check sample growth quality, and provide sample selection criteria when used in conjunction with measured material parameters and optical transmission spectra. Various measurement techniques are compared for the quantification of $\text{Al}_x\text{Ga}_{1-x}\text{As}$ in many-layered structures, including secondary-ion mass spectroscopy (SIMS), X-ray photoelectron spectroscopy (XPS), and electron energy-loss spectroscopy (EELS). SIMS proves to be effective for thick samples, particularly in terms of measurement speed and layer clarity, with XPS and EELS more suited for thinner samples, or where high resolution over a small area is required.

Distributed Bragg reflectors (DBRs) grown at IQE using metalorganic vapour-phase epitaxy (MOVPE) are successfully combined with the QR active region and upper DBR overgrowth using molecular beam epitaxy (MBE) at Lancaster University. The graded IQE DBRs are shown to be very consistent their optical properties, and reduce the electrical resistance and growth time for the remainder of the optical device. SPLED devices are shown to emit light, operating around 1310 nm and 1550 nm. At this time no single-photon emission was observed. VCSEL devices are shown to operate at around 1270 nm, demonstrating the telecoms-wavelength capabilities of the system, while device performance is limited by high resistance and other potential factors. Further improvements are discussed, including reducing device resistance, as well as processing the devices in the Lancaster Quantum Technology Centre cleanrooms.

Acknowledgements

First and foremost, I would like to thank Professor Manus Hayne for providing supervision and support throughout my PhD. His extensive knowledge and encouragement, coupled with his unending tolerance of my unannounced invasions of his office for discussions, helped guide me through the ups and downs of the research.

Special thanks go to all the staff at Lancaster University that supported my work, particularly: Dr Lefteris Danos, for providing access to the Spectrophotometer, as much of the work in this thesis would not have been possible without it; Dr Alex Robson and Lancaster Material Analysis, for cross-sectioning seemingly infinite numbers of our samples; Phelton Stephenson and the team in the mechanical workshop, for their help in creating the custom-built sample mapping system; and Deborah Dunne, for her administrative support and friendly chats throughout my time in the department.

My thanks go to all of our external collaborators: Jonathan Counsell of Kratos Analytical; Charles Jackson and Ben Grew of Loughborough Surface Analysis; Dr Bill Bong at the University of New South Wales, Australia; Dr Maria Delemata and Dr Sergio Molina from Universidad de Cádiz, Spain; and the team at CST global for processing our samples into devices.

I would like to thank all of my fellow students, researchers, and friends in the group, including Dr Laura McIndo, Dr Peter Hodgson, Dr Ofogh Tizno, and Dom Lane. Additionally, my thanks go to all the PhD students who made the office, and the department in general, a welcoming and enjoyable place to be.

I wish to acknowledge EPSRC for providing a studentship and IQE for providing a CASE award. Particular thanks go to Dr Iwan Davies of IQE, for supporting my work, as well as facilitating my placement at their site in Newport, from which I learned a great deal.

My thanks go to my family, for their support and motivation in helping me throughout my time at University. I would also like to thank my friends, particularly Matt McCormack, Matt Blair, Dave Spruce, Rosie Irwin Holbrey, Ollie Cuffley, and Sam Walsh, for providing a much needed substitute for human contact in our weekly online meetups during the COVID-19 lockdown.

Finally, I would like to express my utmost appreciation and love for my partner Ellie, as without her undying love and support, astonishing ability to listen to my rambling ideas, tireless proofreading, and bottomless cups of tea, I would never have made it this far.

Contents

Abstract	i
Acknowledgements	ii
1 Introduction	1
1.1 Motivation	2
1.2 Vertical-Cavity Surface-Emitting Lasers vs Other Laser Technologies . . .	3
1.3 GaAs - Al _x Ga _{1-x} As Material System	4
2 Background	6
2.1 Optical Modelling	7
2.1.1 Transfer Matrix Method	7
2.1.2 TFCalc Modelling Software	16
2.2 Vertical-Cavity Surface-Emitting Lasers	20
2.2.1 Distributed Bragg Reflectors	20
2.2.2 GaSb Quantum Rings in Quantum Well Active Region	25
2.2.3 Cavity Design	27
3 Optical Measurements - Background and Methods	30
3.1 Reflectance and Transmittance Measured By Cary 5000 Spectrophotometer	31
3.1.1 Spectrophotometry - Transmission	31
3.1.2 Reflectance	32
3.2 Wafer Mapping	34
3.2.1 Wafer Mapper Hardware	35
3.2.2 Automatic Data Analysis	35
3.3 Optical Process Monitoring	39
3.3.1 Etch Process Monitoring	39
4 Material Characterisation Techniques	43
4.1 Beam-Exit Cross-Sectional Polishing (BEXP)	44

4.2	Substrate Calibration	46
4.2.1	Modelling a Substrate	46
4.3	$\text{Al}_x\text{Ga}_{1-x}\text{As}$ Compositional Analysis	49
4.3.1	Secondary Ion Mass Spectroscopy (SIMS)	49
4.3.2	X-Ray Photoelectron Spectroscopy (XPS)	53
4.3.3	EELS	54
5	Material Characterisation Results	56
5.1	Short-Period Characterisation Sample	57
5.1.1	Beam-Exit Cross-Sectional Polishing	57
5.1.2	Substrate Calibration	59
5.1.3	Characterisation Results	59
5.1.4	Simulation	62
5.1.5	Aluminium Content of $\text{Al}_x\text{Ga}_{1-x}\text{As}$ Layers	63
5.2	$\text{Al}_x\text{Ga}_{1-x}\text{As}$ Compositional Analysis	64
5.2.1	Layer Average Definition	64
5.2.2	Optical Analysis	64
5.2.3	Secondary Ion Mass Spectroscopy (SIMS)	65
5.2.4	X-Ray Photoelectron Spectroscopy (XPS)	70
5.2.5	Electron Energy-Loss Spectroscopy (EELS)	71
5.2.6	Comparison of Methods	73
5.3	Summary	77
6	SPLEDs	79
6.1	Active Region Design	80
6.2	Optical Design	82
6.2.1	Design 1	82
6.2.2	Design 2	83
6.3	Key Samples	84
6.3.1	Design 1 - Transmission	84
6.3.2	Design 1 - beam-exit cross-sectional polishing (BEXP)	85
6.3.3	Design 1 - x-ray photoelectron spectroscopy (XPS)	87
6.3.4	Design 2 - Transmission	88
6.3.5	Design 2 - BEXP	90
6.4	Testing	91

6.4.1	Design 1 Testing	91
6.4.2	Design 2 Testing	92
6.5	Summary	93
7	VCSELS	97
7.1	Mk. 1 VCSELS	98
7.1.1	Mk.1 Design	98
7.1.2	Key Samples	99
7.1.3	Processing and Testing	103
7.2	Mk. 2 VCSELS	104
7.2.1	Initial Design	104
7.2.2	Key Samples and Redesigns	106
7.2.3	Processing and Testing	115
7.3	Mk. 3 VCSELS	118
7.3.1	Design	118
7.3.2	Key Samples	119
7.3.3	Processing and Testing	120
7.4	Mk. 4 VCSELS	121
7.4.1	Design	121
7.4.2	Key Samples	124
7.4.3	Processing and Testing	127
8	Conclusions	128
	List of Figures	132
	List of Tables	142
	Bibliography	144
	Appendices	157

Acronyms

AFM atomic force microscopy. 45, 57, 58, 100, 113, 129, 135, 138

BEXP beam-exit cross-sectional polishing. iv, 45, 57, 58, 85, 86, 87, 90, 92, 94, 95, 100, 101, 108, 109, 111, 113, 114, 129, 135, 137, 138, 139, 142, 143

DBR distributed Bragg reflector. 3, 5, 20, 21, 23, 24, 25, 26, 27, 28, 31, 37, 38, 40, 42, 44, 45, 49, 57, 58, 60, 82, 83, 85, 86, 87, 89, 93, 94, 95, 98, 99, 100, 101, 102, 103, 104, 105, 106, 107, 108, 109, 110, 111, 112, 113, 114, 115, 116, 117, 118, 119, 121, 122, 123, 124, 125, 126, 130, 133, 134, 135, 137, 138, 139, 140, 143

DFB distributed feedback laser. 2, 4

ECV electrochemical capacitance-voltage. 117, 121, 130, 140

EEL edge-emitting laser. 3, 4

EELS electron energy-loss spectroscopy. 49, 54, 64, 71, 74, 77, 78

FIB focused ion beam. 44

ICP inductively coupled plasma. 40, 134

LED light emitting diode. 27, 133

LMA Lancaster Material Analysis. 45

MBE molecular beam epitaxy. 5, 19, 21, 57, 64, 67, 100, 104, 105, 106, 108, 111, 113, 114, 115, 116, 117, 121, 122, 130, 143

MOVPE metalorganic vapour-phase epitaxy. 3, 5, 21, 24, 104, 105, 113, 115, 121, 129, 130, 143

- MS-SIMS** magnetic sector secondary-ion mass spectroscopy. 49, 50, 63, 65, 67, 68, 69, 70, 73, 74, 75, 77, 78, 135, 136, 142
- PL** photoluminescence. 49
- QD** quantum dot. 26, 81, 83, 94
- QR** quantum ring. 26, 27, 45, 59, 80, 81, 83, 95, 108, 133, 137
- QW** quantum well. 26
- SBW** spectral bandwidth. 46
- SEM** scanning electron microscopy. 74, 136
- SIMS** secondary-ion mass spectroscopy. 49, 50, 51, 65, 67, 68, 69, 70, 71, 76, 77, 78
- SPLED** single photon LED. 80, 81, 82, 84, 87, 88, 89, 92, 93, 94, 95, 137, 138, 142
- TEM** transmission electron microscopy. 44, 49
- TMM** transfer matrix method. 7, 15, 16, 23, 39, 41
- ToF-SIMS** time-of-flight secondary-ion mass spectroscopy. 49, 51, 52, 68, 70, 71, 73, 75, 77, 78, 135, 136, 142
- VCSEL** vertical-cavity surface-emitting laser. 2, 3, 4, 5, 20, 24, 27, 28, 31, 37, 38, 39, 45, 49, 60, 75, 98, 99, 100, 101, 102, 103, 104, 105, 108, 111, 115, 116, 118, 120, 121, 122, 125, 126, 129, 130, 133, 134, 135, 138, 139, 140, 143
- XPS** x-ray photoelectron spectroscopy. iv, 49, 53, 70, 71, 72, 73, 76, 77, 78, 87, 94, 102, 135, 136, 138, 142
- XRD** x-ray diffraction. 49

Chapter 1

Introduction

1.1 Motivation

The use of vertical-cavity surface-emitting laser (VCSEL) technologies has increased dramatically since their development around the 1980s[1], due to their low cost, low power, efficiency, and ease of production. A recent valuation and report estimates the total market value of VCSEL technologies to be at \$1Bn as of 2020, and projects an increase to \$5Bn by 2027 [2]. The gallium arsenide material system dominates, with GaAs - $\text{Al}_x\text{Ga}_{1-x}\text{As}$ VCSELs making up a total of 65% of the 2020 market share. Currently, short wavelength (850 - 950 nm) devices are the primary type of VCSEL in use, with applications in datacoms, laser printing, sensing (including smartphone technology), chip-to-chip optical interconnects, and more.

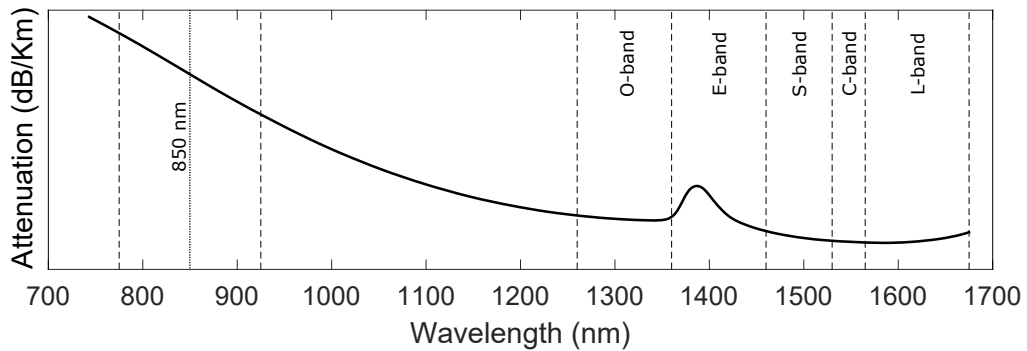


Figure 1.1: Sketch of attenuation over distance for a standard optical fibre showing the short-wavelength datacoms region (850 nm), and the longer-wavelength telecoms bands.[3]

While these shorter wavelengths are widely produced and utilised, there remains a opportunity for devices in the telecoms O-band, shown around 1300 nm in figure 1.1, with reduced transmission loss compared to the datacoms band used in data centres. Less loss over distance means lower power consumption, less error correction required, and longer possible transmission distances. A VCSEL that can compete with the current GaAs-based VCSEL devices in cost and performance, could easily be seen as a viable alternative to reduce energy usage within data centres. If a telecoms VCSEL can match or beat current telecoms O-band devices, primarily distributed feedback lasers (DFBs), they may then find application in mid-range fibre to the premises in commercial broadband. The UK government has expressed its desire to implement optical fibre to the premises (FTTP) to 15M sites by 2025, and all UK premises by 2033. To meet these targets an upstream laser needs to be placed in every premises, meeting the requirements of the XGS-PON standard[4]. This standard centres on an upstream wavelength of 1270 nm, a power output of 2.5 to 7.9 mW, and a speed of 10 Gbs^{-1} [5]. Given that the standard is

international, the market for broadband customer-end devices stretches beyond the UK.

With the rise in smartphone-based sensor technology, built-in VCSEL sensors are set to become a large part of the international market. Current consumer devices hold multiple VCSEL arrays to support advanced camera operation, with more than 400 individual cavities per handset. Current VCSELs in smartphone camera applications are sub-1 μm in wavelength, but moving forward $>1.4 \mu\text{m}$ ‘eye-safe’ devices would be greatly preferred. An active region capable of emitting in the telecoms O-band could potentially be utilised to emit at 1.4 μm or above with a suitable cavity selection.

The two main goals of this work are as follows. Firstly, to determine both the feasibility of a telecoms wavelength GaAs- $\text{Al}_x\text{Ga}_{1-x}\text{As}$ VCSEL, as well as assess the possibility of mass production using IQE plc’s metalorganic vapour-phase epitaxy (MOVPE) reactors. Secondly, to assess and refine the models and analytical techniques used in the design of optical devices such as these, and use them to reduce the time and cost normally associated with semiconductor characterisation.

1.2 Vertical-Cavity Surface-Emitting Lasers vs Other Laser Technologies

Compared to the conventional semiconductor edge-emitting laser (EEL), VCSELs hold a number of important advantages that have led to their widespread use in datacoms and consumer electronics. Firstly, the top-bottom arrangement of the mirrors allows for a larger number of devices to be fabricated from a single wafer. Since the size is limited only by the mesa and contacts, rather than the end facets and gain length of a strip laser, a device count in the hundreds of thousands can be produced from a single 6” wafer. The vertically stacked optical resonator also allows for the inclusion of distributed Bragg reflector (DBR) dielectric mirrors, consisting of alternating layers of high and low refractive index material[6]. The mirrors can be utilised to produce a reflectivity of 99.9%, compared to an EEL end facet reflectivity of around 30%. Reflective coatings can be applied to the end facets of an edge emitter to improve performance, with the drawback of additional processing steps. The primary effect of having high reflectance mirrors is that the gain volume can be drastically reduced, so the cavity can be a micron or less, rather than the hundreds of microns in an edge emitter. Being able to confine the current to the centre of the mesa, through oxidation, proton bombardment, or structural methods, reduces the volume of the cavity and forces the current to travel through

the centre of the active layers[7]. The small cavity volume also lends itself to ultra-low threshold operation [8, 9, 10, 11] and high power conversion efficiency[12]. The shorter cavities and vertical emission allow for easy butt-coupling to multimode optical fibres, as well as high efficiency coupling to single mode fibres with some additional optical components[13]. The small device size directly leads to high speed data transmission with devices reaching over 40 Gb s^{-1} with on-off keying[14], with standard commercial devices operating at 25 Gb s^{-1} or more[15]. The transmission speed is limited by thermal heating, parasitic resistance, and capacitance. Due to the cavity selected output and short cavity length, VCSELs also display excellent temperature stability in both wavelength and threshold[16]. The vertical nature of the devices means that arrays can be easily processed [17], with such arrays being applicable to high-power systems, 3D sensing, optical interconnects and more[18].

In terms of extending GaAs VCSEL technology to the telecoms O-band, the current primary competitors are DFBs. These devices incorporate the Bragg reflector into a lithographically-defined waveguide. The active region has a material with a certain refractive index grown above it, which is then processed into a grating. More material is deposited to produce the index contrast of a Bragg reflector, and the electrode layers are deposited over the device. These edge-emitting single-mode devices have been demonstrated at high-speeds, with precise cleaving required to set the length of the cavity[19]. In order to produce perpendicular beam emission, particularly for integration into arrays, DFBs must be incorporated with a mirror/lens structure requiring yet more high-precision processing[20]. The VCSELs on the other hand, require one single growth, and a straightforward process of mesa definition, current confinement, passivation, and contact deposition. Additionally, the single-epitaxy nature of the structure allows for non-destructive optical testing of the growths before processing has occurred, so that poor samples can be rejected without wasting time and money on a non-viable batch. Fully processed VCSELs can also be tested on-wafer before dicing and packaging, unlike EELs and DFBs, simplifying quality control and reducing the likelihood that non-functional devices are packaged or sold.

1.3 GaAs - $\text{Al}_x\text{Ga}_{1-x}\text{As}$ Material System

The GaAs - $\text{Al}_x\text{Ga}_{1-x}\text{As}$ material pairing was implemented early in the development of the VCSEL, producing high-efficiency 850 nm devices at room temperature [21]. The close to lattice matched nature of GaAs and AlAs allow for monolithic growth of struc-

tures consisting of various compositions of $\text{Al}_x\text{Ga}_{1-x}\text{As}$. The difference in refractive index between the alloy compositions mean that DBRs can be directly grown around a suitable active region using an epitaxial technique such as MOVPE or molecular beam epitaxy (MBE). Doping the DBRs during growth provides the diode behaviour of the VCSEL, and a combination of active region, cavity thickness and DBR centre wavelength select the output wavelength. Short wavelength (800 - 950 nm) emission in a typical VCSEL is generally with GaAs - $\text{Al}_x\text{Ga}_{1-x}\text{As}$ quantum wells within the cavity[22], so that the entire structure is simple and straightforward to grow using as few materials as possible. Utilising the advantages of the GaAs - $\text{Al}_x\text{Ga}_{1-x}\text{As}$ DBR system, while pushing the output wavelength into the telecoms region, requires a change in active region. 1.3 μm emission has been achieved with InAs - $\text{In}_x\text{Ga}_{1-x}\text{As}$ quantum dots [23], however the low emission power $\sim 330 \mu\text{W}$ demonstrated in this instance reduces suitability for longer-range applications, particularly the XGS-PON standard discussed in section 1.1. Having another semiconductor alloy in the device also increases growth complexity and calibration factors, and increases the complexity of any optical simulations of the device. In this work the active region being assessed incorporates GaSb quantum rings into a GaAs - $\text{Al}_x\text{Ga}_{1-x}\text{As}$ quantum well structure previously demonstrated by Lancaster University[24]. The advantages of this system include reduced material complexity, improved lattice matching with all bulk layers consisting of GaAs or $\text{Al}_x\text{Ga}_{1-x}\text{As}$, and improved optical simulations due to the reduced number of alloy types.

Chapter 2

Background

2.1 Optical Modelling

2.1.1 Transfer Matrix Method

The optical transfer matrix method (TMM) is a calculation technique by which the reflection and transmission coefficients of a multilayer system can be numerically obtained. Widely used across the field of optics, the method assumes homogeneous and optically isotropic layers and smooth interfaces to combine the entire stack into a set of propagation and interface matrices. The end result is a so-called system matrix, from which the Fresnel coefficients of the structure can be obtained.[25, 26, 27]

2.1.1.1 Notation

Notation can vary greatly across field of waves and optics, so the notation used here will be outlined for the benefit of the reader. An electric field is defined as oscillating in the y (up-down) direction and propagating in the x (left-right) direction. The field on either side of an interface will have the current layer subscript, the direction denoted using a superscript + or - for rightwards and leftwards, respectively, and the prime notation marks the side of the interface, with prime on the right and non-prime on the left. A single interface example is shown in figure 2.1. The complete form of a single right-bound component on the left of an interface for example is

$$\vec{E}_m^+ = E_m^+ e^{i\vec{k}x} \quad (2.1.1)$$

for any layer m .

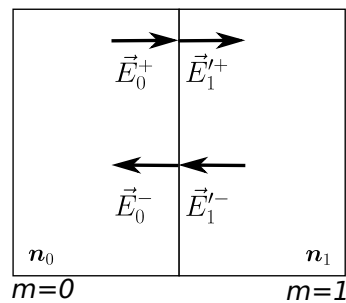


Figure 2.1: A typical interface between two layers of complex refractive index n_m explaining the electric field propagation notation in this work.

2.1.1.2 The Propagation Matrix

Propagation through a single, homogeneous layer of material can be calculated using the wavevector dispersion relation $\vec{k}_i(\omega) = \omega/v$ for a wave of frequency ω and phase velocity

v. The dispersion relation for a homogeneous medium is

$$|\vec{k}_i| = \frac{\omega}{v} = \frac{2\pi\mathbf{n}_i}{\lambda_0}, \quad (2.1.2)$$

where \vec{k}_i is the wavevector in the medium, \mathbf{n}_i the complex refractive index of the material, and λ_0 the vacuum wavelength. The complex refractive index \mathbf{n}_m in layer m is represented as

$$\mathbf{n}_m = n_m + i\kappa_m, \quad (2.1.3)$$

where n_m is the refractive index and κ_m is the extinction coefficient. The standard equation for a wave propagating in one dimension through a homogeneous medium can be written in matrix form as follows:

$$\vec{E}_0(x) = E_0^+ e^{i\vec{k}x} + E_0^- e^{-i\vec{k}x} \quad (2.1.4)$$

$$\therefore \begin{pmatrix} \vec{E}(x)^+ \\ \vec{E}(x)^- \end{pmatrix} = \begin{pmatrix} e^{i\vec{k}x} & 0 \\ 0 & e^{-i\vec{k}x} \end{pmatrix} \begin{pmatrix} E_0^+ \\ E_0^- \end{pmatrix}. \quad (2.1.5)$$

Equation (2.1.5) directly gives the propagation Matrix:

$$\mathbf{P} = \begin{pmatrix} e^{i\vec{k}x} & 0 \\ 0 & e^{-i\vec{k}x} \end{pmatrix}. \quad (2.1.6)$$

2.1.1.3 The Interface Matrix

At the interface between two layers the fields must be continuous, *i.e.*

$$\vec{E}_1 = \vec{E}'_2, \quad (2.1.7)$$

$$\vec{E} = (0, E_y, 0), \quad (2.1.8)$$

and

$$\vec{H}_1 = \vec{H}'_2. \quad (2.1.9)$$

With right-moving (+) and left-moving (-) components equation (2.1.7) becomes

$$\vec{E}_{1y}^+ + \vec{E}_{1y}^- = \vec{E}_{2y}^+ + \vec{E}_{2y}^-. \quad (2.1.10)$$

From this we can immediately obtain the matrix relation

$$\begin{pmatrix} 1 & 1 \end{pmatrix} \begin{pmatrix} \vec{E}_{1y}^+ \\ \vec{E}_{1y}^- \end{pmatrix} = \begin{pmatrix} 1 & 1 \end{pmatrix} \begin{pmatrix} \vec{E}_{2y}^+ \\ \vec{E}_{2y}^- \end{pmatrix}. \quad (2.1.11)$$

Using Faraday's law of induction

$$\vec{\nabla} \times \vec{E} + \frac{\partial \vec{B}}{\partial t} = 0, \quad (2.1.12)$$

and that $\vec{B} = \mu \vec{H}$, it follows that

$$\vec{\nabla} \times \vec{E} + \mu \frac{\partial \vec{H}}{\partial t} = 0. \quad (2.1.13)$$

Substituting the plane waveform $\vec{H}(x, y, z) = \vec{H}_0 e^{i\vec{k}\vec{r} - i\omega t}$, where \vec{r} is the position vector, into equation (2.1.13) we find that

$$\vec{\nabla} \times \vec{E} + i\omega\mu\vec{H} = 0. \quad (2.1.14)$$

The curl of \vec{E} is then calculated:

$$\vec{\nabla} \times \vec{E} = \begin{vmatrix} \hat{x} & \hat{y} & \hat{z} \\ \frac{\partial}{\partial x} & \frac{\partial}{\partial y} & \frac{\partial}{\partial z} \\ 0 & E_y & 0 \end{vmatrix}, \quad (2.1.15)$$

$$\vec{\nabla} \times \vec{E} = \left(\frac{\partial}{\partial x} \right) \hat{z}. \quad (2.1.16)$$

Combining equations 2.1.14 and 2.1.16 gives

$$\vec{H}_1 = \frac{1}{i\omega\mu} \frac{\partial}{\partial x} \left(\vec{E}_{1y}^+ + \vec{E}_{1y}^- \right) \hat{z}, \quad (2.1.17)$$

then rewriting the full form of the electric field as shown in equation (2.1.1) gives

$$\vec{H}_1 = \frac{1}{i\omega\mu} \frac{\partial}{\partial x} \left(E_{1y}^+ e^{i\vec{k}_1 x} + E_{1y}^- e^{-i\vec{k}_1 x} \right) \hat{z}, \quad (2.1.18)$$

thus

$$\vec{H}_1 = \frac{1}{i\omega\mu} \left(ik_1 E_{1y}^+ e^{i\vec{k}_1 x} - ik_1 E_{1y}^- e^{-i\vec{k}_1 x} \right) \hat{z}. \quad (2.1.19)$$

We know that the imaginary part of \mathbf{n}_m only affects propagation since it is a measure of absorption over distance so cannot have an effect on the behaviour at the interface.

As such equation (2.1.2) becomes

$$|\vec{k}_i| = \frac{\omega}{v} = \frac{2\pi n_m}{\lambda_0}, \quad (2.1.20)$$

where n_m is the real refractive index in layer m . Substituting equation (2.1.20) into equation (2.1.19) we obtain

$$\vec{H}_1 = \frac{1}{\mu c_0} \left(n_1 \vec{E}_{1y}^+ - n_1 \vec{E}_{1y}^- \right) \hat{z}, \quad (2.1.21)$$

and similarly for the right hand side of the interface

$$\vec{H}'_2 = \frac{1}{\mu c_0} \left(n_2 \vec{E}'_{2y}{}^+ - n_2 \vec{E}'_{2y}{}^- \right) \hat{z}. \quad (2.1.22)$$

We therefore know from equation (2.1.9) that

$$\left(n_1 \vec{E}_{1y}^+ - n_1 \vec{E}_{1y}^- \right) = \left(n_2 \vec{E}'_{2y}{}^+ - n_2 \vec{E}'_{2y}{}^- \right). \quad (2.1.23)$$

Equation 2.1.23 can be written in matrix form as

$$\begin{pmatrix} n_1 & -n_1 \end{pmatrix} \begin{pmatrix} \vec{E}_{1y}^+ \\ \vec{E}_{1y}^- \end{pmatrix} = \begin{pmatrix} n_2 & -n_2 \end{pmatrix} \begin{pmatrix} \vec{E}'_{2y}{}^+ \\ \vec{E}'_{2y}{}^- \end{pmatrix}. \quad (2.1.24)$$

Combining equations 2.1.11 and 2.1.24 results in the interface relation

$$\underbrace{\begin{pmatrix} 1 & 1 \\ n_1 & -n_1 \end{pmatrix}}_{\mathbf{D}_1} \begin{pmatrix} \vec{E}_{1y}^+ \\ \vec{E}_{1y}^- \end{pmatrix} = \underbrace{\begin{pmatrix} 1 & 1 \\ n_2 & -n_2 \end{pmatrix}}_{\mathbf{D}_2} \begin{pmatrix} \vec{E}'_{2y}{}^+ \\ \vec{E}'_{2y}{}^- \end{pmatrix}. \quad (2.1.25)$$

So, for the field on either side of the interface

$$\begin{pmatrix} \vec{E}_{1y}^+ \\ \vec{E}_{1y}^- \end{pmatrix} = \mathbf{D}_1^{-1} \mathbf{D}_2 \begin{pmatrix} \vec{E}'_{2y}{}^+ \\ \vec{E}'_{2y}{}^- \end{pmatrix}. \quad (2.1.26)$$

We can thus define the interface matrix $\mathbf{T}_{1,2}$ as follows:

$$\mathbf{T}_{1,2} = \mathbf{D}_1^{-1} \mathbf{D}_2 = \begin{pmatrix} \frac{1}{2} & \frac{1}{2n_1} \\ \frac{1}{2} & \frac{-1}{2n_1} \end{pmatrix} \begin{pmatrix} 1 & 1 \\ n_2 & -n_2 \end{pmatrix} = \begin{pmatrix} \frac{n_1+n_2}{2n_1} & \frac{n_1-n_2}{2n_1} \\ \frac{n_1-n_2}{2n_1} & \frac{n_1+n_2}{2n_1} \end{pmatrix}. \quad (2.1.27)$$

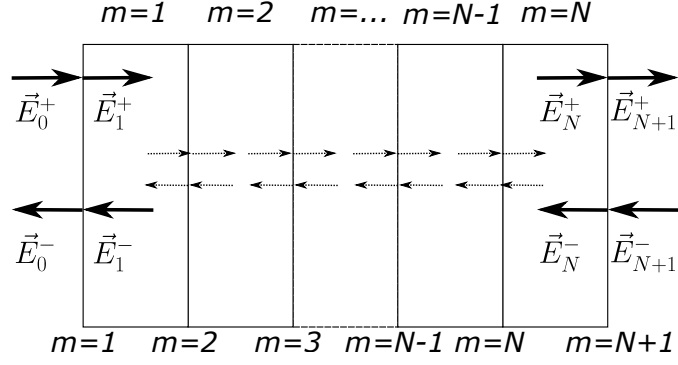


Figure 2.2: Propagation of the electric field components through a full system of N layers and $N + 1$ interfaces.

2.1.1.4 The System Transfer Matrix

Given a multilayer system as shown in figure 2.2 with N coherent layers and $N + 1$ interfaces, a system matrix, \mathbf{S} can be constructed by multiplying each matrix in sequence:

$$\begin{pmatrix} \vec{E}_{0y}^+ \\ \vec{E}_{0y}^- \end{pmatrix} = \mathbf{D}_0^{-1} \underbrace{\left[\prod_{m=1}^N \mathbf{D}_m \mathbf{P}_m^{-1} \mathbf{D}_m^{-1} \right]}_{\mathbf{S}} \mathbf{D}_{N+1} \begin{pmatrix} \vec{E}_{(N+1)y}^+ \\ \vec{E}_{(N+1)y}^- \end{pmatrix}, \quad (2.1.28)$$

or alternatively in terms of the interface matrix \mathbf{T}

$$\begin{pmatrix} \vec{E}_{0y}^+ \\ \vec{E}_{0y}^- \end{pmatrix} = \mathbf{T}_{0,1} \underbrace{\left[\prod_{m=1}^N \mathbf{P}_m^{-1} \mathbf{T}_{m,m+1} \right]}_{\mathbf{S}} \begin{pmatrix} \vec{E}_{(N+1)y}^+ \\ \vec{E}_{(N+1)y}^- \end{pmatrix}. \quad (2.1.29)$$

The system matrix will be a 2x2 matrix of the form:

$$\mathbf{S} = \begin{pmatrix} S_{11} & S_{12} \\ S_{21} & S_{22} \end{pmatrix}. \quad (2.1.30)$$

Using this matrix the reflection and transmission coefficients can be calculated by first analysing the ratios between the various field components in equation (2.1.28). It can be seen from the diagram in figure 2.2 that the total reflection and transmission coefficients r_s and t_s are

$$r_s = \frac{E_{0y}^-}{E_{0y}^+} \quad \text{and} \quad t_s = \frac{E_{(N+1)y}^+}{E_{0y}^+}. \quad (2.1.31)$$

At this point, equation (2.1.29) can be rewritten as

$$\begin{pmatrix} \vec{E}_{0y}^+ \\ \vec{E}_{0y}^- \end{pmatrix} = \begin{pmatrix} S_{11} & S_{12} \\ S_{21} & S_{22} \end{pmatrix} \begin{pmatrix} \vec{E}'_{(N+1)y}^+ \\ \vec{E}'_{(N+1)y}^- \end{pmatrix}, \quad (2.1.32)$$

which, when expanded, creates the following equations

$$\vec{E}_{0y}^+ = S_{11}\vec{E}'_{(N+1)y}^+ + S_{12}\vec{E}'_{(N+1)y}^-, \quad (2.1.33)$$

$$\vec{E}_{0y}^- = S_{21}\vec{E}'_{(N+1)y}^+ + S_{22}\vec{E}'_{(N+1)y}^-. \quad (2.1.34)$$

By once again referring to figure 2.2, it is evident that if the final layer is assumed to be infinite, the field component $\vec{E}'_{(N+1)y}^-$ must be zero. Doing so immediately reveals that the expression for t_s becomes

$$\vec{E}_{0y}^+ = S_{11}\vec{E}'_{(N+1)y}^+, \quad (2.1.35)$$

$$\therefore t_s = \frac{\vec{E}'_{(N+1)y}^+}{\vec{E}_{0y}^+} = \frac{1}{S_{11}}. \quad (2.1.36)$$

Finally, one can take the ratio of equations 2.1.34 to 2.1.33 to obtain

$$r_s = \frac{\vec{E}_{0y}^-}{\vec{E}_{0y}^+} = \frac{S_{21}}{S_{11}}. \quad (2.1.37)$$

Considering the interface matrix $\mathbf{T}_{m,m+1}$ in equation (2.1.27) for a single boundary using equation (2.1.36) and equation (2.1.37), the reflection and transmission coefficients take the form

$$r_{m,m+1} = \frac{n_m - n_{m+1}}{n_m + n_{m+1}}, \quad (2.1.38)$$

and

$$t_{m,m+1} = \frac{2n_m}{n_m + n_{m+1}}. \quad (2.1.39)$$

which are equivalent to the Fresnel coefficients. The interface matrix $\mathbf{T}_{m,m+1}$ can now be simplified to become

$$\mathbf{T}_{m,m+1} = \frac{1}{t_{m,m+1}} \begin{pmatrix} 1 & r_{m,m+1} \\ r_{m,m+1} & 1 \end{pmatrix}. \quad (2.1.40)$$

The reflectance, R , and transmittance, T , are found by taking the square of the magnitudes of r_s and t_s respectively:

$$R_s = |r_s|^2 = \left| \frac{S_{21}}{S_{11}} \right|^2, \quad (2.1.41)$$

and

$$T_s = |t_s|^2 = \left| \frac{1}{S_{11}} \right|^2. \quad (2.1.42)$$

The transmission in equation (2.1.42) must also be normalized with respect to the phase velocities of the originating and exit mediums. In an optical system this ratio directly translates to a ratio of the real part of the refractive indices,

$$T_{normalized} = \frac{n_{exit}}{n_{origin}} \left| \frac{1}{S_{11}} \right|^2. \quad (2.1.43)$$

2.1.1.5 Incoherent Substrate Reflection

A major limitation of the basic form of the transfer matrix method is its inability to handle incoherent layers, i.e. layers with a thickness above the coherence length of the travelling light. This becomes an issue when a substrate underneath the layers of interest (the sample) has a low extinction coefficient, resulting in light emerging from the rear of the device. Light is therefore reflected from the interior of the substrate's back surface, which in turn interacts with the overall sample spectrum. An extension to include partial coherence and incoherence was attempted using analytical expressions, but was limited to a multilayer on a single thick substrate[28]. While this version would be suitable for most of our samples, a more complete version with full matrix formulation has been developed[29].

For a thick layer, the back reflectance and transmittance coefficients also need to be included to account for backwards propagating light within the layer. These are simply the mirror images of r_s and t_s :

$$r'_s = \frac{E'_{(N+1)y}{}^+}{E'_{(N+1)y}{}^-} \quad \text{and} \quad t'_s = \frac{E'_{0y}{}^-}{E'_{(N+1)y}{}^-}. \quad (2.1.44)$$

Using equation (2.1.33) and equation (2.1.34) and setting $E'_{0y}{}^+$ it is straightforward to show that

$$r'_s = \frac{E'_{(N+1)y}{}^+}{E'_{(N+1)y}{}^-} = -\frac{S_{12}}{S_{11}}, \quad (2.1.45)$$

and

$$t'_s = \frac{E'_{0y}{}^-}{E'_{(N+1)y}{}^-} = \frac{Det(S)}{S_{11}}, \quad (2.1.46)$$

where $Det(S) = S_{11}S_{22} - S_{12}S_{21}$. By substituting the above coefficients into the system matrix, a more general form can be written as

$$\mathbf{S}_{general} = \frac{1}{t_s} \begin{pmatrix} 1 & -r'_s \\ r_s & t_s t'_s - r_s r'_s \end{pmatrix}. \quad (2.1.47)$$

To now include a thick incoherent layer into the multilayer stack, the system matrices of the multilayers on either side of the thick layer must be calculated, and the generic intensity matrix found for each side. In order to create an incoherent layer, the general matrix is replaced with its square-amplitude counterpart, thus removing the phase information and preserving the intensity of the propagating light. For example, if the thick layer is layer m , then all the layers from the surface to the interface with m would be combined into a single system matrix

$$\mathbf{S}_{(0,m)}^{incoh} = \frac{1}{|t_{s(0,m)}|^2} \begin{pmatrix} 1 & -|r'_{s(0,m)}|^2 \\ |r_{s(0,m)}|^2 & |t_{s(0,m)} t'_{s(0,m)}|^2 - |r_{s(0,m)} r'_{s(0,m)}|^2 \end{pmatrix}. \quad (2.1.48)$$

Similarly, the layers from m to the back of the sample would be calculated as

$$\mathbf{S}_{(m,N+1)}^{incoh} = \frac{1}{|t_{s(m,N+1)}|^2} \begin{pmatrix} 1 & -|r'_{s(m,N+1)}|^2 \\ |r_{s(m,N+1)}|^2 & |t_{s(m,N+1)} t'_{s(m,N+1)}|^2 - |r_{s(m,N+1)} r'_{s(m,N+1)}|^2 \end{pmatrix}. \quad (2.1.49)$$

The next stage is to take into account the light propagation within the thick layer. The same process used above is used to remove the phase information, and thus the interference effects, from the propagation matrix in equation (2.1.6). The resulting matrix

$$\mathbf{P}_m^{incoh} = \begin{pmatrix} |e^{i\vec{k}x}|^2 & 0 \\ 0 & |e^{-i\vec{k}x}|^2 \end{pmatrix} \quad (2.1.50)$$

preserves any attenuation due to a non-zero extinction coefficient. Finally, the incoherent system matrices for each of the coherent layer stacks can be multiplied along with the incoherent propagation matrix for the thick layer itself,

$$\mathbf{S}_{total} = \mathbf{S}_{(0,m)}^{incoh} \mathbf{P}_m^{incoh} \mathbf{S}_{(m,N+1)}^{incoh}. \quad (2.1.51)$$

Since the amplitudes of the Fresnel coefficients are already incorporated into this matrix,

the total reflectance and transmittance are calculated as

$$R_s = \frac{\vec{E}_{0y}^-}{\vec{E}_{0y}^+} = \frac{S_{21}}{S_{11}}, \quad (2.1.52)$$

and

$$T_s = \frac{\vec{E}'_{(N+1)y}}{\vec{E}_{0y}^+} = \frac{1}{S_{11}}. \quad (2.1.53)$$

Using this extended form of the TMM, it is possible to simulate samples with a thick substrate that is transparent enough for light to reach the back surface. To demonstrate the difference the coherence consideration makes, a plain GaAs substrate with a thickness of 350 μm , suspended in air, was simulated with both the original and extended versions of the TMM. The results are shown in figure 2.3. It is immediately clear that the upper simulation is suggesting a huge amount of interference, which would make any transmission measurement unintelligible. Once the phase information is removed from the substrate, as in the lower simulation, the model loses the artificial interference and matches the real behaviour of a substrate.

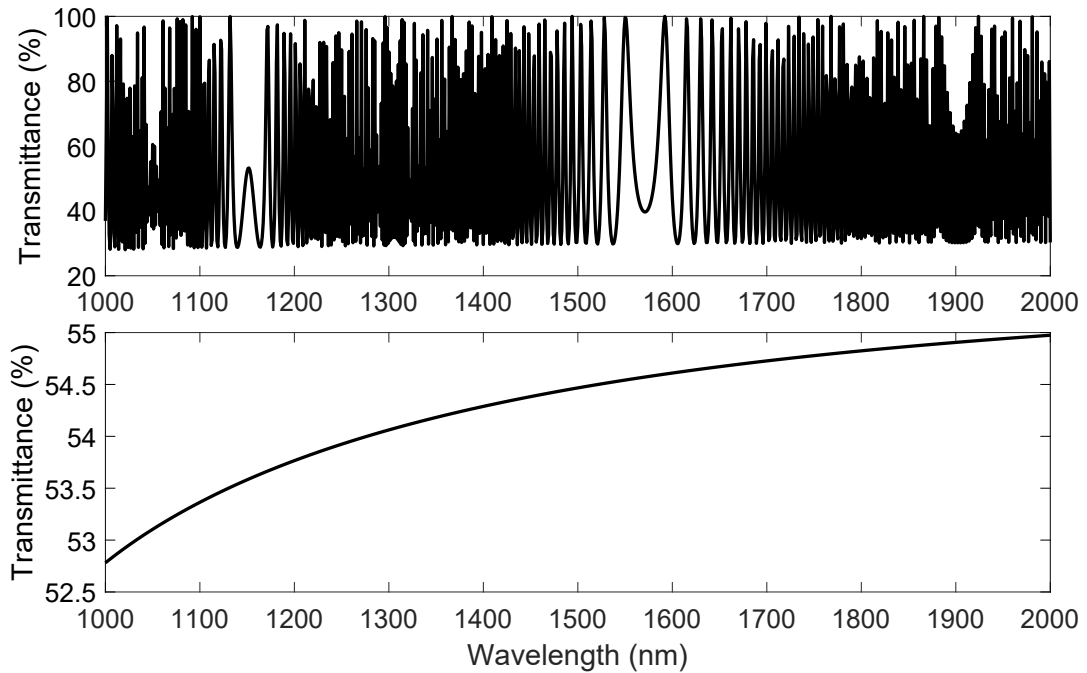


Figure 2.3: **Top:** The simulated transmittance of a transparent 350 μm GaAs substrate in air with no corrections for incoherence. **Bottom:** The same substrate corrected for incoherent reflections inside the thick material.

2.1.1.6 Programming Requirements

MATLAB was chosen to implement the TMM due to its inherent ability to handle matrix manipulation and complex numbers. The resultant function requires the focus wavelength, an array of layer thicknesses, and an array of complex refractive indices, corresponding to the individual layers of the sample. The function then returns the normal reflectance and transmittance at the focus wavelength, meaning that simulating a full spectrum is a matter of looping the function over the desired range of wavelengths. Support functions were also made to simplify the implementation of the method, mainly to find the matrices \mathbf{P}_m and $\mathbf{T}_{m,m+1}$. The full code can be seen in chapter 8.

2.1.1.7 Advantages and Disadvantages of the TMM

The transfer matrix method is simply a numerical calculation, however long the matrix multiplication may be. The result of this is that it can be incorporated into any program as a stand-alone function, allowing for almost limitless freedom in automation and iterative design. This functional nature also allows complex simulations to be built around systems with varying layer properties. One example that is examined later in this work is the optical monitoring of semiconductor etching process, where the reflectance of a sample is measured as material is removed. The time-varying intensity can be used to very accurately predict the end point for the process. However, the TMM is computationally intensive and the basic function is limited to the reflectance and transmittance. While it is possible to get the electric field profile, it adds a great deal of complexity and running time to the program. Additionally, any statistical analysis requiring many small changes to the structure would be extremely time intensive, and these kind of analyses are essential for optical design and optimisation. It was decided that for intensive design work a commercial piece of software should be used for speed and accuracy.

2.1.2 TFCalc Modelling Software

The pre-made software TFCalc from Software Spectra Inc. was selected for more in-depth optical modelling and design. TFCalc has several advantages over the TMM as well as a small number of drawbacks:

Some examples of TFCalc's more advanced features are described below.

Advantages	Disadvantages
Fast. Self-contained (no programming needed). Automatic optimization to targets. Electric field modelling. Design sensitivity modelling (Monte Carlo). Refractive index interpolation.	Manual refractive index entry (one file per material). Manual layer variations (see etch simulation).

2.1.2.1 Example: Cavity Optimisation

One of the more powerful tools within the software is the ability to optimize to a target. In the following example, a resonator is constructed using a pair of GaAs/AlAs distributed Bragg reflectors (DBRs) and an AlAs cavity with the aim to create a resonance at 1550 nm. TFCalc will automatically calculate the quarter-wave thickness required for the DBRs and the cavity was given a starting thickness of 200 nm. The starting and resulting spectra are shown in figure 2.4(a) and figure 2.4(b) respectively.

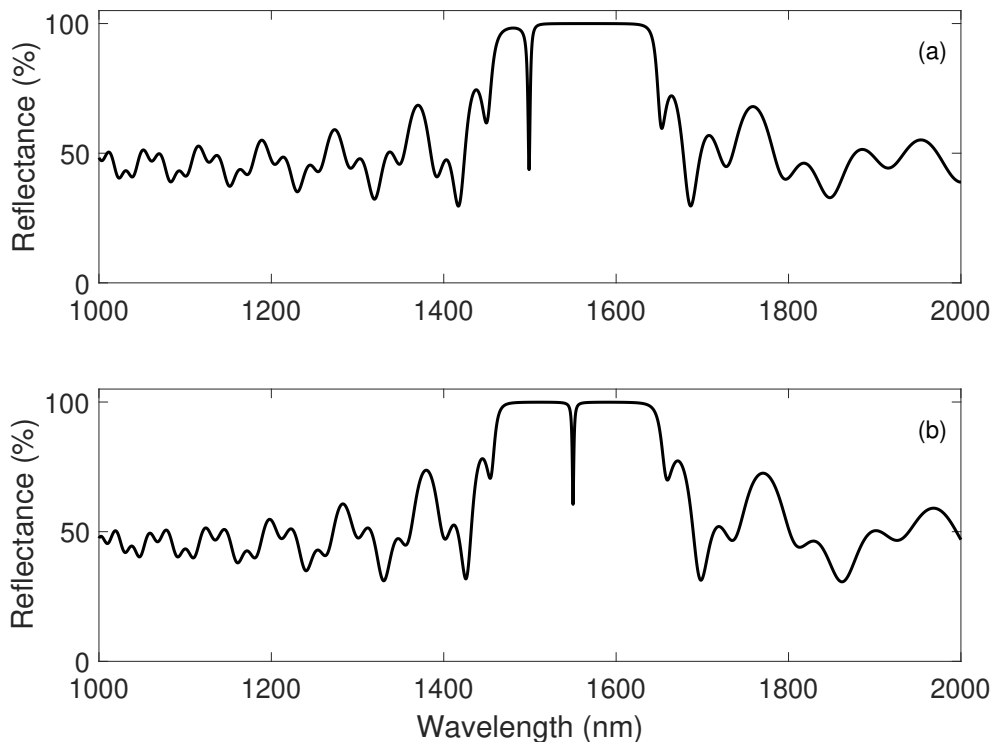


Figure 2.4: (a) The simulated reflectance of an example GaAs/AlAs 1550 nm resonator with an estimated AlAs cavity thickness of 200 nm showing the Fabry-Perot dip at 1498 nm. (b) The simulated reflectance of the same resonator after the TFCalc optimisation of the cavity thickness, with the Fabry-Perot dip now at the correct (1550 nm) wavelength.

Figure 2.4(a) shows the stop band is correctly centred and the cavity resonance is

around 50 nm too short. It would be possible to change the layer thickness by hand and until the correct position is achieved but the process is both inaccurate and time-consuming. Instead, TFCalc's native optimisation can be utilised by giving the software the target of minimising reflectance at 1550 nm, and selecting the cavity layer for optimisation. The cavity will be iteratively varied until a closest match is found. TFCalc determined that the cavity should be 268 nm thick to produce a resonance at our desired wavelength. The optimised spectrum can be seen in figure 2.4(b), clearly showing the cavity at 1550 nm. The process took a few seconds, making it an obvious choice for designing optical structures with specific wavelength goals in mind.

2.1.2.2 Example: Sensitivity Analysis

Another useful tool from the software is the sensitivity analysis. This utility takes a structure and varies the layer thicknesses according to a specified distribution and number of trials. By overlaying the result of each trial the user gains insight into how real layer thickness variations, for example due to growth inconsistencies, affect the final product. In the case of a resonator it can tell us whether the cavity resonance is tolerant to an imperfect design.

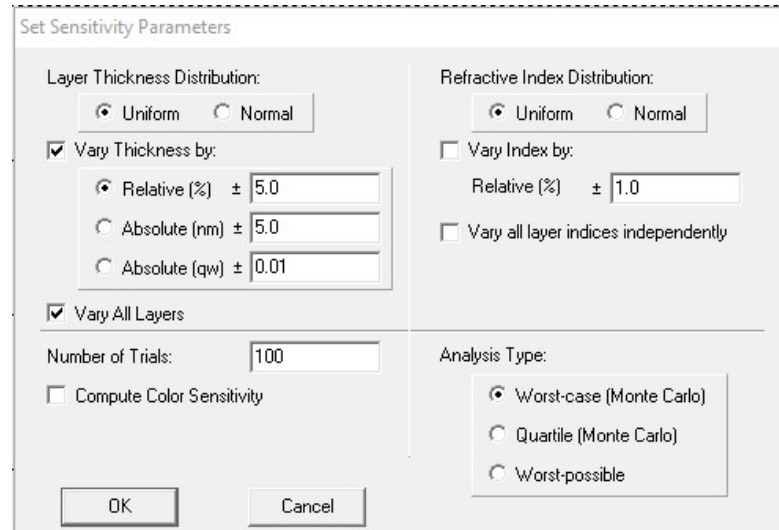


Figure 2.5: TFCalc window for assigning the sensitivity parameters to the model. Both layer thickness and refractive index can be varied, with distribution type determining whether the values are varied depending on a fixed uniform value, or by a normal distribution of thicknesses within the range set by the user. The type of variation can be a relative percentage, or by a fixed thickness. The number of trials can be set, as well as the type of Monte Carlo analysis to run. A worst-possible analysis will set all parameters as far from specification as possible within the set parameters to determine the outcome.

The parameters used to assess the tolerance of a design are entered as shown in fig-

ure 2.5. Most are self explanatory: the thickness variation can be a relative percentage, or a maximum value. The absolute value can either be in the physical thickness (nm), or the optical thickness in units of quarter-wavelengths with respect to the target wavelength (set during structure entry). In the case of our MBE machine, 5% is a reasonable value. A larger number of trials will result in a smoother output trace, but will take longer to run. It is worth noting that in the case of a sample with a large number of layers, 1000 trials may take around 30 minutes to run. A Monte Carlo technique was used rather than the worst-case.

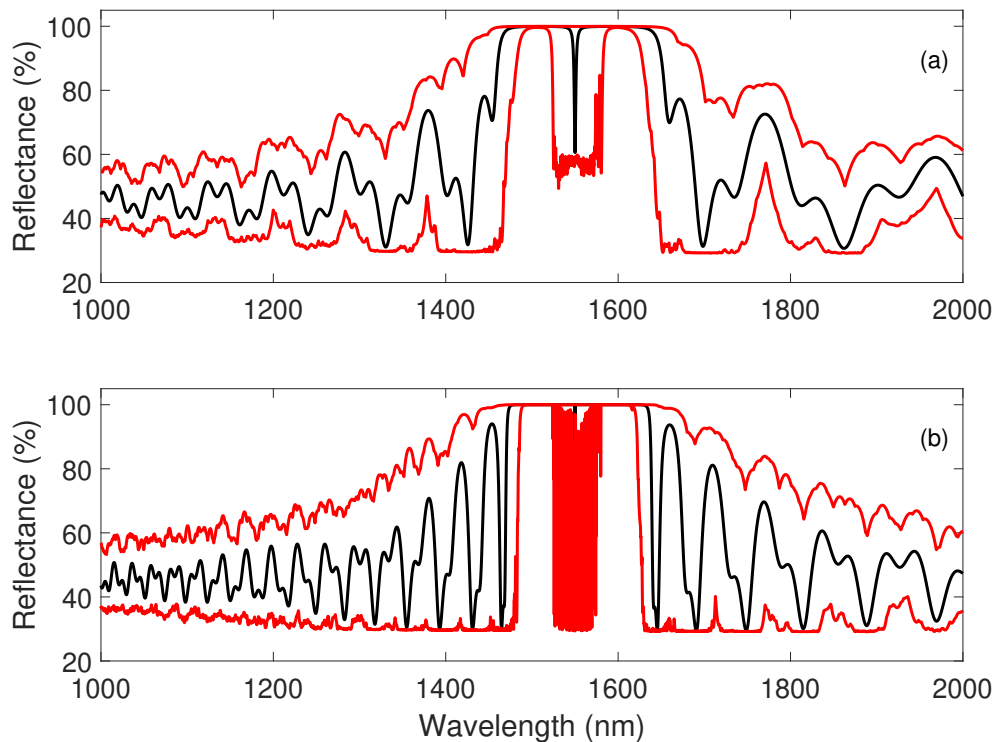


Figure 2.6: (a:) The simulated reflectance from figure 2.4(b) after 1000 randomised thickness variation trials using a uniform distribution of $\pm 5\%$. The red lines show the superposition of every trial. (b:) An identical trial performed on a design with a much stronger resonance due to a larger number of DBR repeats on either side of the cavity.

Figure 2.6(a) shows the tolerance of the sample design in figure 2.4b after 1000 randomised thickness trials. The red curves show the maximum combined variance of every trial and can show us the level of tolerance the design has to variations in thickness. Cavity sensitivity is low, which is evidenced by the large amount of white space beneath the red curve around 1550 nm. As a comparison, a similar resonator with a much larger number of DBR repeats, and thus a stronger resonance, is shown in figure 2.6(b) after the same analysis. It is clear that the structure in figure 2.6(b) is much more sensitive to small changes, so while one may think that a stronger resonance may make it a better

design, lack of tolerance would likely make it difficult to produce a working device.

2.2 Vertical-Cavity Surface-Emitting Lasers

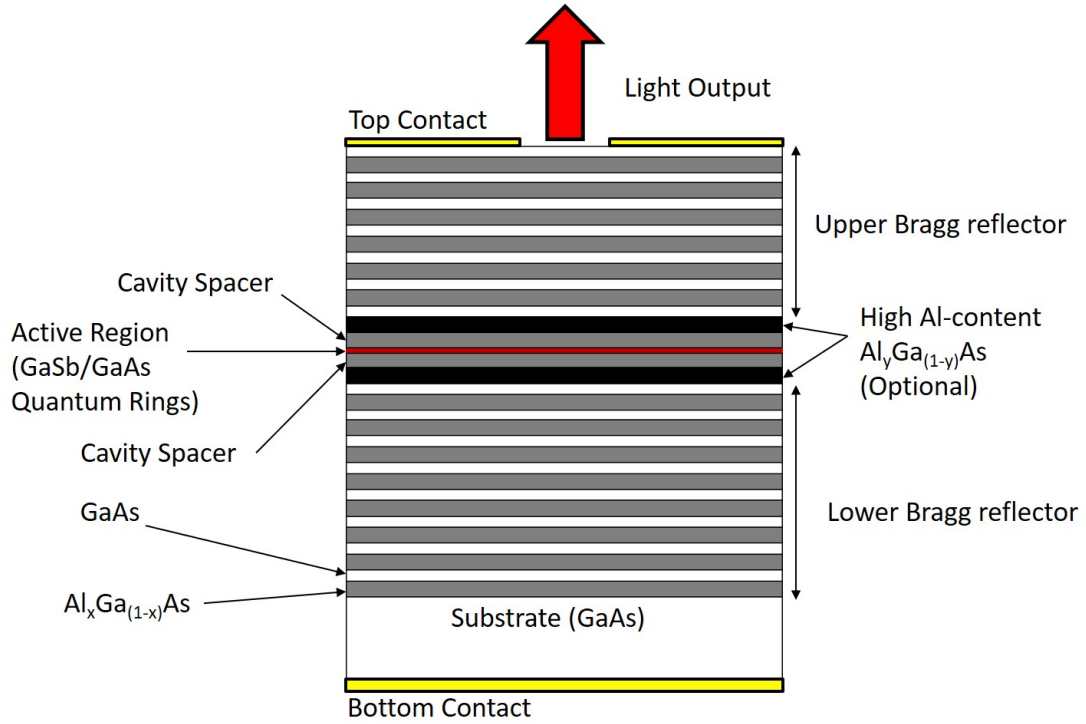


Figure 2.7: Schematic showing the primary components of a GaAs - $\text{Al}_x\text{Ga}_{1-x}\text{As}$ VCSEL

A VCSEL consists of three primary components: a lower DBR, the active region embedded in a cavity, and the upper DBR. The diagram in figure 2.7 shows a cross-section of a typical GaAs - $\text{Al}_x\text{Ga}_{1-x}\text{As}$ device, with top-bottom contacts and top surface light emission. The active region is embedded within $\text{Al}_x\text{Ga}_{1-x}\text{As}$ spacer layers to provide the necessary thickness of material for a cavity resonance at the chosen wavelength, and to act as a well containing the carriers around the active region. More detail on the active region and cladding layers is provided in section 2.2.2. The high Al-content layers provide the option to perform wet oxidation, creating an insulating ring of AlO_2 with an unoxidised central window. The purpose of this step is to force the carriers into the centre of the device, increasing current density and reducing carriers lost around the edge of the mesa.

2.2.1 Distributed Bragg Reflectors

An essential component of many vertical cavity resonators is the pair of DBRs tuned to create a band-stop mirror around the desired wavelength of the outgoing light. DBRs

are simple in design, comprising quarter-wave-optical-thickness layers with alternating high and low refractive index material to create an interference mirror. Two types of GaAs - $\text{Al}_x\text{Ga}_{1-x}\text{As}$ DBRs will be used in this work, one grown at Lancaster by MBE and one at IQE by MOVPE. For the purposes of this discussion, the primary difference between the two methods is the nature of the layer interfaces. An MBE system can produce very abrupt interfaces between materials due to the low growth speed and fine source control. MOVPE, on the other hand, is a much faster chemical-based process, and as such lacks the ability to change sources quickly. To ensure quality growths while maintaining speed, the sources switch to the new layer settings over some thickness t_g . This additional thickness will certainly impact the optical behaviour of the mirrors, and will be discussed in the following sections.

2.2.1.1 Square-Interface Distributed Bragg Reflectors

The core physics of a DBR system will be discussed using the assumption that the layer interfaces are perfectly abrupt. Therefore, it will be assumed that the interfaces can be described using standard Fresnel expressions outlined above in section 2.1.1.4. To demonstrate the interference effect in a DBR system we will look at the path difference between a wave reflected from the first interface, and one reflected by pair of layers with differing refractive indices.

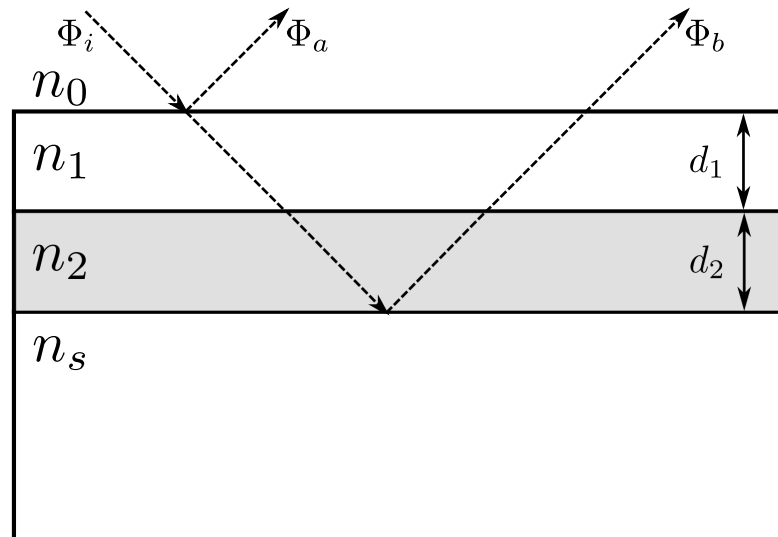


Figure 2.8: Schematic showing paths a and b travelling through a structure with two layers on a substrate, where $n_1 = n_s > n_2 > n_0$. All interfaces produce a reflected and transmitted component, so other paths through the structure are neglected for this example. Additionally, the paths are drawn at an angle for clarity, all paths are normal to the surface of the structure.

To compare the two paths in figure 2.8 the path length in each layer must be found.

The straight-line optical path length Λ in a homogeneous medium is

$$\Lambda = nd, \quad (2.2.1)$$

where n is the refractive index in the medium and d is the geometric length of the path. The other factor to be considered is the phase change upon reflection, for which there are three cases:

$$\text{Case 1: } n_1 = n_2,$$

$$\text{Case 2: } n_1 > n_2,$$

$$\text{Case 3: } n_1 < n_2.$$

Each of these cases can be easily interpreted using the Fresnel reflection coefficient from equation (2.1.38) and the field relation

$$\vec{E}_r = r_{1,2}\vec{E}_i, \quad (2.2.2)$$

giving

$$\vec{E}_r = \frac{n_1 - n_2}{n_1 + n_2}\vec{E}_i, \quad (2.2.3)$$

where \vec{E}_i is the incident electric field and \vec{E}_r the field upon reflection. In Case 1, $r_{1,2}$ is zero, resulting in no reflection. This is consistent with a uniform refractive index across a boundary. Case 2 results in a positive reflection coefficient, and thus no change in phase upon reflection. However, Case 3 will produce a negative $r_{1,2}$, which is equivalent to the following:

$$\vec{E}_r = -|r_{1,2}|\vec{E}_i. \quad (2.2.4)$$

It is easily determined from equation (2.2.4) that the reflected electric field is inverted. Thus, any time a wave reflects from an optically denser medium, it undergoes a phase change of π or an optical path difference of $\lambda/2$. [25] The optical path difference in figure 2.8 can now be calculated:

$$\Phi_a = \frac{\lambda}{2}, \quad (2.2.5)$$

and

$$\Phi_b = 2(n_1d_1 + n_2d_2) + \frac{\lambda}{2}. \quad (2.2.6)$$

By choosing to give each layer an optical thickness of $\lambda/4$ equation (2.2.6) becomes

$$\Phi_b = 2\left(\frac{\lambda}{4} + \frac{\lambda}{4}\right) + \frac{\lambda}{2} = \frac{3\lambda}{2}. \quad (2.2.7)$$

So the path difference between Φ_a and Φ_b is given as

$$\Phi_b - \Phi_a = \frac{3\lambda}{2} - \frac{\lambda}{2} = \lambda. \quad (2.2.8)$$

A path difference of lambda means the two waves are in phase, and thus constructively interfere, reflecting light of that wavelength. Therefore, for a DBR with N pairs of repeating layers, the reflected light always constructively interferes producing a high-reflectivity band-stop mirror centred around some wavelength λ_0 .

2.2.1.2 Reflectivity of a DBR

It can be shown ([25]) that for N pairs of layers, the overall reflectivity R at λ_0 is

$$R = \left(\frac{1 - \frac{n_s}{n_0} \left(\frac{n_1}{n_2}\right)^{2N}}{1 + \frac{n_s}{n_0} \left(\frac{n_1}{n_2}\right)^{2N}} \right)^2, \quad (2.2.9)$$

where n_0 is the refractive index of the originating medium, n_1 and n_2 the high and low refractive indices of the DBR respectively, and n_s the refractive index of the substrate, all at the centre wavelength λ_0 . For a GaAs - Al_{0.9}Ga_{0.1}As DBR at a centre wavelength of 1550 nm (telecoms C band) the following reflectivity is produced [30, 31, 32].

Figure 2.9 demonstrates the effect of increasing the number of quarter-wave repeats in a typical DBR. While the reflectance initially increases rapidly, it soon becomes evident that to achieve an extremely high reflectance a much greater number of layers is required.

Equation (2.2.9) is not sufficient to understand the wavelength dependent behaviour of the DBR, as only the peak reflectivity is calculated. A simulation based on the TMM in section 2.1.1 is required, which in turn means that the full wavelength dependent refractive indices are needed for each layer of the structure. The results of a full wavelength TMM simulation of the same DBR from figure 2.9 are shown in figure 2.10. These demonstrate the effect of adding more layers to the DBR on the peak reflectivity, and to both the width and shape of the stop band.

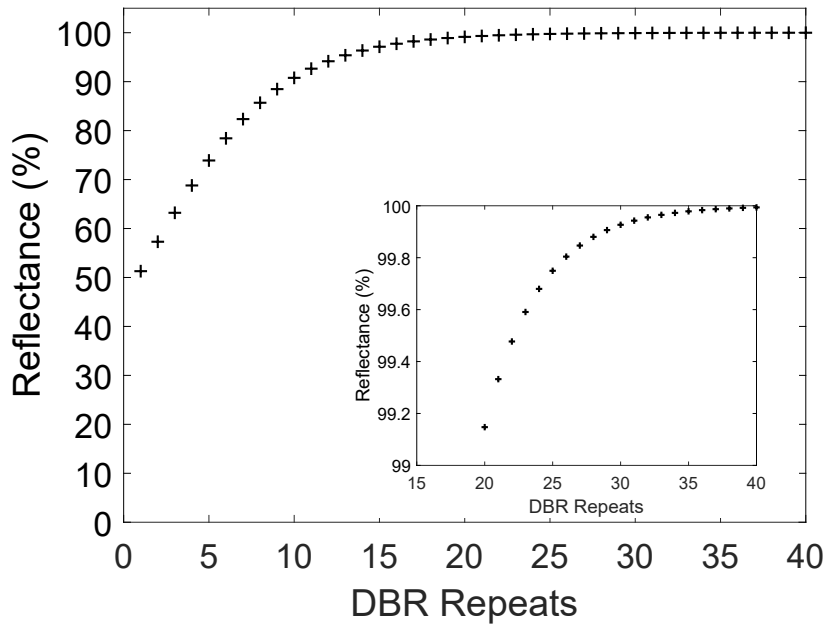


Figure 2.9: Calculated peak reflectance of a GaAs - $\text{Al}_{0.9}\text{Ga}_{0.1}\text{As}$ DBR with an increasing number of quarter-wave pairs. The inset shows a zoomed view of the high (greater than 99%) reflectivity behaviour as the number of repeats increases.

2.2.1.3 Graded-Interface Distributed Bragg Reflectors

MOVPE is desirable for mass-production of VCSELs due to its growth speed and scalability. With the chemical nature of the process, along with the rapid growths, abrupt interfaces are replaced with a gradual change between the two material compositions. For our GaAs - $\text{Al}_x\text{Ga}_{1-x}\text{As}$ system this presents an additional challenge, since the aluminium source needs to be shut off entirely for the GaAs layers. To ensure consistency between layers, the IQE DBR instead uses $\text{Al}_{0.12}\text{Ga}_{0.88}\text{As}$ - $\text{Al}_{0.9}\text{Ga}_{0.1}\text{As}$ with the layer change occurring over a t_g of 20 nm. In order to model the new system, alterations need to be made to the structure used in the simulations. By dividing the 20 nm region by the average monolayer thickness of the two DBR layers, utilising the fact that GaAs- $\text{Al}_x\text{Ga}_{1-x}\text{As}$ are almost lattice-matched, the linear grading is replaced with a digitally graded staircase as seen in figure 2.11.

To correct for the additional thickness of the graded layer, the optical path length of the entire staircase Λ_g must first be calculated. This is the sum of the refractive indices n_m multiplied by the average monolayer thickness $t_{monolayer}$ for a total number of steps M , where

$$M = \frac{t_{grading}}{t_{monolayer}}, \quad (2.2.10)$$

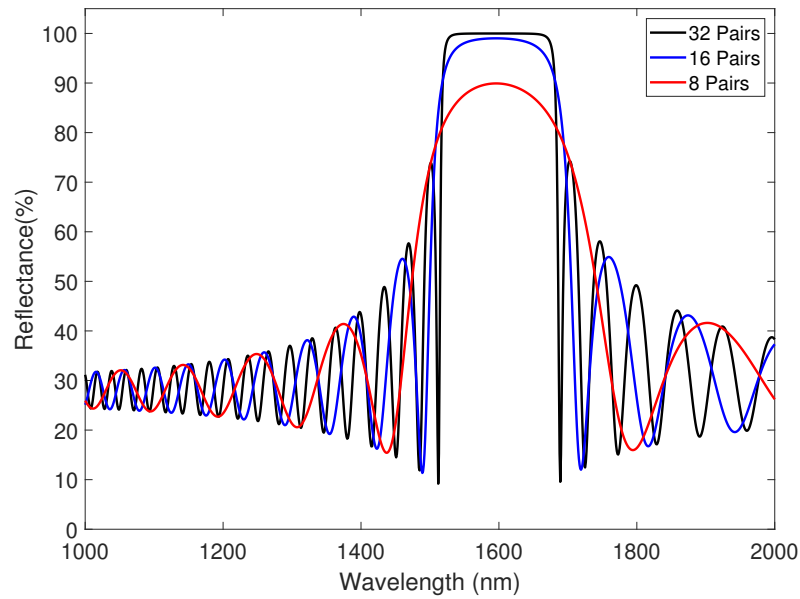


Figure 2.10: Simulated reflectance spectra of a GaAs - $\text{Al}_{0.9}\text{Ga}_{0.1}\text{As}$ DBR with an increasing number of quarter-wave pairs.

for a grading total thickness $t_{grading}$ (20 nm in figure 2.11. The optical thickness can then be written as

$$\Lambda_g = t_{monolayer} \sum_{m=1}^M n_m. \quad (2.2.11)$$

The thickness of the fixed material (flat) section of the DBR layer then becomes:

$$t_{layer} = \frac{1}{n_{layer}} \left(\frac{\lambda}{4} - \Lambda_g \right), \quad (2.2.12)$$

where t_{layer} is the physical thickness of the layer, n_{layer} the refractive index of that layer, and λ is the target reflected wavelength. Using the structure generated by this method, the optical simulation can be carried out as normal. The major disadvantage of this technique is the large increase in the number of layers that the model has to handle, since each step in the grading layer becomes its own layer with interface and propagation matrices. More layers means increased computation time, and the potential for the build-up of errors if there are inaccuracies in the refractive index data.

2.2.2 GaSb Quantum Rings in Quantum Well Active Region

Long wavelength emission has been achieved with multiple active regions on GaAs, including InAs quantum dots and GaInNAs quantum wells. InAs quantum dots demonstrate low-threshold and low resistance devices at the target wavelength, however the output power is very low and thus not suitable[33]. GaInNAs quantum wells perform

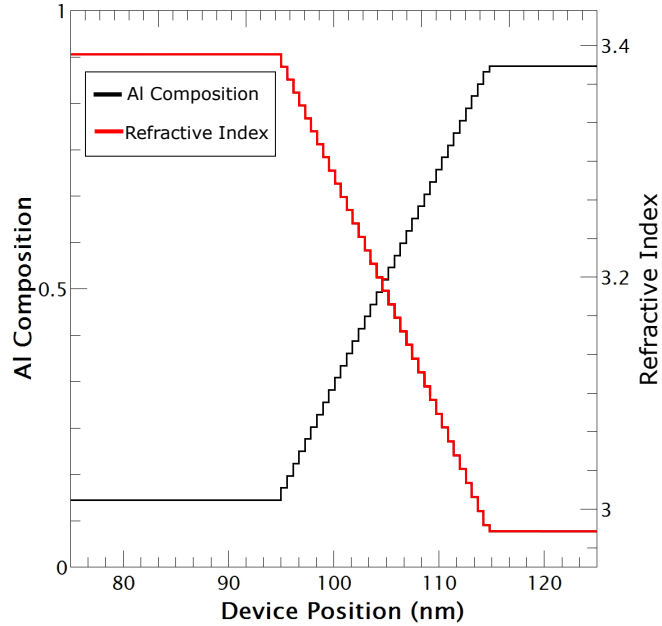


Figure 2.11: Digital-monolayer approximation of the graded interface for a $\text{Al}_{0.12}\text{Ga}_{0.88}\text{As} - \text{Al}_{0.9}\text{Ga}_{0.1}\text{As}$ DBR showing the changes in composition and refractive index.[30, 31, 32]

well at $1.18\ \mu\text{m}$, with high temperature operation and output powers above $5\ \text{mW}$, but have difficulty in reaching the $1.3\ \mu\text{m}$ target wavelength. Additionally the incorporation of nitrogen can increase the number of defects, affecting device performance[34, 35]. Following on from the work of P.Hodgson[24], GaSb quantum rings (QRs) embedded inside a GaAs - $\text{Al}_x\text{Ga}_{1-x}\text{As}$ quantum well were selected to determine their suitability as the active region to produce $1.3\ \mu\text{m}$ laser emission. A small number of GaSb monolayers deposited on GaAs will form quantum dots (QDs) via the Stranski–Krastanov method, due to the large (78 %) lattice mismatch between the two materials ($5.654\ \text{\AA}$ for GaAs versus $6.096\ \text{\AA}$ for GaSb) [36][37]. By then capping the GaSb with a layer of GaAs, the increased strain in the centre of the QD will lead to the Sb diffusing away, forming a ring-like structure[38][39]. Through further investigation it has been determined that ring formation can be improved by first capping with a thin, lower-temperature GaAs layer, then a second GaAs layer with a temperature increase of approximately $100\ ^\circ\text{C}$ [40]. The type-II system serves to deeply confine the holes within the GaSb layer[41], while the electrons remain unconfined. However, the Coulomb interaction binds electrons to the ring [42][43]. To complete the active region, the GaSb QRs are grown inside a GaAs - $\text{Al}_x\text{Ga}_{1-x}\text{As}$ quantum well (QW)[24]. The schematic of the active region is shown in figure 2.12(a), demonstrating the confinement of the holes in the GaSb and the electrons held by the Coulomb interaction. The well may serve to confine electrons that are fur-

ther away from the ring and prevent them escaping the active region, and allows the system to be more easily incorporated into a cavity.

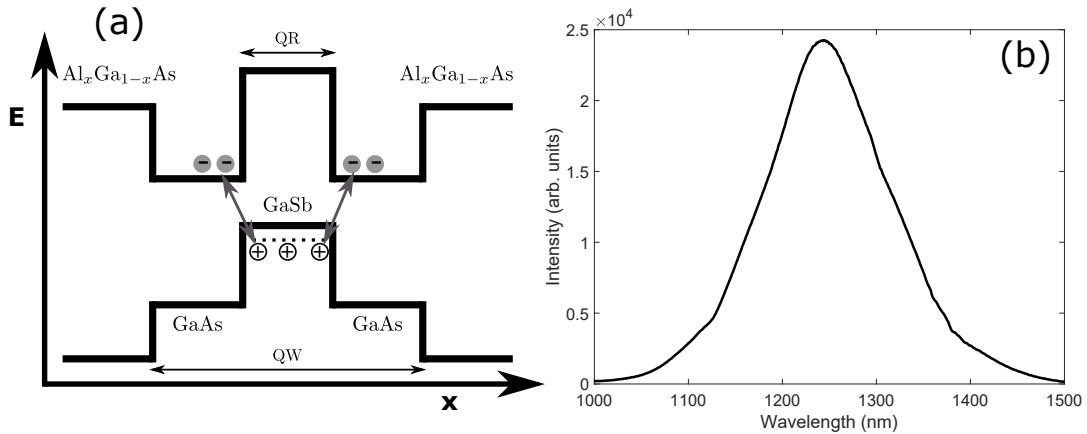


Figure 2.12: **(a)**: A schematic of the type-II GaAs - GaSb - GaAs structure showing the confined holes and unconfined electrons. **(b)**: Typical room-temperature light emitting diode (LED) emission from a QR active region measured by P. Hodgson.

Dr. P. Hodgson grew several of these active regions with varying well widths, doping, number of quantum ring layers and they were processed by CST to produce a set of LEDs[44]. A typical room-temperature emission is visible in figure 2.12(b) showing that light is emitted from 1 - 1.5 μm , the implication of this is that with the right wavelength-selective cavity, any wavelength within that range could be generated in a VCSEL device.

2.2.3 Cavity Design

At the core of a VCSEL design is the active region embedded in an optical cavity resonator. While high-reflectivity mirrors are obtained via the use of DBRs, the interface between the active region and the mirrors must be taken into consideration. As discussed in section 2.2.1, when light is incident on an optically denser medium its reflection undergoes a change of phase. This is essential for the production of the standing wave required to resonate at whichever wavelength the designer has chosen[25]. Therefore, in a GaAs - $\text{Al}_x\text{Ga}_{1-x}\text{As}$ system such as ours, the higher-index GaAs is needed to form the boundary of the cavity and ensure that the resonant frequency is consistent with the designer's expectations.

If the active region was simply the GaSb QRs in bulk GaAs, the optical design would be challenging, as there would need to be a material with an even higher refractive index to provide the phase change required. By incorporating the QRs into a quantum well as shown in figure 2.12, the $\text{Al}_x\text{Ga}_{1-x}\text{As}$ barrier layers can be extended to make up the majority of the cavity. Their thickness can then be tuned to select the wavelength and

the order of resonance within the cavity itself, and their index contrast with GaAs can be exploited to interface the cavity with the last layer of the upper and lower DBRs.

The next task in the design of a cavity is to set the optical length of the resonator. In our case, this is achieved by changing the thickness of the two $\text{Al}_x\text{Ga}_{1-x}\text{As}$ spacers on either side of the active region. Since the electric field has a certain penetration depth into the DBRs, the actual cavity resonance will not be exactly equal to the optical length of the actual cavity. By using TFCalc's optimization as outlined in section 2.1.2, the spacer layers can be varied to produce a cavity resonance at the target wavelength. The electric field can then be calculated to confirm the presence of an antinode centred over the active region to provide maximum coupling between the carriers and the field. The final consideration is to adjust the position of the ring layers to correspond with an antinode of the electric field through the device to ensure that the field couples with the carriers to the fullest extent.

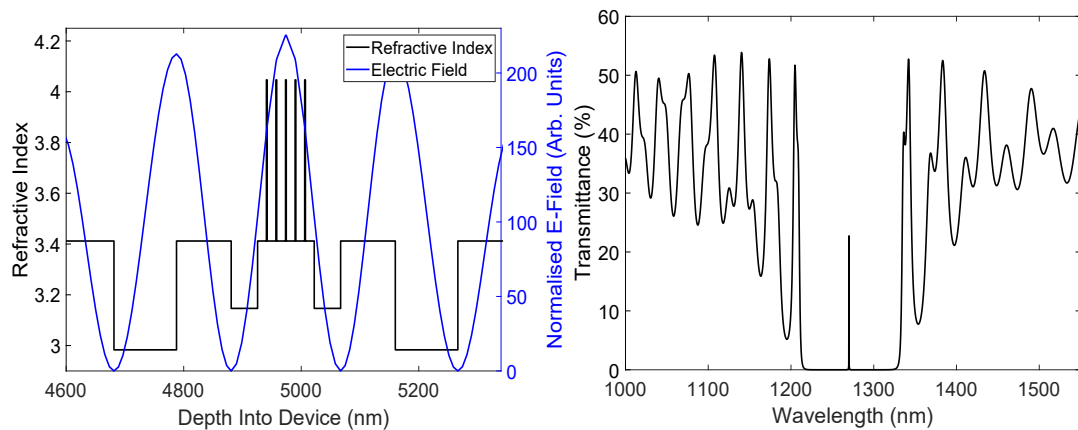


Figure 2.13: **Left:** Overlay of the normalised electric field profile and the refractive index profile of the cavity inside a simulated VCSEL at a target wavelength of 1270 nm. **Right:** The modelled transmittance spectrum of the VCSEL containing the optimised cavity.

The left of figure 2.13 shows an antinode of the electric field inside a simulated $\lambda/2$ VCSEL cavity with 24 and 30 upper and lower DBR pairs, respectively. The field clearly aligns with the GaSb quantum ring layers to provide maximum coupling between the field and the carriers. The right of figure 2.13 shows the simulated transmittance spectrum with a clear peak at the target wavelength of 1270 nm.

With the simulated VCSEL design optimised, the next stage in the process is to grow the structure and optically test it to ensure the growth meets design specifications. In the event that it does not, characterisation methods are required to determine the cause of any discrepancies and match the measured transmission to the modelled values.

The following chapters detail the methods used to characterise semiconductor material to determine its physical and optical properties, allowing for more accurate models and future growths.

Chapter 3

Optical Measurements - Background and Methods

Optical methods are extensively used in semiconductor resonant cavity characterisation due to their speed and non-destructive nature[16, 45, 46, 47, 48]. Measuring the optical reflectance or transmittance spectrum of a sample and comparing it to the modelled spectrum allows for the determination of growth parameters and overall quality. For a VCSEL the Fabry-Perot dip and the alignment of the DBRs can be measured without the need for cross-sectioning or processing. Being able to non-destructively measure the deviation from specification can prevent a researcher or manufacturer from wasting time and resources processing a sample which had little chance of functioning.

3.1 Reflectance and Transmittance Measured By Cary 5000 Spectrophotometer

3.1.1 Spectrophotometry - Transmission

Spectrophotometry is a technique used to determine the optical properties of a material or structure by sending a beam of monochromatic light through the sample and measuring the intensity of the exiting beam. Generally this is done using a white light source, which is then collimated and passes through a monochromator before hitting the sample. The beam intensity is measured on the far side of the sample by a detector. A general schematic of a spectrophotometer is shown in figure 3.1.

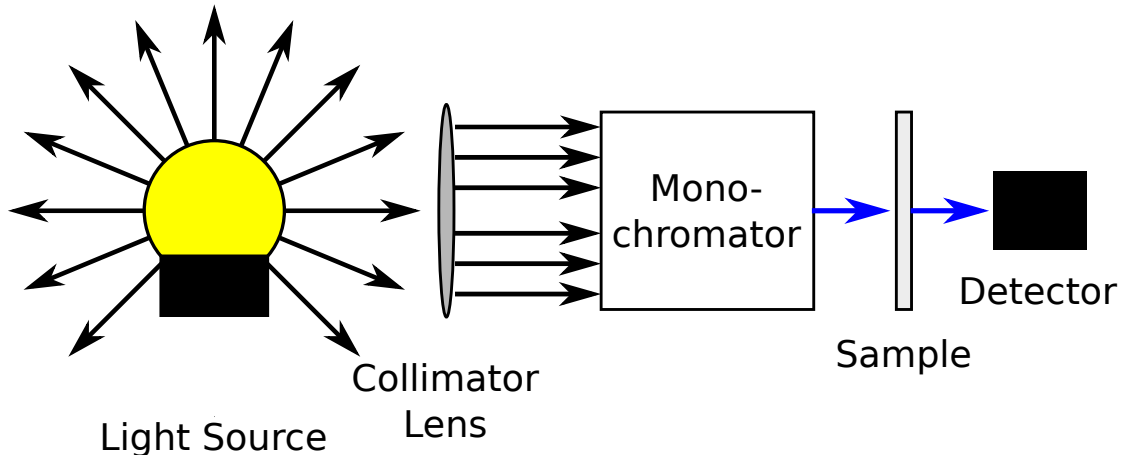


Figure 3.1: Schematic of a spectrophotometer.

A Cary 5000 spectrophotometer from Agilent Technologies was used to measure the optical properties of our samples. A halogen lamp is used to produce the light and is coupled to the rest of the spectrophotometer via a set of Schwarzschild optics. The wavelength is selected using an out-of-plane double Littrow monochromator intended to reduce noise and stray light. Beam measurement is via an Agilent ‘PbSmart’ detector.

To increase precision, the Cary 5000 uses a dual-beam system whereby the intensity of the sample beam is compared to a rear reference passing through a control sample. It is therefore possible to measure at extremely low light levels, as long as the reference is suitably attenuated. A key advantage of the Cary system is the large sample chamber allowing for a large number of accessories to be used, each with their own specific functions. For a simple transmission measurement on a piece of semiconductor, the solid state sample holder was used. The empty chamber and the solid sample holder are visible in figure 3.2.

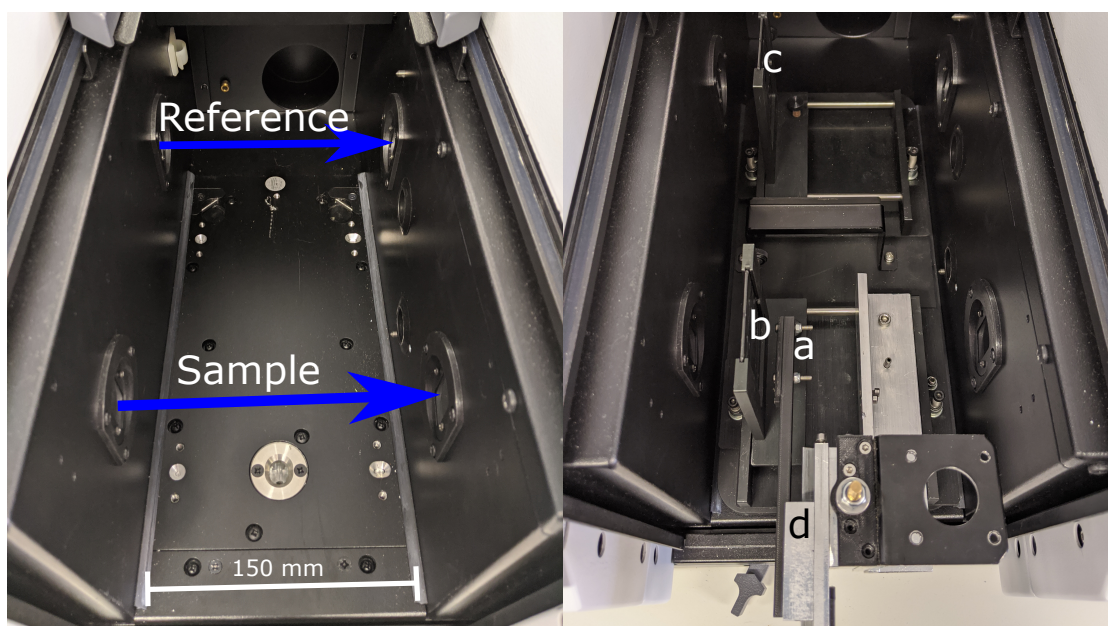


Figure 3.2: **Left:** Cary 500 sample chamber showing the parallel sample and reference beam paths. **Right:** Sample chamber with solid state sample holder fitted. **a:** Sample holder arm. **b:** Sample beam aperture plate. **c:** Reference beam aperture plate. **d:** Adjustable mount for sample arm (with optional motorisation).

Setting up a transmission measurement is straightforward: mount the sample by its edge in the holder arm (figure 3.2a), select a beam aperture of the desired size if required ensuring both beams are set equally (figure 3.2b and c), and position the sample using the adjustable mount (figure 3.2d).

3.1.2 Reflectance

In order to measure the reflectance of a sample, the reflected beam must be directed towards the detector. This is difficult to achieve if a normal incidence is required and is normally approached with redirecting optics or an integrating sphere. Optics are required to direct the beam to the sample, and then to detector, often requiring beam splitting, multiple mirrors, or optical fibres. The drawback of an optical system like this, while it

may approach normal incidence, is the loss occurring from interaction with the various components in the system. Absolute reflectance measurements are therefore difficult to obtain without extensive calibration and pre-made standard samples. An integrating sphere collects all of the reflected light using an extremely reflective coating, allowing it to be collected onto a detector. Since the sphere collects the majority of the light, finding the absolute reflectance is possible with appropriate baseline measurements. A useful feature of many integrating spheres is the ability to isolate the specular and diffuse components of the reflection, thus qualitatively characterising the surface of the sample. For example, a poorly grown surface will be more diffuse than a perfect crystalline finish. Figure 3.3a shows a sphere with the sample at an angle θ to collect all components of the reflection while figure 3.3b demonstrates how a normally oriented sample can re-reflect the incident beam, removing it from the sphere and isolating the diffuse components. By measuring a sample in both orientations and then subtracting one from the other, the specular component can be isolated as well.

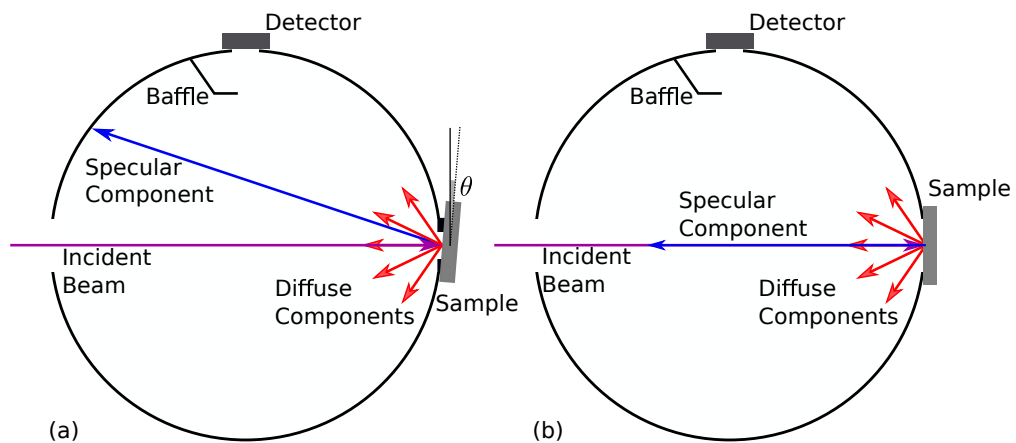


Figure 3.3: An integrating sphere collecting reflected light from a sample with **a**: all components included and **b**: the specular component removed thus collecting only the diffuse reflections.

An integrating sphere was used for reflectance measurements primarily because there was already one with the system, and buying a mirror-based reflectance accessory would have been expensive and unnecessary. The Agilent diffuse reflectance accessory (DRA 1800) can measure reflectance up to 1800 nm in wavelength, and comes with calibration standards for achieving accurate baselines.

3.1.2.1 Reflectance Baselines

Measuring absolute reflectance at normal interface is challenging due to the difficulty in collecting the reflected light without allowing the incident light to affect the measure-

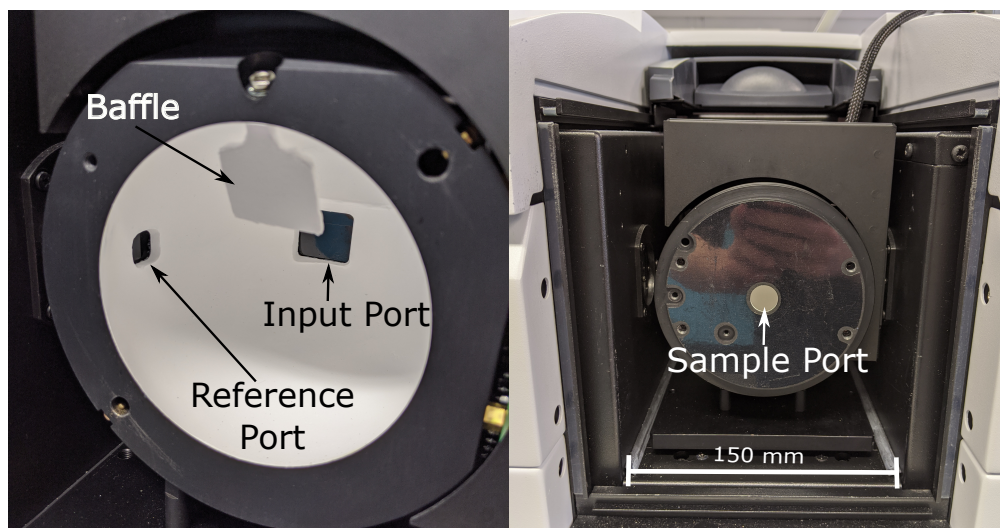


Figure 3.4: **Left:** the integrating sphere with cover removed, showing the reflective coating and access ports. **Right:** The sphere with cover in place, showing the port used for measurements.

ment. To calibrate the integrating sphere correctly, the sample port must be covered with one of the standards shown in figure 3.5. These samples are made from the same material as the inside of the sphere, and as such behave similarly to an ideal, highly diffuse reflector. Placing the large standard (figure 3.5(a)) over the sample port provides an accurate representation of an ideal but diffuse reflector. As shown in figure 3.5(c), the thickness of the chamber wall means that when light is reflected at a very high angle, it will hit the sides of the port and be terminated. When a sample is highly specular, such as the semiconductor wafers used in this work, virtually all of the light will be reflected according to the angle of incidence. In this case, no light would be lost to the sample port wall and the calibration would be inaccurate. To combat this, a second protruding reference is used as shown in figure 3.5(b). Figure 3.5(d) explains how a diffuse surface emulates a specular one, by sitting flush inside the chamber allowing all reflected light to be collected.

Finally, a zero baseline must be taken to complete an accurate background measurement. Simply leaving the sample port uncovered and allowing the beam to terminate against the matt black surface of the sample chamber is sufficient for a low-noise zero baseline.

3.2 Wafer Mapping

A benefit of the Cary 5000's large sample chamber is the possibility to add various accessories to aid and enhance sample measurements. A particularly useful application is

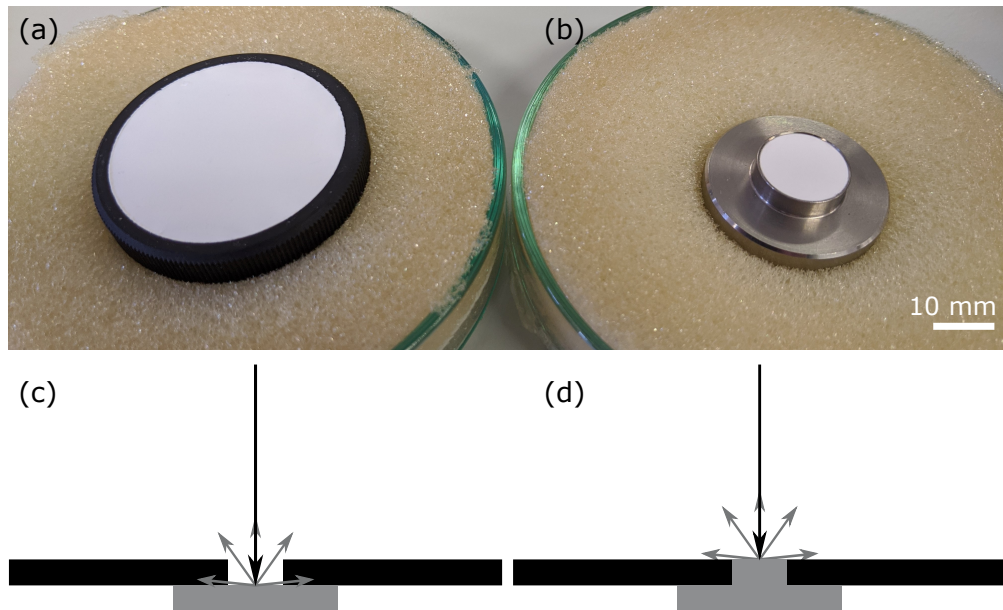


Figure 3.5: **(a)**: The flat calibration standard used to calibrate for diffuse samples. **(b)**: The protruding calibration standard used to emulate highly specular samples. **(c)**: The flat calibration standard in position showing how high-angle reflections are lost to the sample port wall. **(d)**: The protruding standard allows all of the reflected light to be collected, thus behaving more as a specular surface.

the potential to measure the transmission of a sample at different points on the surface, thus giving an idea of the consistency of the growth and how it affects the optical properties.

3.2.1 Wafer Mapper Hardware

An in-house automated system was designed to map samples up to 60×52 mm in size and is shown in figure 3.6.

The wafer mapper uses a precision linear rail for the horizontal x-axis, moving in-plane and perpendicular to the sample beam, and rod-mounted slide bearings for the vertical y-axis. Stepper motors allow for precise sub mm positioning, with the smallest aperture producing a spot size of 0.5 mm. The system is automated with a custom user interface for the adjustment of scanning parameters, while the sample mounting system allows different arms to be used for different sample shapes and sizes. Manual position selection is also available, allowing for specific targeting of areas of interest.

3.2.2 Automatic Data Analysis

While a human can immediately identify the features of a transmission spectrum, a computer must follow a fixed program, making it very difficult to automatically isolate

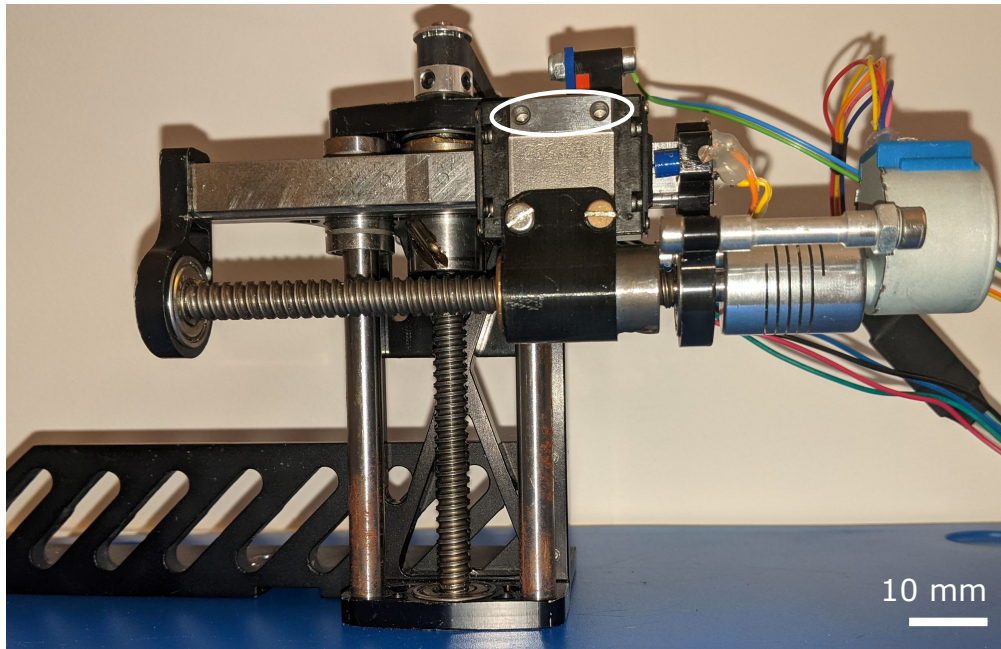


Figure 3.6: Automated sample mapper compatible with the Cary 5000's rail mounting system produced in-house at Lancaster University. The sample arm mount (circled), allows for the use of machined or 3D printed parts to suit the sample being measured.

the same desired parameters. However, a wafer map could have thousands of individual spectra, making manual analysis unfeasible. In order to produce a useful visualisation from the large amount of data the mapping produces, an automated analysis must be developed. Ideally, this would include feature detection (specific to the sample in question), point selection/rejection, and automatic scaling of heatmap data.

3.2.2.1 Single Feature Detection

Often it is useful to map a single peak or trough on a spectrum in order to determine the uniformity of a sample growth. In practice the automation of this is very straightforward, with the only consideration being for rejected measurements. Generally, a scan point would be dismissed for not being on the sample, characterised by a very low (hitting the sample holder) or very high (missing the sample) transmittance. Sometimes the beam can clip the sample giving a trace with a small contrast between the maximum and minimum values. These cases are often poor measurements with little useful data, and are filtered using a simple comparison to a pre-selected minimum amplitude range. Figure 3.7(a) gives an example of a basic feature detection on a calibration sample, along with a rejected scan from the same wafer (b).

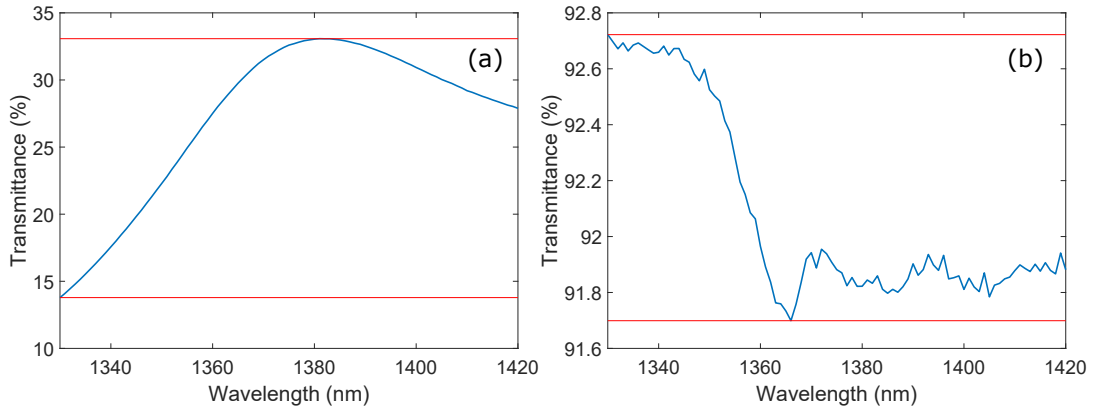


Figure 3.7: **(a)**: An example peak detection from a calibration sample showing the maximum value of the transmittance. **(b)**: A rejected scan from the same wafer map, due to the range being smaller than some pre-set value. In this case the low amplitude is due to the sample beam clipping the edge of the wafer.

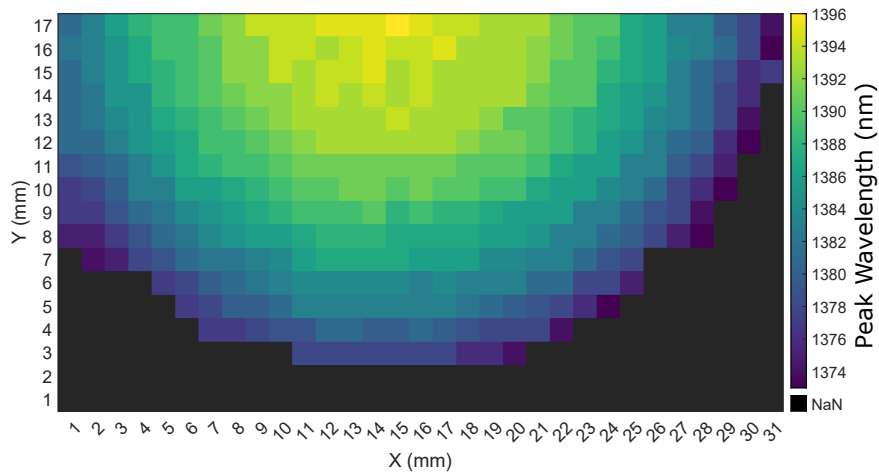


Figure 3.8: An example wafer map of the sample in figure 3.7

3.2.2.2 VCSEL Analysis

Compared to a simple peak detection, automatically finding and measuring the parameters of a VCSEL spectrum presents much more of a challenge. The stop-band must first be identified in order to determine the width and check the alignment of the two mirrors. Once found, the stop-band can then be swept to find the cavity peak (if present). These tasks are made much more complicated by the presence of the periodic side-bands characteristic of any DBR based system, since they rule out using a slope detection algorithm. A customised algorithm was developed to detect a stop-band and thus isolate it from the rest of the spectrum. The basis of finding the stop-band is to first take the derivative of the dataset, followed by finding all sections of the derivative that are less than a specified value (usually noise limited but close to 0.1 nm^{-1}). The actual selection

of the stop-band can become difficult at this point, the ‘ideal’ case is to simply take the largest, and second largest flat sections and use their outer limits as the stop-band edge. The drawback of this occurs when a stop-band has no cavity, thus the flat section is a single piece, or when there are multiple peaks inside the stop-band. In the case of the latter, the model is modified so that several flat sections are used.

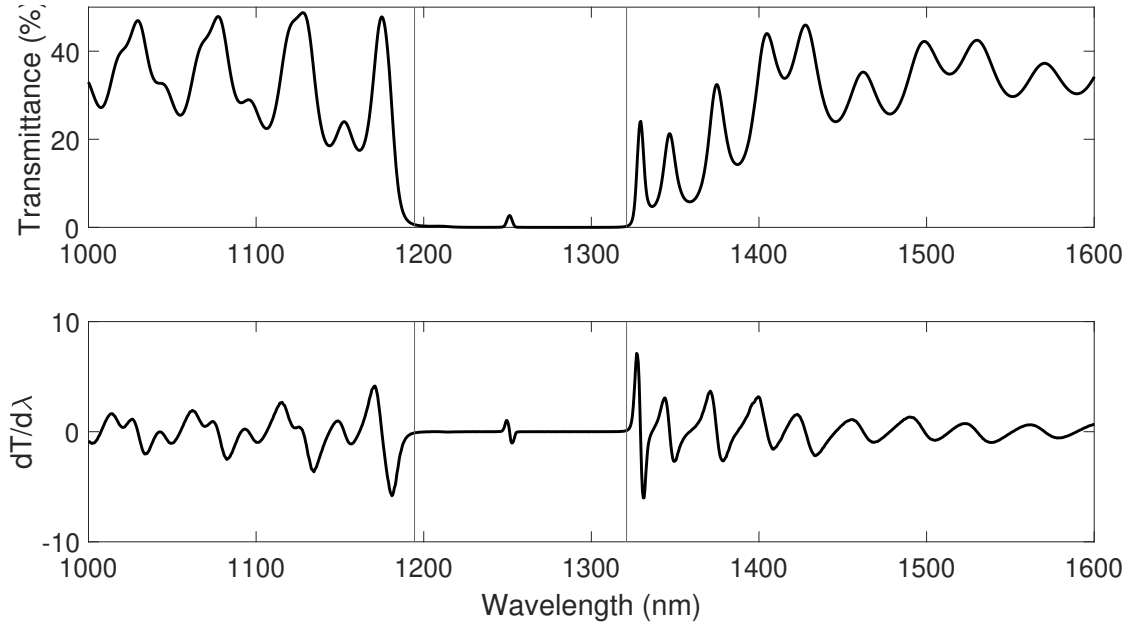


Figure 3.9: **Top:** An example VCSEL transmission spectrum with easily visible stop-band and cavity resonance. **Bottom:** The derivative of the same spectrum, showing the section of near-zero differential

An example of the automatic detection is shown in figure 3.9. Once the stop-band has been found, it is then a simple matter of peak detection to find the cavity resonance. Theoretically this method can be applied to any DBR based structure’s transmission spectrum allowing for massively reduced data analysis time for large sample maps. In the event of the upper DBR being misaligned with the lower DBR, this detection method would give a very large value for the stop-band width. An example analysis of a misaligned growth is in figure 3.10, showing the misaligned DBRs in the upper portion of the figure. The lower section of figure 3.10 shows the two sections of near-zero differential, with a set of peaks between the two. The program has difficulty distinguishing this from a normal stop-band, and additional filters need to be implemented to identify it as a ‘bad’ growth.

In addition to the increased width, it is likely that multiple peaks would be detected within the stop-band, corresponding to the overlap of DBR side-bands causing a drop in reflectivity. For a misaligned VCSEL the map could indicate areas of the wafer that are more, or less aligned, giving an idea of the changes needed to improve the accuracy

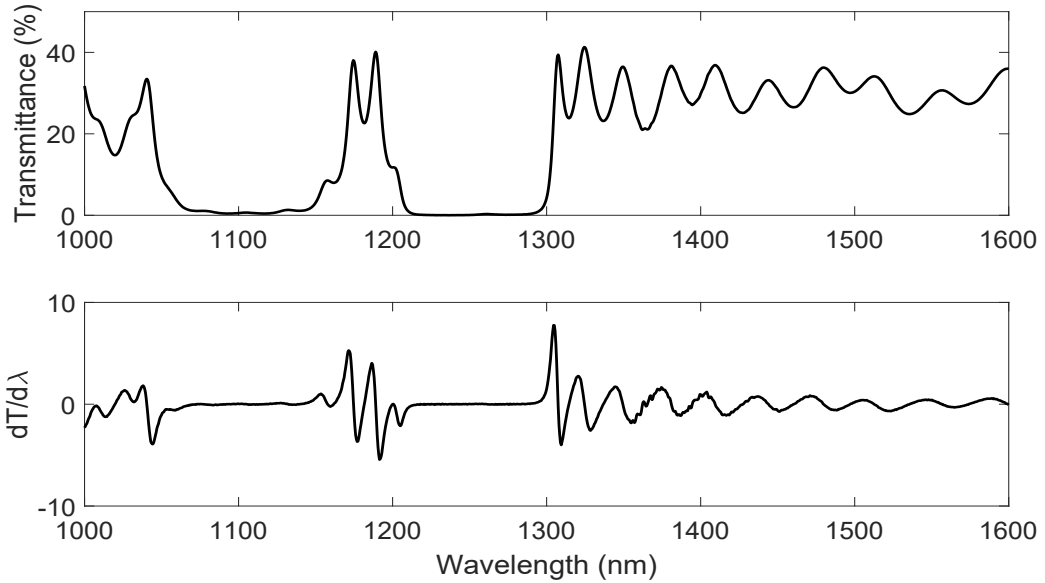


Figure 3.10: **Top:** An example VCSEL transmission spectrum with misaligned stopbands. **Bottom:** The derivative of the same spectrum, showing two sections of near-zero differential, with multiple peaks between them.

of the growth.

3.3 Optical Process Monitoring

Another potential application for the optical modelling in chapter 2 is to optically monitor an etch or growth process by measuring the intensity of a laser beam reflected from the surface of the sample during the process. As the thickness changes with the removal or addition of material, the reflectivity will also change, and can potentially be predicted using the TMM.

3.3.1 Etch Process Monitoring

A common first step in the processing of a semiconductor device is the definition of the device mesa. This is an essential step as it forms the basis of the rest of the device, and it is often useful to know the progress of the etch within the structure. Accuracy is of particular importance with structures that have multiple mesa definitions, as an over- or underetch can result in the wrong layer being contacted[49][50]. Figure 3.11 depicts a basic monitoring setup, whereby a laser is incident on the sample through a viewport, and the reflected beam is collected by a detector. As the etch progresses and material is removed, the interference pattern generated by the sample layers can be plotted and compared to a simulation of the reflectance.

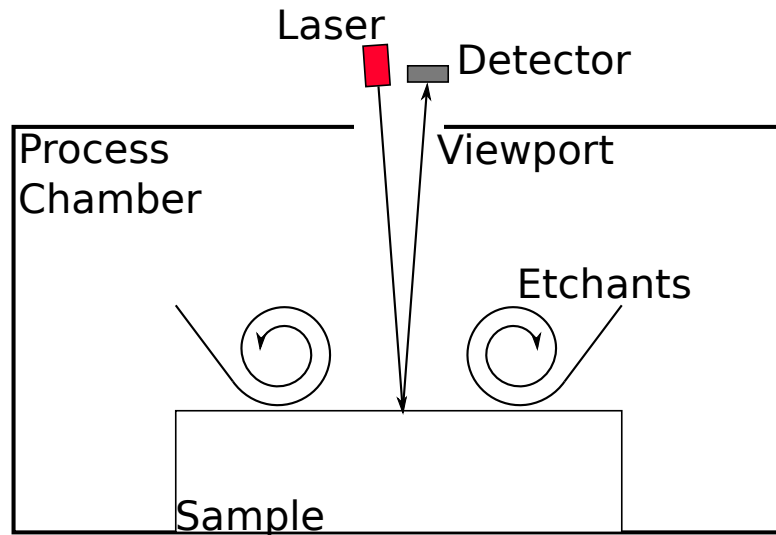


Figure 3.11: A basic process monitoring setup utilizing a viewport on the chamber to measure the interference generated by the sample.

3.3.1.1 Lancaster’s inductively coupled plasma (ICP) System

Lancaster’s QTC cleanroom has an Oxford Instruments ICP etching machine to provide highly uniform and controllable etch rates. The ICP is fitted with a 670 nm laser reflectometer system to provide endpoint detection and to assess the etch rate during the process. This information is displayed on-screen during the etch, as shown in figure 3.12.

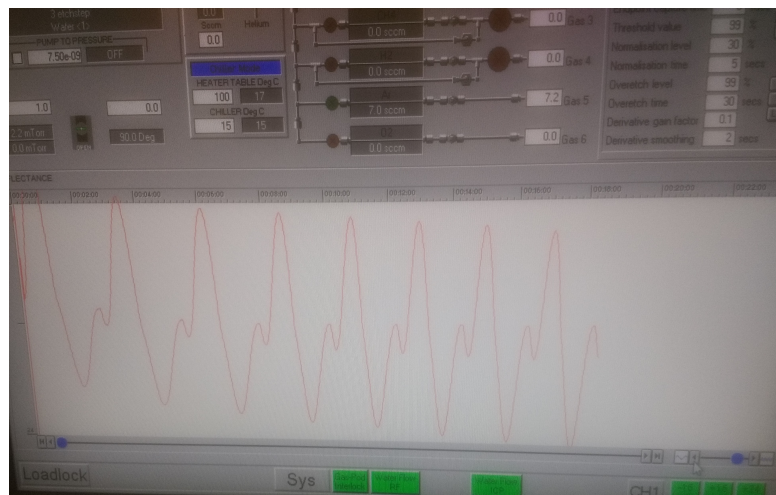


Figure 3.12: An example of the ICP reflection intensity vs time measurement showing the periodic nature of the DBR sample being etched.

If the pattern in figure 3.12 can be predicted, then the etch can be halted at a precise location based on the amplitude of the reflection.

3.3.1.2 Etch Simulation

In order to effectively use the information in figure 3.12, a simulation of the structure must be carried out. The format of the model is fairly straightforward:

1. Simulate the reflectance at the laser wavelength using one of the models in section 2.1
2. Remove some preset thickness from the front of the top layer
3. Repeat 1 and 2 until the layer is fully removed
4. Repeat until the substrate is reached

The TFCalc software is fast and powerful, so would be the ideal choice for an accurate etch simulation. However, while material can be interactively removed, it must be done manually. When a sample has many layers each around 100 nm, removing material by hand would be unreasonably time-consuming. Fortunately, since the wavelength of the laser is above the band gap for our material system, the TMM can be utilized. The key factor is that since photons above the band gap in energy will be absorbed, the substrate can be treated as infinite and thus will produce no incoherent reflections. It is now a matter of integrating the TMM into an iterative piece of code so that any structure with known refractive indices can be accurately modelled and etched. Once written, this program was compiled so that it could be deployed onto a computer inside the cleanroom for users to model their own structures to make their etch processes more accurate and repeatable.

Making the software easy to use and reliable was of key importance, so simplicity was the main design requirement. Figure 3.13 shows the software user interface with straightforward sample selection, material addition, and data manipulation. Initially the entire code was written in MATLAB, since the native handling of matrices and complex numbers produced short, simple code. However, MATLAB is fundamentally a slow language and for a large optically graded structure (nearly 3000 layers) the etch would take over 5 minutes to be simulated. By converting the transfer matrix calculation to c code and interfacing it with the other MATLAB functions, that time was reduced to a little over 20 seconds. Having a code that runs at this speed means that in-situ simulation of etches and growths is much more feasible.

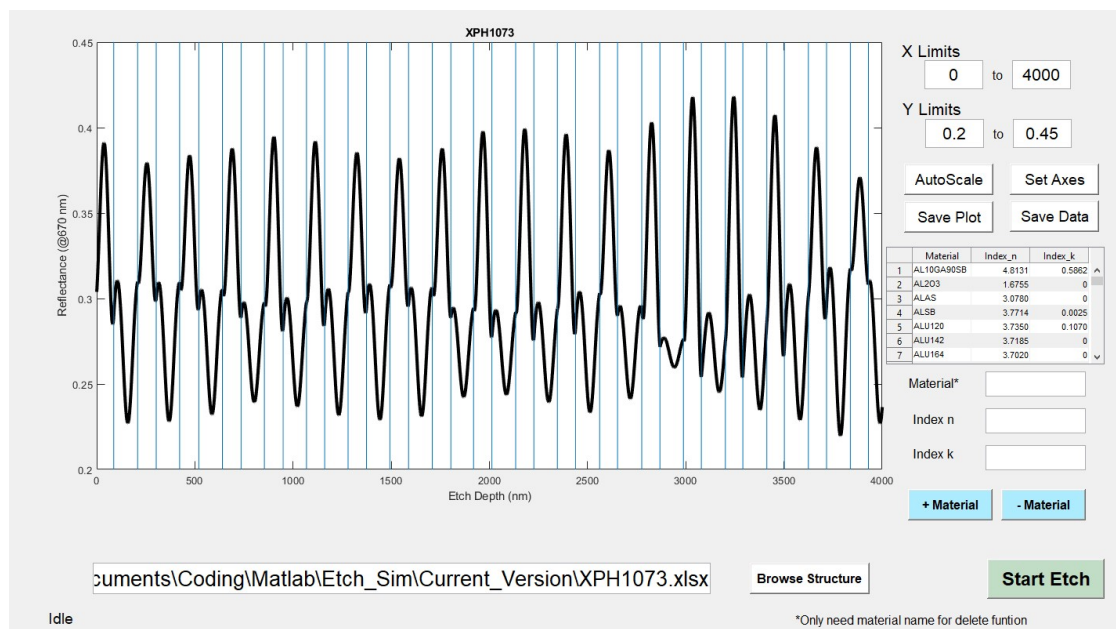


Figure 3.13: A screen shot of the implemented etch simulation software showing an example DBR structure similar to the one in figure 3.12.

Chapter 4

Material Characterisation Techniques

In order to produce the most accurate simulations possible, the material properties of the system must be known to a high degree of accuracy. The composition, layer thicknesses, and dopants all have the potential to alter the behaviour of the model and reduce its accuracy when compared to measured data. Some material data can be measured, others have to be calculated from theoretical models due to difficulties in measurement [30, 31, 32]. For example, it is challenging to measure the refractive index and extinction coefficient of $\text{Al}_x\text{Ga}_{1-x}\text{As}$ due to the rapid oxidation of the aluminium altering the optical properties. One could perform ellipsometry on samples capped with GaAs, but the addition of more layers increases the complexity of the measurement analysis, and increases the uncertainty on the measurement itself. Alternatively, ellipsometry could be performed in a vacuum, but such equipment is complex and expensive.

The techniques used to characterise our samples needed to be accessible, scalable to mass-production levels, and not prohibitively expensive. While some characterisation could be performed in Lancaster's Physics and Chemistry Departments, others needed to be carried out by our collaborators off-site. The following details the processes or methods used in each form of material analysis.

4.1 Beam-Exit Cross-Sectional Polishing (BEXP)

To maximise the accuracy of an optical stack model, the thicknesses of each layer in the system must be known. Variations in thickness change the path lengths of the layers, in turn affecting the phase difference between the layer interfaces. In a DBR based system, a change in the reflected phase can change the operating wavelength, and have an impact on performance. The thickness of a layer also determines how much light is absorbed, impacting the intensity of reflected and transmitted components[25, 26, 27]. With a device that has many layers, cross-sectioning and the subsequent analysis has the potential to be extremely time-consuming, with additional difficulty if the structure has thin layers (less than about 100 nm). While mechanical polishing can be used for this purpose[51], the technique generally favours thicker layers as the possibility of sample chipping exists, damaging layers near the surface. It is more appropriate therefore to use an ion-beam method. Focused ion beam (FIB) is one such technique, often used to prepare areas for transmission electron microscopy (TEM)[52, 53]. However, FIB has a small beam area making it generally unsuitable for use on a vertical-cavity structure with many layers. Ar-ion beam based cross-sectioning is used to prepare samples for various types of electron microscopy[54, 55, 56], placing the layers of interest against a

mask so the beam is at a normal incidence. Unfortunately, due to the proximity of the mask, the first section of the sample often has a poor quality surface, making nanoscale characterisation difficult or impossible. To successfully cross-section the numerous thin layers in the QR devices, modifications can be made to prepare a suitable surface for atomic force microscopy (AFM) imaging.

BEXP, performed by Dr Alex Robson of Lancaster Material Analysis (LMA), is a patented Ar-ion milling technique[57], by which the layers of a sample are exposed at a shallow angle, producing a larger surface area for imaging and measurement as shown in figure 4.1. As well as broadening the area of interest, the angle distances sample layers from the mask producing a measurable surface with a much lower overall roughness. Combining this milling with AFM allows for a detailed analysis of a many-layered structure to assess layer thickness, interface quality, and material defects [58, 59]. Figure 4.2 is a composite AFM image of a cross-sectioned VCSEL prepared using this technique, showing each layer of the DBR along with the cavity region.

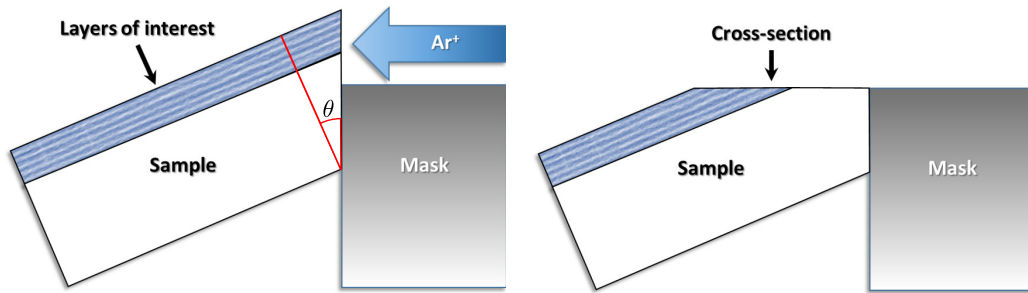


Figure 4.1: Diagram of the BEXP process showing the angled sample, mechanically polished to some shallow angle θ , serving to broaden the cross-section and distance the layers of interest from the effects of the mask during Ar-ion milling.

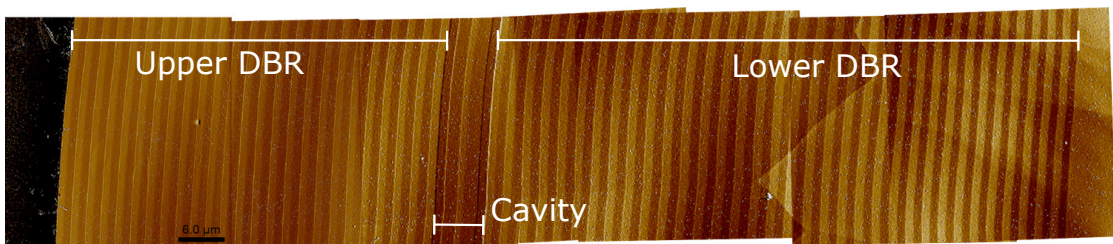


Figure 4.2: Composite AFM image of a cross-sectioned VCSEL prepared using BEXP clearly showing the upper DBR, cavity region, and lower DBR.

4.2 Substrate Calibration

The substrate of an optical semiconductor device is often ignored, its large thickness in comparison to the device itself means that it can be frequently treated as semi-infinite. When light is above or close to the band gap energy, this is an accurate assumption, as no light will reach the back wall of the substrate and thus no reflected light will return to affect the device. In the case of telecoms wavelengths on pure GaAs, it is possible for light to reach the back of the substrate due to the low extinction coefficient[60]. While this is useful in that it allows for on-wafer transmission measurements, extra steps are needed in order to include the thick (hundreds of microns) layer in any models.

4.2.1 Modelling a Substrate

4.2.1.1 Coherence

A plain substrate can be modelled either as a single coherent layer suspended in air, or as a thick incoherent layer with two substrate-air boundaries. To determine which model should be used, the coherence length of the measurement's light source must be estimated. The quartz-iodide lamp in the Cary 5000 can be approximated as a blackbody emitter operating at approximately 3000K[61], and the coherence length, l_c , of a blackbody spectrum with temperature T is given as

$$l_c \simeq \frac{hc}{4kT}, \quad (4.2.1)$$

resulting in a coherence length of 1.2 μm [62]. This is far less than the thickness of GaAs substrates, all of which are several hundred microns thick. However, monochromation within the spectrophotometer must be taken into account. The monochromator produces a Gaussian emission profile with a certain spectral bandwidth (SBW), $\Delta\lambda$, which is much narrower than the lamp's emission profile. It can be shown for a slab of thickness d_{sub} and refractive index n , the minimum bandwidth to ensure incoherence is

$$\Delta\lambda > \frac{\lambda_0^2}{2\pi n d_{sub}}, \quad (4.2.2)$$

where λ_0 is the centre wavelength of the light source[63]. For a 2 inch GaAs wafer with a nominal thickness of 350 μm , a centre wavelength of 1.3 μm , and an average refractive index of 3.4 the resultant minimum SBW is approximately 0.2 nm. The spectrophotometer has an operating range of 0.01 - 20 nm SBW, so care must be taken to

avoid the lower bandwidths so that the transmission is not affected by partial coherence and can be modelled as a thick slab.

4.2.1.2 Doped GaAs Substrate Simulation

Full refractive index data for doped substrates can be difficult to obtain. The data could be dependent on material, dopant, doping level, and wavelength. As such the most straightforward means of gathering the required information is to measure a substrate from the same batch as those being used for device growth. An additional assumption that can be made is that the real part of the refractive index is not significantly affected far from the band gap edge[64]. In effect, this means that the free carrier absorption is the only parameter that needs to be determined. To simulate the optical properties of a thick single material substrate, three factors need to be accounted for: the air-semiconductor interface, the propagation through semiconductor with a certain thickness d_{sub} , and the semiconductor-air interface on the back of the sample. These three events will repeat until the internally propagating light is fully absorbed.

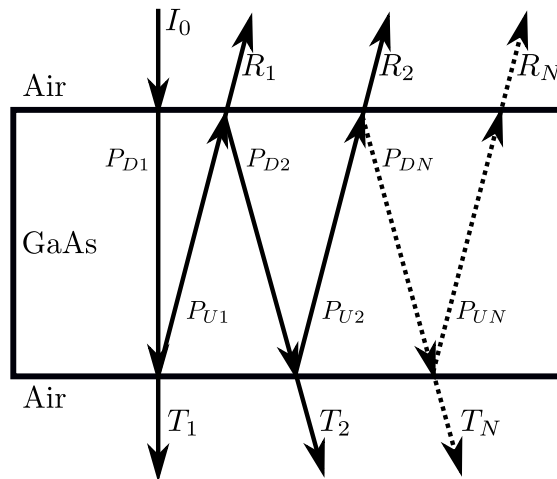


Figure 4.3: A schematic of the propagation of light within a thick substrate. With incident light of intensity I_0 , reflected and transmitted components R_i and T_i , respectively, and the upwards and downwards internally propagating components P_{U_i} and P_{D_i} , respectively. (Paths are angled for clarity, all components are normal to the surface.)

The model uses the Fresnel interface equations as derived in section 2.1.1.4, and obtains the reflected and transmitted intensities by squaring their respective coefficients:

$$R_{m,m+1} = \left(\frac{n_m - n_{m+1}}{n_m + n_{m+1}} \right)^2, \quad (4.2.3)$$

$$T_{m,m+1} = \frac{4n_m n_{m+1}}{(n_m + n_{m+1})^2}. \quad (4.2.4)$$

Additionally, the expression

$$I = I_0 e^{-\alpha x}, \quad (4.2.5)$$

which describes the intensity of a propagating wave through an absorbing medium, where α is the absorption coefficient of the substrate, is included to determine the loss due to each pass inside the substrate. The simulation iterates over many internal reflections N , summing the externally reflected and transmitted components

$$R_T = \sum_{i=1}^N R_i, \quad T_T = \sum_{i=1}^N T_i. \quad (4.2.6)$$

It can be shown that for infinite internal reflections in a thick slab of material suspended in air at normal incidence the summations above can be written as

$$R_T = \frac{R_{air,sub} [1 - e^{-2\alpha d_{sub}} (2R_{air,sub} - 1)]}{1 - R_{air,sub}^2 e^{-2\alpha d_{sub}}}, \quad (4.2.7)$$

and

$$T_T = \frac{(1 - R_{air,sub})^2 e^{-\alpha d_{sub}}}{1 - R_{air,sub}^2 e^{-2\alpha d_{sub}}}, \quad (4.2.8)$$

where d_{sub} the substrate thickness, and $R_{air,sub}$ is the Fresnel reflection at the air-semiconductor boundary as calculated using equation (4.2.3)[63].

Using equation (4.2.7) and equation (4.2.8) the absorption coefficient, α , of a thick layer of material can be determined using a sweeping iteration algorithm until the calculated R and T match the measured value to within a pre-determined amount depending on the desired number of significant figures. The extinction coefficient k of the substrate can then be calculated using the relation

$$\alpha = \frac{4\pi k}{\lambda}. \quad (4.2.9)$$

Any batch of semiconductor substrates will have some range of thicknesses as measured by the manufacturer, giving an uncertainty value for the thickness of the wafer. Incorporating this uncertainty will give a range of values for k reducing the precision of the result.

The calculated extinction coefficient for a particular wafer batch can then be incorporated into the optical models, providing additional information about the intensity of reflected or transmitted light.

4.3 $\text{Al}_x\text{Ga}_{1-x}\text{As}$ Compositional Analysis

There are multiple techniques to determine the fractional composition, x , of $\text{Al}_x\text{Ga}_{1-x}\text{As}$. Some common methods include: high-resolution x-ray diffraction (XRD) [65, 66, 67, 68], TEM [65], photoluminescence (PL) [65, 66, 68], Raman spectroscopy [66, 67], secondary-ion mass spectroscopy (SIMS) [69, 70], and XPS [71]. The main limitation with XRD, PL, and Raman is that they work well on bulk samples, or with single layers on or near the surface, but cannot analyse many-layered structures; especially if the structure has multiple layers with similar compositions. Most also require complex fitting analyses, and there are often discrepancies between techniques [68]. Devices that use DBRs are usually relatively thick, with many thinner layers. For example, a typical VCSEL can have ~ 100 layers, each of the order of 100 nm, making compositional analysis of individual layers with these techniques very difficult or even impossible. To find a suitable means of characterising the composition of our devices, an up-to date comparison of methods was required. Each technique would need to be able to measure each layer of a many-layered sample independently, while avoiding surface damage or loss of information. Unlike some of the older techniques, current methods are all destructive by nature and so it is accepted that a piece of material be sacrificed for the measurement. By collaborating with groups at other universities, as well as with material analysis companies, the following techniques were chosen:

Technique	Performed by
X-ray photoelectron spectroscopy	B. Gong (University of New South Wales, Australia)
Magnetic sector secondary-ion mass spectroscopy	Loughborough Surface Analysis
Time-of-flight secondary-ion mass spectroscopy	B.Gong (UNSW, Australia)
Electron energy-loss spectroscopy	M. Delamata, S. Molina (University of Cádiz, Spain)

4.3.1 Secondary Ion Mass Spectroscopy (SIMS)

Secondary-ion mass spectroscopy (SIMS) is a technique used to determining the elemental makeup of a sample by first bombarding the surface with primary ions, for example Ar-ions, which in turn triggers the release of secondary particles. The ejected particles can be atoms or clusters of atoms, both charged and uncharged. The uncharged species are of little use, but by applying some electric field, the charged secondary ions can be accelerated away from the surface and transferred to a mass spectrometer for

analysis[72]. While the general process for obtaining the sample ions is the same, multiple variations of mass spectrometer exist for the analysis of those ions. Two of the more commonly used variations were used in the study, and their operating principles are discussed below.

4.3.1.1 Magnetic Sector SIMS (MS-SIMS)

Magnetic sector, dual sector, or simply sector SIMS uses the primary ion beam as both the etchant and to probe the sample. Sputtered material is removed from the sample area and accelerated using a system of transfer ion optics to the first deflection sector. While there are many arrangements and combinations of electrostatic and magnetic deflection sectors, the example given here is a basic version of the CAMECA IMS 4f tool used to analyse our sample. The main selection mechanism consists of an electrostatic sector and a magnetic sector to separate the ions by energy and then mass respectively.

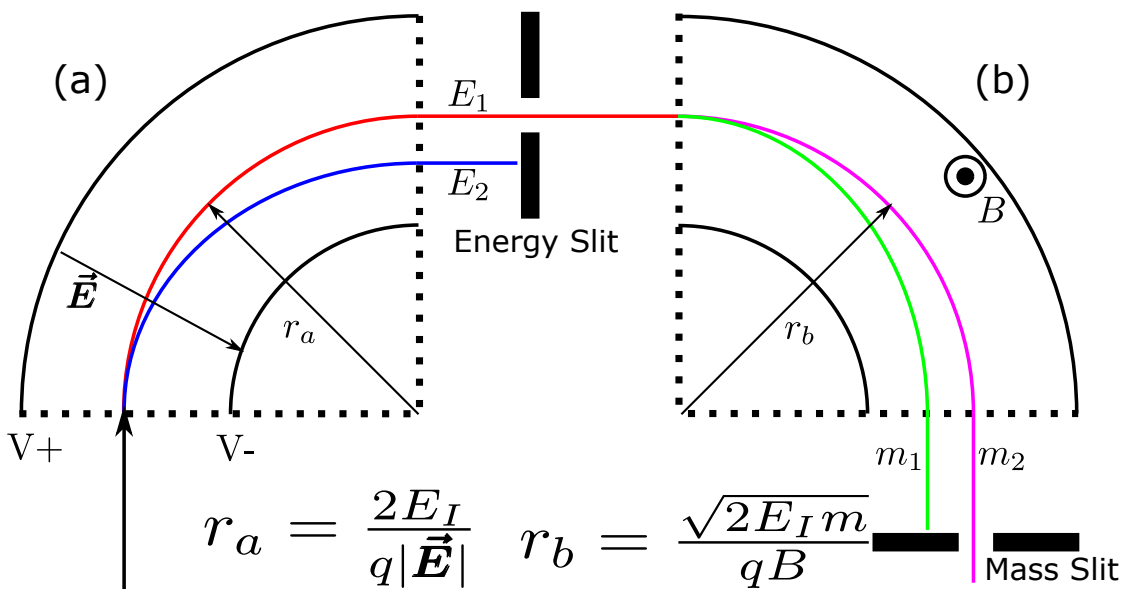


Figure 4.4: A simplified schematic of the MS-SIMS tool's energy and mass selectors. (a) is the electrostatic sector, where the radius of curvature r_a depends on the ion kinetic energy E_I and the electric field $|\vec{E}|$. (b) is the magnetic sector, where ions enter with selected energy E_I , so that the radius of curvature becomes dependant on the mass m and magnetic field strength B .

Figure 4.4 displays a simplified schematic of the selection sectors in the spectrometer. The electrostatic sector uses parallel plates with a circular curvature and a potential difference to produce an electric field \vec{E} . The deflection radius for an incident ion is then dependant on the kinetic energy E_I and charge q of the particle, as well as the strength of the field. Once the energy of the ions is selected with a slit, they enter the magnetic sector. Since the ions now have equal energy, the deflection radius will only

depend on the strength of the magnetic field B , and the mass of the ion. This allows for the separation of different elements by atomic mass, and can again be selected using a movable slit. The energy- and mass-selected ions then proceed to the detection part of the spectrometer, not shown, to determine the amount of the chosen elemental ions. A relative sensitivity factor, determined by calibration standards, is then used to find the elemental composition of the sample under investigation.

Magnetic-sector SIMS depth profiling was carried out for our study using a CAMECA IMS 4f secondary-ion mass spectrometer by Loughborough Surface Analysis Ltd. The analysis conditions used a Cs^+ primary ion beam with an impact energy of 5.5 keV and beam current of 30 nA. The beam was rastered across the sample surface with an area of $125\ \mu\text{m} \times 125\ \mu\text{m}$ and positive secondary ions collected from an analysis area of approximately $80\ \mu\text{m}^2$. The CsAl^+ , CsGa^+ and CsAs^+ polyatomic species were detected as these are reported to be relatively free of SIMS matrix effects, where the chemical state of the surrounding material affects the elemental ion yield. The relative levels of gallium and aluminium were then calculated using a correlation plot of the $\text{CsAl}^+/\text{CsAs}^+$ and $\text{CsGa}^+/\text{CsAs}^+$ signals [73][74].

4.3.1.2 Time-of-Flight SIMS (ToF-SIMS)

As the name suggests, time-of-flight secondary-ion mass spectroscopy (ToF-SIMS) uses a time-of-flight mass analyser to isolate and identify the various secondary ions ejected from the sample surface. The mass analyser uses a linear electrostatic section to accelerate the ions, and their velocity is dependant on their mass to charge ratio. The time of arrival at the end of the flight region is therefore also dependant on this ratio. The schematic in figure 4.5 shows the main sections of a ToF mass analyser with an incorporated reflectron.

Secondary ions enter the acceleration region with mass m and charge q . The energy, E_I , gained by the ion when accelerated through the potential difference, V , is calculated as

$$E_I = qV. \quad (4.3.1)$$

Assuming that the initial drift velocity of the ions is much smaller than the final accelerated velocity, the ions enter the flight region with the approximate velocity

$$v \approx \sqrt{\frac{2qV}{m}}. \quad (4.3.2)$$

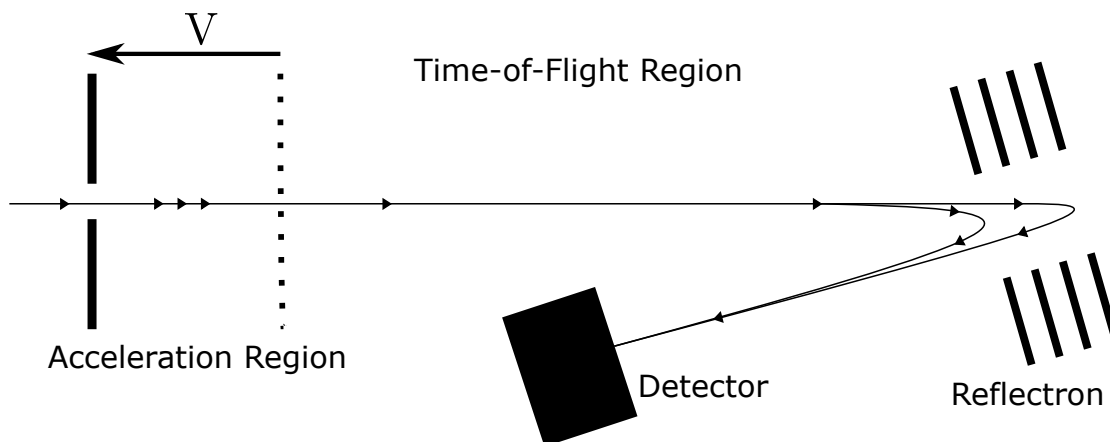


Figure 4.5: A simplified schematic of an example time-of-flight secondary-ion mass spectroscopy (ToF-SIMS) mass spectrometer section. The ejected ions are accelerated by an electric field into the flight region. The ions are then redirected and energy-separated by a reflectron before hitting the detector.

Since the velocity, and therefore the flight time, is dependant on the charge to mass ratio, heavier ions will take longer to reach the detector. In addition to this mass selection, the TOF.SIMS5 from IONTOF GmbH, utilised in this comparison uses a reflectron, which is a series of parallel plates utilising a potential gradient to redirect the ions towards the detector. Ions with a higher energy will penetrate further into the reflectron, and will have a longer flight time as a result. The effect of the redirection is that ions with the same charge to mass ratio will be separated by energy as well. Ions are detected using a single channel-plate photomultiplier combination detector.

The surface is sputtered by a lower-energy ion beam to etch deeper into the material, while a higher power, more focused beam is used to probe a point on the surface. With this interlaced approach it is possible to create a 3D compositional map of the sample under investigation. However, to reduce measurement time and since our devices are uniform in the x-y plane, this feature was not used at this time. The depth profiling measurements were conducted by Dr Bill Gong (University of New South Wales, Australia) on a TOF.SIMS 5 instrument (ION-TOF GmbH) using a Bi cluster ion source as the analysis projectile at 15 keV in Bi_3^+ mode. The field of analysis was $100 \times 100 \mu\text{m}$ for both the positive and negative polarities. Sputtering was performed using a Cs^+ beam of 1 keV and 109 nA in interlaced operation to produce a crater of $300 \times 300 \mu\text{m}$. The analysis was conducted to a depth of $5 \mu\text{m}$ over 6500 s. Sample rotation was not used [75].

4.3.2 X-Ray Photoelectron Spectroscopy (XPS)

X-ray photoelectron spectroscopy (XPS) is a spectroscopic technique used to analyse the surface composition of a target material. By irradiating the surface with an X-ray beam, electrons are ejected that carry compositional information within their respective kinetic energies. Quantitative analysis of the chemical makeup of the surface can then happen by measuring the energy of the emitted electrons. While XPS has a penetration depth of approximately 10 nm, suggesting poor performance for thick or multilayered samples, the technique can be combined with an etch process to allow for full depth profile measurement.

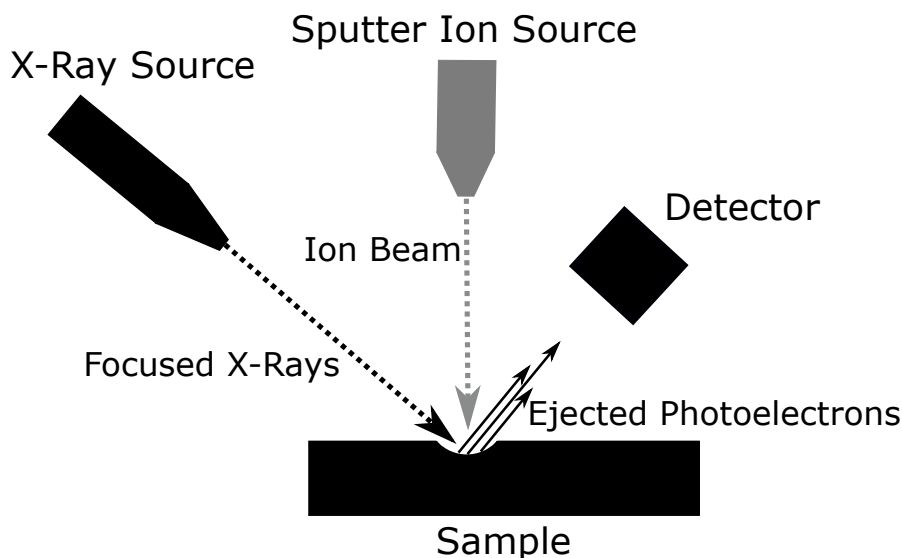


Figure 4.6: A simplified schematic of an example XPS system. The energy of the ejected photoelectrons is dependent on the element and orbital they were released from. The ion beam sputters the surface while the X-ray beam is focused at the bottom of the etch crater to create a depth-based measurement.

The kinetic energy of the electrons to be measured depends on both the element that the electron is ejected from, and the binding energy of the electron itself. In turn, the binding energy is effected by specific orbital that it occupies, so that an XPS spectrum may consist of many peaks, each corresponding to a different electron orbital from the varying elements that make up the sample. Each orbital peak in a spectrum will have a specific relative sensitivity factor, which will allow for the conversion from number of ejected electrons at that energy to the amount of the corresponding element in the surface under scrutiny. Standard reference spectra are used to identify and quantify the elemental orbitals present in the sample [76]. Selecting orbitals with distinct peaks, as well as good contrast with the scattered background electrons, allows for the fractional composition of the material to be determined. The XPS used in our comparison was

conducted on an ESCALAB 250Xi instrument (Thermo Scientific) by Dr Gong using a monochromated Al $K\alpha$ source with a 500 μm spot and a 3 keV Ar⁺ sputter beam scanning over an area of 2.5×2.5 mm.

4.3.3 EELS

It is possible to use a transmission electron microscope operating in scanning mode (STEM) to determine the compositional makeup of a given sample. To perform electron energy-loss spectroscopy (EELS), the region of interest on the sample is first cross-sectioned using an ion-beam polishing technique, then subjected to a small focused electron beam, which in turn produces a selection of elastically scattered electrons as a result of the electron-matter interaction. The composition of the sample has a great effect on the amount of energy lost by the incident electrons, so it is therefore possible to determine the chemical constituents of the material by collecting and analysing these scattered electrons [77]. It is also possible to assess certain information about the optoelectronic properties of the sample, such as bandgap and plasmon resonances [78, 79]. To determine the energy loss, a spectrometer is used, grouping electrons by their final energy. Energy losses above 50 eV, also known as the core-loss spectral region, are caused by interactions between the scanning electrons and the core electrons of the atomic species of the sample. This region holds the characteristic signals needed to determine the chemical composition of the sample, along with information on the electronic state and fine structure of the sample.

In the measurement performed by Dr Maria Delamata (University of Cádiz, Spain), the window method employed for the chemical quantification requires subtracting a background and fitting the signal cross-sections, which is carried out in one step with the DigitalMicrograph™ commercial software. In the analysis, a power law function has been used for the background subtraction, and integrated signals over 50 eV energy windows. Importantly, as plural scattering events influence the spectral shape, especially for thick samples, we quantify the deconvoluted EELS signal for regions thicker than 0.3 times the inelastic mean free path. The relative thickness of the areas studied is extracted from the zero-loss spectra. All the data have been filtered before quantification to increase the signal-to-noise ratio by applying singular value decomposition routines, implemented using the Hyperspy Python package. The STEM-EELS experiments were performed in a FEI Titan Cube G2 60-300 kV operated at 200 kV and equipped with a Gatan DualEELS™ spectrometer, using an energy dispersion of 0.5 eV/channel. The

equipment was set-up to achieve convergence and collection semi-angles of 20.5 and 41 mrad, respectively.

Chapter 5

Material Characterisation Results

5.1 Short-Period Characterisation Sample

In order to test the results of each stage of the characterisation process, a short-period DBR was grown and the optical transmission measured. The sample consisted of a 6-period GaAs - $\text{Al}_{0.9}\text{Ga}_{0.1}\text{As}$ DBR on an n-doped GaAs substrate grown using a Veeco GenXplor MBE machine. A target centre wavelength of $1.55\ \mu\text{m}$ was selected to coincide with the telecoms C band, as well as being roughly in the centre of the 1 - 2 μm measurement range of the spectrophotometer. A schematic of the structure is shown in figure 5.1. An initial simulation of the design was performed which uses the assumptions that all layers are grown to specification and that the substrate is transparent, thus requiring the inclusion of back side internal reflections. The result of the initial design model is shown alongside the measurement in figure 5.2, displaying a clear shift in wavelength and a higher transmission than expected.

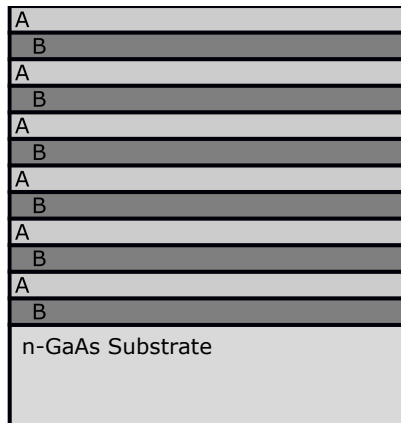


Figure 5.1: A schematic of the structure of the DBR, where layers A are GaAs with a target thickness of 115.0 nm and layers B nominally consist of $\text{Al}_{0.9}\text{Ga}_{0.1}\text{As}$ with a target thickness of 130.7 nm.

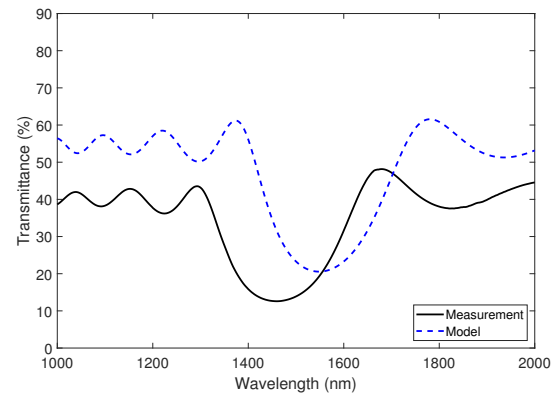


Figure 5.2: Measured and simulated (designed) transmission of the calibration sample incorporating a transparent substrate and backside reflection.

5.1.1 Beam-Exit Cross-Sectional Polishing

While BEXP was used extensively in developing the models and devices in this project, an example will be given here to show the usefulness and accuracy of the technique. The model used in figure 5.2 makes the assumption that the sample was grown exactly to specification. This particular sample was grown in an unconditioned chamber with minimal calibration, and as such is expected to vary from the ideal design. In order to produce a more accurate picture of the sample the actual thickness and condition of the layers must be determined. Combining BEXP with AFM allows the precise measurement

of the layer thicknesses[59], as well as providing an idea of the interface quality.

Layer No.	Material	Target Thickness (nm)	BEXP Thickness (nm)	Difference (nm)
1	GaAs	115	108 ± 4	-7
2	$\text{Al}_{0.9}\text{Ga}_{0.1}\text{As}$	131	122 ± 5	-9
3	GaAs	115	107 ± 4	-8
4	$\text{Al}_{0.9}\text{Ga}_{0.1}\text{As}$	131	122 ± 5	-9
5	GaAs	115	110 ± 4	-5
6	$\text{Al}_{0.9}\text{Ga}_{0.1}\text{As}$	131	125 ± 5	-6
7	GaAs	115	112 ± 4	-3
8	$\text{Al}_{0.9}\text{Ga}_{0.1}\text{As}$	131	121 ± 5	-10
9	GaAs	115	112 ± 4	-3
10	$\text{Al}_{0.9}\text{Ga}_{0.1}\text{As}$	131	123 ± 5	-8
11	GaAs	115	113 ± 4	-2
12	$\text{Al}_{0.9}\text{Ga}_{0.1}\text{As}$	131	128 ± 5	-3
Substr.	GaAs	-	-	-

Table 5.1: Table comparing target layer thicknesses to those acquired using BEXP.

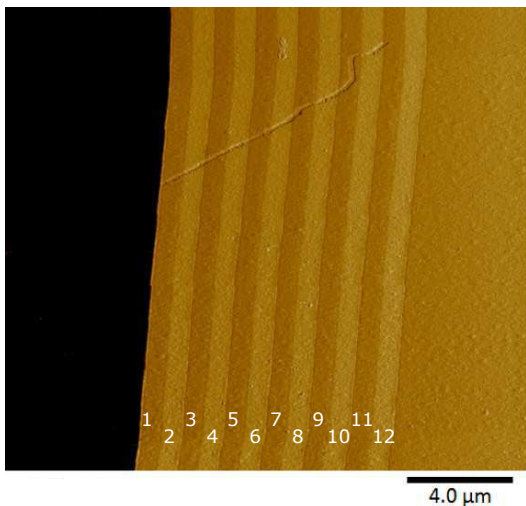


Figure 5.3: AFM image of the cross-sectioned sample showing clear layers and interfaces.

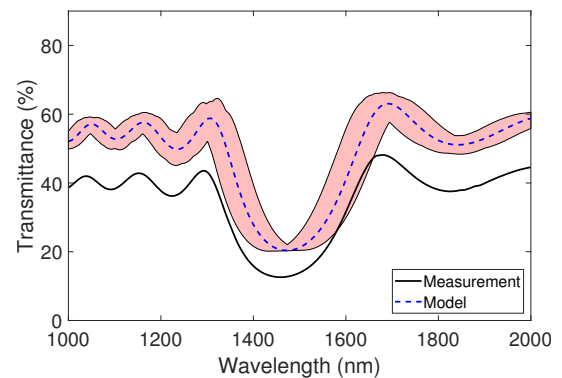


Figure 5.4: Updated model using the layer thicknesses from table 5.1 compared to the measured transmission. The shaded area marks the uncertainty in the model.

Figure 5.3 clearly shows the sample layers, with the darker being GaAs and lighter $\text{Al}_{0.9}\text{Ga}_{0.1}\text{As}$. The cross-section also indicates that the interfaces are of a high quality, and so there should be little impact on the transmitted light. From the measured layer thicknesses shown in table 5.1 it is clear that overall the layers were thinner than the thickness targets. Thinner DBR layers would suggest a shift towards shorter wavelengths, which agrees with the measured data in figure 5.2. Introducing the measured layer thicknesses into the model from figure 5.2 produces the transmission shown in

figure 5.4. The stop bands now align, showing good agreement with the shape of the measured data. The remaining difference in transmission appears to be uniform across the wavelength range, implying that the cause is either due to an unresolved property of the substrate, or due to some systematic effect in the measurement/equipment.

5.1.2 Substrate Calibration

To test the effect of the substrate on the overall sample transmission, its absorption needed to be measured. The sample being used so far in this characterisation was grown on the same type of Si-doped (n-type) GaAs as the majority of the GaSb QR devices. As well as using a wafer from the same batch, two more 2" wafers were selected for testing: an undoped GaAs wafer, and a Zn-doped (p-type) GaAs wafer for comparison purposes. The specifications for each are shown in table 5.2. By measuring the transmission of each wafer, and following the procedure in section 4.2, the extinction coefficient was calculated.

Wafer	Dopant	Carrier Concentration (cm^{-3})	Thickness (μm)
n-type	Silicon	$(1.21 - 3.69) \times 10^{18}$	352 - 370
Undoped	-	$(0.74 - 1.56) \times 10^7$	369 - 370
p-type	Zinc	$(1.00 - 1.10) \times 10^{19}$	362 - 370

Table 5.2: Stated batch specifications of the wafers used in this calibration as provided by Wafer Technologies Ltd.

5.1.3 Characterisation Results

The measured transmission of the substrates is shown in figure 5.5(a). Using this data, alongside the mean thickness measurement from table 5.2 and equation (4.2.8), the extinction coefficient was calculated for each substrate. The results are displayed in figure 5.5(b). The undoped wafer has, as expected, a very low extinction coefficient. As the energy approaches that of the band-gap, the extinction coefficient begins to increase, and may have a small impact on the measured transmission for growths on these substrates at shorter wavelengths. For the n type wafer approximately 10 percent more of the incident light is absorbed than the undoped sample, visible in figure 5.5(a), leading to a significant extinction coefficient. As the substrates for the QR devices are generally n-type, it is likely that there will be a noticeable effect on the device transmission measurements. Finally, the p-type substrate, with the highest carrier concentration, only allows a small fraction of light to pass through at shorter wavelengths before the

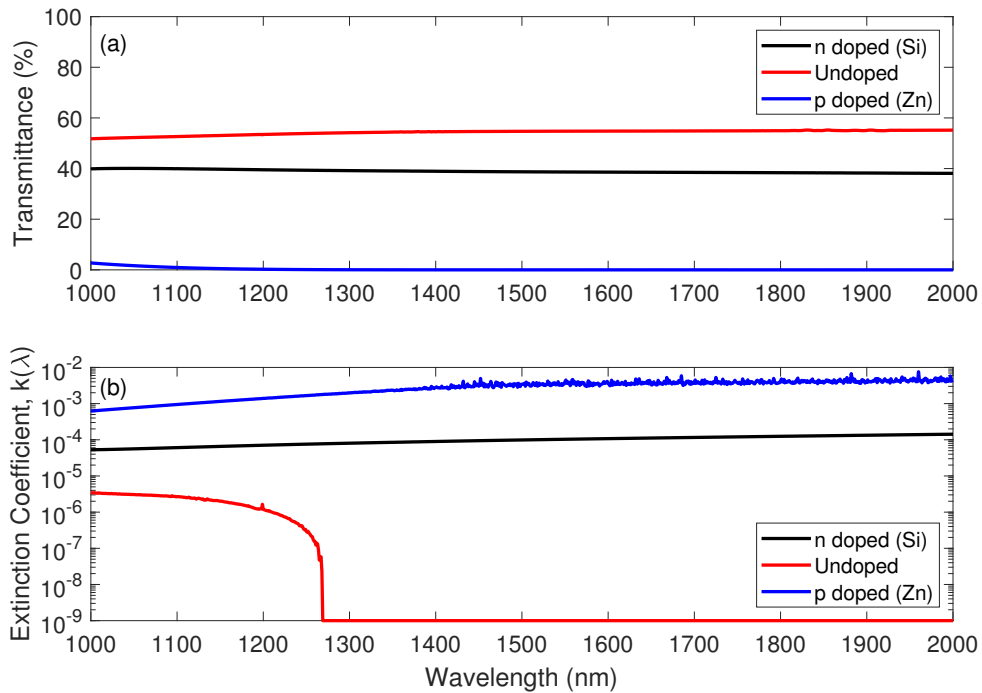


Figure 5.5: (a) Measured transmittance of three GaAs substrates with different doping types. (b) Calculated extinction coefficients of the GaAs wafers as a function of wavelength.

transmission hits the noise floor making the wafer opaque above $\sim 1.4 \mu\text{m}$. This can be seen on the graph in figure 5.5(b) by the noise increase and the value for k becoming constant. However, the extinction coefficient is likely to be inaccurate here, as the value calculated equates to the minimum k required to absorb all light, without a thinner substrate more accurate measurements are not possible. The high carrier concentration, coupled with the highly absorbing free-carrier effects[80], make p-type GaAs a poor choice of substrate when transmission measurements are desired. The p-type absorption should also be noted when designing optical structures such as VCSELs, as thick p-DBRs could be detrimental to the output of a device.

5.1.3.1 Uncertainty in Results

The primary source of uncertainty in the substrate calibrations is from variation in the wafer thickness during manufacture. Each batch of crystals has a range of thicknesses as measured by the producer, as seen in table 5.2, which can be used to provide a range of extinction coefficients during the calculation step. A more accurate model could be produced if each wafer's thickness was known individually, however equipment with suitable precision to do so was not available during this work. A zoomed view of each

dataset can be seen below in figure 5.6.

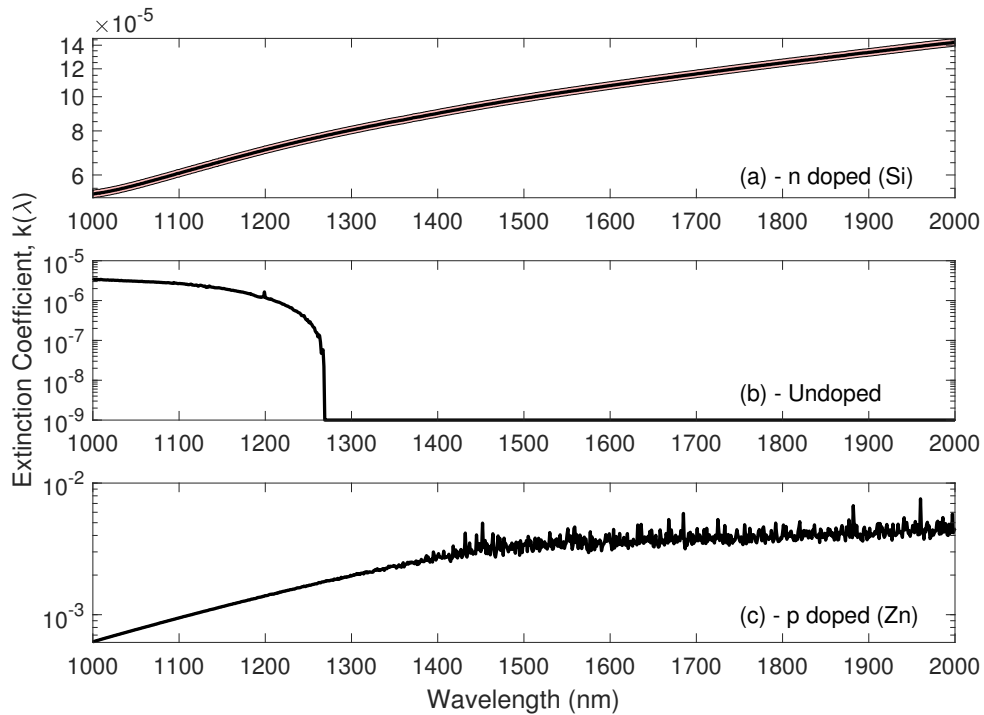


Figure 5.6: The shaded areas indicate the range of possible k values for: **(a)** n doped (Si), **(b)** undoped, and **(c)** p doped (Zn).

Wafer	Thickness	Uncertainty	
		Extinction Coefficient (Absolute)	Extinction Coefficient (Percentage)
n Type	$\pm 9 \mu\text{m}$	2.4×10^{-6}	2.5%
Undoped	$\pm 0.5 \mu\text{m}$	7.4×10^{-10}	0.1%
p Type	$\pm 4 \mu\text{m}$	3.1×10^{-5}	1.1%

Table 5.3: Batch thickness uncertainty (table 5.2) and the corresponding average uncertainty in the extinction coefficient for each wafer as calculated from the data in figure 5.6. Percentage error uses the average k value and uncertainty for each substrate.

Comparing the uncertainties in figure 5.6 to the thickness uncertainties in table 5.3 it is clear that the undoped and p-doped batches benefit from a very small range of thicknesses. However, when the percentage uncertainties are compared in table 5.3, it becomes clear that the high absorptance of the p-type wafer dominates the small variation in thickness, leading to a 1.1% error in the k values. The n-doped substrate has a larger variation in thickness across the batch, which in turn produces a noticeable 2.5% uncertainty in the extinction coefficient. Finally, the batch of undoped wafers has an unusually precise thickness range. Pairing this with the low absorption level of the intrinsic material results in a precision of 0.1%.

5.1.4 Simulation

The device from figure 5.1 can now be simulated using the extinction coefficient from figure 5.6a, as well as the improvements from earlier characterisation (substrate reflections and layer thicknesses). The resultant TFCalc transmission model can be seen in figure 5.7. The error range was produced by varying the layer thicknesses within their respective uncertainties, as well as varying the thickness and extinction coefficient according to the data in table 5.3, to produce a worst-case maximum and minimum transmission. The modelled and measured data now agree within the combined error of the various characterisation methods. The somewhat extensive characterisation is time consuming, with these measurements occurring over several days, but the results are a striking example of how essential it is to rerun theoretical models with up to date system parameters. By understanding the effect of layer thickness, dopant absorption, and other parameters being outside specification, it is possible to provide more accurate estimations of device performance and errors in the production process.

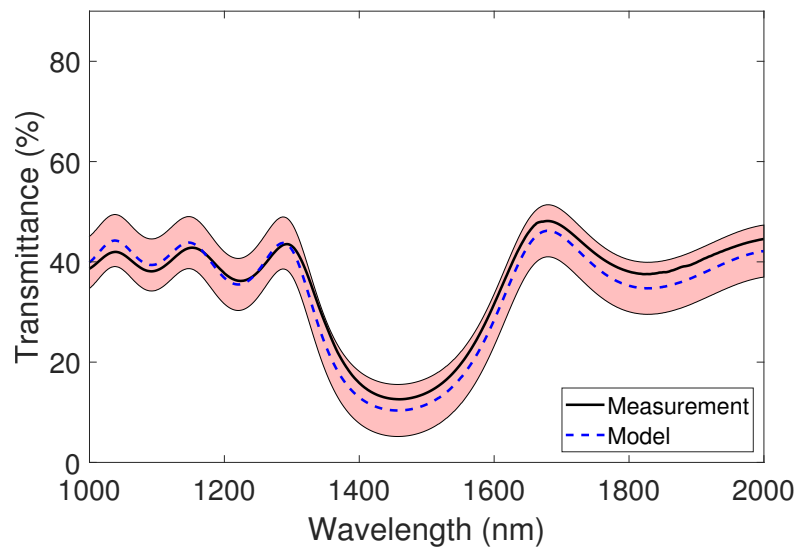


Figure 5.7: An up-to-date model of the short-period characterisation sample showing clear agreement with the measured transmission. The shaded region represents the cumulative error in the model.

While it would be incredibly useful to be able to model a doped device using the data from this section, the absorption data is only useful for a substrate with a known doping level. Without knowing the effect of varying carrier concentration on the extinction coefficient, it is extremely difficult to include absorbing GaAs layers in the device. In addition to this, it is impossible to know if the dopants behave the same way in the $\text{Al}_x\text{Ga}_{1-x}\text{As}$ layers. Since uncapped $\text{Al}_x\text{Ga}_{1-x}\text{As}$ oxidises much more readily than GaAs, it is not possible to measure a solid piece in the same way as above. Until further

investigation can take place, the model will use only the substrate absorption, with the analytical understanding that too many doped layers will have a detrimental impact on device output.

5.1.5 Aluminium Content of $\text{Al}_x\text{Ga}_{1-x}\text{As}$ Layers

One of the material parameters yet to be obtained is the actual composition of the $\text{Al}_x\text{Ga}_{1-x}\text{As}$ alloy layers. Since the refractive index of $\text{Al}_x\text{Ga}_{1-x}\text{As}$ is dependent on the alloy fraction, x , it is reasonable to suggest that if the sample is grown out of spec, the optical properties would be affected. The composition of every layer in the sample was measured using magnetic sector secondary-ion mass spectroscopy (MS-SIMS) by Loughborough Surface Analysis. The depth profile visible in figure 5.8 shows clear and consistent layers down to the substrate, with only slight rounding of the layer interfaces, likely due to the speed the material was sputtered at.

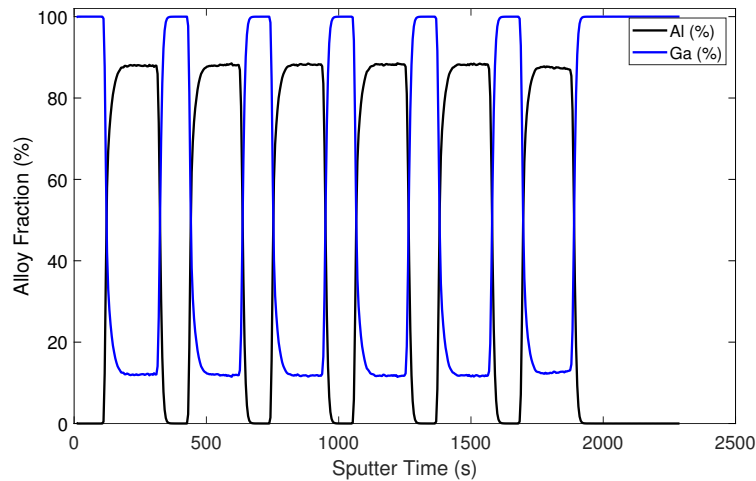


Figure 5.8: Depth profile performed using magnetic-sector SIMS with the top layer on the left and the substrate on the right.

The average Al content, calculated using the data in figure 5.8, is $88.0 \pm 0.3\%$. While this value is a little lower than the target (90%), it is still within a reasonable margin of the specifications. A simulation was performed using the reduced Al content, and showed only marginal changes. The closeness of the agreement of the measured data and simulation in figure 5.7, despite the slightly low $\text{Al}_x\text{Ga}_{1-x}\text{As}$ composition, implies that the optical properties of the structure are relatively tolerant to variations in composition.

5.2 $\text{Al}_x\text{Ga}_{1-x}\text{As}$ Compositional Analysis

Alongside the parameters that were investigated in the previous section, knowing the alloy composition of the $\text{Al}_x\text{Ga}_{1-x}\text{As}$ layers can provide a useful insight into the accuracy of a device growth. In order to compare the various methods available, a staircase sample was grown to the target specification in table 5.4. This section should be prefaced with the fact that the actual composition of the layers cannot be known without extremely precise calibration of all MBE growth rates and the flux of each molecular beam in use. Alternatively, an atom-by-atom post-growth characterisation such as atom probe tomography could be used, but is expensive and time consuming. These calibrations are next to impossible on a tool that is in regular use. As such this will be a comparison of each method as a whole, any pros/cons they may have, as well as how well they agree with one another. A 2" undoped GaAs wafer provided the substrate, and a GaAs buffer layer was used between each $\text{Al}_x\text{Ga}_{1-x}\text{As}$ layer. The buffers aimed to prevent layer mixing, and to improve contrast on the layers of interest. Each layer had a target thickness of 100 nm, making the total thickness of the epilayers approximately 2.9 μm . The sample was cleaved in half for optical characterisation, and then into quarters to be sent to each collaborator for measurement.

Note: All following figures and tables refer to the aluminium percentage with respect to the AlAs-GaAs alloy. In other words, x in $\text{Al}_x\text{Ga}_{1-x}\text{As}$ is represented as a percentage and not a decimal.

5.2.1 Layer Average Definition

For each analysis except EELS, the average Al composition of each $\text{Al}_x\text{Ga}_{1-x}\text{As}$ layer was determined using a layer detection algorithm. The layer interfaces were identified using a peak in the first differential of Al fraction vs sputter time, while the points within the layer were then filtered using 95% of the maximum value. The value of 95% was chosen to ensure that the points included in the average were well within the layer of interest.

5.2.2 Optical Analysis

To assess the uniformity of the sample, a position-dependant transmission map was performed on half of the wafer. The sample transmission spectrum, visible on the top of figure 5.9, had an interference peak that could be easily measured and was sharper than the adjacent trough. This was selected for the mapping parameter. The resultant plot

Layer No	Material	Al % (estimated)	Layer No	Material	Al % (estimated)
1	GaAs		16	$\text{Al}_x\text{Ga}_{1-x}\text{As}$	50
2	$\text{Al}_x\text{Ga}_{1-x}\text{As}$	100	17	GaAs	
3	GaAs		18	$\text{Al}_x\text{Ga}_{1-x}\text{As}$	40
4	$\text{Al}_x\text{Ga}_{1-x}\text{As}$	99	19	GaAs	
5	GaAs		20	$\text{Al}_x\text{Ga}_{1-x}\text{As}$	30
6	$\text{Al}_x\text{Ga}_{1-x}\text{As}$	95	21	GaAs	
7	GaAs		22	$\text{Al}_x\text{Ga}_{1-x}\text{As}$	20
8	$\text{Al}_x\text{Ga}_{1-x}\text{As}$	90	23	GaAs	
9	GaAs		24	$\text{Al}_x\text{Ga}_{1-x}\text{As}$	10
10	$\text{Al}_x\text{Ga}_{1-x}\text{As}$	80	25	GaAs	
11	GaAs		26	$\text{Al}_x\text{Ga}_{1-x}\text{As}$	5
12	$\text{Al}_x\text{Ga}_{1-x}\text{As}$	70	27	GaAs	
13	GaAs		28	$\text{Al}_x\text{Ga}_{1-x}\text{As}$	1
14	$\text{Al}_x\text{Ga}_{1-x}\text{As}$	60	29	GaAs	
15	GaAs		30	GaAs Substrate	

Table 5.4: The target structure to be used in comparing the methods of compositional characterisation. GaAs layers between the $\text{Al}_x\text{Ga}_{1-x}\text{As}$ layers provide a buffer to prevent mixing, as well as make it easier to view the layers of interest in a depth profile.

is shown on the bottom of figure 5.9. A radial wavelength variation of approximately 20 nm is evident in the peak position, indicating a variation in thickness across the sample. Given the large number of layers it is not possible from this data to determine how much the thickness varies, but it is reasonable to suggest that the centre of the wafer has a greater optical thickness than the edge. Using this information, the collaborators were instructed to take their measurements from as close to the centre of the wafer as possible. Thus reducing the layer variation between the different techniques.

5.2.3 Secondary Ion Mass Spectroscopy (SIMS)

As discussed in section 4.3.1, two variants of SIMS were used to produce compositional depth profiles of the sample structure. Both techniques use a Cs^+ primary ion beam to remove material from the sample, but use different methods to isolate the secondary ions.

5.2.3.1 Magnetic Sector SIMS

MS-SIMS measured the entire structure of the characterisation sample by sputtering away the surface with a 5.5 keV Cs^+ primary ion beam and characterising the secondary ions using sequential electrostatic and magnetic deflection. Relative levels of gallium and aluminium were then calculated using a correlation plot of the $\text{CsAl}^+/\text{CsAs}^+$ and

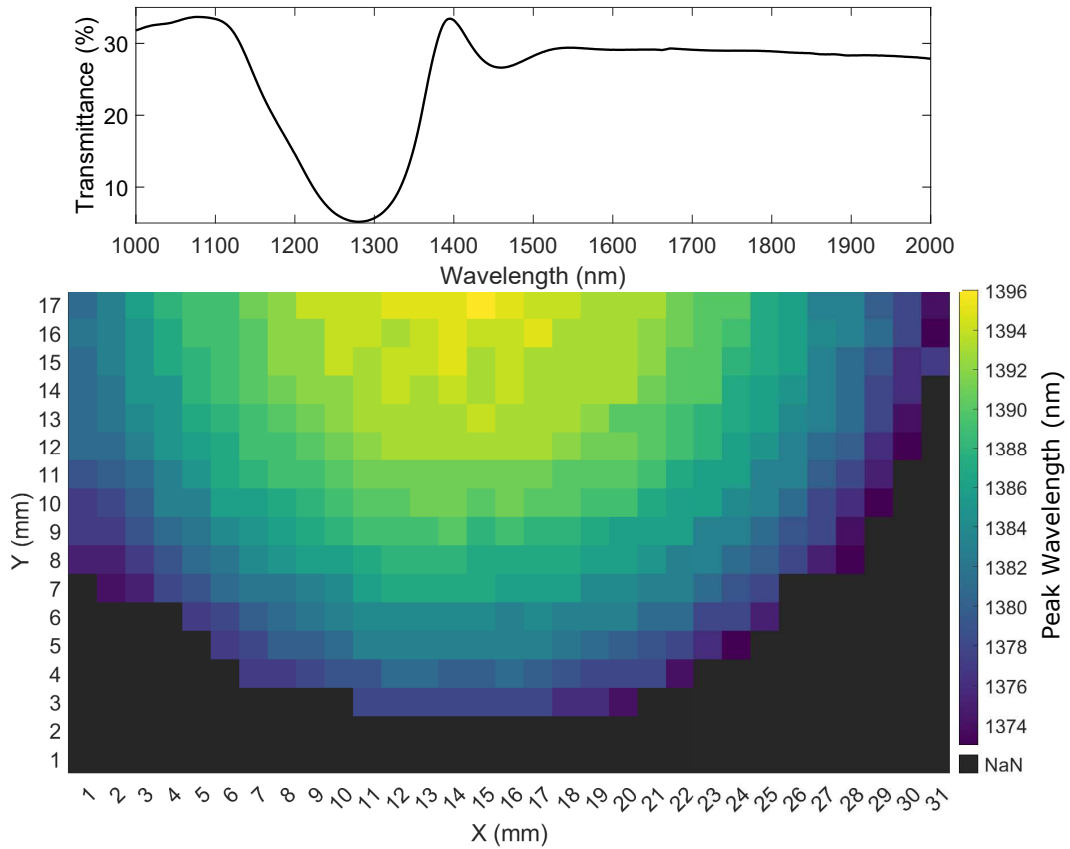


Figure 5.9: **Top:** An example transmission spectrum from the centre of the sample wafer showing the transmission peak at around 1395 nm. **Bottom** A map of the transmission peak’s wavelength in respect to the position on the sample wafer.

CsGa⁺/CsAs⁺ signals. The composition could not be directly compared to the depth within the structure, due to variable sputter speeds in the different layers of the device, but plotting the alloy percentage against the sputter time gives a clear depth profile. The whole structure was characterised in a little under an hour. Figure 5.10 displays the profile of the structure in table 5.4, with clear GaAs layers between the layers of interest. The GaAs layers appear thinner, with more rounded interfaces. It is likely that these layers sputter more quickly, thus reducing the number of data points and lowering the definition of the interfaces. A plot of the sputter time for each layer of the sample, displayed in figure 5.11, clearly demonstrates the difference in sputter rate between GaAs and Al_xGa_{1-x}As. With that being the case, it is also expected that as the Al fraction, x , decreases, the sputter rate will increase and approach that of GaAs. Once again figure figure 5.11 agrees with this prediction, implying that later layers in the analysis contained fewer data points per layer. While slowing the sputter rate would remedy this, that would increase the overall characterisation time, and simply seeing that there appears to be no Al contamination in the GaAs layers is good enough

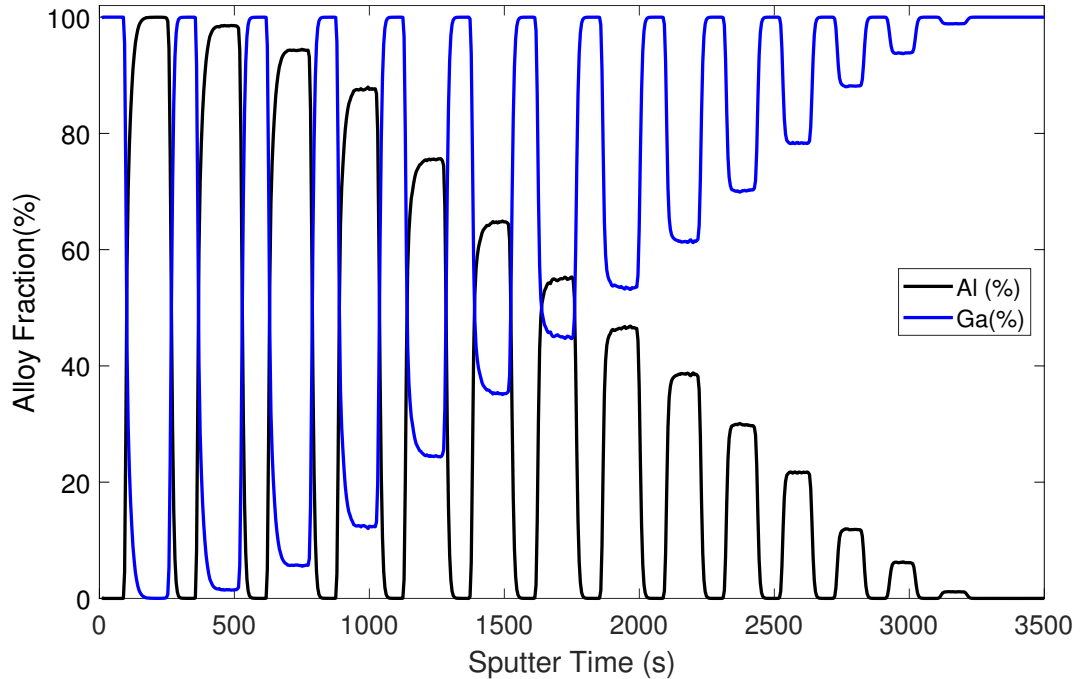


Figure 5.10: MS-SIMS alloy percentage for aluminium and gallium against the sputtering time. Actual depth in the device is not stated as the sputtering rate varies by material and is not accurately known.

for the current work. Alternatively, the etch power could be reduced in line with the expected Al fraction in order to maintain a constant etch and avoid loss of data. The larger uncertainties in layer sputter time stem from the sloped interfaces, making the identification of the true layer boundaries more difficult.

A slight rounding at the start of each $\text{Al}_x\text{Ga}_{1-x}\text{As}$ layer could be due to layer mixing, where some of the previous layer remains as the etch front reaches the new material, but this is difficult to avoid without again slowing down the etching. By taking an average of each peak in the $\text{Al}_x\text{Ga}_{1-x}\text{As}$ layers using the definition in section 5.2.1, the difference from the target value for each layer was calculated and is shown in table 5.5. The average values in table 5.5 show fairly good agreement with the targets, with the middle values having the greatest deviation. Combining this with the low deviation on the end points, it is possible that the fitting parameters used to extract the percentage values from the SIMS data have an incorrect curvature, and that more bowing needs to be accounted for. Alternatively, the sample may have been grown out of specification due to incorrect MBE calibration. However, it is more likely that a combination of both factors contribute to the deviation from target values.

Layer No	Material	Al % (Target)	Average Al %
2	$\text{Al}_x\text{Ga}_{1-x}\text{As}$	100	99.5 ± 2.2
4	$\text{Al}_x\text{Ga}_{1-x}\text{As}$	99	97.9 ± 2.1
6	$\text{Al}_x\text{Ga}_{1-x}\text{As}$	95	93.8 ± 2.1
8	$\text{Al}_x\text{Ga}_{1-x}\text{As}$	90	87.1 ± 1.9
10	$\text{Al}_x\text{Ga}_{1-x}\text{As}$	80	75.0 ± 1.6
12	$\text{Al}_x\text{Ga}_{1-x}\text{As}$	70	64.3 ± 1.4
14	$\text{Al}_x\text{Ga}_{1-x}\text{As}$	60	54.7 ± 1.2
16	$\text{Al}_x\text{Ga}_{1-x}\text{As}$	50	46.3 ± 1.1
18	$\text{Al}_x\text{Ga}_{1-x}\text{As}$	40	38.4 ± 0.7
20	$\text{Al}_x\text{Ga}_{1-x}\text{As}$	30	29.8 ± 0.6
22	$\text{Al}_x\text{Ga}_{1-x}\text{As}$	20	21.6 ± 0.3
24	$\text{Al}_x\text{Ga}_{1-x}\text{As}$	10	11.8 ± 0.2
26	$\text{Al}_x\text{Ga}_{1-x}\text{As}$	5	6.1 ± 0.2
28	$\text{Al}_x\text{Ga}_{1-x}\text{As}$	1	1.1 ± 0.1

Table 5.5: Averaged MS-SIMS results compared to target values.

5.2.3.2 Time-of-Flight SIMS

Layer No	Material	Al % (Target)	Average Al %
2	$\text{Al}_x\text{Ga}_{1-x}\text{As}$	100	98.7 ± 2.2
4	$\text{Al}_x\text{Ga}_{1-x}\text{As}$	99	97.3 ± 2.3
6	$\text{Al}_x\text{Ga}_{1-x}\text{As}$	95	95.2 ± 2.4
8	$\text{Al}_x\text{Ga}_{1-x}\text{As}$	90	92.0 ± 2.2
10	$\text{Al}_x\text{Ga}_{1-x}\text{As}$	80	85.6 ± 2.0
12	$\text{Al}_x\text{Ga}_{1-x}\text{As}$	70	78.4 ± 1.9
14	$\text{Al}_x\text{Ga}_{1-x}\text{As}$	60	70.6 ± 1.6
16	$\text{Al}_x\text{Ga}_{1-x}\text{As}$	50	62.2 ± 1.5
18	$\text{Al}_x\text{Ga}_{1-x}\text{As}$	40	52.8 ± 1.2
20	$\text{Al}_x\text{Ga}_{1-x}\text{As}$	30	41.5 ± 1.0
22	$\text{Al}_x\text{Ga}_{1-x}\text{As}$	20	30.4 ± 0.7
24	$\text{Al}_x\text{Ga}_{1-x}\text{As}$	10	16.8 ± 0.4
26	$\text{Al}_x\text{Ga}_{1-x}\text{As}$	5	8.8 ± 0.2
28	$\text{Al}_x\text{Ga}_{1-x}\text{As}$	1	1.7 ± 0.1

Table 5.6: Averaged ToF-SIMS results compared to target values.

The ToF-SIMS investigation also measured the entire structure of the characterisation sample by sputtering away the surface and characterising the secondary ions. Depth sputtering was achieved using a Cs^+ beam of 1 keV, while a secondary analysis beam at 15 keV in Bi^{3+} was used to probe the sample surface. Analysis used time-of-flight mass separation to isolate the ions of interest. Once again the composition could not be directly compared to the depth within the structure, due to the variable sputter speed in the different layers of the device, but plotting the alloy percentage against the sputter

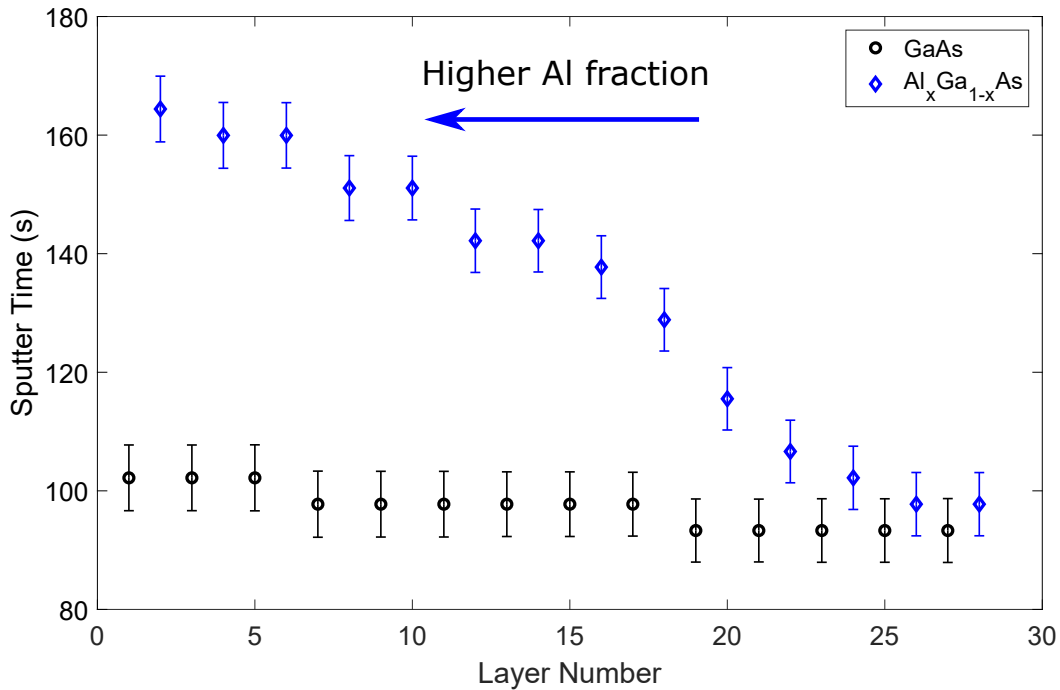


Figure 5.11: Sputter time for each layer of the staircase sample analysed using MS-SIMS, with the surface on the left and the substrate on the right.

time gives a depth profile. This can be seen in figure 5.12. As with the previous SIMS technique, a clear profile of the entire structure was produced. The first thing to note is that the time taken for the etch is much longer, and the layers are more symmetrical. The slower profile produces more data points and less rounding at the layer interfaces, while the interlaced ion etching seems to result in less layer intermixing from the etch itself. However, a small rounding is still visible at the start of the first few layers, suggesting a certain amount of intermixing occurring as the next layer becomes visible to the probing beam before the previous layer is fully etched away. The longer etch time, combined with the more sloped layer interfaces compared to figure 5.10, indicate that the change between layers is more gradual than when using MS-SIMS. The etch time per layer was once again calculated, and is visible in figure 5.13. The higher Al layers once again appear to etch more slowly, increasing in speed as x is reduced, while the GaAs appears to slightly decrease in etch speed as the characterisation progresses. This could potentially be due to layer intermixing, with some aluminium being pushed into the GaAs layers, or alternatively could be due to some drift in the sputter beam power over time.

The average alloy percentage was calculated to the parameters in section 5.2.1 and is shown in table 5.6, along with the deviation from the expected values. The difference

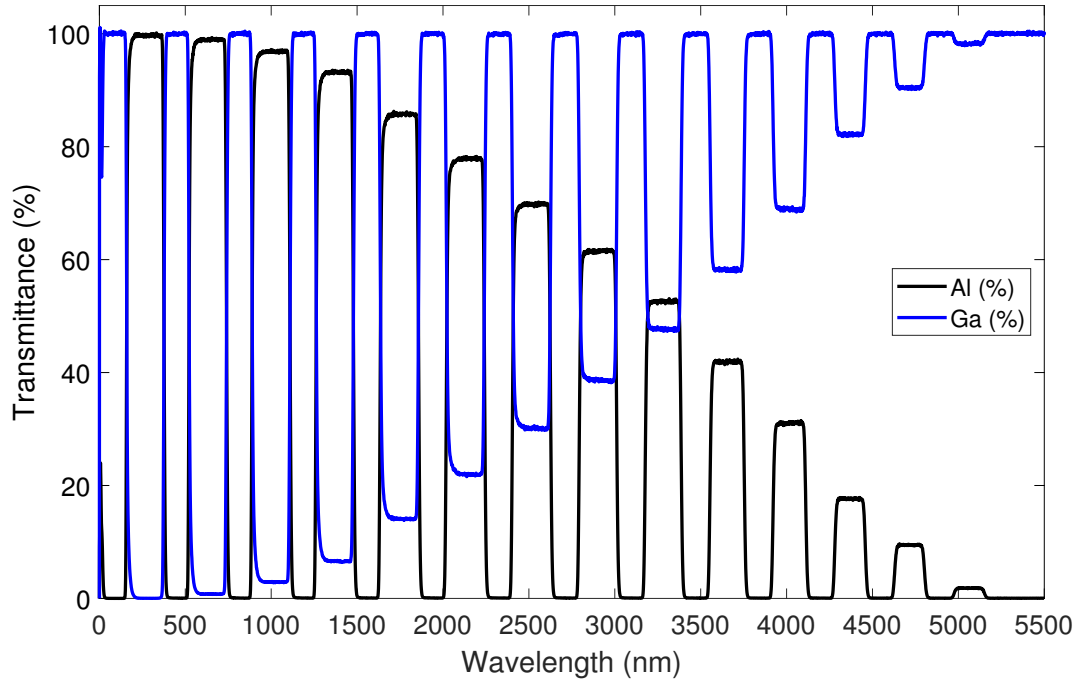


Figure 5.12: ToF-SIMS alloy percentage for aluminium and gallium against the sputtering time. Actual depth in the device is not stated as the sputtering rate varies by material and is not accurately known.

from target once again appears non-linear, with a larger deviation from the target values in the middle of the sample. This bowing, which is in the opposite direction to the MS-SIMS, once again suggests that the fitting parameters of one or both SIMS techniques could need some adjustment.

5.2.4 X-Ray Photoelectron Spectroscopy (XPS)

An XPS depth profile was taken using a 1 keV argon-ion beam with an etch step of 30 s, followed by the X-ray measurement producing the profile in figure 5.14. A few differences from the SIMS measurements are immediately noticeable. Firstly, the time frame over which the measurement occurred is much larger, taking nearly ten times longer than the MS-SIMS, and five times longer than the ToF-SIMS. Secondly, the definition of the layers degrades as the etch gets deeper into the device, causing the final layers to be very difficult to characterise, and the final layer cannot be distinguished from the noise. The rounding of the layer interfaces is caused by a combination of the X-ray penetration depth, and the impact of the etch itself. Since an etch crater is generated, and the etched material is not accelerated away from the surface as in SIMS, material from earlier layers can be sputtered onto the measurement surface at the base of the crater.

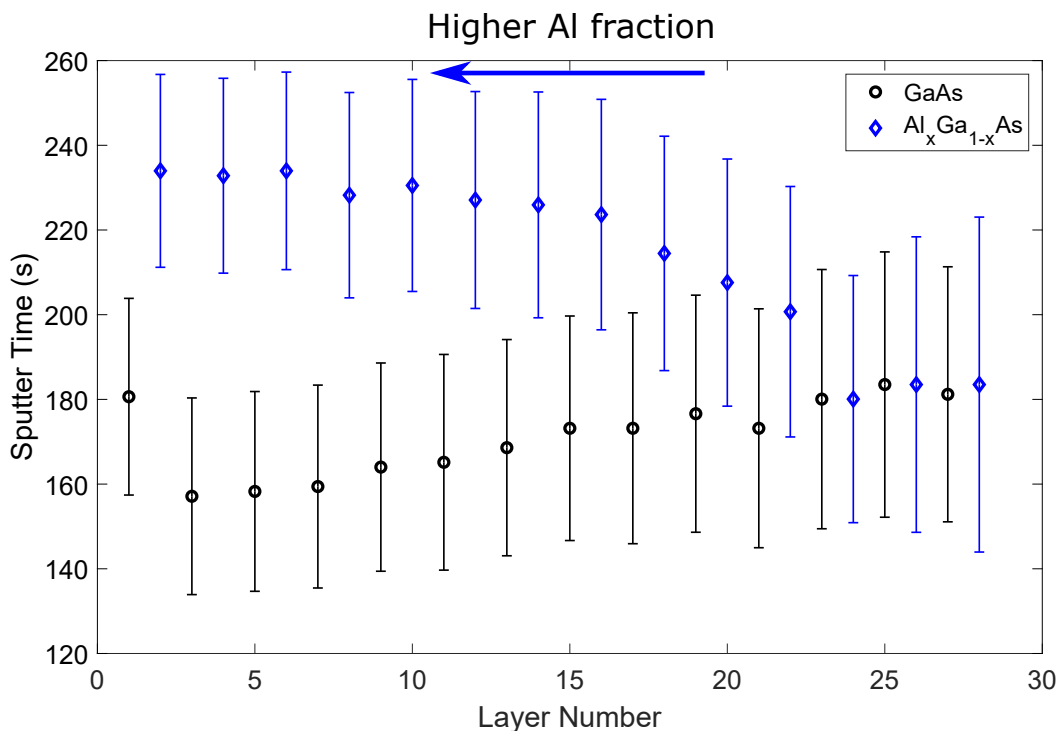


Figure 5.13: Sputter time for each layer of the staircase sample analysed using ToF-SIMS, with the surface on the left and the substrate on the right.

This leads to a blending of the layer data, loss of definition, and raising of the profile's baseline. Improvements could be made to the layer definition by slowing the analysis, which would increase the time taken for the measurement even further. The average Al fraction in table 5.7 displays much greater linearity than either of the SIMS techniques, with a fractional positive bowing. This could imply that the more quantitative nature of XPS produces more accurate measurements since a calibration curve is not used, thus will not negatively affect the data. However, caution should be taken when making this assumption, as there could be some bowing in the data that is countered by inaccuracies in the growth, producing the appearance of linearity. Generally speaking, XPS requires less calibration to elemental signals than SIMS, making it useful for instances where the elements present are not already known e.g. contamination. A plot of sputter time per layer (figure 5.11 and figure 5.13) was not made in this case, primarily due to the lack of layer definition making that analysis essentially useless.

5.2.5 Electron Energy-Loss Spectroscopy (EELS)

EELS data was successfully gathered for the top 12 $\text{Al}_x\text{Ga}_{1-x}\text{As}$ layers in the sample, with the deeper layers suffering from both the thickness of the sample, and damage due to ion-beam polishing step. Results from the measured layers, along with the measurement

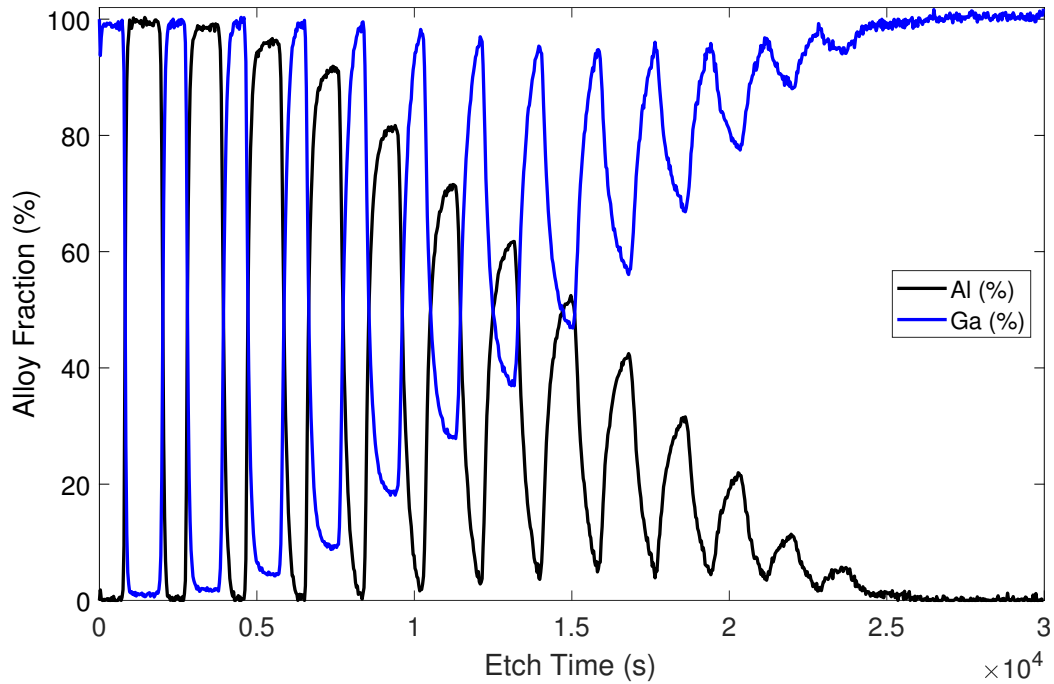


Figure 5.14: XPS alloy percentage for aluminium and gallium against the etch time. Actual depth in the device is not stated as the sputtering rate varies by material and is not accurately known.

errors, are shown in figure 5.15. The measured values show good agreement with what was intended for the growth. A 2D map showing some of the sample's upper layers can be seen in figure 5.15, clearly demonstrating the sharp layer interfaces of the growth.

A drawback of this method is the potential for contamination due to the ion polishing step of the sample preparation. The ion beam, while creating the surface finish required for an electron transparent sample, also sputters some copper from the grid that serves as a sample support. The extent of this contamination was assessed and some data from the lower layers of the sample is visible in figure 5.16. A low-level contamination is detected, and appears to affect the base As concentration which will be a source of uncertainty in the final composition data. Overall the measurement uncertainty is high, but it varies layer by layer, indicating that layer quality may be a factor. Repeating the analysis may reduce the size of the errors. Layer one and layer six have very low uncertainties, as the data for those layers is from single point measurements, rather than the area-averaged values used for the other layers. Averaging over a certain area within the layer is more useful however, as this reduces the impact of any impurities or inconsistencies that may be inadvertently measured.

Layer No	Material	Al % (Target)	Average Al %
2	$\text{Al}_x\text{Ga}_{1-x}\text{As}$	100	99.3 ± 1.5
4	$\text{Al}_x\text{Ga}_{1-x}\text{As}$	99	98.1 ± 2.3
6	$\text{Al}_x\text{Ga}_{1-x}\text{As}$	95	95.4 ± 1.9
8	$\text{Al}_x\text{Ga}_{1-x}\text{As}$	90	90.2 ± 2.2
10	$\text{Al}_x\text{Ga}_{1-x}\text{As}$	80	80.5 ± 1.9
12	$\text{Al}_x\text{Ga}_{1-x}\text{As}$	70	70.5 ± 1.6
14	$\text{Al}_x\text{Ga}_{1-x}\text{As}$	60	60.7 ± 1.5
16	$\text{Al}_x\text{Ga}_{1-x}\text{As}$	50	51.1 ± 1.3
18	$\text{Al}_x\text{Ga}_{1-x}\text{As}$	40	41.5 ± 1.0
20	$\text{Al}_x\text{Ga}_{1-x}\text{As}$	30	30.8 ± 0.8
22	$\text{Al}_x\text{Ga}_{1-x}\text{As}$	20	21.4 ± 0.5
24	$\text{Al}_x\text{Ga}_{1-x}\text{As}$	10	11.1 ± 0.3
26	$\text{Al}_x\text{Ga}_{1-x}\text{As}$	5	5.6 ± 0.2
28	$\text{Al}_x\text{Ga}_{1-x}\text{As}$	1	-

Table 5.7: Averaged XPS results compared to target values.

5.2.6 Comparison of Methods

Target (%)	MSSIMS	ToF-SIMS	XPS	EELS
100	99.5 ± 2.2	98.7 ± 2.2	99.3 ± 1.5	98.4 ± 0.3
99	97.9 ± 2.1	97.3 ± 2.3	98.1 ± 2.3	97.9 ± 6.1
95	93.8 ± 2.1	95.2 ± 2.4	95.4 ± 1.9	92.1 ± 25.9
90	87.2 ± 1.9	92.0 ± 2.2	90.2 ± 2.2	90.1 ± 9.9
80	75.0 ± 1.6	85.6 ± 2.0	80.5 ± 1.9	84.0 ± 6.1
70	64.3 ± 1.4	78.4 ± 1.9	70.5 ± 1.6	72.0 ± 0.1
60	54.7 ± 1.2	70.6 ± 1.6	60.7 ± 1.5	60.1 ± 16.1
50	46.3 ± 1.1	62.2 ± 1.5	51.1 ± 1.3	48.1 ± 8.0
40	38.4 ± 0.7	52.8 ± 1.2	41.5 ± 1.0	40.2 ± 14.0
30	29.8 ± 0.6	41.5 ± 1.0	30.8 ± 0.8	34.2 ± 5.8
20	21.6 ± 0.3	30.4 ± 0.7	21.4 ± 0.5	18.0 ± 8.7
10	11.8 ± 0.2	16.8 ± 0.4	11.1 ± 0.3	16.1 ± 18.1
5	6.2 ± 0.2	8.8 ± 0.2	5.6 ± 0.2	-
1	1.1 ± 0.1	1.7 ± 0.1	-	-

Table 5.8: Table of measured aluminium fraction for each method of analysis.

The average layer Al content for each technique is compared to the target values in figure 5.17, with all techniques agreeing more at the end points of the measurement. MS-SIMS shows good agreement with the targets, with a small bowing occurring in the centre values. The ToF-SIMS displays a much larger bowing than the other methods, implying that the fitting parameters used need to be adjusted to compensate for any curvature. While the XPS data suffered from the depth of the etch, the data is still relatively close to the target. The loss of definition will have pulled the Al content down when the average was calculated, which agrees with the generally low values of the XPS.

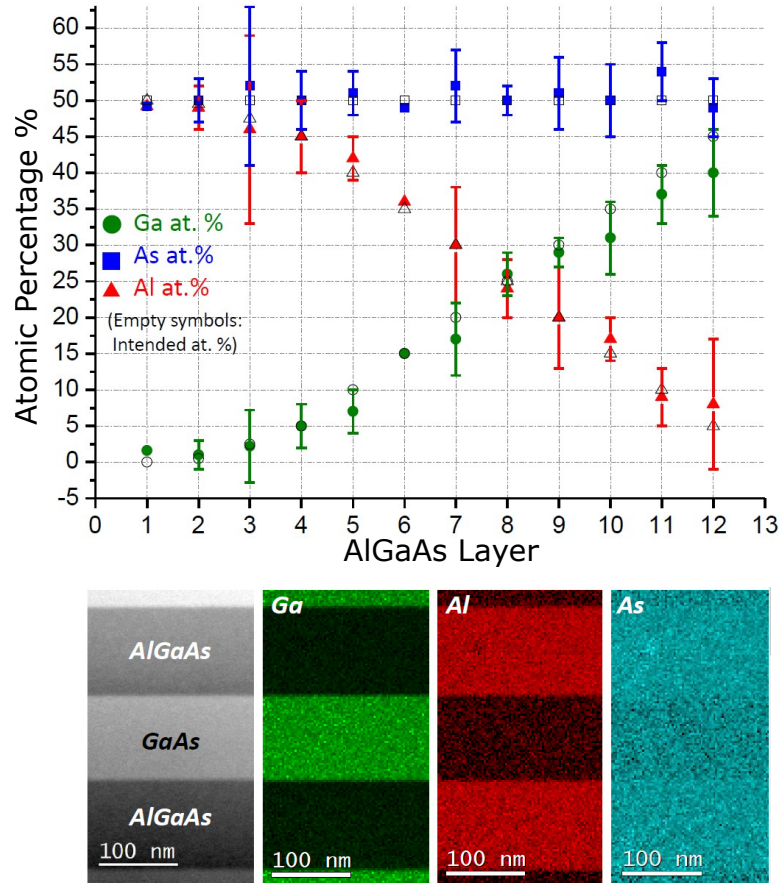


Figure 5.15: **Top:** The atomic percentages of gallium, aluminium, and arsenic for the first 12 $\text{Al}_x\text{Ga}_{1-x}\text{As}$ layers in the sample with empty symbols showing the desired percentage. **Bottom:** scanning electron microscopy (SEM) image and 2D maps of some of the sample's upper layers showing elemental concentration

EELS data could not be gathered for all layers, but the measurements that could be taken show decent agreement with the expected Al content. Some values are further from specification than others, but there is no general trend. This indicates that the deviation is either due to the error range in the measurement, or simply that the layer's Al percentage is out of spec. The general agreement of all techniques shows that each can be used to gain a general picture of the composition within a multilayer device, but some may need additional calibration and corrections. The following sections give a breakdown of each method's positives and negatives, to detail under which circumstances they can be used.

5.2.6.1 MS-SIMS Pros/Cons

MS-SIMS was by far the fastest technique, able to characterise the entire sample in just under an hour. This speed is massively important when dealing with industrial and bulk analysis, as any delay to production can be detrimental and costly. There is some

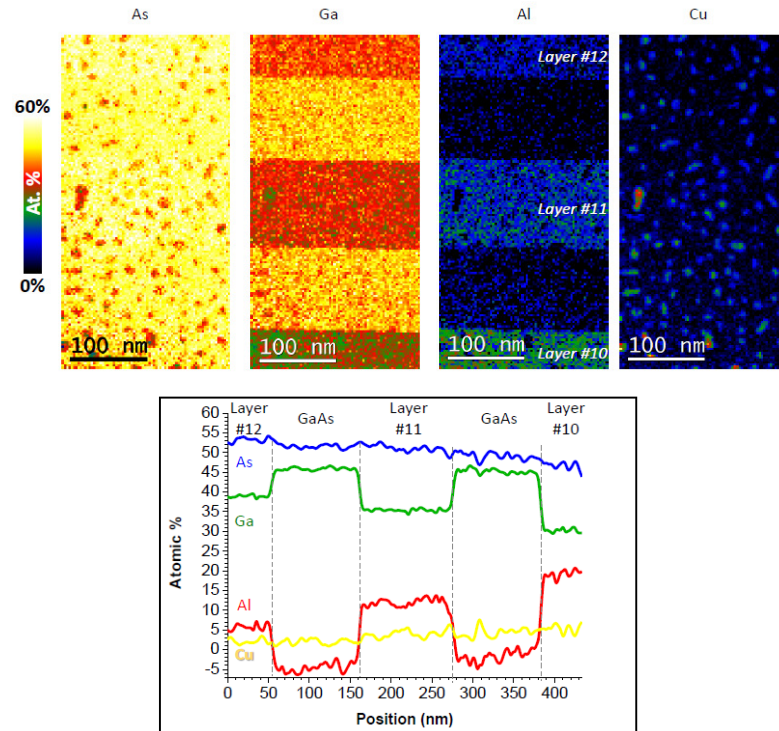


Figure 5.16: **Top:** 2D elemental maps showing lower layers in the device, as well as contamination due to sputtered copper. **Bottom:** graph of atomic percentages showing the copper contamination and corresponding variation in arsenic concentration.

layer intermixing, indicated by curving at the start of the layers, which could possibly be improved by slowing down the etching. Given the speed of the technique, slowing down when more detail is needed is still feasible. While there is a little bowing in the measurement, more time could be spent procuring and measuring a precise calibration standard, which could then be used to correct for the variation in sensitivity to different secondary ions. The downside to these calibrations is that a new measurement would need to be done for every new element, and possibly each semiconductor alloy as combinations of elements may behave differently.

5.2.6.2 ToF-SIMS Pros/Cons

ToF-SIMS shares many characteristics with MS-SIMS, with relatively fast acquisition time and clear layers throughout the device. The obvious benefit to ToF-SIMS is the sharpness of the layer interfaces, likely due to the lower energy interlaced Cs^+ ion beams used while sputtering. The narrower secondary beam allows for precise selection of the sample area, reducing layer intermixing and giving the option for fully 3-dimensional measurements. There also seems to be little degradation of the signal with depth, so thicker devices, such as VCSELs for example, could also be characterised. The technique

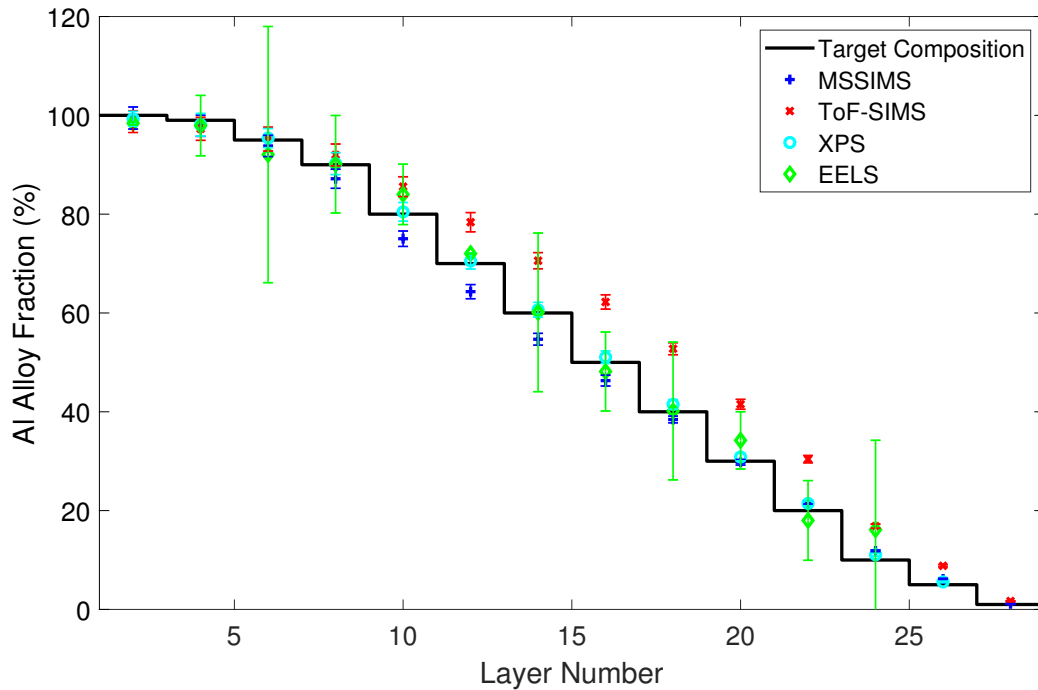


Figure 5.17: Direct comparison of the measured aluminium content of each of the $\text{Al}_x\text{Ga}_{1-x}\text{As}$ layers, by all four different techniques.

appears to suffer from greater bowing around the middle of the $\text{GaAs}/\text{Al}_x\text{Ga}_{1-x}\text{As}$ stack, but this could simply be due to the calibration having too great/small a curvature. As above, comparison with an accurate known standard could reduce the discrepancy in the measurement.

5.2.6.3 XPS Pros/Cons

Unlike the SIMS measurements, XPS benefits from a more quantitative approach. The researcher does not need to know fully the elements present within the sample, and can determine the most likely composition with a standard set of reference spectra and sensitivity factors. This approach makes XPS incredibly useful for finding contaminants within sample layers or surface contacts, and in particular carbon or oxygen contamination can even be used to calibrate the energy detection of the spectrometer. The downside of the technique is the layer intermixing caused by the Ar-ion etching. Since the etched material is not accelerated away for characterisation, as in SIMS, material from previous layers has the potential to be sputtered onto the surface under investigation before it can be pumped away. The effect of this is very obvious in figure 5.14, with an extreme loss of layer definition and baseline. Deeper etches are therefore much less feasible with XPS, and while the process can be slowed to improve definition, the

already long (more than 8 hours) measurement would become even longer.

5.2.6.4 EELS Pros/Cons

EELS stands out from the other measurements due to the data being gathered from an ion polished cross-section rather than a top-down etch. This approach results in incredibly detailed compositional data, and can produce 2D images of the distribution of elements within the sample, as seen in figure 5.15. The other obvious benefit of having such a small measurement area is that the quality of the layer interfaces can be observed, showing any intermixing between the materials, and contaminants that might otherwise be part of a general contamination level can be visualised in-situ. The cross-sectioning makes sample preparation much more challenging, with thicker samples being both harder to prepare and more prone to damage at the beam exit. One other problem with the method of preparation is the possibility for contamination from the support material during ion polishing, as it can be sputtered onto the surface of the sample. Finally, the high precision and intensive preparation make EELS slow for multi-layered samples, and while the detail is excellent, the long time frame makes industrial use unfeasible.

5.3 Summary

Several techniques have been assessed to determine their suitability for use in the quantification of GaAs - $\text{Al}_x\text{Ga}_{1-x}\text{As}$ layered structures. All methods demonstrated the ability to measure the compositional data of the staircase sample structure, with MS-SIMS, ToF-SIMS, and XPS producing depth profiles of alloy fraction vs etch time. EELS on the other hand was able to map the atomic composition over an area of the sample's cross-section, allowing for the visualisation of sample uniformity and layer interface quality, but could not reach the deepest layers in the sample due to limitations of the technique and damage caused by cross-section polishing. In terms of ease of analysis for a many-layered structure, both SIMS techniques produced clean layer interfaces with relatively fast acquisition times, and allowed for easy calculation of average layer composition. XPS suffered from the aggressive nature of its etching process, with evidence of layer intermixing becoming more prominent further into the sample. Slowing down the etch and measurements would improve the layer clarity, but would increase the time taken for an already lengthy measurement. The highly detailed nature of the EELS analysis makes it time intensive and prone to uncertainty over an averaged area of the

sample, and would generally be most suited to samples with few layers, where high resolution is required. MS-SIMS and ToF-SIMS both use calibration standards for the relative intensities of the elemental signals, and both display non-linear ‘bowing’ of the average layer Al fraction but in opposite directions. This could indicate that the calibration curves used have an incorrect curvature, and could need adjusting. Alternatively, the growth could be out of spec with a non-linear composition variation, affecting the values produced in the analysis. XPS uses standard reference values for determining the relative composition of a sample, and displays much more linear results in line with the target layer composition. In general, the SIMS techniques are more suitable for thick, many-layered structures where speed and layer clarity are the most important. MS-SIMS has the higher rate of analysis, while ToF-SIMS benefits from symmetric layer interfaces and smoother peak values. When a surface or thinner sample with some unknown composition or contaminant is present, the quantitative nature of XPS reduces the need for extensive calibration. Finally, when a high level of detail of a layer and its interfaces is needed, EELS provides high-resolution compositional maps of a cross-section, allowing for small-scale analysis of the material quality.

Chapter 6

SPLEDs

6.1 Active Region Design

Electrically-driven single-photon sources are highly desirable in the field of quantum information technology, with room-temperature operation being a key feature [81, 82, 83]. The designs in the following section aim to use a method of confining electrons into a single state, combined with a GaSb QR recombination layer to generate single photons from a semiconductor device. A resonant cavity design was also implemented to provide wavelength selection for a single photon LED (SPLED) capable of operating in the telecoms O or C bands. By embedding a single-electron generating structure inside a resonant cavity the emission wavelength can be tuned and amplified.

Two designs were produced to form the single-electron tunnelling structure. In both designs at zero bias an electron confined state begins high above the conduction band edge. Once a bias is applied, the state moves down until the highest available electron can then tunnel into the confined state. Further tunnelling is then blocked until it proceeds to the next stage of the process, depending on the design. Design 1 is shown in figure 6.1, with the energy diagram shown in figure 6.3a, relies on the accumulation of charge in both the n-type GaAs and the GaSb quantum rings, so that band bending would occur and form a tunnelling barrier. Once the single electron is occupying the confined state, recombination can occur with a confined hole from a quantum ring, producing a single photon. However, monochromatic emission is very unlikely. This is due to variations in the thickness across the layer, material quality and the presence of any defects altering the energy levels of the confined state.

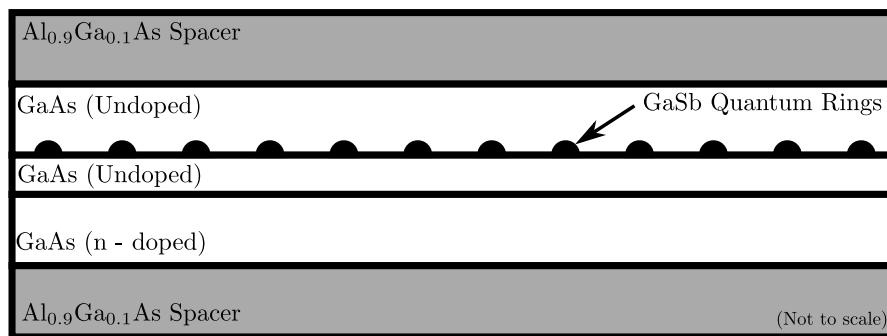


Figure 6.1: A diagram of the first version of the SPLED active region (not to scale) showing the GaSb quantum ring layer embedded within the GaAs structure

Design 2 is shown in figure 6.2, with the energy diagram shown in figure 6.3b, employs a GaAs quantum dot between $\text{Al}_{0.6}\text{Ga}_{0.4}\text{As}$ barriers to provide the confined state, as well as an n-type $\text{Al}_x\text{Ga}_{1-x}\text{As}$ layer to act as the electron reservoir. GaAs quantum dots were selected for their ability to be made in $\text{Al}_x\text{Ga}_{1-x}\text{As}$ via droplet epitaxy, which can be

employed to produce non-uniform dots in a range of sizes. By slowly increasing the bias, the largest QD, with the lowest energy level, should be occupied first and therefore the occupying electron will tunnel through the second barrier for recombination first[84, 85]. Factoring the single-dot tunnelling, alongside the much smaller tunnelling area of the device, would theoretically produce single electron tunnelling, and hence single photon emission upon recombination.

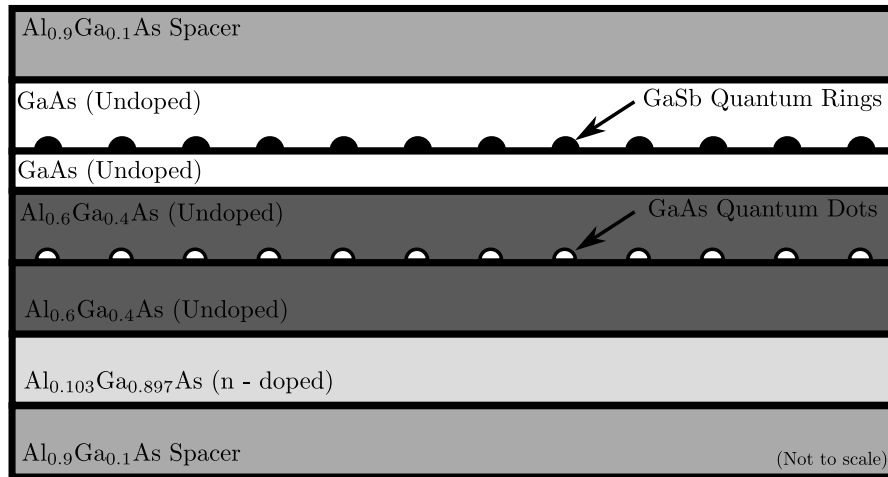


Figure 6.2: A diagram of the second version of the SPLED active region (not to scale) showing the quantum dot layer embedded within the $\text{Al}_{0.6}\text{Ga}_{0.4}\text{As}$ structure below the GaSb quantum ring light-generating layer.

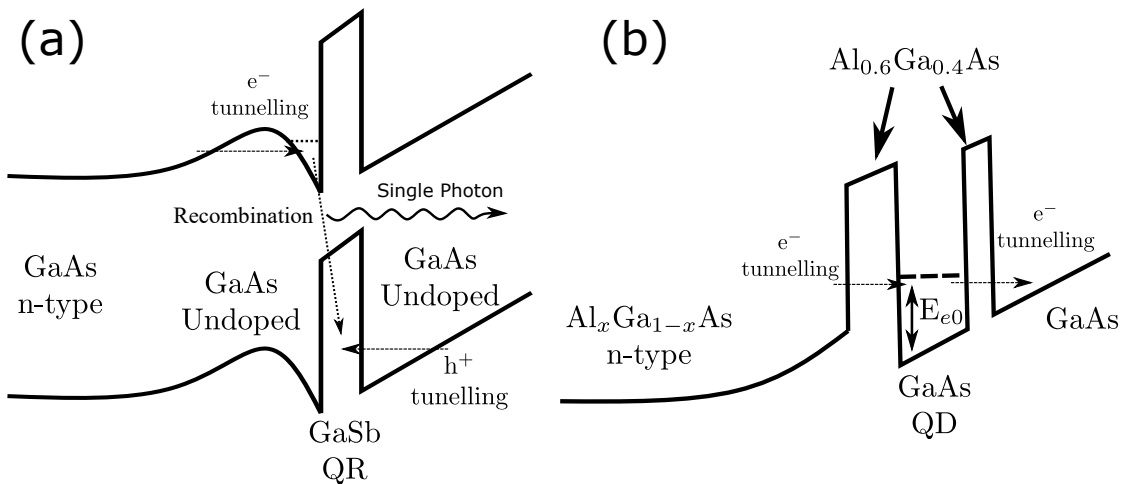


Figure 6.3: (a): Design 1 band diagram showing the triangle well confined state and carrier tunnelling. (b): Design 2 band diagram showing dual barrier structure and GaAs quantum dot. The light emitting region is still a GaSb QR structure to the right of the barrier structure, and is not shown.

6.2 Optical Design

6.2.1 Design 1

The initial target wavelength for the single photon LEDs was the telecoms C-band at 1550 nm. The primary design consideration in this case was retuning the DBR layers to the new centre wavelength. Using the refractive index generated from Adachi and Aspnes [30, 31, 32] at 1550 nm, a GaAs-Al_{0.9}Ga_{0.1}As DBR was generated. Table 6.1 shows the embedded Design 1 single electron generation structure and the surrounding optical cavity. The lower DBR has a large number of repeats to produce a high reflectivity, while the upper DBR has far fewer to allow the single photons to escape the cavity. Al_{0.9}Ga_{0.1}As spacers have been added to ensure the resonance of the cavity is at the desired wavelength, and could potentially also be used to produce an oxide aperture if the Al content was increased. The i-n GaAs layer below the quantum rings produces the barrier and well region, with the undoped layer having thickness d nm, and the doped layer has a thickness of $65 - d$ nm. While the total thickness of this region remained constant, resulting in an unchanged cavity length, the ratio of undoped to doped GaAs was varied between samples. This was to determine the effect of changing the barrier/well region thickness on device performance.

Layer (s)	Material	Composition		Doping		Thickness (nm)
		Al	Ga	Type	Level (cm ⁻³)	
Upper DBR Final	GaAs	0	1	p++		115.0
Upper DBR x 7	AlGaAs	0.9	0.1	p	4.0e+18	130.7
	GaAs	0	1	p	2.0e+18	115
Cavity Spacer	AlGaAs	0.9	0.1	p	4.0e+18	50
Hot-GaAs	GaAs	0	1	p	5.0e+17	55
	GaAs	0	1	i		10
Cold-GaAs	GaAs	0	1	i		5
QR Layer	GaSb	-	-			2.1ML
GaAs	GaAs	0	1	i		d
	GaAs	0	1	n	2.0e+16	$65 - d$
Cavity Spacer	AlGaAs	0.9	0.1	n	4.0e+18	50
Lower DBR x 30	GaAs	0	1	n	2.0e+18	115.0
	AlGaAs	0.9	0.1	n	4.0e+18	130.7
Substrate	GaAs	0	1	n	-	350000

Table 6.1: Initial resonant-cavity SPLED structure for Design 1 with variable lower i-n barrier region.

Figure 6.4 shows the simulated characteristics of the sample in table 6.1. The electric field at 1550 nm is easily centred on the quantum rings due to the symmetric nature of

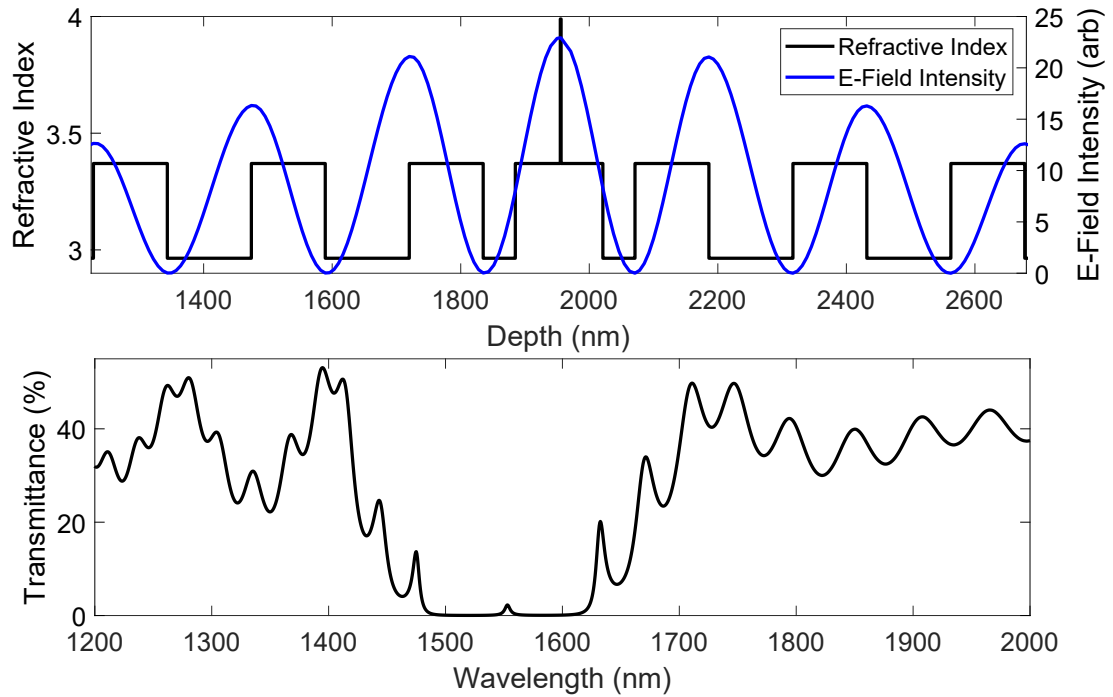


Figure 6.4: **Top:** Refractive index profile of the Design 1 cavity region with simulated electric field profile centred on the quantum ring region. **Bottom:** Simulated transmittance spectrum of the Design 1 SPLED with stop-band and resonance both centred on 1550 nm.

the electron-generating region. The spacers combine with the electron region to produce $\lambda/2$ cavity, as demonstrated by the peak at 1550 nm in the transmission spectrum. The peak is of a low amplitude due to the low number of repeats in the upper DBR, a higher number of repeats would produce a stronger resonance, but would also create more optical absorption and electrical resistance in the device.

6.2.2 Design 2

The second design used the more complex quantum-dot-based electron generation structure shown in figure 6.3b. Two wavelength variations were designed, one in the C-band at 1550 nm and one in the O-Band at 1310 nm, as well as two quantum dot layer thicknesses. Table 6.2 shows the general design used for all samples, with A and B denoting the thicknesses of the DBR layers, C_1 and C_2 the cavity spacer thicknesses, and l is the thickness of the $\text{Al}_{0.6}\text{Ga}_{0.4}\text{As}$ tunnelling barrier between the GaAs QD and the GaAs with the light-emitting GaSb QR.

Layer (s)	Material	Composition		Doping		Thickness (nm)
		Al	Ga	Type	Level (cm ⁻³)	
Upper DBR Final	GaAs	0	1	p++		<i>A</i>
Upper DBR x 7	AlGaAs	0.9	0.1	p	4.0e+18	<i>B</i>
	GaAs	0	1	p	2.0e+18	<i>A</i>
Cavity Spacer	AlGaAs	0.9	0.1	p	4.0e+18	<i>C</i> ₁
Hot-GaAsx1	GaAs	0	1	p	5.0e+17	58.5
	GaAs	0	1	i		7
Cold-GaAs	GaAs	0	1	i		5
QR Layer	GaSb	-	-			2.0 ML
	GaAs	0	1	i		15
Tunnelling Structure	AlGaAs	0.6	0.4	i		<i>l</i>
	GaAs QD	0	1	i		2.0 ML
	AlGaAs	0.6	0.4	i		4
	AlGaAs	0.103	0.897	n	5.0e+17	42
Cavity Spacer	AlGaAs	0.9	0.1	n	4.0e+18	<i>C</i> ₂
Lower DBR x 30	GaAs	0	1	n	2.0e+18	<i>A</i>
	AlGaAs	0.9	0.1	n	4.0e+18	<i>B</i>
Substrate	GaAs	0	1	n		350000

Table 6.2: The Design 2 resonant-cavity SPLED design with quantum dot-based electron generation region.

Parameter (nm)	Design 2.1	Design 2.2	Design 2.3	Design 2.4
Target Wavelength	1550	1550	1310	1310
<i>A</i>	115.0	115.0	96.2	96.2
<i>B</i>	130.7	130.7	109.9	109.9
<i>C</i> ₁	49.1	49.1	29.1	29.1
<i>C</i> ₂	49.1	49.1	29.1	29.1
<i>d</i>	13	11	13	11

Table 6.3: The parameters for each of the 4 Design 2 devices.

6.3 Key Samples

6.3.1 Design 1 - Transmission

Design 1 was produced with varying p-i-n spacing to determine the effect of barrier thickness on the performance of the device. The three samples had target i-region thicknesses, *d*, of 15, 20 and 25 nm but were otherwise designed to be identical. The optical transmission of each unprocessed SPLED was measured and compared to the ideal transmission, and can be seen in figure 6.6. All three samples have shifted stop-bands when compared to the intended spectrum, indicating that in general the structure was grown thinner than expected. Sample 1.1 in figure 6.6a has mostly maintained the correct shape, and is overall at a shorter wavelength, with a cavity resonance at 1477 nm. Sample 1.2 has

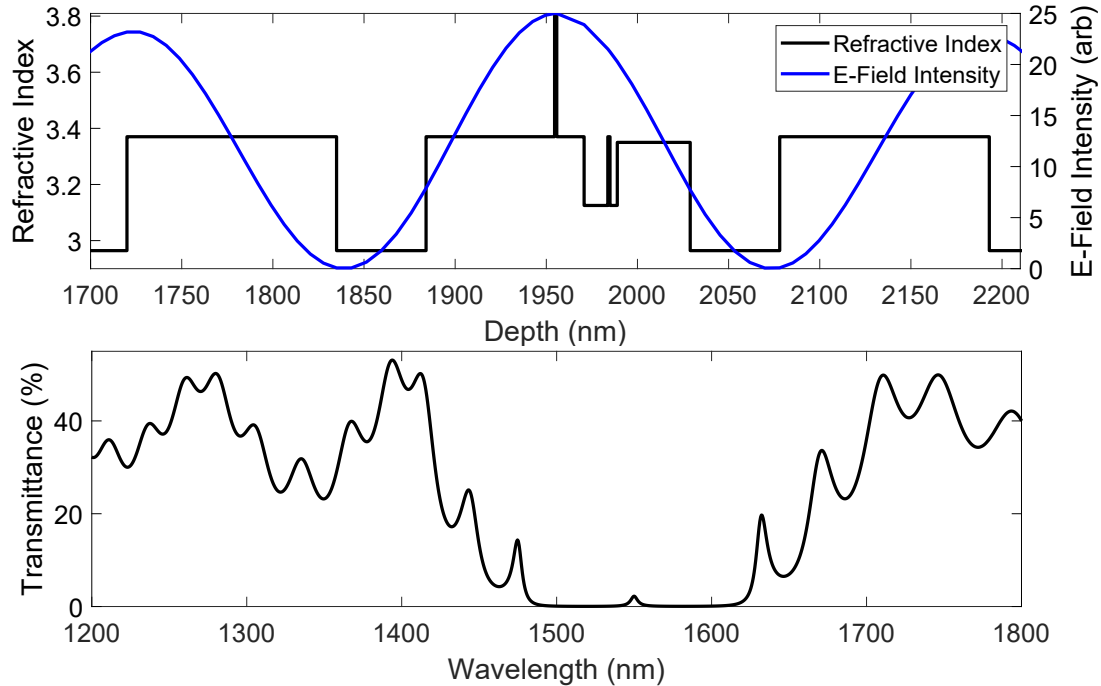


Figure 6.5: **Top:** An example refractive Index profile of the Design 2.1 cavity region with simulated electric field profile centred on the quantum rings. **Bottom:** Example simulated transmittance spectrum of the Design 2.1 SPLED with stop-band and resonance both centred on 1550 nm.

a broadened, poorly defined stop-band visible in figure 6.6b, potentially indicating that the upper and lower DBRs are misaligned. The cavity resonance for sample 1.1 was closer to specification at 1506 nm. Sample 1.3 is mostly correct in terms of stop-band width, shown in figure 6.6c, but all features are at much too short a wavelength with the cavity occurring at 1466 nm. It is worth noting that for the following characterisations, the specific piece of sample used was based on availability. This means that while ideally we would have performed all measurements on the same pieces, sections being taken for processing meant that analyses had to be performed on remaining available pieces of wafer. This is generally not ideal as there is often variation in the growth across the wafer.

6.3.2 Design 1 - BEXP

To determine the severity of the layer inaccuracies, BEXP was performed on sample 1.2. It is important to note that it is impossible to determine the thicknesses of the doped GaAs layers in the active region using standard AFM so we cannot estimate the performance of the electron confinement at this time. It can also be difficult to get a match between model and measurement even with the BEXP, without knowing exactly

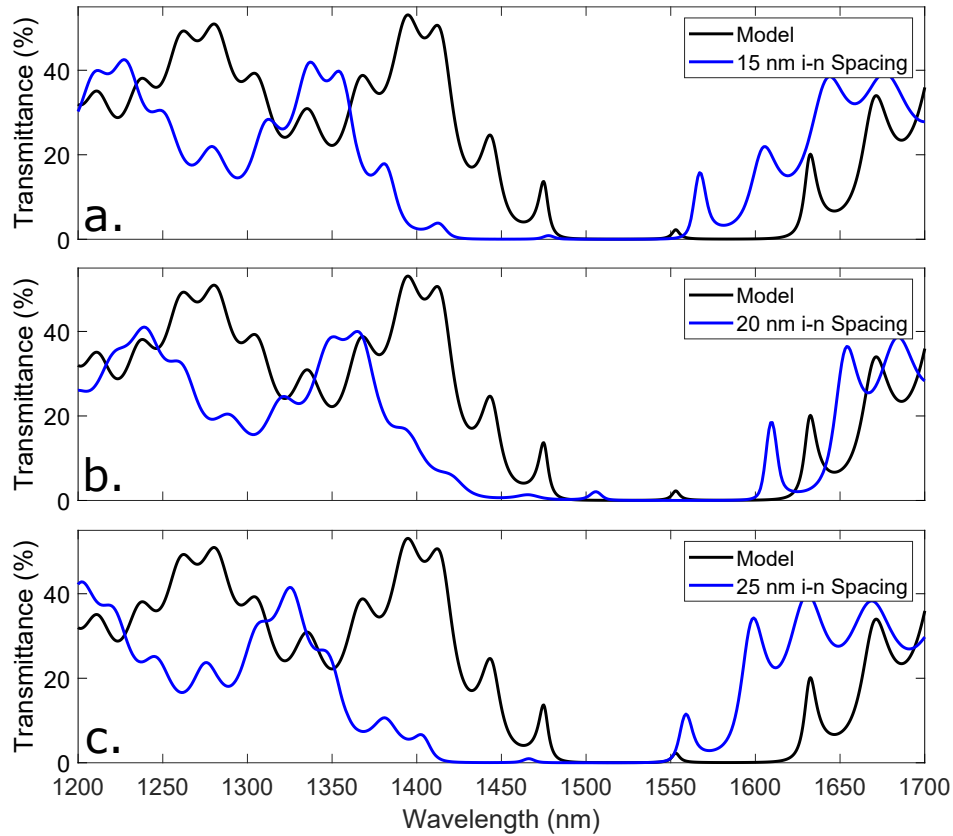


Figure 6.6: The measured transmission spectra of the three samples compared to the ideal (simulated) transmission, **a**: sample 1.1 ($d = 15$ nm), **b**: sample 1.2 ($d = 20$ nm), **c**: sample 1.3 ($d = 25$ nm).

where on the wafer the measurement was taken.

Table 6.4 shows the results of the thickness characterisation of sample 1.2. Overall the layer thicknesses are lower than specified, with the GaAs layers experiencing a much larger deviation from the intended values. The cavity region is also thinner than expected, pushing the resonance to a shorter wavelength. The upper DBR deviates more than the lower, giving a reason for the misaligned and broadened stop-band. Figure 6.7 shows the updated model using full individual layer thicknesses compared to the measurement. The transmission now agrees to a good extent, with a small shift in wavelength. It is likely that this shift is due to the BEXP and the transmission measurements being performed on different areas of the sample. The drop in transmission compared to the model is likely due to absorption in the DBR layers due to p-type free carrier absorption (see section 5.1.2), which is difficult to account for. To assess the variation in the sample growths, a piece of sample 1.1 was mapped at a low resolution. The map in figure 6.8 shows significant variation from the centre of the wafer to the edge, with a peak shift of around 18 nm. Given this variation, the ~ 9 nm shift in figure 6.7 is also

Layer	Material	Target Thickness (nm)	BEXP (nm)	Error (nm)
Upper DBR Final x1	GaAs	115	108.7	5.1
Upper DBR x7	AlGaAs	130.7	129.7	5.7
	GaAs	115	109.6	5.2
Cavity Spacer	AlGaAs	50.0	47.9	3.7
Active Region	GaAs	135	123.6	5.6
Cavity Spacer	AlGaAs	50.0	48.5	3.8
Final DBR	GaAs	115	107.1	5.1
Lower DBR x30	AlGaAs	130.7	130.6	5.8
	GaAs	115	111.9	5.2
Buffer	GaAs	~500		
Substrate	GaAs			

Table 6.4: The thicknesses of sample 1.2 as measured using BEXP. For layers with multiple repeats, thicknesses shown are the average of every repeated layer.

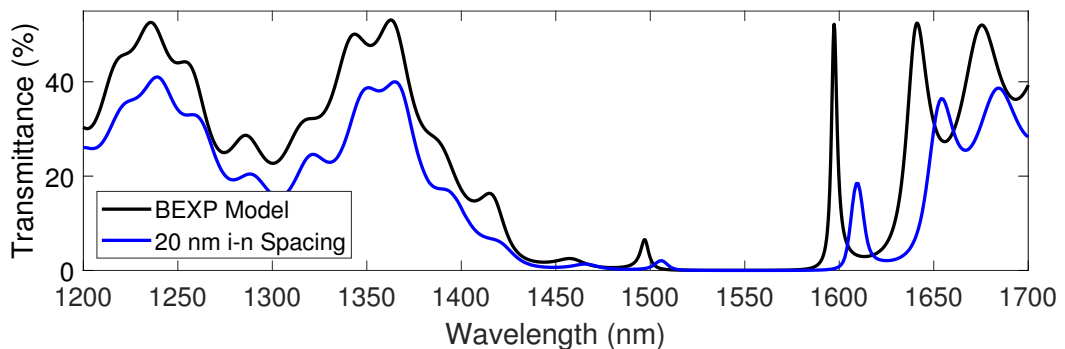


Figure 6.7: Transmission model of sample 1.2 updated with BEXP layer thicknesses from table 6.4 compared to the measurement.

likely to be due to variation across the sample.

6.3.3 Design 1 - XPS

As part of a collaboration with Kratos Analytical, one of the Design 1 SPLED samples was taken for compositional analysis using XPS. Sample 1.3 (25 nm i-n spacing) was measured using an Axis Nova XPS machine. The etch was performed with an Ar-ion beam operating at 4 kV, with an etch area of 2.5×2.5 mm. The measurement area was 110 μ m wide and was with an incident X-ray power of 450 W. The results of the profile are in figure 6.9, with a full view in the upper profile and a zoomed view in the lower. Overall the aluminium fraction is higher than expected, with an average upper DBR value of 92.5 ± 0.2 %. The cavity spacers were very close to specification at 90.9 % and 89.4 % for the upper and lower spacers respectively. The composition is generally consistent, and thus could be adjusted to correct the next growths. It should also be

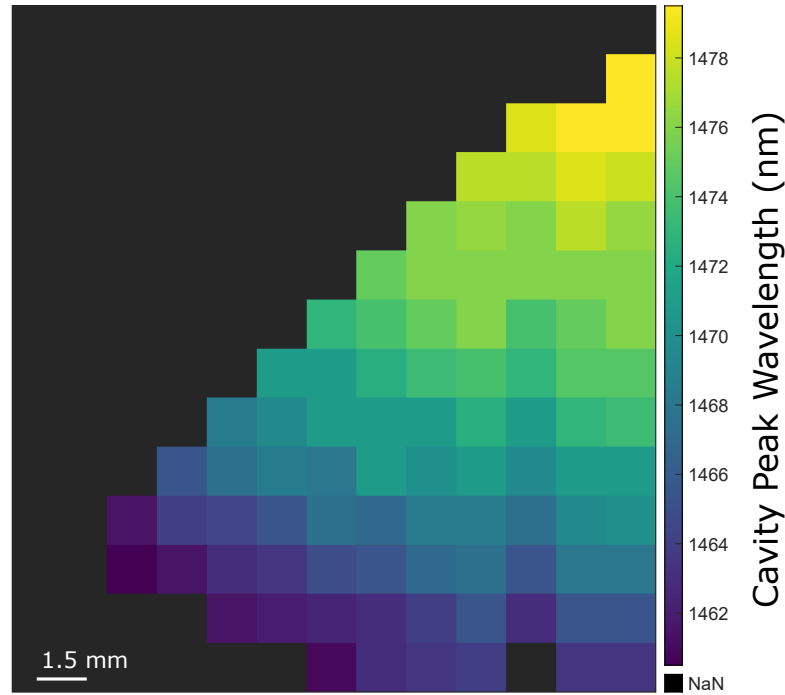


Figure 6.8: Low-resolution wafer map of a fragment (1/8th of a wafer) of sample 1.2 showing cavity peak wavelength across the sample.

noted that a small variation in Al composition has little impact on the optical properties of the structure[86].

The top profile of figure 6.9 shows the aluminium composition throughout the entire device, and clearly shows how the depth of the etch starts to cause a drift in the composition over time. This is primarily due to material from upper layers being forced downwards by the ion beam, contaminating the measurement layer and pushing the composition towards an average value. The sharp troughs in the GaAs layers also indicates that they etch faster than $\text{Al}_x\text{Ga}_{1-x}\text{As}$ so less data could be extracted. Both of these issues could be improved with a gentler, and thus slower etch. However, with the measurement already taking in excess of five hours, this would produce an unreasonably long acquisition time.

6.3.4 Design 2 - Transmission

Four samples were grown for the second series of SPLEDs according to the parameters in table 6.3. The first two samples had a target wavelength of 1550 nm, the same as the previous set of devices. The transmission spectra were measured to determine the deviation from specification and the potential for use in working devices, and can be seen in figure 6.10. Both samples have stop-bands centred at too short of a wavelength, and the weak cavity peaks are both below 1500 nm. It is reasonable to suggest that the layers

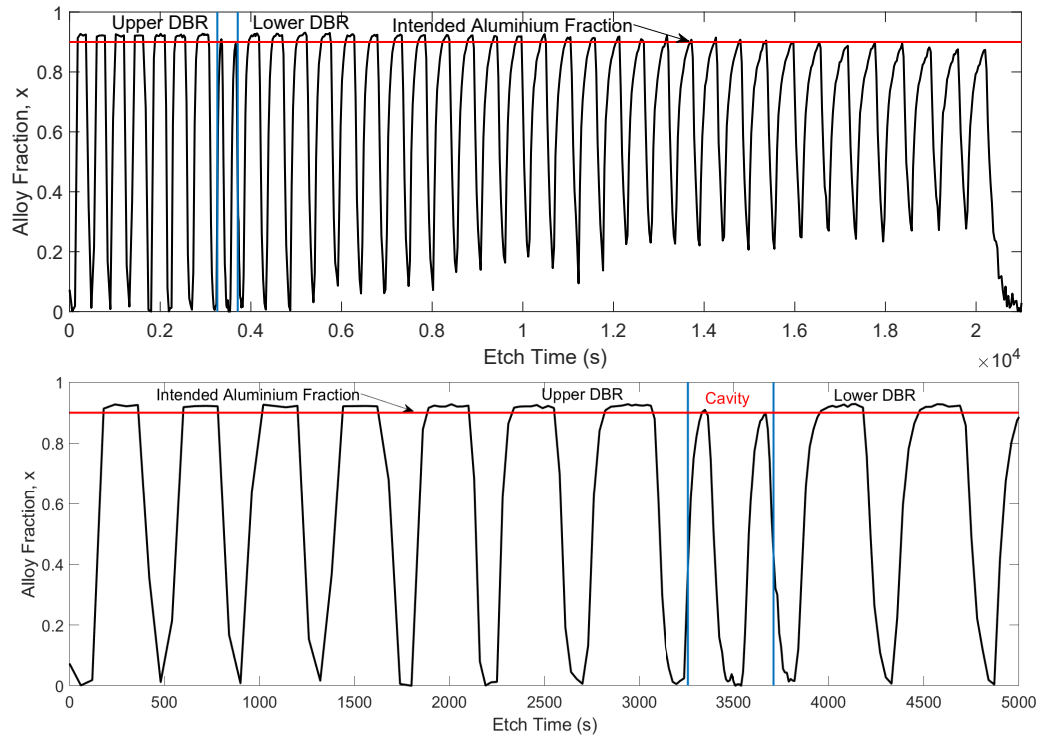


Figure 6.9: **Top:** Aluminium depth profile of a SPLED showing the target Al fraction. **Bottom:** Zoomed view of the upper DBR and cavity region.

are, on average, thinner than intended but the stop-band shape is generally the same as the model implying a good alignment between the top and bottom DBRs. While both samples have weak resonances, around 25% the intensity of the model, they are fairly well-centred in the stop-bands, at 1496 nm and 1475 nm, which implies that the shift in wavelength is due to a general growth rate calibration issue rather than any particular layer being out of spec.

The second pair of samples had a target cavity wavelength of 1310 nm. As above, the transmission was measured for each sample, and compared to the theoretical ideal transmission. Looking in figure 6.11, the features in the spectra are significantly shorter than expected, implying that the growth layers are once again too thin. The side-bands are unusually asymmetric, possibly indicating a misalignment or a mismatch in the DBR pair thicknesses. The cavity resonances are off-centre in the stop-bands for these devices, at 1260 nm and 1257 nm, so the cavity and DBR layer thicknesses could vary by different percentages. Sample 2.4 has the most visible cavity, with a similar resonance strength to the model while being slightly broadened. This broadening could be due to inconsistencies in the cavity layers, or be affected by the bandwidth of the measurement itself.

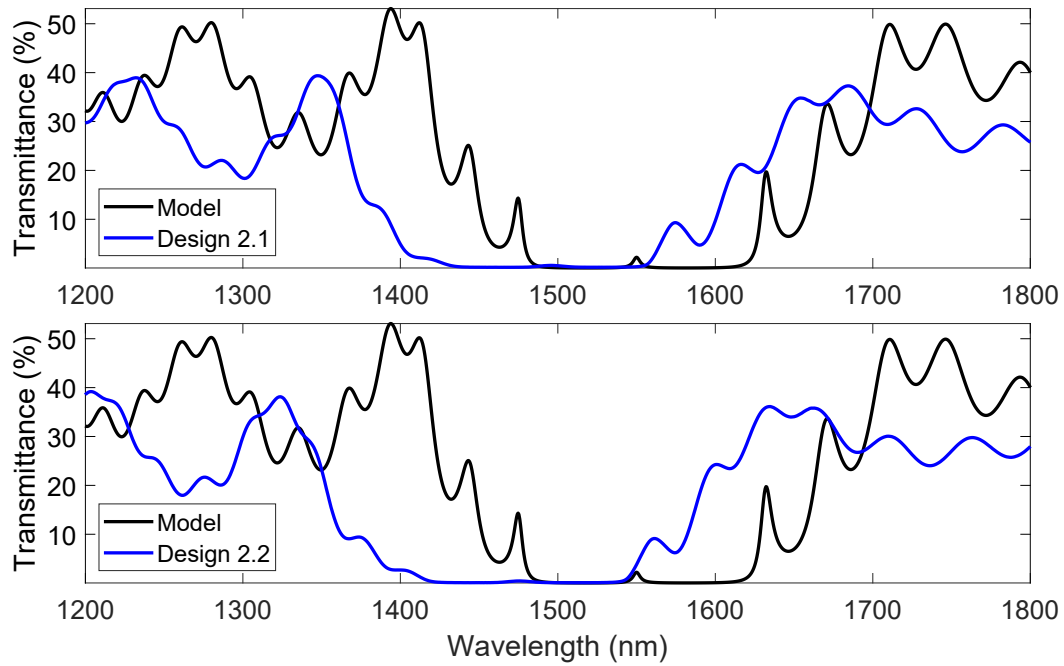


Figure 6.10: **Top:** Transmission spectrum of sample 2.1. **Bottom:** Transmission spectrum of sample 2.2.

6.3.5 Design 2 - BEXP

It is evident for all samples that some characterisation would be required to determine the exact cause of the shifted stop-bands, however, due to availability of sample pieces only sample 2.2 was cross-sectioned. Table 6.5 details the results for that device, showing that the majority of layers were grown too thin. To compare this to the measured data, a new simulation was run using the updated individual layer thicknesses in figure 6.12. The general positioning of the stop-band in figure 6.12 shows agreement with the measured data, however there is a discrepancy in the shape and symmetry of the stop-band. It is difficult to pinpoint a reason for this, as it could be due to a number of factors: errors in the simulation data (refractive indices etc), the calibration of the BEXP, measurement position on the wafer, or errors in the transmission measurement itself. So while we cannot be exact with the model in this case, the general data agrees that the layers were grown thinner than specification.

One of the samples was mapped to determine the variability of the growth, which would affect how much of the sample was usable once processed. Due to material availability, a quarter-wafer of sample 2.4 was used and the cavity peak wavelength was plotted as a function of position on the wafer. Figure 6.13 shows the extent of the variation across the sample wafer, revealing that the cavity resonance is longer in the centre of the wafer. From this it is reasonable to suggest that the growth is thicker towards

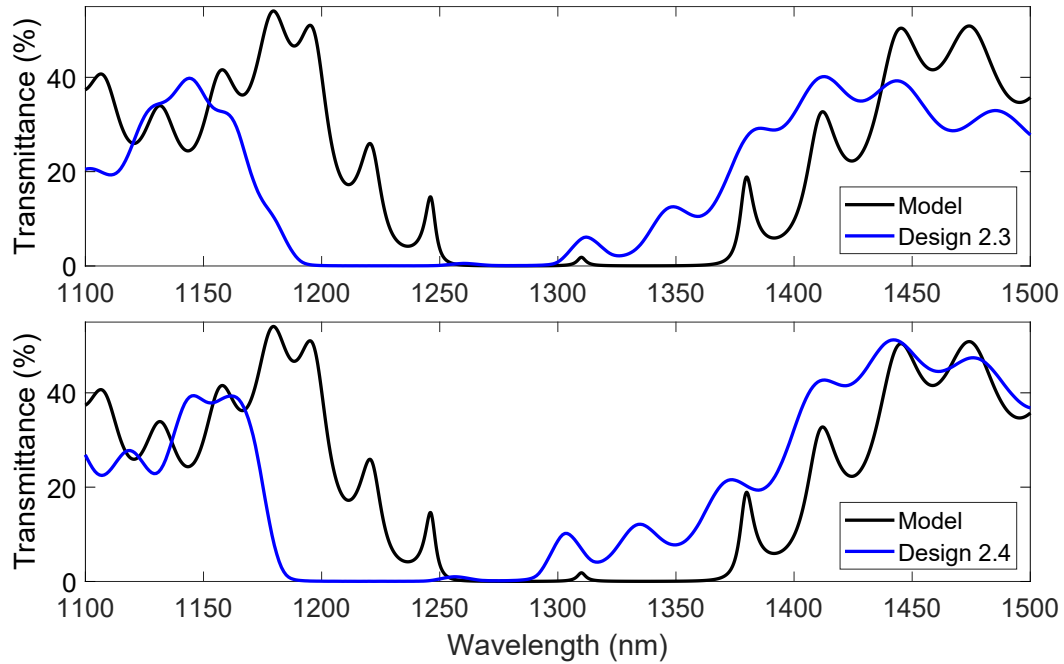


Figure 6.11: **Top:** Transmission spectrum of sample 2.3. **Bottom:** Transmission spectrum of sample 2.4.

the centre, and gradually gets thinner in the direction of the edge. The map highlights the importance of being consistent in the locations of measurements, as well as helping to select devices processed from areas of the sample with favourable characteristics.

6.4 Testing

6.4.1 Design 1 Testing

Some material was processed by CST to produce vertical-emitting devices with circular mesas and top ring-contacts, with a typical mounted device shown in figure 6.15. An I-V sweep of a processed device from sample 1.2 is visible in figure 6.14, displaying clear diode behaviour and a turn-on voltage of around 2 V.

The emission profile of an example sample 1.2 device is also shown in figure 6.15, demonstrating a very strong cavity enhancement of $>700\times$ at room temperature, and good agreement between the cavity emission and the dip in the reflectance. While there is strong cavity emission from the device, there is also a large amount of light being produced at the peak emission wavelength of the quantum rings. It is likely that this is escaping the device through the less reflective side-bands, and the cavity emission is not strong enough to suppress this. It is unclear as to whether the extra light generation would be a problem for single-photon level emission, but at this time no single-photon

Layer	Material	Target Thickness (nm)	BEXP (nm)	Error (nm)
Upper DBR Final x1	GaAs	115	106.5	± 5.6
Upper DBR x7	$\text{Al}_{0.9}\text{Ga}_{0.1}\text{As}$	130.7	124.4	± 6.3
	GaAs	115	106.7	± 5.6
End of Cavity	$\text{Al}_{0.9}\text{Ga}_{0.1}\text{As}$	49.1	46.6	± 2.8
QR Region	GaAs	85.5	79.3	± 3.5
QD Region	$\text{Al}_{0.6}\text{Ga}_{0.4}\text{As}$	15	13.4	± 2.0
	$\text{Al}_{0.103}\text{Ga}_{0.897}\text{As}$	42	45.6	± 2.5
Start of Cavity	$\text{Al}_{0.9}\text{Ga}_{0.1}\text{As}$	49.1	47.6	± 2.8
Final DBR	GaAs	115	111.3	± 5.6
Lower DBR x30	$\text{Al}_{0.9}\text{Ga}_{0.1}\text{As}$	130.7	128.3	± 6.3
	GaAs	115	113.4	± 5.6
Buffer	GaAs	~ 500	-	-
Substrate	GaAs	-	-	-

Table 6.5: The averaged thicknesses of sample 2.2 as measured using BEXP. For layers with multiple repeats, thicknesses shown are the average of every repeated layer.

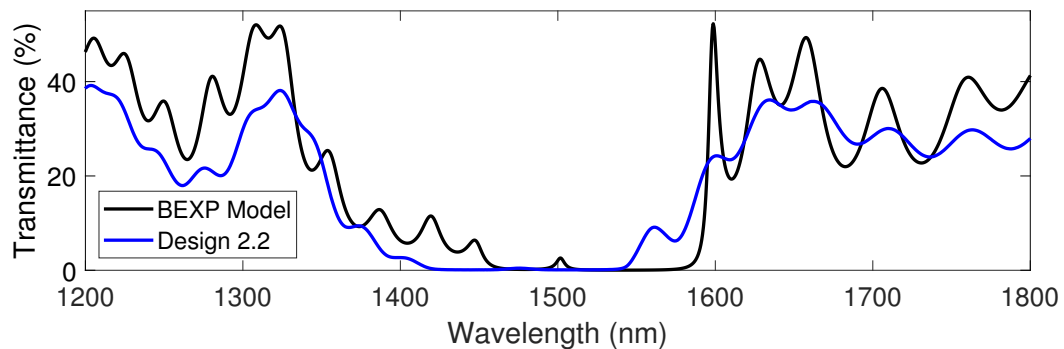


Figure 6.12: Comparison of the measured vs the simulated transmission incorporating the measured cross-section data.

operation has been achieved with the Design 1 devices.

6.4.2 Design 2 Testing

Material from sample 2.3 was processed into devices with the same circular mesa profile as the device on the right of figure 6.15. Sample 2.2 was also processed, however no useful data has been obtained at this time. A room-temperature I-V sweep was performed to check the diode properties of the SPLED, with the result plotted in figure 6.16(a). The I-V is very similar to the Design 1 device in figure 6.14, with closely matching turn-on and reverse breakdown voltages. The current increases more sharply in the Design 1 device, indicating a lower overall resistance. The reason for the difference in resistance is not known, although variations in doping, as well as different contact qualities may have an impact. The room-temperature emission of the sample 2.3 device is demonstrated

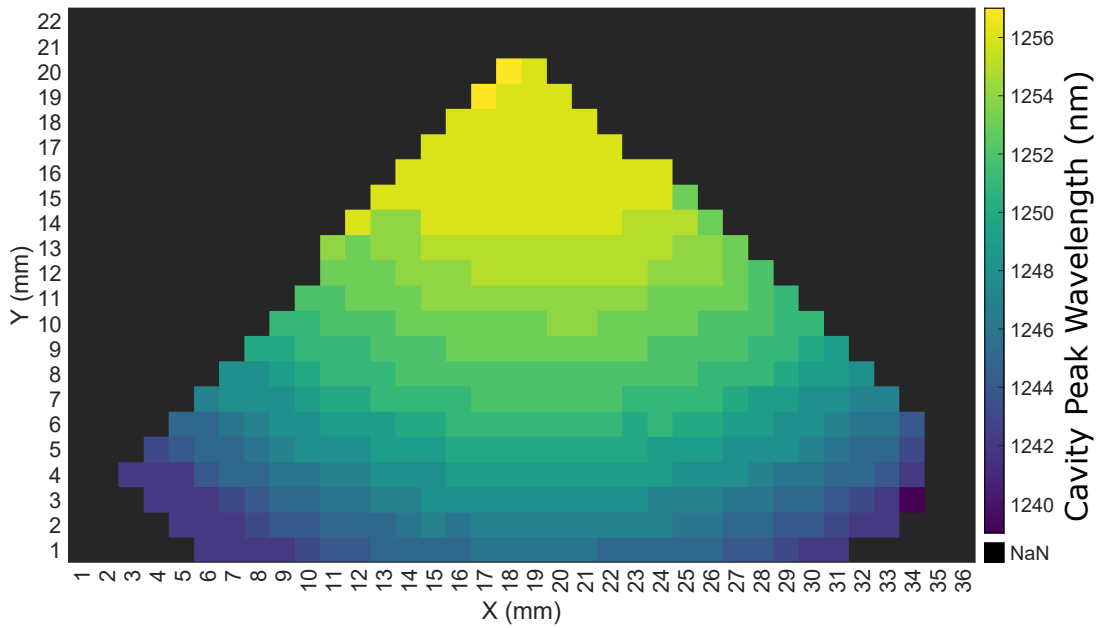


Figure 6.13: Wavelength of cavity resonance map of sample 2.4 on a quarter wafer of unprocessed material.

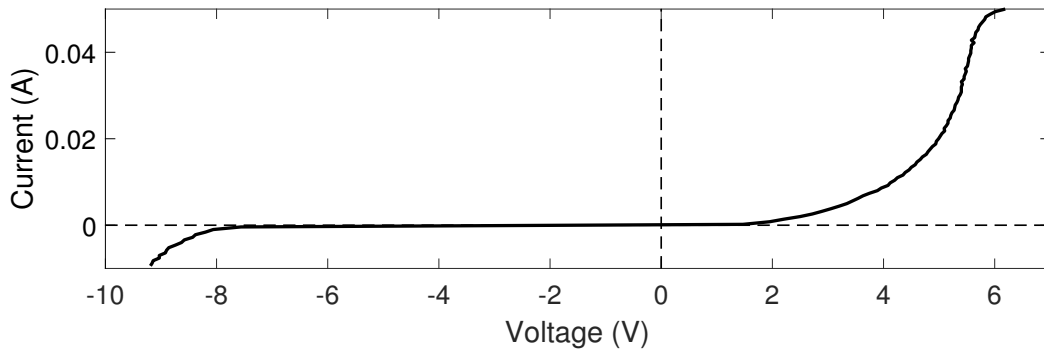


Figure 6.14: I-V profile of a processed device from sample 1.2, with a turn-on voltage of around 2 V.

in figure 6.16(b), showing a weaker output than the Design 1 device. The additional resistance could be the cause of the lower output, or alternatively variations in the upper DBR doping could be absorbing some of the produced light. As with the previous device, single-photon emission has yet to be observed.

6.5 Summary

Two designs of SPLED active region were incorporated into GaAs - $\text{Al}_x\text{Ga}_{1-x}\text{As}$ vertical-cavity resonant structures, with simulations showing resonances at target wavelengths of 1550 nm for Design 1, and at 1550 nm and 1310 nm for Design 2. Slight variations to the

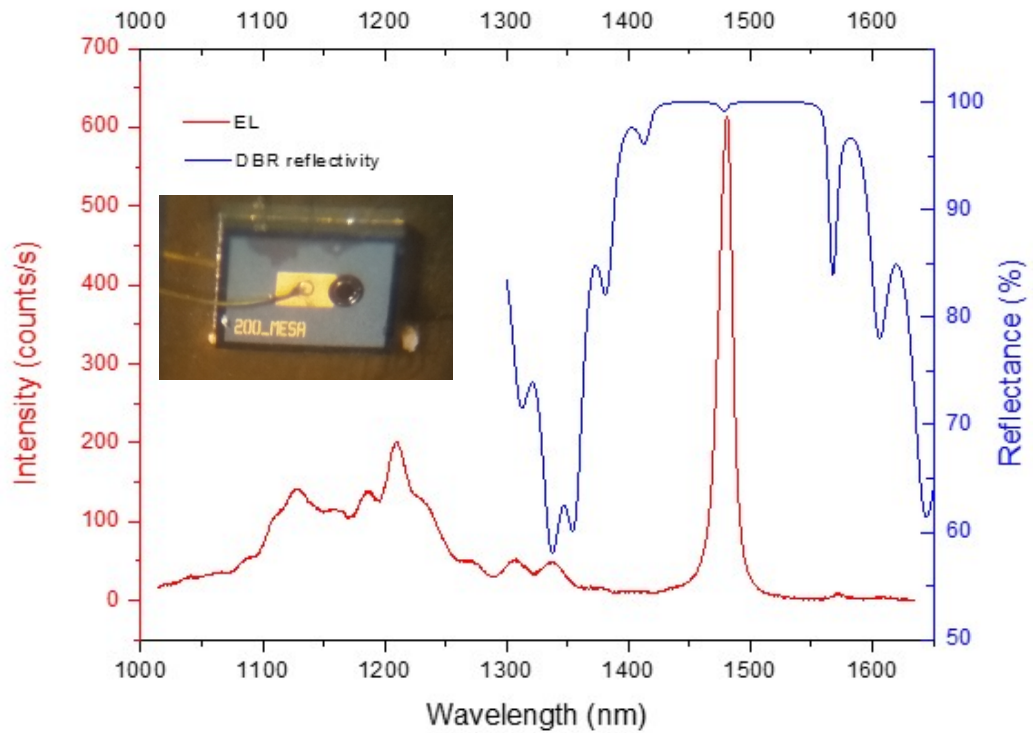


Figure 6.15: The room-temperature emission of one of the sample 1.2 SPLEDs compared to the reflectance spectrum. **Inset:** An optical microscope image of a typical processed device, with a mesa diameter of 200 μm .

active region structure were made in both cases to assess the effect of the tunnelling barrier thickness on the performance of the device. In the Design 1 devices, which utilised a n-GaAs/i-GaAs triangular well confined state for the carrier selection, all three transmission spectra were shifted towards the shorter wavelengths, indicating that the DBR layers were, on average, too thin. BEXP cross-sectional measurement on sample 1.2 confirmed this assumption, with the updated model incorporating all BEXP layer thicknesses matching the measured spectrum much more closely. A cavity peak wavelength variation of around 18 nm was observed on sample 1.1, highlighting the importance of position on the wafer when it comes to characterisation and device processing. An XPS depth-profile was carried out to check the composition of the $\text{Al}_x\text{Ga}_{1-x}\text{As}$ layers in sample 1.3, showing only a small deviation from specification, and an overall consistent Al level throughout the DBRs.

In Design 2, a GaAs quantum dot layer between $\text{Al}_{0.6}\text{Ga}_{0.4}\text{As}$ barriers provides the electron selection layer, allowing tunnelling through the largest QDs first as the bias is increased. Four different variations on Design 2 were grown, with wavelengths at 1550 nm and 1310 nm, and two different $\text{Al}_{0.6}\text{Ga}_{0.4}\text{As}$ barrier thicknesses were trialled for each

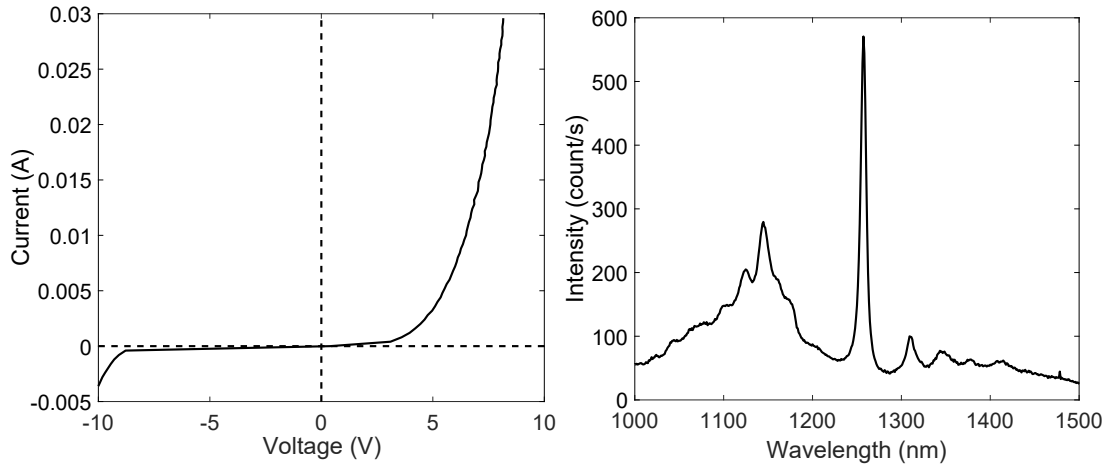


Figure 6.16: **(a)**: The I-V characteristics of one of the sample 2.3 SPLEDs. **(b)**: The emission of the same sample 2.3 device at room temperature, with a bias voltage of 8.2 V.

wavelength. All four samples showed stop-bands and weak cavity resonances, with the shorter-wavelength samples having an asymmetric stop-band profile. Once again, the transmission spectrum for each sample is shifted to a shorter wavelength, indicating that the growth rates were lower than expected. BEXP layer thicknesses agree, with layers being too thin across both DBRs. The optical model incorporating the BEXP data shows poor agreement with the measured transmission, possibly indicating discrepancies in the model, layer thickness measurements, or in the measurement of the transmission. A quarter wafer of sample 2.4 was mapped, displaying a significant (~ 15 nm) variation in the resonance peak wavelength.

Devices were processed from both Design 1 and Design 2 samples, with the same 200 μm mesa profile and contact design. Both devices show good diode behaviour and similar turn-on and reverse breakdown voltages. The Design 2 SPLED displayed a higher resistance overall, possibly due to different doping levels, or variations in growth, processing, and contact quality. Emission was observed for both designs, with the Design 1 SPLED demonstrating a very strong ($>700\times$) cavity enhancement at nearly 300 nm away from the peak QR emission. This behaviour is incredibly promising for the production of GaSb quantum ring ‘eye-safe’ devices above 1400 nm, where the QR emission is a mere fraction of its peak value. A Design 2 device showed emission at around 1250 nm, but was weaker than the Design 1 device despite being closer to the peak QR emission. It is possible that the increased resistance is the cause, or that variations in upper DBR doping are affecting the level of light absorbed by the top mirror.

Neither design demonstrated single-photon emission as of the time of writing, so

further work must be done to improve the performance of the devices. Given that all samples were grown thinner than expected, calibrating the growths closer to specification for the next generation of devices is essential, as thin barrier layers within the active region may be heavily affected by inaccurate growths. Additionally, focusing on characterisation at each step, paying particular attention to the position on the wafer, can help to isolate any issues with growths and/or processing. Reducing the resistance of the devices is a possible improvement to be made, as being able to operate at lower currents with less heating will be greatly beneficial to a single-photon emitter. Finally, refining the processing for the devices so that they can be produced in-house is a crucial step towards being able to iteratively improve the performance, without the long wait times associated with external processing.

Chapter 7

VCSELs

7.1 Mk. 1 VCSELS

7.1.1 Mk.1 Design

Note: The initial VCSEL was produced before the commencement of this PhD, and as such, all simulations and optical tests were done after the fact and on leftover pieces of material.

The first design had an initial wavelength target of 1350 nm, within the telecoms O-band, and used GaAs - Al_{0.6}Ga_{0.4}As DBRs as the mirror system, with the upper and lower mirrors consisting of 24 and 34 repeats respectively. The lower DBR was Si doped to provide n-type behaviour, and the upper DBR was Be doped so as to be p-type. Further details of the GaSb QRs growth has been published elsewhere[24, 40]. Al_{0.6}Ga_{0.4}As spacers were positioned either side of the QR active region in order to provide a total cavity wavelength of $3\lambda/2$. Also acting as part of the cavity, as well as providing a high-Al layer for potential oxidation, are quarter-wave layers of Al_{0.9}Ga_{0.1}As. The structure and layer targets are shown below in table 7.1, with the simulated electric field profile and transmittance visible in figure 7.1.

Layer (s)	Material	Composition		Doping		Thickness (nm)
		Al	Ga	Type	Level (cm ⁻³)	
Upper DBR Final	GaAs	0	1	p++	-	99.4
Upper DBRx24	AlGaAs	0.6	0.4	p	4.0E+18	107.5
	GaAs	0	1	p	2.0E+18	99.4
High Al Layer	AlGaAs	0.9	0.1	p	2.0E18	113.4
Upper Spacer	AlGaAs	0.6	0.4	-	-	165
Quantum Ring x5	GaAs - Hot	0	1	i		10
	GaAs -Cold	0	1	i		5
	GaSb	-	-	i	-	2.1ML
	GaAs	0	1	i		15
Lower Spacer	AlGaAs	0.6	0.4	-	-	165
High Al Layer	AlGaAs	0.9	0.1	n	2.0E+18	113.4
Lower DBRx34	GaAs	0	1	n	5.0E+18	99.4
	AlGaAs	0.6	0.4	n	2.0E+18	107.5
Buffer	GaAs	0	1	n	5.0E+18	~1000
Substrate	GaAs	0	1	n		

Table 7.1: VCSEL structure for the Mk1 design grown entirely at Lancaster.

Figure 7.1 shows both the simulated electric field profile, and the simulated transmittance of the target structure. The overlaid e-field shows the $3\lambda/2$ cavity wave having good alignment with the quantum rings, while the transmittance model demonstrates a cavity resonance at the target wavelength of 1350 nm.

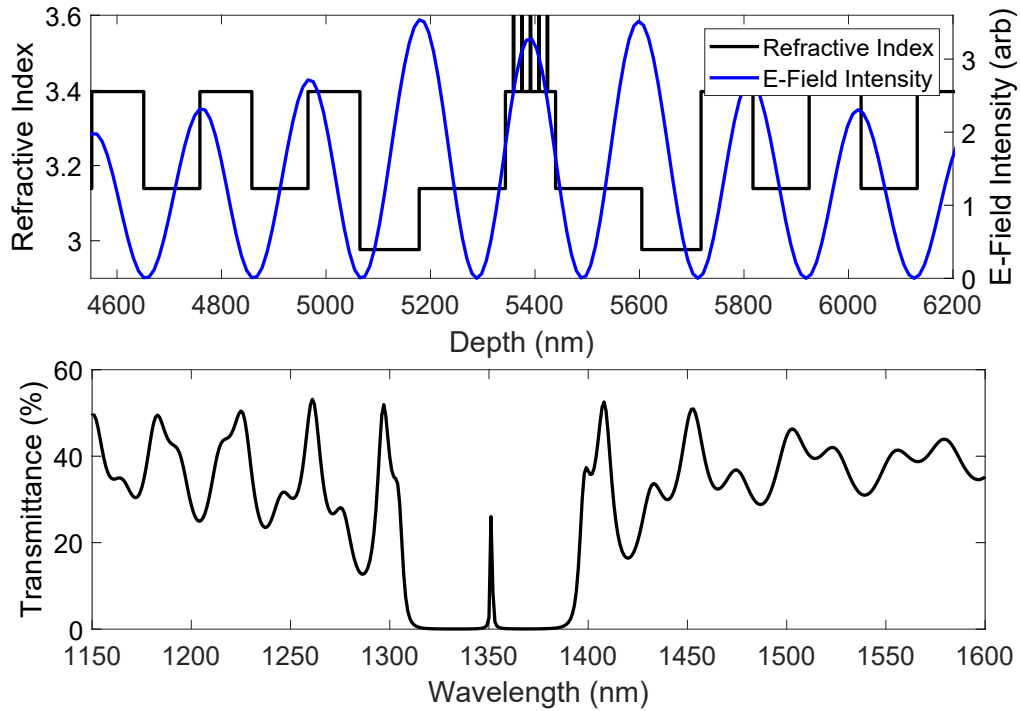


Figure 7.1: **Upper:** The simulated electric field profile overlaid with the refractive index at the target wavelength of 1350 nm. **Lower:** The simulated transmittance spectrum of the target structure, showing the cavity resonance at the target wavelength.

7.1.2 Key Samples

The design in table 7.1 was grown and a piece was sent to CST for processing into VCSEL devices. A remaining piece was optically tested to determine the accuracy of the growth, and quality of the optical properties. The measured transmittance is shown in the upper part of figure 7.2, alongside the ideal modelled spectrum. It is evident from the shifted wavelength that on average, the structure was grown too thin, and as such the cavity resonance is around 1335 nm rather than the expected 1350 nm. Unfortunately, the wafer mapping facilities were unavailable at this point, and much of the remaining sample consisted of small sections, so position-based measurements were impossible to make. However, multiple small pieces were measured to gather a rough idea of how much the spectra shifted with varying position on the sample wafer. The 5 measurements are shown on the bottom of figure 7.2.

Figure 7.2 clearly shows a cavity resonance in the sample, demonstrating that the DBR system is functioning as expected, with the resonance being well positioned towards the centre of the stop-band. While the transmission peak is not as strong as the one in the model, it remains measurable and well placed within the telecoms O-band as targeted. The reduction in resonance strength is likely due to uneven interfaces and unmatched

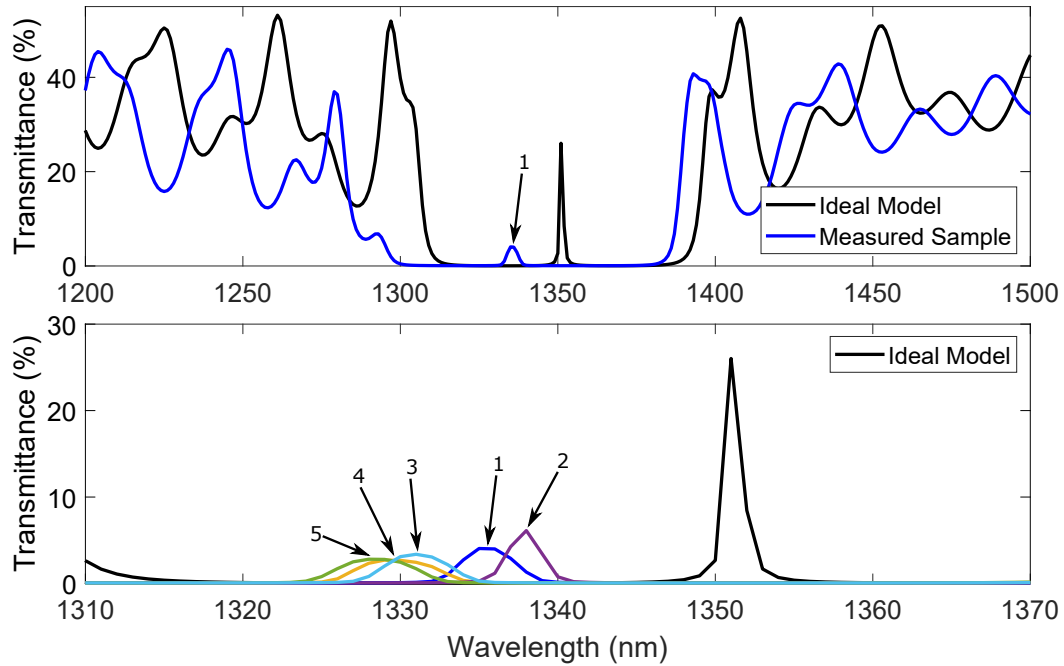


Figure 7.2: **Upper:** The measured transmittance of piece 1 of the VCSEL compared to the modelled spectrum of the ideal structure showing a shift to shorter wavelengths. **Lower:** Zoomed cavity transmittance of various small pieces of sample (1-5), where the position on the original wafer is unknown.

DBR layers, which come from deviations in the growth rate of the MBE. Additionally, the ideal nature of the simulation will tend to over-estimate the strength of the resonance, as scattering events at layer interfaces and imperfections are not taken into account. The cavity peak shifts by around 10 nm, which indicates an optical thickness variation across the wafer. While this does not push the output wavelength outside of the target telecoms band, this variation would need to be reduced for production devices. A cross-section was taken using BEXP to find the layer thicknesses, as well as to determine the quality of the layers and layer interfaces.

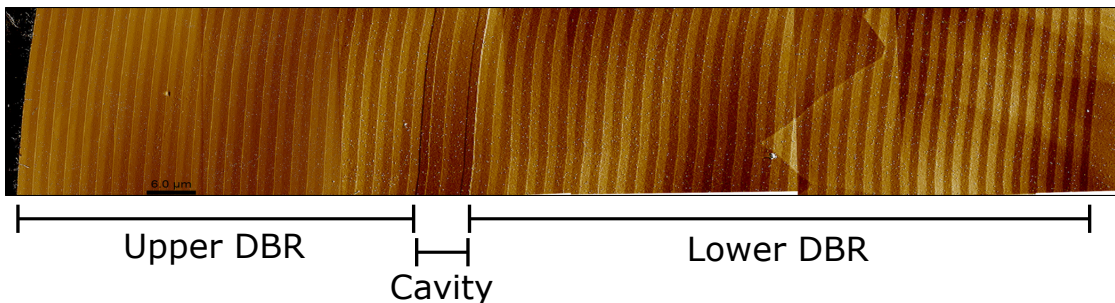


Figure 7.3: A composite AFM image showing a cross-section of the full device. The dark layers are the $\text{Al}_x\text{Ga}_{1-x}\text{As}$ with the darkest layers inside the cavity being $\text{Al}_{0.9}\text{Ga}_{0.1}\text{As}$ oxidation candidate layers.

The composite AFM image in figure 7.3 shows uniform DBR layers, as well as clear

and smooth layer boundaries. Both of these factors indicate a high quality growth, with a lower number of defects and layer roughness that would influence the optical qualities of the device. The layer thicknesses were measured and the averaged results are shown in table 7.2, where the overall trend is that the average layer thicknesses are smaller than their target values. This matches with the prediction from the optical measurement above, and the cavity thickness shift of -6.7 nm corresponds to an optical thickness change of -59 nm. When applied to the target cavity optical thickness of $3\lambda/2 = 2025$ nm, the resulting FP dip is estimated to occur at 1310.7 nm. While this is thinner than the measured values, the impact of the DBRs will lengthen the cavity, so a simulation with the full layer values is needed to avoid an oversimplified approach.

Layer	Material	Target Thickness (nm)	BEXP (nm)	Error (nm)
Upper DBR Final x1	GaAs	99.4	99.9	± 4.3
Upper DBR x 24	$\text{Al}_{0.6}\text{Ga}_{0.4}\text{As}$	107.5	107.1	± 4.6
	GaAs	99.4	96.5	± 4.2
High Al Layer	$\text{Al}_{0.9}\text{Ga}_{0.1}\text{As}$	113.4	106.9	± 4.5
Cavity Spacer	$\text{Al}_{0.6}\text{Ga}_{0.4}\text{As}$	165	161.8	± 6.0
Active Region	GaAs	90	83.3	± 3.9
Cavity Spacer	$\text{Al}_{0.6}\text{Ga}_{0.4}\text{As}$	165	165.7	± 6.1
High Al Layer	$\text{Al}_{0.9}\text{Ga}_{0.1}\text{As}$	113.4	110.4	± 4.7
Lower DBR x 34	GaAs	99.4	98.7	± 4.3
	$\text{Al}_{0.6}\text{Ga}_{0.4}\text{As}$	107.5	105.4	± 4.5
Buffer	GaAs	~ 500		
Substrate	GaAs			

Table 7.2: The averaged thicknesses of the Mk1 VCSEL as measured using BEXP.

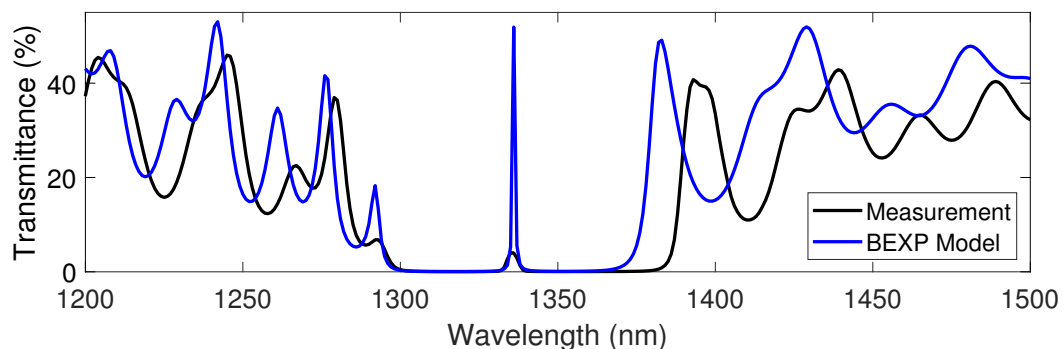


Figure 7.4: The updated model comprised of the full BEXP data compared to the measured transmittance.

The new version of the model, which uses the full BEXP data for each layer (not the average values in table 1.2), shows far better agreement with the measured transmittance spectrum, as is clear in figure 7.4. The cavity is in almost perfect agreement, and the

stop-band has a small difference in width. The remaining deviation in the model is likely to be caused by the variation across the wafer, or a number of other factors, including incorrect $\text{Al}_x\text{Ga}_{1-x}\text{As}$ composition, inconsistencies in the layer interfaces, and inaccuracies in the model itself.

7.1.2.1 XPS Measurement

Since the model still has some deviation from the measured data, an experimental attempt was made to determine the Al content of the GaAs - $\text{Al}_{0.6}\text{Ga}_{0.4}\text{As}$ DBR layers using XPS at Kratos Analytical. An Axis Nova XPS machine was used, incorporating a step-wise rotation after each etch cycle. The X-ray power was set to 300 W with an acquisition time of 20 s. All three compositional elements were measured, and the chosen binding energy peaks corresponded to Al 2p, Ga 3d, and As 3d. These peaks were chosen for their clarity and convenience due to their proximity.

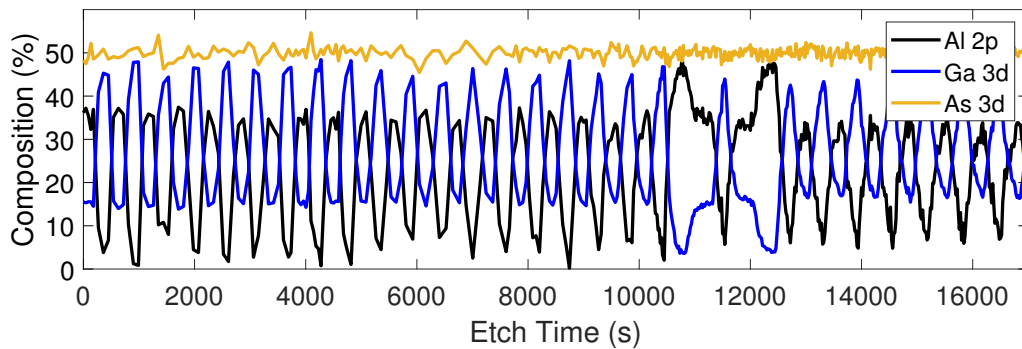


Figure 7.5: An XPS depth profile of the VCSEL structure shown in figure 7.3. The profile stops partway into the lower DBR due to time constraints and layer mixing.

Figure 7.5 displays the XPS depth profile of the VCSEL down to the first few repeats of the bottom DBR. While the layers are clearly visible, the data is noisy and generally has few points per layer, primarily due to the speed of the etch. Even so, the total measurement time was still over 4 hours and did not reach the substrate of the sample. The aluminium content does not regularly reach zero, as would be expected in the GaAs layers, and the sharp peaks also indicate a loss of data due to etch speed or low acquisition rate. Thus the data has little quantitative use, but we can still determine some useful information from it. Firstly, the layers are generally consistent in aluminium content, with no drastic differences. Secondly, the high-Al content layers and the cavity region are visible and have good contrast from the surrounding DBRs. As with most of the compositional measurements, improvements could be made with slower etches and a higher rate of data acquisition. Unfortunately, this was simply not feasible at the time.

7.1.3 Processing and Testing

It should be noted that the vast majority of the testing was done by Dr Peter Hodgson, and as such only demonstrative examples of the electrical testing of the devices will be discussed. Detailed comparisons of very similar processed devices are outside the scope of this work.

A portion of the sample was sent to CST to be processed into VCSEL devices. Standard circular mesas were used with top-bottom contacts and no current confinement was applied, with mesa sizes ranging from 50 μm to 200 μm . A typical I-V curve was taken up to 10 mA, and is shown in figure 7.6. Clear diode-like behaviour is observed, with a visible knee voltage of around 2.3 V. This is not unreasonable for a typical GaAs- $\text{Al}_x\text{Ga}_{1-x}\text{As}$ VCSEL, though it should be noted that if oxidation were to be implemented, this voltage would increase along with the general resistance of the mesa[87].

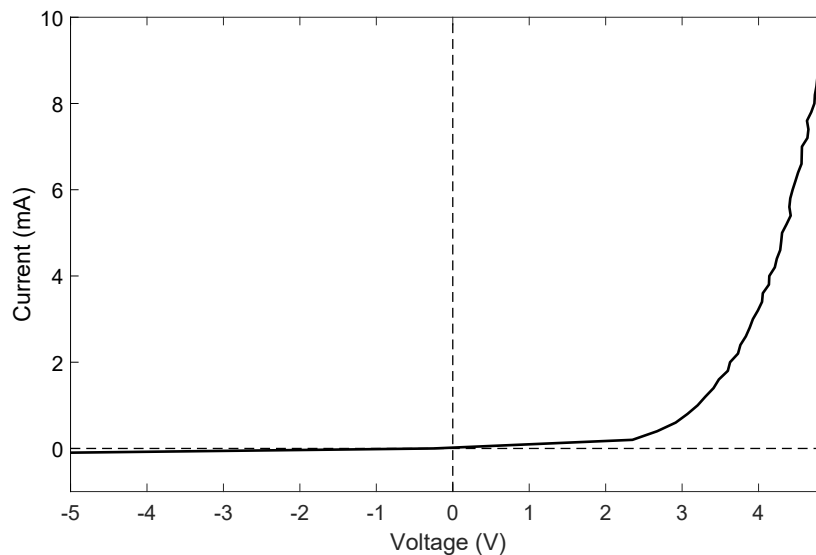


Figure 7.6: An example I-V curve from a 200 μm diameter device, showing clear diode behaviour and a knee voltage of 2.3 V.

The device was then driven at 30 mA, with a 100 Hz, 10% duty cycle pulsed operation. As expected from the measured transmittance in figure 7.4, the device emits at around 1330 nm at room temperature. The emission, plotted in figure 7.7, displays a clear resonance peak, alongside a less intense comb of peaks seemingly centred around 1230 nm. The emission power of the device is extremely low, and is not measurable with a standard power meter. Additionally, no lasing threshold was observed during device testing. The side emissions correspond to the room-temperature emission of the quantum rings overlaid with the side-bands of the upper and lower DBRs. Reducing the

unwanted emissions could be achieved either by improving the strength of the stimulated emission, thus suppressing the non-resonating wavelengths, or by shifting the wavelength of the laser such that the stop-band of the device blocks the majority of the unwanted light.

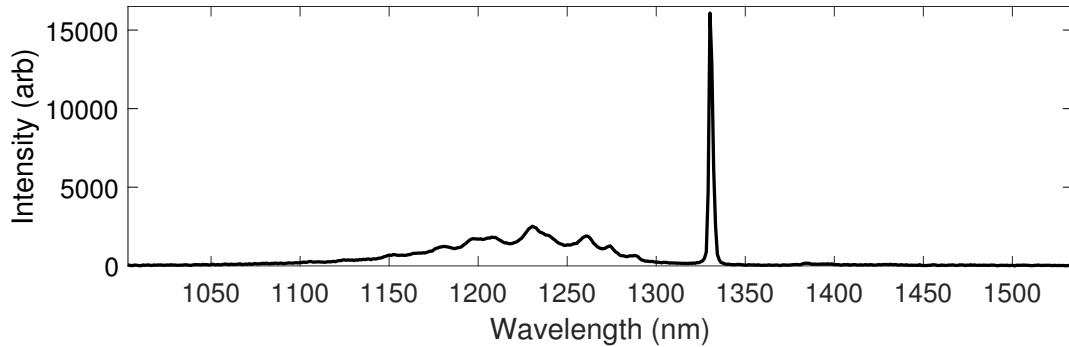


Figure 7.7: Room temperature 30 mA emission of a 200 μm diameter VCSEL device showing resonance at 1330 nm and a side emission around 1230 nm. The device was operated at 100 Hz with a 10 % duty cycle.

7.2 Mk. 2 VCSELS

The previous devices lacked a strong emission profile and generally operated with a low efficiency. One possible reason for the low power performance is the relatively low-contrast upper and lower DBRs with simulated reflectances of 94.2 % and 98.6 % respectively. A greater refractive index contrast between the GaAs and $\text{Al}_x\text{Ga}_{1-x}\text{As}$ would produce more reflective mirrors, so the next iteration of devices will use up to $\text{Al}_{0.9}\text{Ga}_{0.1}\text{As}$ with the aim of producing a stronger resonant cavity.

7.2.1 Initial Design

7.2.1.1 IQE Lower DBR

Given IQE plc's ability to grow high-quality VCSEL material at industrial levels, utilising the consistency and growth speed of their DBRs is an obvious choice. While it would be ideal to grow the entire VCSEL structure using MOVPE at IQE, the process for growing the rings could take significant time and effort to develop on an MOVPE system. As such the active region had to be grown using Lancaster's MBE machine. Since it would be unreasonable to then send the sample for a third epitaxy back at IQE, the upper DBR was included in the MBE overgrowth.

The Mk.2 lasers were the first to be designed with the IQE lower DBR in mind, with

a similar DBR layout to a standard mass-production VCSEL. A high number of repeats was chosen for the lower DBR so as to maximise the reflectivity and utilise the accuracy and repeatability of the MOVPE growths. Table 7.3 shows the calculated design for a high-reflectivity graded interface DBR that alternates between $\text{Al}_{0.12}\text{Ga}_{0.88}\text{As}$ and $\text{Al}_{0.9}\text{Ga}_{0.1}\text{As}$ with a smoothly graded region in-between. The benefit of having two $\text{Al}_x\text{Ga}_{1-x}\text{As}$ layers rather than a GaAs - $\text{Al}_x\text{Ga}_{1-x}\text{As}$ system is that the cell rates can be smoothly varied during growth, and don't have to be turned off completely. This improves layer interfaces and reduces overall growth time. Additionally, the graded interfaces greatly reduce the resistance of the DBR, allowing for lower threshold currents and higher efficiencies[88]. It would be ideal to end the DBR on the final $\text{Al}_{0.12}\text{Ga}_{0.88}\text{As}$ layer so that the active region could be smoothly incorporated, however due to the rapid oxidation of $\text{Al}_x\text{Ga}_{1-x}\text{As}$ a GaAs cap must be grown to cover the sensitive layers. A half-layer (eighth-wave optical thickness) was chosen so that the remaining thickness of the layer could be grown at the start of the MBE process as a buffer between the two growth types.

Layer (s)	Material	Composition		Doping		Thickness (nm)
		Al	Ga	Type	Level (cm^{-3})	
Cap	GaAs	0	1	n	3.00E+18	47
DBR x40	AlGaAs	0.12	0.88	n	2.00E+18	75
	AlGaAs	0.12-0.9	0.88-0.1	n	2.00E+18	20
	AlGaAs	0.9	0.1	n	2.00E+18	85
	AlGaAs	0.9-0.12	0.1-0.88	n	2.00E+18	20
Buffer	GaAs	0	1	n	3.00E+18	500

Table 7.3: One of the lower DBR designs to be grown by MOVPE with graded interfaces and a half layer GaAs cap. The target centre wavelength for this structure was 1270 nm.

Several DBR designs were fabricated with varying stop-band centres so as to cover a wide range of possible wavelengths. The design in table 7.3 has a target centre wavelength of 1270 nm, and four more DBRs were designed at 1350 nm, 1433 nm, 1517 nm, and 1600 nm. The simulated reflectances of the various lower DBRs are shown in figure 7.8 giving coverage of much of the standard telecoms regions.

7.2.1.2 MBE VCSEL Overgrowth

An initial simulation was performed in order to assess the interaction between a graded lower DBR and a square upper DBR. Analysing the electric field with respect to position is key here, as the asymmetric layout of the device could push the peak of the resonant

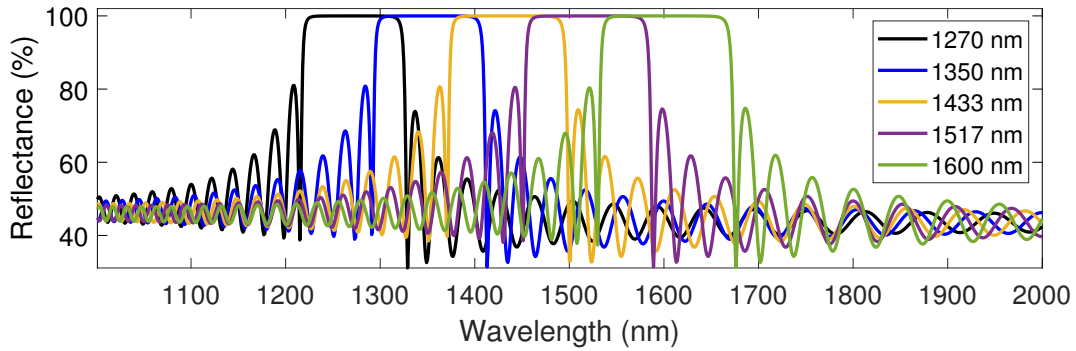


Figure 7.8: Simulated transmittances of the proposed lower DBR designs with the aim of covering the majority of the telecoms region.

field away from the quantum rings, affecting the overall efficiency. Five layers of quantum rings are embedded inside a $\lambda/2$ active region, with a single $\text{Al}_{0.97}\text{Ga}_{0.03}\text{As}$ layer above the cavity to allow for the generation of an oxide aperture during processing. The buffer layer thickness, D , was varied to determine the position and shape of the electric field within the active region. From this point onwards, the target wavelength was selected to be 1270 nm so as to comply with the XGS-PON upstream standard, as discussed in section 1.1[5]. The GaAs cap on the lower DBR had an optical thickness equivalent to one-eighth of a wavelength, so the initial buffer matched that thickness to bring the total to a quarter-wave to match the DBR layers and minimise the impact of the buffer. However, it is evident from figure 7.9a that this layer effectively kills the resonance in the device and shifts the field away from the active region. Recreating the resonance was possible, but only for a λ cavity, which would require two sets of rings to align with the peaks in the electric field. The simulation in figure 7.9b brings the total thickness of the buffer layer to $\lambda/2$, creating a region of constant amplitude and allowing the half-wavelength resonance to align exactly with the active region. While the extra thickness may introduce some loss, it does allow the MBE to grow a smooth surface on which to begin the active region. The design is detailed in table 7.4, with a high number of upper repeats being chosen to produce as strong a resonance as possible.

The simulated transmittance of the design in table 7.4 is shown in figure 7.10, displaying a clear cavity dip and a wide, flat stop-band. The cavity resonance is narrow, indicating the possibility for a narrow operating bandwidth of the laser itself.

7.2.2 Key Samples and Redesigns

Initially, a piece of material from IQE was measured to observe the lower DBR before any overgrowth occurred. The purpose of this was to compare the growth to the simulated

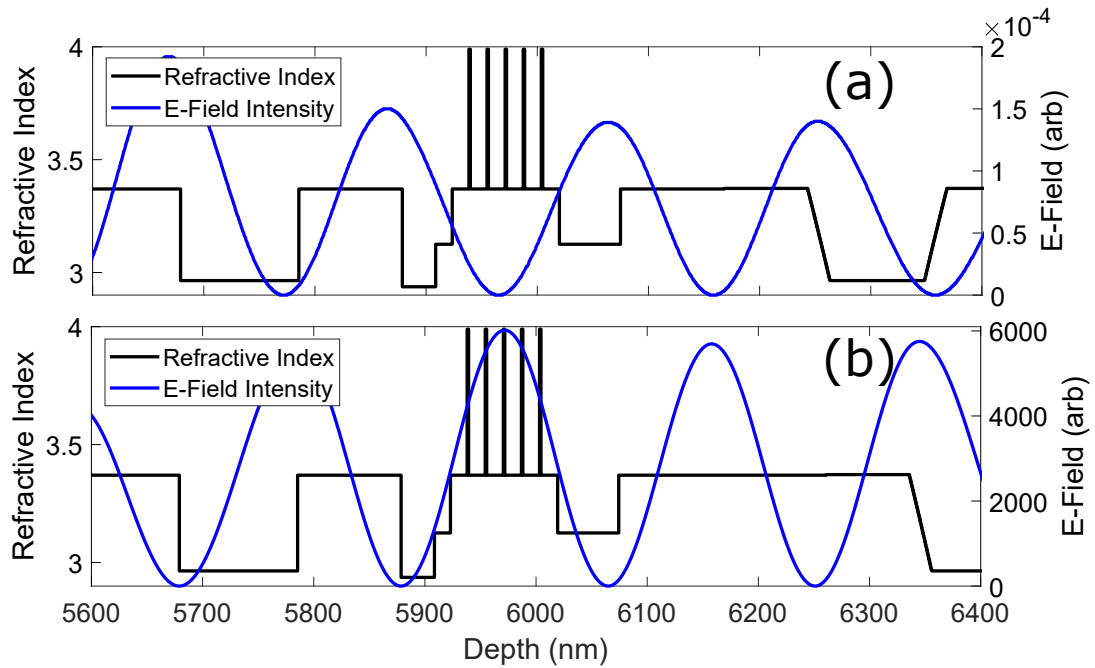


Figure 7.9: Electric field simulation centred around the active region, with the graded lower DBR on the right and the square upper DBR on the left. **(a)** has a buffer optical thickness equivalent to a quarter wavelength and **(b)** has a buffer optical thickness equivalent to a half wavelength.

design, as well as to check the calibration and clarity of the transmission measurements on the thicker substrates that IQE used. Figure 7.11 compares the measured transmittance of the sample DBR alongside the model. The measurement is close to the ideal model, with a slight shift in wavelength indicating that the layers may be slightly thinner on average. A slight difference in side-band amplitude could be attributed to the doping in the lower layers, which is not included in the model. Slight differences aside, the DBR is very close to specification and can therefore be used for the next stage of overgrowth.

The first growth to be made using the Mk 2 design was a test to ensure that the cavity and upper mirror could be grown onto the substrates provided by IQE. The growth is as described in table 7.4, with the key difference being the lack of quantum rings. A bulk layer of GaAs was used instead to reduce the overall growth time of the test sample.

Once grown and measured the sample showed good agreement with the model in terms of DBR position and width, as well as the general shape of the side bands as shown in the upper portion of figure 7.12. There is a very small cavity resonance visible on the bottom of figure 7.12, with an amplitude of around 0.15 %, indicating a poor resonance which needs to be addressed. The position of the peak is very close to the target, which is promising for the accuracy of the cavity thickness.

The next step was to reproduce the test growth, this time adding the quantum ring

Layer (s)	Material	Composition		Doping		Thickness (nm)
		Al	Ga	Type	Level (cm ⁻³)	
Final Layer	GaAs	0	1	p++		93.1
Upper DBR x29	AlGaAs	0.9	0.1	p	4.0E+18	106.4
	GaAs	0	1	p	2.0E+18	93.1
Oxidation Layer	AlGaAs	0.97	0.03	p	4.0E+18	30
Upper Spacer	AlGaAs	0.6	0.4	i	-	12.2
Quantum Ring x5	GaAs - Hot	0	1	i	-	10
	GaAs - Cold	0	1	i	-	5
	GaSb	-	-	i	-	2.1 ML
	GaAs	0	1	i	-	15
Lower Spacer	AlGaAs	0.6	0.4	i	-	45
Buffer	GaAs	0	1	n		D
IQE DBR x40	-	-	-	-	-	-

Table 7.4: Design of the MBE section of the VCSEL growth, with 29 upper repeats, a half-wavelength cavity, and 5 sets of quantum rings. A 30 nm Al_{0.97}Ga_{0.03}As layer is included so that an oxide aperture may be incorporated when processed.

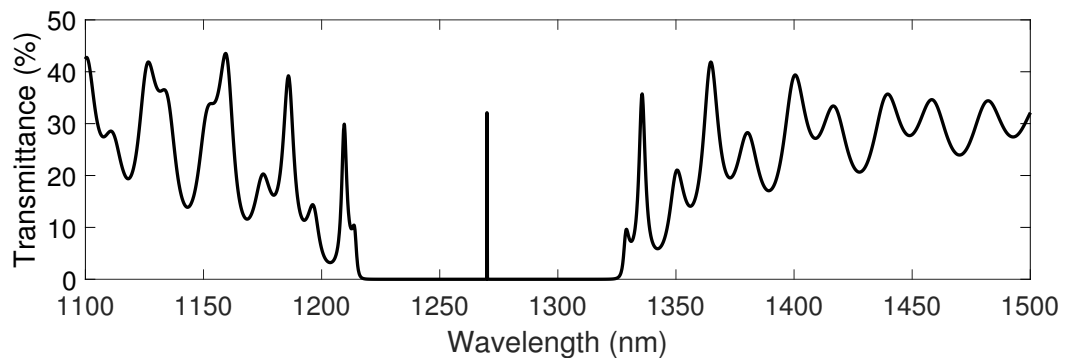


Figure 7.10: Optical transmittance simulation of the design in table 7.4 showing a strong resonance at the target wavelength.

layers in the active region. Ideally, the transmittance would look the same (the QR layers have little effect on the passive optical behaviour), and cross-sectioning of the sample would reveal any issues or inaccuracies.

It is immediately evident from figure 7.13 that there is no cavity resonance present in the central region of the stop band. There is a small peak at the short wavelength end around 1220 nm, but this is likely to be due to DBR overlap rather than a resonance. The stop-band is broader than the model, which indicates that the top and bottom DBRs are not perfectly aligned, supporting the theory that the small peak on the left of the stop band is due to a side-band rather than the cavity. The reason for a lack of resonance needed to be determined, so a cross section was performed using BEXP. The averaged layer thicknesses are shown in table 7.5.

The GaAs layers in the upper DBR are generally a little too thin, while the Al_{0.9}Ga_{0.1}As

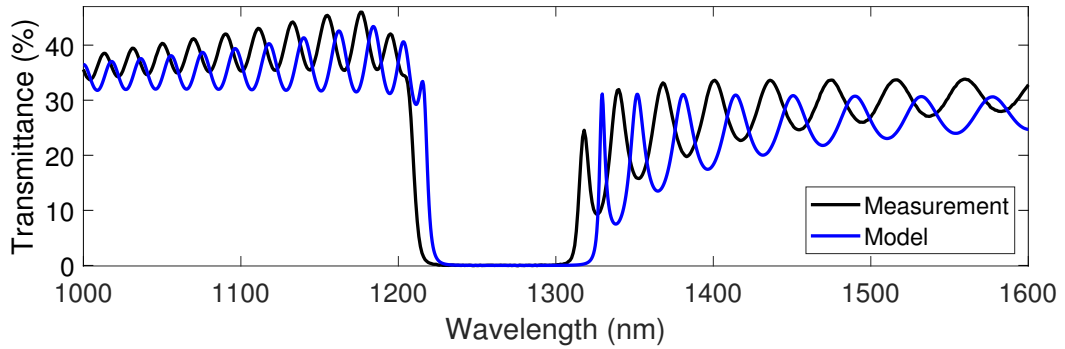


Figure 7.11: Measured transmittance of a sample 1270 nm DBR grown at IQE compared to the simulated transmittance of the design.

Layer	Material	Target Thickness (nm)	BEXP (nm)	Error (nm)
Upper DBR Final x1	GaAs	93.1	89.3	± 4.2
Upper DBR x 29	$\text{Al}_{0.9}\text{Ga}_{0.1}\text{As}$	106.4	106.0	± 4.6
	GaAs	93.1	96.6	± 4.4
Oxidation Layer	$\text{Al}_{0.97}\text{Ga}_{0.03}\text{As}$	30	33.2	± 2.9
Upper Spacer	$\text{Al}_{0.6}\text{Ga}_{0.4}\text{As}$	12.2	20.7	± 2.8
Active Region	GaAs	90	90.3	± 4.2
Lower Spacer	$\text{Al}_{0.6}\text{Ga}_{0.4}\text{As}$	45	48.7	± 3.2
Buffer	GaAs	139.1	166.9	± 7.9
Lower DBR	-	-	-	-

Table 7.5: The averaged thicknesses of the sample in figure 7.13 as measured using BEXP.

are much closer to specification. On the other hand the active region layers are proportionally much more varied, with the upper spacer suffering from as much as a 70 % difference from its intended thickness. The buffer is also thicker than intended, however it is more challenging to measure. This is due to the lack of contrast between the GaAs cap and the $\text{Al}_{0.12}\text{Ga}_{0.88}\text{As}$ layer. On the whole, the spectrum is similar to the test growth in figure 7.12, indicating that the cavity resonance may be very sensitive to small changes in the structure of the active region. To check the accuracy of the cross section, the values were incorporated into the model, which is shown alongside the measurement in figure 7.14. The stop-band of the model now matches the measurement to a good extent, with the side-bands generally agreeing as well. The model's cavity resonance is to the right of the target wavelength, agreeing with the assertion that the peak at the edge of the stop-band was not a resonance, but rather due to stop-band overlap. The lack of cavity peak in the measurement is still a major problem, and steps now need to be taken to assess and improve the issue for the next set of growths.

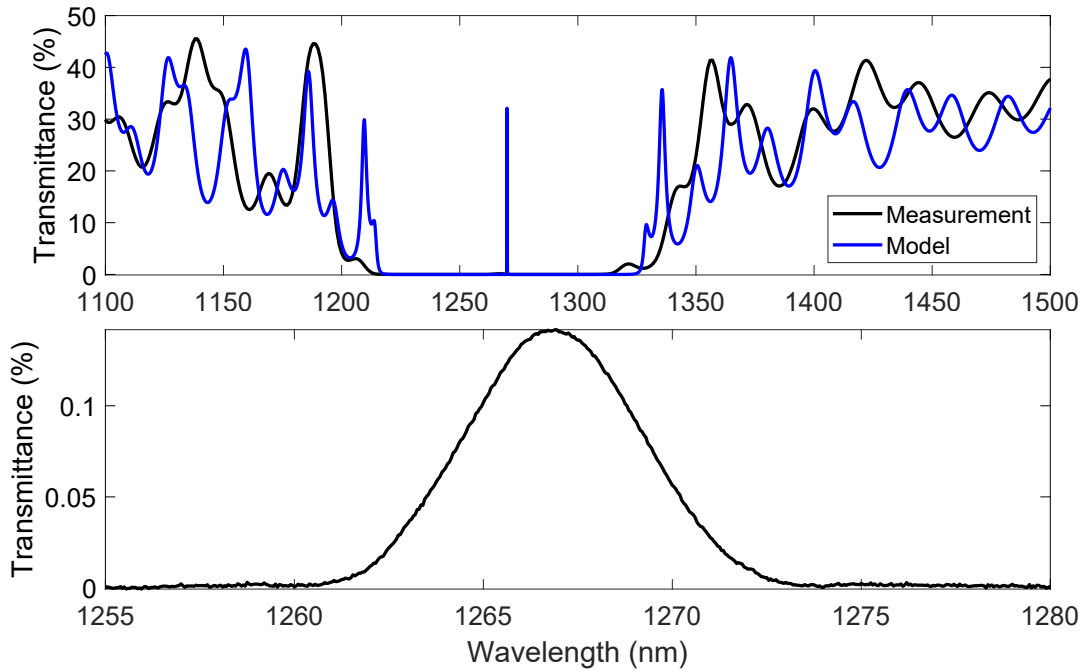


Figure 7.12: **Top:** Transmittance spectrum of the test growth compared to the modelled transmittance of the ideal structure. **Bottom:** Zoomed view of the cavity peak showing good positioning but poor resonance strength.

The lack of strong resonances in the previous two samples calls for an adjustment to the design. It is distinctly possible that the high reflectivity of both mirrors is making the cavity highly sensitive to small variations, making it extremely difficult to produce a stable resonance. To improve tolerance to variations in the design, the number of upper layers was reduced from 29 pairs to 24. This reduction would decrease the strength of the resonance in the model, but could make producing a peak more reliable. The sample was grown to the same specification as before, with the new number of upper layers.

A comparison of the measured transmittance and the idealised model is shown in figure 7.15. It is immediately evident that the stop-band is much wider than expected, with the right-hand edge roughly aligning with the model. The implication of this is that the entire upper stop-band is shifted into the shorter wavelengths, and that the peak visible around 1220 nm is not due to a cavity resonance, but rather the overlap in the upper and lower DBRs. Further evidence to support the misalignment is visible on the bottom of figure 7.15, with the peak aligning closely with the edge of the ideal stop-band. It can be assumed that the IQE lower DBR dominates the model due to its higher reflectivity and stop-band width, so the edge of the model's stop-band corresponds to the edge of the lower DBR. The upper DBR must therefore be shifted almost entirely out of alignment, with the false peak marking where the two mirrors meet.

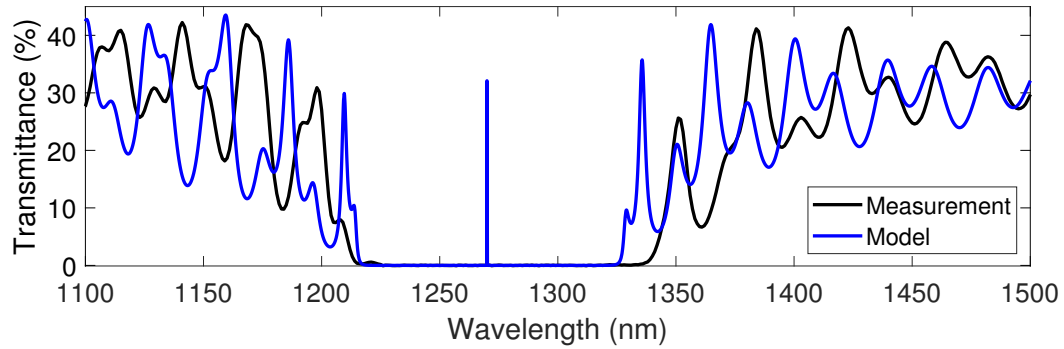


Figure 7.13: Transmittance spectrum of the growth incorporating quantum rings compared to the modelled transmittance of the ideal structure. No cavity resonance is distinguishable from the noise floor.

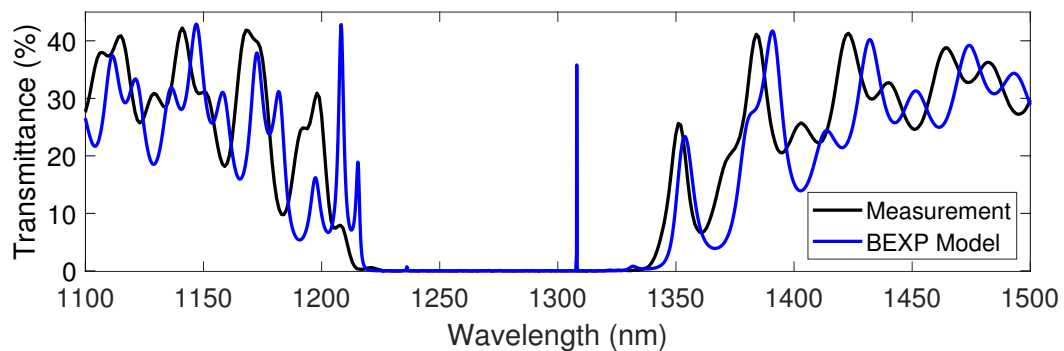


Figure 7.14: Transmittance spectrum of the growth incorporating quantum rings compared to the modelled transmittance of the ideal structure using BEXP measured layer thicknesses.

Once again it was deemed necessary to cross-section the sample to determine the cause of the large shift in wavelength, especially if more of the error comes from a particular material as this could point to issues within the MBE itself. The averaged thicknesses are outlined in table 7.6.

As before, the GaAs layers are too thin on average, with the active region being particularly outside specifications. In this sample the $\text{Al}_{0.9}\text{Ga}_{0.1}\text{As}$ DBR layers are also thinner than expected, which explains the large shift observed in the stop-band of figure 7.15. The consistently thin GaAs layers, combined with the thin $\text{Al}_{0.9}\text{Ga}_{0.1}\text{As}$ layers indicates either a lowered gallium volume inside the MBE cell, or a calibration issue with the growth rates. Another possible source of variability in the layers is due to the MBE growth drifting over time. Whether this is due to substrate temperature fluctuation, or cell growth rate over time or a combination of both, a drift in a long growth such as a VCSEL could have a large impact on the final device. Figure 7.16 plots the thickness of each upper DBR layer as determined using BEXP to assess any overall trends as the

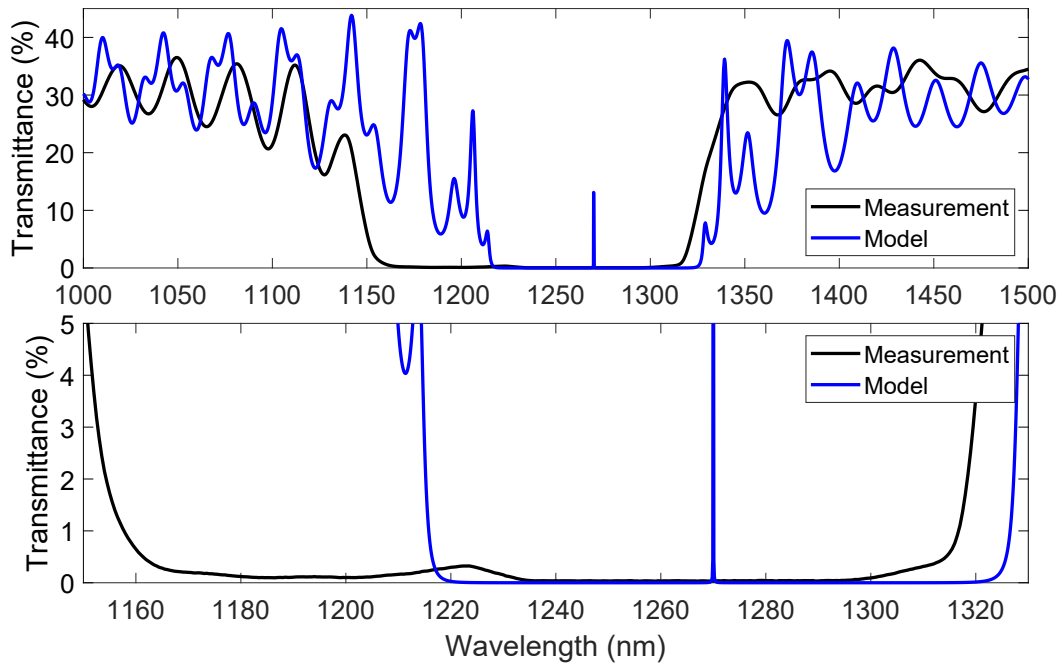


Figure 7.15: **Top:** Transmittance spectrum of the growth with 24 upper DBR repeats compared to the modelled transmittance of the ideal structure. **Bottom:** Zoomed view of the stop-band showing a small transmittance peak roughly aligned with the edge of the modelled stop-band.

growth progresses. The GaAs layers are varied but no obvious upward or downward drift is visible. The $\text{Al}_{0.9}\text{Ga}_{0.1}\text{As}$ layers on the other hand display an overall downward trend, with the final (topmost) layers being nearly 10 % thinner than the initial layers close to the active region. It is possible that the elevated temperature of the aluminium cell (around 300°C hotter than the gallium) makes the material more sensitive to fluctuations caused by the power supply, coolant flow, or temperature controller. Additionally, the Al cell requires the tip to be cooler than the base to prevent the Al from creeping out of the crucible. This is non-optimal for growth and could result in an excess of Al wetting the crucible at the start of the growth, which burns off towards the end reducing the growth rate. However, both materials are consistent within their own error ranges, so while the values match the measured data, one should be cautious about drawing detailed conclusions from the cross-sectional data.

With the individual layer thickness information for the upper DBR and active region, a new model was produced and compared to the measurement to confirm the relationship between the layer variation and optical properties. The updated model is shown in figure 7.17 and displays excellent agreement with the measured data. A clear peak is visible in the model at 1220 nm is coincident with the peak in the data, confirming that the mirrors are not aligned in wavelength. While the growth lacks the potential to

Layer	Material	Target Thickness (nm)	BEXP (nm)	Error (nm)
Upper DBR Final x1	GaAs	93.1	89.2	4.6
Upper DBR x 24	Al _{0.9} Ga _{0.1} As	106.4	99.8	4.8
	GaAs	93.1	88.3	4.4
Oxidation Layer	Al _{0.97} Ga _{0.03} As	30	31.1	3.2
Upper Spacer	Al _{0.6} Ga _{0.4} As	12.2	19.2	3.0
Active Region	GaAs	90	72.0	4.0
Lower Spacer	Al _{0.6} Ga _{0.4} As	45	46.3	3.5
Buffer	GaAs	139.1	113.7	9.6
Lower DBR	-	-	-	-

Table 7.6: The averaged thicknesses of the sample in figure 7.15 as measured using BEXP.

resonate, given the lack of mirror alignment, the data gained here shows that a general picture of the device growth can be obtained simply using the transmittance, observing misaligned DBRs and errors in thickness without the need to cross-section every sample saving time and money. A poorly aligned growth can be discarded outright, and optically aligned structures can be progressed to the next phase of testing.

In order to reduce the effect of any drifting in the growth, as well as to increase the likelihood of producing a cavity, the upper DBR repeats were further reduced to 20. The modelled resonance produced by this number is low, but if a working cavity is produced then steps can be taken to improve performance in following growths. As before, the same general design was used as in table 7.4 with the exception of the change in upper layers. The growth and optical testing proceeded as normal with the transmittance and model compared in figure 7.18.

A small shift in the stop-band is evident, with the extra width of the measured stop-band being potentially due to a slightly misaligned upper mirror. However, a resonance is clearly visible on the bottom of figure 7.18 at 1250 nm, and although the peak is small, this is a promising step towards a working MOVPE-MBE hybrid device. In an attempt to improve the cavity stability and overall resonance quality, the oxide forming layer and the upper spacer were combined into a single layer. The new high-Al spacer still forms part of the cavity, and serves to reduce the number of layers and interfaces. In doing so, the hope is that less material changes and fewer interfaces will lead to more accurate and higher quality layers. In addition to the cavity change, a 5 nm Al_{0.6}Ga_{0.4}As layer was added to allow the AFM used in cross-sectioning to determine where the MBE growth began, thus improving the cross-sectional data.

Three samples with the exact same recipe were grown to the specification in table 7.7,

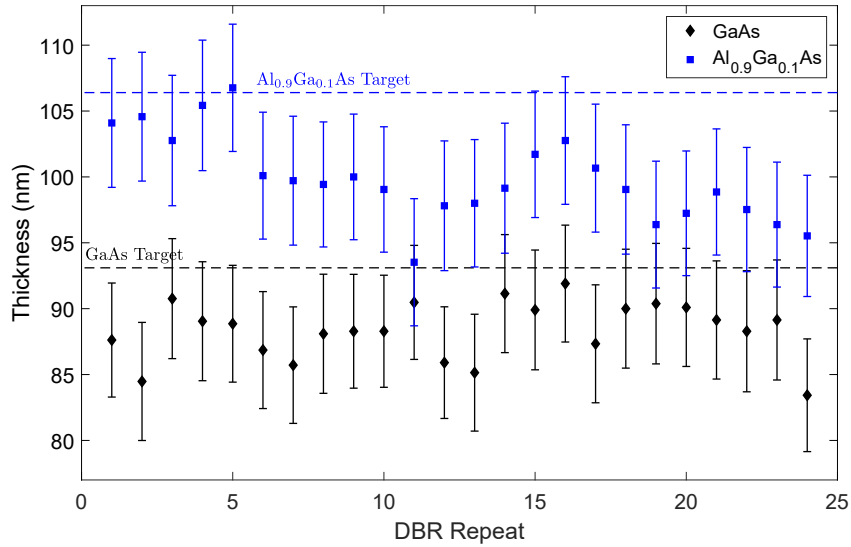


Figure 7.16: The thickness of each layer of the upper DBR of the device in figure 7.15 showing the layer variation over the duration of the growth. The repeats are in order of growth, i.e. layer 1 is next to the active region and 24 is at the surface.

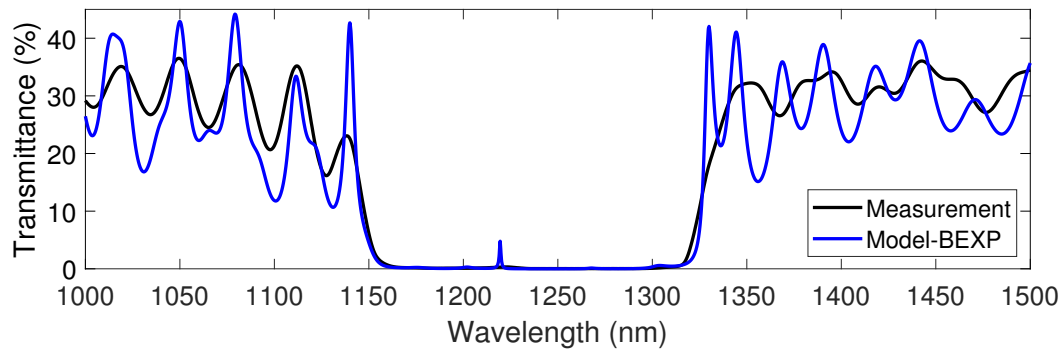


Figure 7.17: Updated modelled transmittance of the structure using BEXP individual layer thicknesses alongside the measured transmittance of the sample.

to check repeatability and to improve chances of a working device. The growths were as close to each other as time would allow and with as few other samples as possible being grown in the MBE in between. Figure 7.19 shows the optical results of all three growths alongside the simulation of the ideal design. All three samples show excellent agreement with the model, indicating that the growths are accurate to specification. Sample c in particular is extremely close to the simulation, with the side-bands agreeing to a good extent.

All three samples had measurable cavity peaks, though all at a very low amplitude ($\sim 0.15\%$). A zoomed view of the samples' stop-bands is shown in figure 7.20, with each sample being close to the target wavelength of 1270 nm. Although the resonances appear to be quite weak, the consistency of the growths is very encouraging. It is clear that

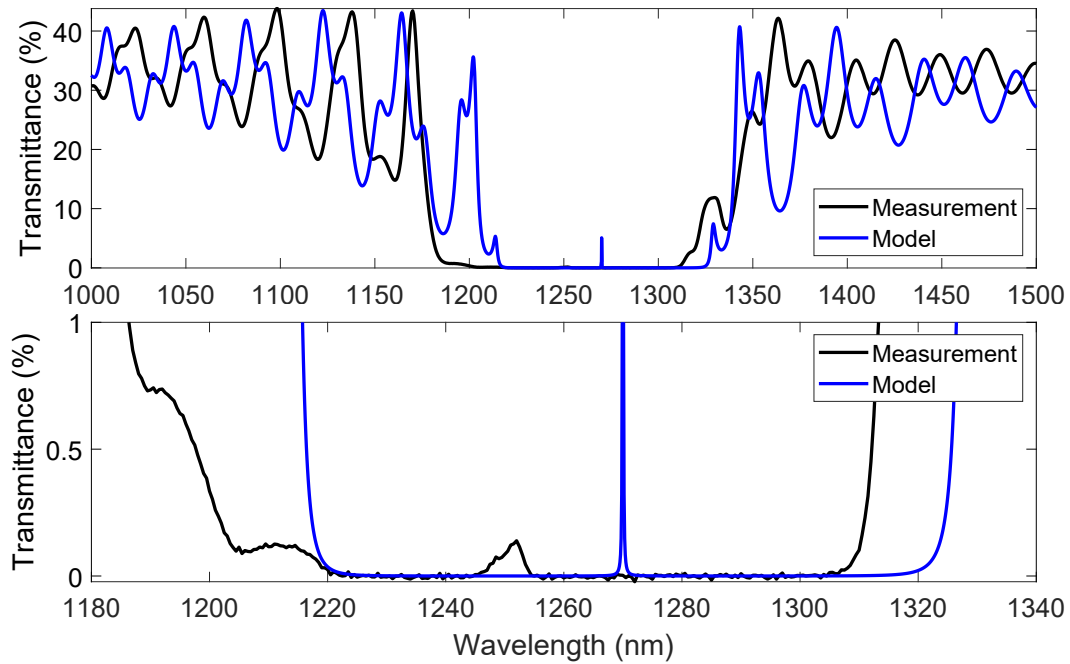


Figure 7.18: **Top:** Transmittance spectrum of the growth with 20 upper DBR repeats compared to the modelled transmittance of the ideal structure. **Bottom:** Zoomed view of the stop-band showing a small transmittance peak at around 1250 nm.

with the proper calibration, a two part MOVPE-MBE growth can be repeatable and reliable.

7.2.3 Processing and Testing

A piece of one of the samples was sent to CST to be processed into VCSEL devices using much the same processing design as the Mk 1 VCSELS. A range of mesa sizes was produced, from $29\ \mu\text{m}$ up to $90\ \mu\text{m}$, with an example of the smallest and largest mesas shown in figure 7.21. The VCSELS use a top-bottom arrangement with the top bond pad connecting to a ring contact on the mesa's surface. The thinned substrate serves as the back contact and can be attached to the mount with either silver paste or via reflow soldering. The chips themselves are $300 \times 300\ \mu\text{m}$.

The largest of the devices was used in testing to aid in aligning the mesa with the measurement fibre, maximising the collected light. An I-V profile of a $90\ \mu\text{m}$ VCSEL is shown in figure 7.22. The primary difference between the Mk 2 I-V and the one shown in figure 7.6 is the extremely high resistance shown by the new devices. Almost 30 V is required to drive any significant current through the device, which will almost certainly result in large amounts of heating inside the device due to the resistive nature of the sample. There are multiple possibilities for the cause of the increased resistance, with

Layer (s)	Material	Composition		Doping		Thickness (nm)
		Al	Ga	Type	Level (cm ⁻³)	
Final Layer	GaAs	0	1	p++		93.1
Upper DBR x20	AlGaAs	0.9	0.1	p	4.0E+18	106.4
	GaAs	0	1	p	2.0E+18	93.1
Oxidation Layer	AlGaAs	0.97	0.03	p	4.0E+18	45.6
Quantum Ring x5	GaAs - Hot	0	1	i	-	10.0
	GaAs - Cold	0	1	i	-	5.0
	GaSb	-	-	i	-	2.1 ML
	GaAs	0	1	i	-	15.0
Lower Spacer	AlGaAs	0.6	0.4	i	-	45.0
Buffer	GaAs	0	1	-		139.1
Marker Layer	AlGaAs	0.6	0.4	i	-	5.0
IQE DBR x40	-	-	-	-	-	-

Table 7.7: Design of the MBE section of the 1270 nm VCSEL growth, with 20 upper repeats, a half-wavelength cavity, and 5 sets of quantum rings. The upper spacer has been replaced with a solid Al_{0.97}Ga_{0.03}As layer and a thin marker layer has been added to allow for the start of the growth to be identified in a cross-section.

the smaller mesa certainly having an effect. Contact resistance, poor layer interfaces, poor processing, or issues with doping are all candidates that could negatively impact the electrical performance of the device. However, it is most likely that the high-Al content in the square-interfaced upper DBR is the root cause of the majority of the resistance. While the high-Al contrast improves the optical performance of the DBRs, the aluminium content and square interfaces will increase resistance and reduce device efficiency[88, 89].

The same 90 μm device was then driven at 1 mA with continuous (100% duty cycle) operation producing an extremely low intensity output at 1260 nm, which can be seen on the top of figure 7.23. In an attempt to produce a greater output intensity, the drive current was increased to 6 mA, requiring more than 20 V to achieve. The result of the higher current is visible on the bottom of figure 7.23, displaying a small increase in intensity, with a dramatic increase in the side emission outside of the stop-band. This implies that while more current is reaching the rings, the resonance is not being strongly selected by the DBRs and cavity. This device is clearly not suitable for use, as the output efficiency is extremely low, and the drive voltage is unreasonably high. It is likely that any extended operation would result in the devices failing due to the high voltage and internal heating.

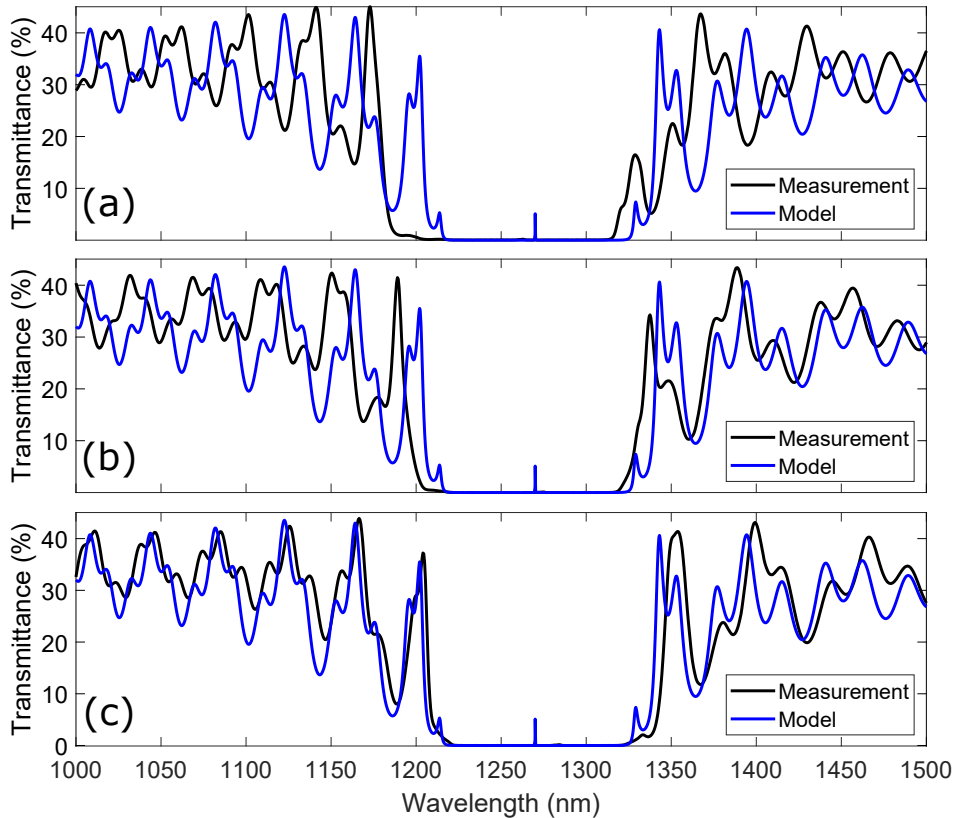


Figure 7.19: Transmittance of samples a-c compared to the simulated structure from table 7.7.

7.2.3.1 Electrochemical Capacitance-Voltage (ECV) Measurement

One potential factor affecting the high resistance of the devices is the distribution of dopants within the upper (MBE-grown) DBR. The lower DBR was grown by IQE under industrial conditions to a standard recipe, and thus is unlikely to be the cause of the electrical problems. The upper DBR was beryllium doped, with target carrier concentrations as shown in table 7.7.

An ECV profile was performed on the upper DBR at IQE to observe the distribution of carriers within the MBE epilayers. This technique employs an electrochemical cell, with the sample covering a port in the cell to act as one electrode. A bias is then applied between the sample and another electrode to create a depletion region close to the sample's surface. By measuring the capacitance-voltage profile of the cell, a measurement of the carrier concentration may be obtained. Using controlled electrochemical etching, the sample surface is incrementally removed allowing for depth-dependant measurements of carrier concentration. Further details can be seen in reference [90].

The ECV profile is plotted in figure 7.24, showing a low carrier concentration, with clear diffusion between layers. The carriers appear relatively stable within the GaAs

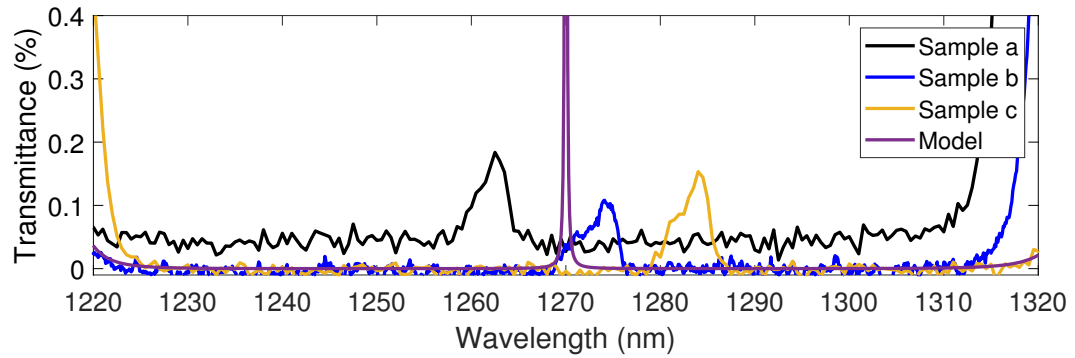


Figure 7.20: A zoomed view of the transmittance of samples a-c compared to the simulated structure from table 7.7. Sample a has an elevated baseline, likely due to a calibration issue with the spectrophotometer.

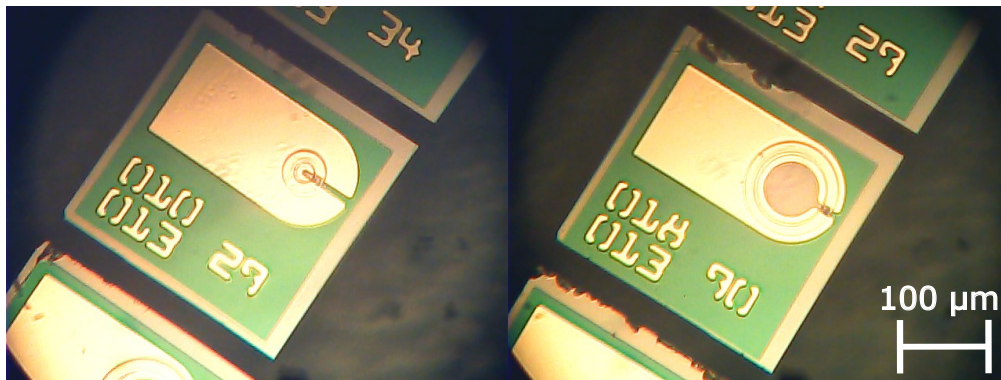


Figure 7.21: Optical microscope images of the processed VCSEL devices with mesa sizes of 29 μm (left) and 90 μm (right).

layers, but show a definite diffusion toward the layer interfaces, particularly within the $\text{Al}_x\text{Ga}_{1-x}\text{As}$ layers. This is consistent with work done to study the diffusion of Be doping in $\text{GaAs-Al}_x\text{Ga}_{1-x}\text{As}$ systems [91, 92]. This low and inconsistent doping will almost certainly have an effect on the device performance, and should be considered in future work.

7.3 Mk. 3 VCSELS

7.3.1 Design

From the results in section 7.2.2 it is clear that a more major design change was needed to improve the characteristics of the VCSEL structures. The extremely high reflectance of the bottom DBR that was meant to reduce the gain requirements and improve resonance strength appears to only hinder the formation of a stable cavity. A more reasonable number of lower repeats was suggested to reduce the sensitivity of the design to small changes, and to allow for fewer upper layers to reduce growth time and complexity.

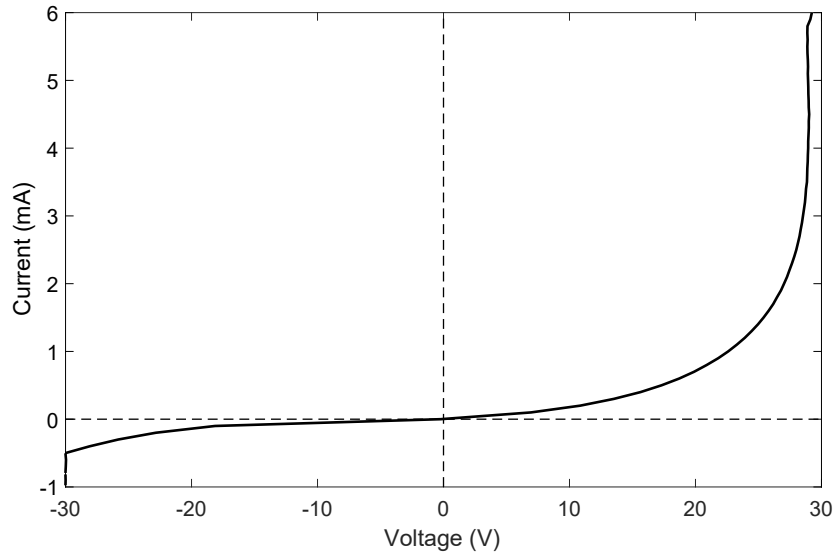


Figure 7.22: An example I-V curve from a 90 μm diameter device with extremely high resistance. Reverse breakdown begins to occur at -20 V .

The core of the design was identical to the Mk2 design in table 7.7, with the primary change being fewer lower DBR pairs (30 pair substrates once again provided by IQE). The cavity spacers were adjusted to keep the target wavelength at 1270 nm as the change in mirror reflectivity alters the effective length of the cavity resonance. The number of upper DBR pairs was set at 15, and while this may reduce the strength of the cavity, the added stability of a ‘softer’ design aims to make obtaining a resonance and troubleshooting the designs more straightforward. The thinner samples should also reduce the high resistance shown in the previous versions.

7.3.2 Key Samples

The first of these less sensitive samples was grown and optically tested after some calibration and test samples that are not shown. The measured transmittance is seen alongside the modelled design in figure 7.25. The entire spectrum is shifted by around 20 nm towards the shorter wavelengths, indicating a slightly low growth rate or other small calibration offset. There is a clearly visible cavity peak at around 1240 nm (dependent on position on wafer) with a much higher transmittance than the previous design. For reference, the peaks in figure 7.20 are between 0.1 and 0.2%, while the sample in figure 7.25 has a cavity peak amplitude of 4.2%. This improvement can be attributed to the softer mirrors that allow for greater variation from the design specification before the resonance is lost. Since the design must be repeatable, another growth was performed to the exact same specifications in an attempt to reproduce or improve on the clear cavity

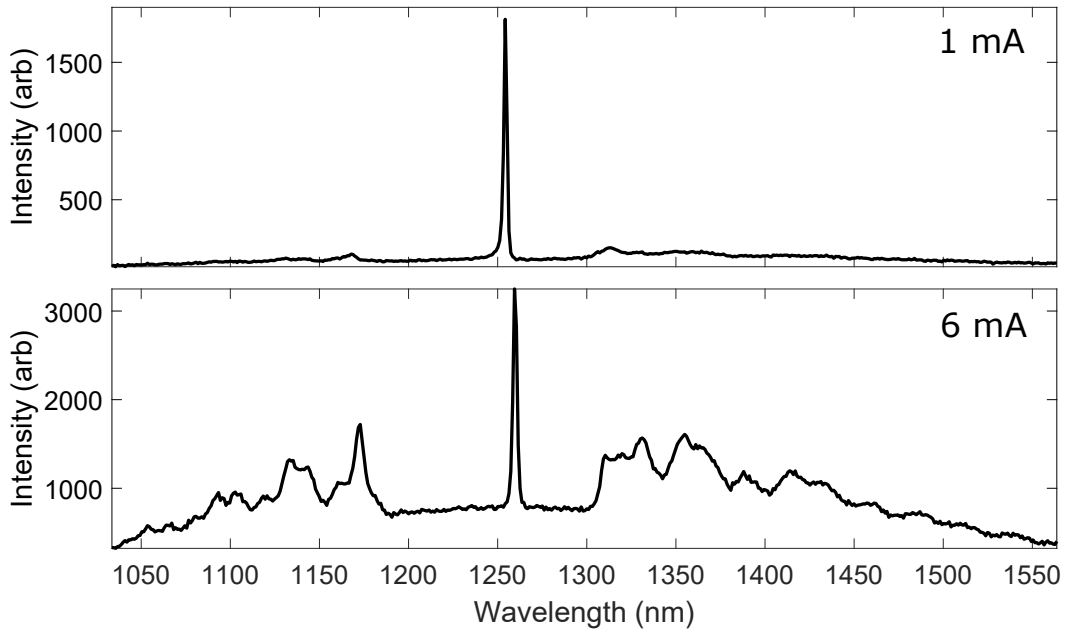


Figure 7.23: **Top:** 1 mA emission of a 90 μm diameter device operating around 1260 nm. **Bottom:** 6 mA emission from the same device, showing increased intensity, particularly outside the stop-band region.

resonance. The measured transmittance of the repeated growth, shown in figure 7.26, once again displays a slight shift towards the shorter wavelengths and a clearly visible cavity this time at around 1255 nm. While the amplitude of the cavity peak is smaller than the previous sample, 2.7%, this is still significantly larger than the Mk 2 structures and could simply be affected by slight inconsistencies in the growth or transmittance measurements. Both samples have provided clear cavity resonances and relatively good stop-band alignment, showing that the less reflective design is much more tolerant and makes the production of a suitable optical profile far more reliable. Since the first of the two samples has a higher cavity peak amplitude, it was selected to be sent for processing into VCSEL devices.

7.3.3 Processing and Testing

Once processed to the same specifications as the Mk 2 devices, 90 μm devices were measured for their I-V and output characteristics. The devices showed a low resistance, albeit noisy I-V as pictured in figure 7.27. The reason for the lower resistance could be the reduced layer count, a generally improved growth, or improved processing quality. However, it was virtually impossible to get the devices to produce any light. All but one had zero output, with one device having a brief emission at a drive current of 50 mA. As expected with such an enormous current in a small device, it failed shortly after

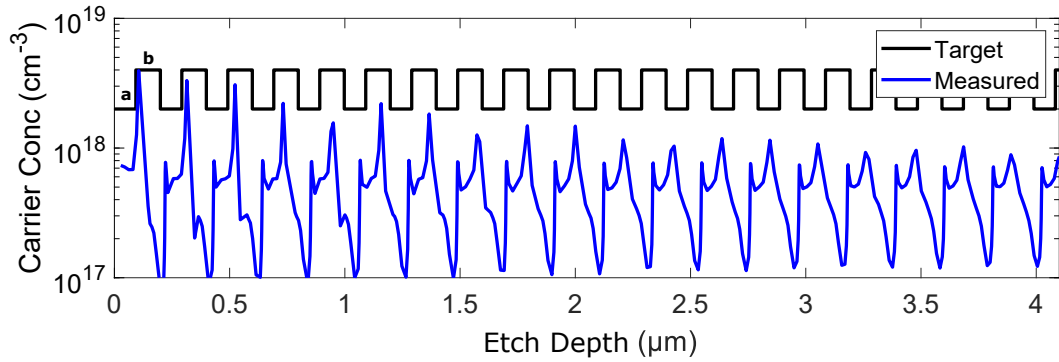


Figure 7.24: Electrochemical capacitance-voltage (ECV) depth profile of the sample as measured by IQE showing the carrier concentration through the upper DBR. The GaAs layers, **a**, have a target doping of $2.00 \times 10^{18} \text{ cm}^{-3}$, and the $\text{Al}_{0.9}\text{Ga}_{0.1}\text{As}$, **b**, have a target doping of $4.00 \times 10^{18} \text{ cm}^{-3}$.

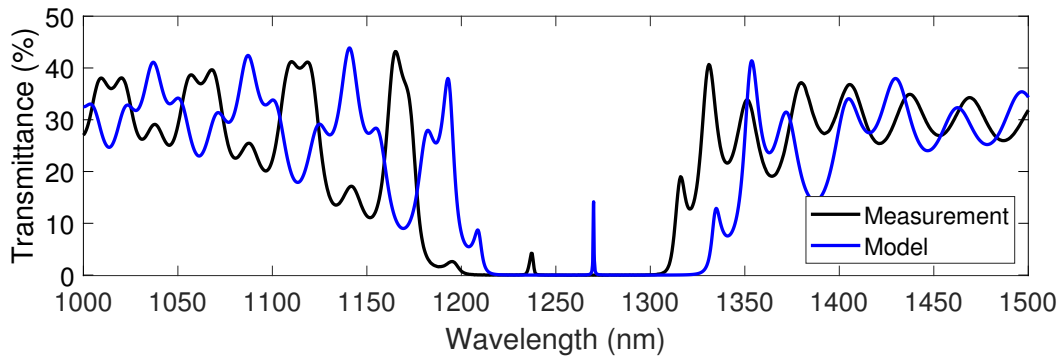


Figure 7.25: Measured transmittance of the VCSEL structure with 30 lower DBR repeats and 15 upper repeats compared to the simulated design.

the spectrum in figure 7.28 was observed. The intensity of the brief output was very low, indicating that the majority of the current was travelling somewhere other than the active region. It is possible that some aspect of the growth or processing had caused a path for current to flow around the mesa, making the devices all but useless.

7.4 Mk. 4 VCSELS

7.4.1 Design

It was decided that a full, MBE-grown VCSEL would be produced at Lancaster. The goal of this was to avoid the inherent issues of a multi-stage growth and to keep the design as simple and symmetric as possible. If the MBE is not fully calibrated then the risk of the upper DBR being out of alignment with the lower MOVPE mirror is high. On the other hand, growing the entire structure in one run on the MBE, while slow, means that even if the thickness calibration is out, the whole device will be shifted rather than

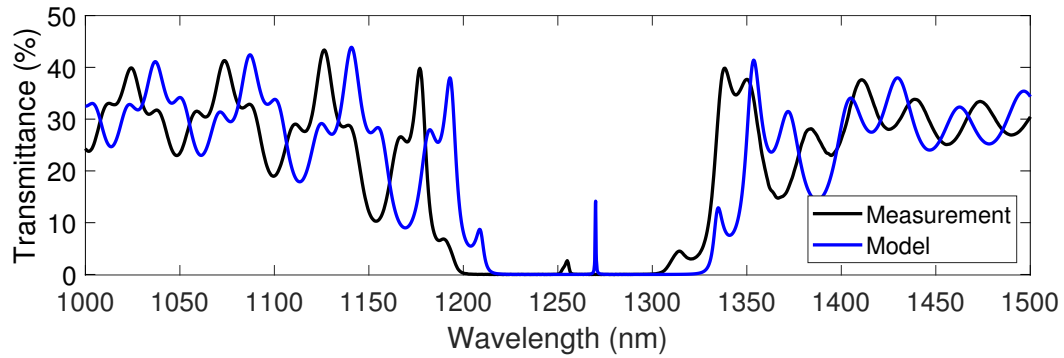


Figure 7.26: Measured transmittance of the repeated VCSEL structure with 30 lower DBR repeats and 15 upper repeats compared to the simulated design. The specification is identical to the sample in figure 7.25.

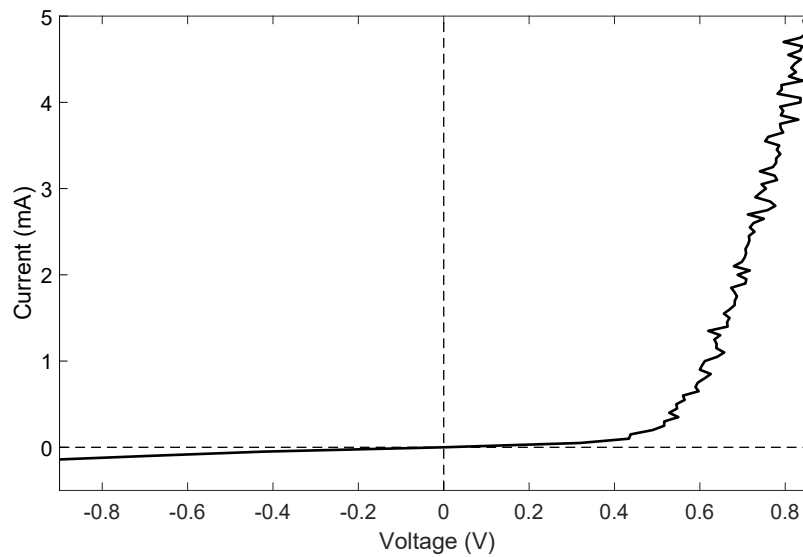


Figure 7.27: An example I-V curve from a 90 μm diameter device, with a generally low resistance.

just the upper mirror. The end result would be a functioning resonator at the ‘wrong’ wavelength, which is preferable to a completely non-functional device. The same GaAs - $\text{Al}_{0.9}\text{Ga}_{0.1}\text{As}$ DBR system that was utilised as the upper mirror for the hybrid samples was used for both the upper and lower reflectors in this design. Table 7.8 outlines the design for the fully MBE VCSEL to be grown at Lancaster. The lower DBR has a total of 30 repeats, with the upper mirror having 24 or 15 pairs of layers. The two different amounts of upper DBR pairs is to see the difference in optical behaviour at high and low upper reflectivity.

Table 7.8 details the growth design for the Mk 4 VCSEL. Notably, this design lacks a high-Al layer in the cavity for creating an oxidation layer. It was decided that since Lancaster lacks the equipment for oxidation, an attempt would be made to confine the

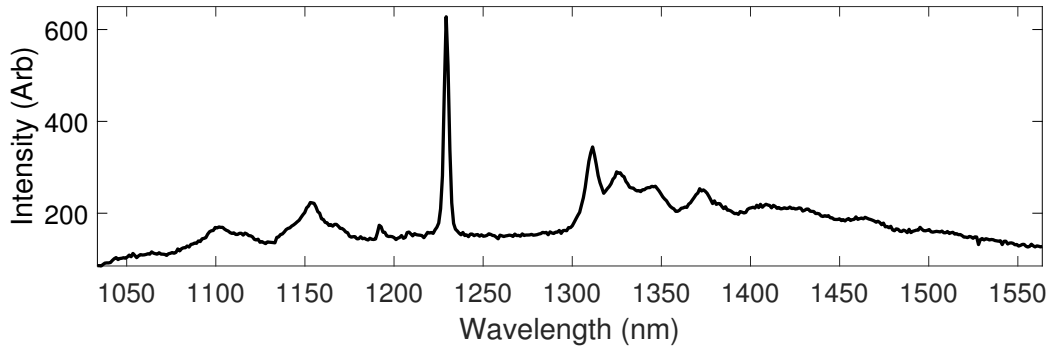


Figure 7.28: The emission of a processed Mk 3 device with a drive current of 50 mA. The device failed after the measurement was taken.

current using the geometry of the processed device. As such the oxidation layer became superfluous and was removed. Additionally, in an attempt to reduce the high resistance of the previous designs, two mesas will be defined as shown in figure 7.29.

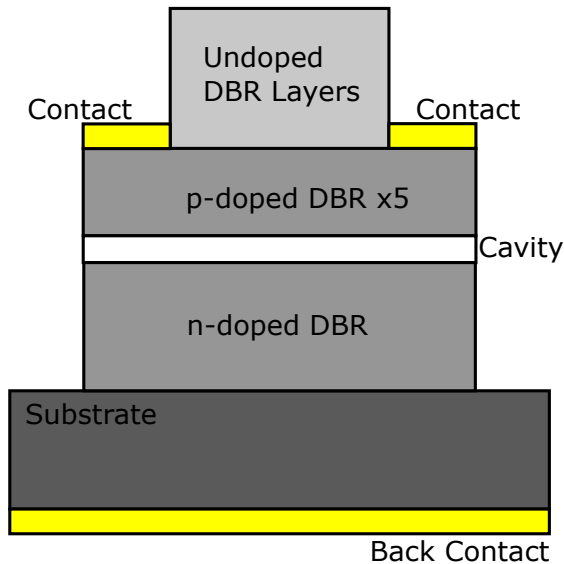


Figure 7.29: Schematic of the proposed mesa definition for the Mk 4 devices. The first 5 DBR repeats after the cavity are doped, providing the upper contacting site. The rest of the upper DBR is undoped, providing a low-absorption section of the device.

Only the first 10 layers after the cavity are p-doped, with the rest remaining undoped until the end of the growth. By contacting to the doped layers and not the top of the upper DBR, the overall resistance of the device should be lower than in previous samples. Less doped material means less optical absorption, as the p-type material displayed a much higher extinction coefficient in section 5.1.2. Lower absorption should lead to improved device performance and efficiency. Ideally, the end result should be both more transmissive, and less resistive once processed. The simulated electric field of the device is shown in figure 7.30, displaying clear alignment with the quantum ring layers. The

Layer (s)	Material	Composition		Doping		Thickness (nm)
		Al	Ga	Type	Level (cm ⁻³)	
Upper DBR Final	GaAs	0	1	i		93.1
Upper DBR x 24,15	AlGaAs	0.9	0.1	p	4.0E+18 *	106.4
	GaAs	0	1	p	2.0E+18 *	93.1
Cavity Spacer	AlGaAs	0.6	0.4	p	4.0E+18	44.9
Quantum Ring x5	GaAs - Hot	0	1	i		10
	GaAs -Cold	0	1	i		5
	GaSb	-	-	i	-	2.1ML
	GaAs	0	1	i		15
	Cavity Spacer	AlGaAs	0.6	0.4	n	4.0E+18
Lower DBR x 30	GaAs	0	1	n	2.0E+16	93.1
	AlGaAs	0.9	0.1	n	4.0E+18	106.4
Buffer	GaAs	0	1	n	2.0E+16	~500
Substrate	GaAs	0	1	n		

Table 7.8: VCSEL structure for the Mk4 design to be produced entirely at Lancaster. 30 lower DBR repeats is combined with either 24 or 15 upper repeats to assess both a high and low reflectivity design. * To reduce the resistance and optical absorption of the upper DBR, the goal is to etch the upper DBR mesa so that only the ten layers closest to the cavity are contacted. These ten layers will be doped, while the rest remain intrinsic.

field is also much more symmetrical than the previous designs due to both DBRs having the same design, as well as the structure being continuous without the GaAs cap and buffer layer inherent to the Mk 2 and 3 designs.

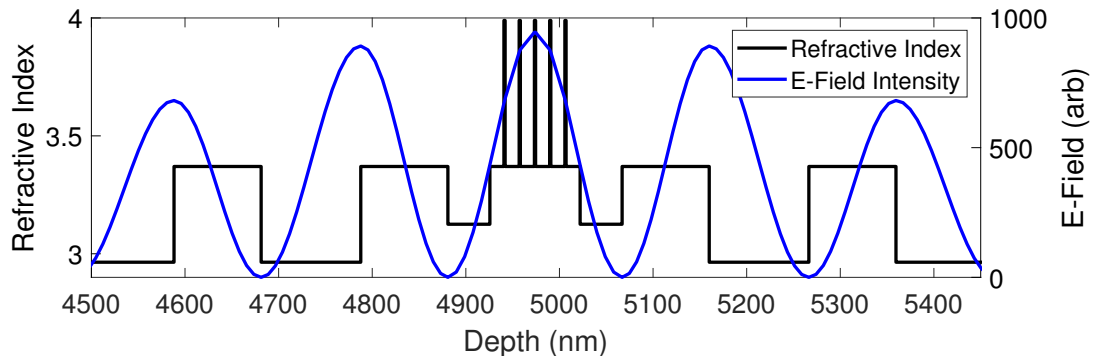


Figure 7.30: Simulated electric field profile of the design outlined in table 7.8 showing clear symmetry and alignment with the quantum ring layers.

7.4.2 Key Samples

The first growth was run using the design from table 7.8 and had an upper DBR consisting of 24 pairs of GaAs - Al_{0.9}Ga_{0.1}As repeats. The optical transmittance of the sample is shown in figure 7.31, with a zoomed view of the stop-band in the lower portion

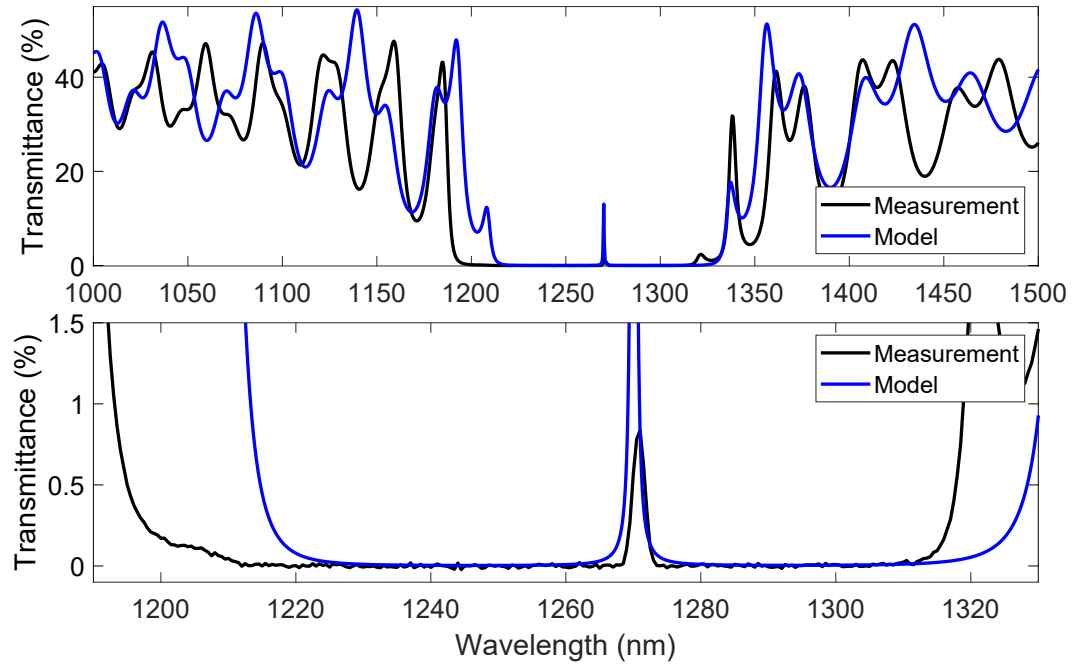


Figure 7.31: **Top:** Transmittance spectrum of the growth from table 7.8 with 24 upper repeats compared to the modelled transmittance of the ideal structure. **Bottom:** Zoomed view of the stop-band showing a transmittance peak at around 1270 nm.

of the figure. In general the data aligns with the model, with a slight broadening of the stop-band at the short wavelength end. It is possible that over the duration of the growth, the cells have drifted causing the growth rate to drop and the layers to become thinner. However, the effect is minimal and a resonance is clearly visible at ~ 1270 nm, aligning almost perfectly with the target wavelength. Most growths have had a certain variation across the wafer which affects the entire structure, so it is likely that this exact alignment is somewhat of a coincidence. To be certain, a line of points was taken across the wafer, and the wavelength of the resonance peak was measured. This is displayed in figure 7.32. The position of the cavity peak changes by as much as 15 nm between the centre of the wafer and the edge, with a symmetrical variation around the centre. It is likely that the variation is caused by a slight change in thickness, either due to a small temperature gradient, or due to the flux profile of the molecular beams. Whatever the cause, it is probable that the middle of the wafer is the thickest, and that in general one should avoid taking samples for processing from outside the central region, unless the intention is to produce VCSELS with varying output wavelengths.

The first Mk 4 produced a cavity resonance that while measurable, had an amplitude of less than 1%. This is larger than the Mk 2 designs, but smaller than the Mk 3 structures that had the same number of lower DBR repeats. The next growth used

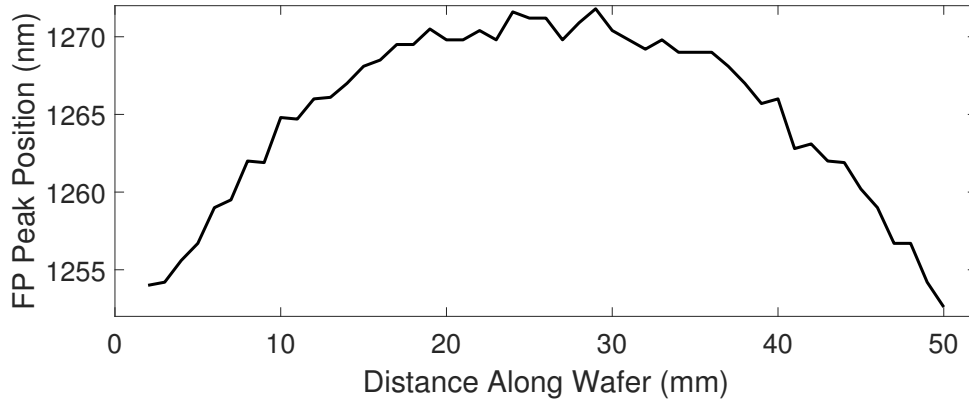


Figure 7.32: Cavity peak amplitude with respect to position across the wafer showing up a 15 nm variation towards the edge of the wafer.

15 upper pairs instead of 24, with the aim to reduce sensitivity and produce a larger resonance much in the same way as the Mk 3 samples.

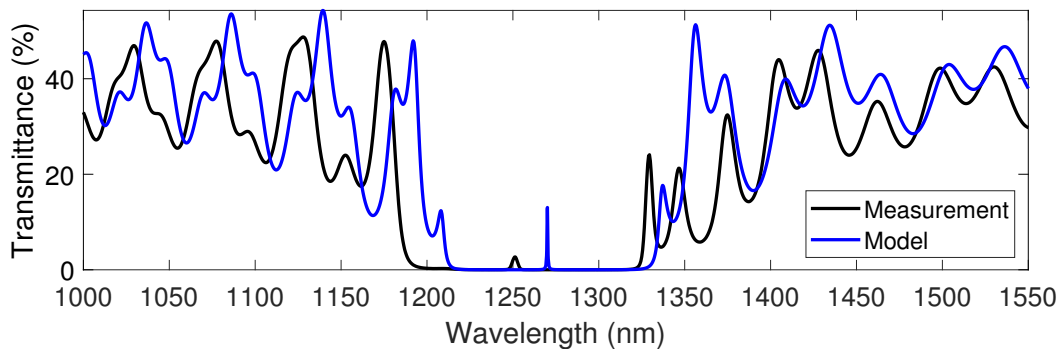


Figure 7.33: Transmittance spectrum of the growth from table 7.8 with 15 upper repeats compared to the modelled transmittance of the ideal structure.

Figure 7.33 shows the measured transmittance of the latest sample with 15 upper DBR repeats compared to the ideal simulated transmittance. A clear cavity resonance is visible at around 1250 nm with an amplitude of approximately 3%. This is a definite improvement over the previous growth in figure 7.31, and is consistent with the Mk 3 samples. The stop band appears to be broadened, potentially due to drift in the growth over time. Since a full VCSEL will have a longer growth time than the overgrowth from previous versions, drift may be more of a factor. However, without extensive calibration and testing it would be very difficult to confirm and mitigate these effects, and since a cavity resonance has been achieved at this time no action will be taken on that front.

7.4.3 Processing and Testing

A section of material from the final Mk 4 growth was processed in the Lancaster QTC cleanroom, producing devices with a mesa diameter of $200\ \mu\text{m}$. An example I-V profile of one of the processed devices is visible in figure 7.34, showing unusually symmetric behaviour compared to the previous generations of devices. The lack of diode behaviour could be due to the lower number of doped layers, or an issue with the doping throughout the device. Unfortunately, no cavity emission was observed for these samples, indicating either an issue with the structure or doping parameters, or problems with the processing.

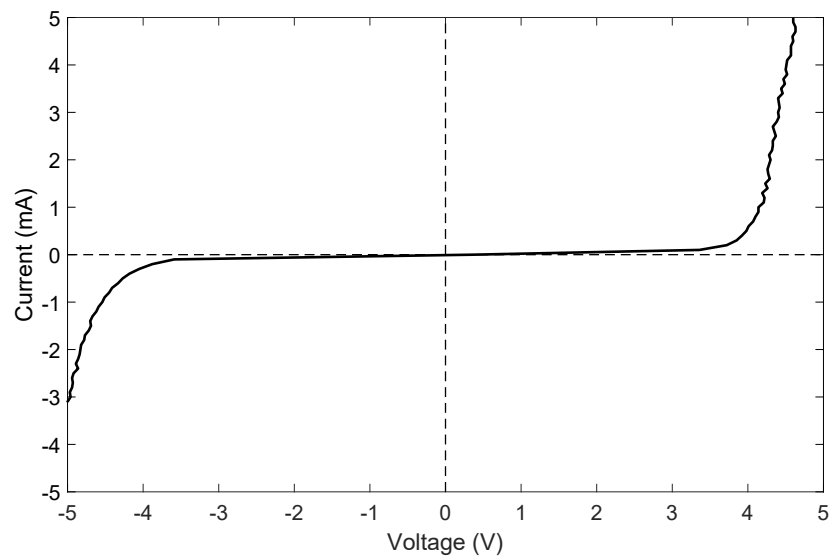


Figure 7.34: An example I-V curve from a $200\ \mu\text{m}$ diameter device.

Chapter 8

Conclusions

A goal of this work was to determine both the feasibility of a telecoms wavelength GaAs - Al_xGa_{1-x}As VCSEL, as well as assess the possibility of mass production using IQE's MOVPE reactors. A second objective was to refine the models and analytical techniques used in the design of optical devices such as these, and use them to reduce the time and cost normally associated with semiconductor characterisation. Throughout the iterations of the design, optical models have been used to determine layer thicknesses and cavity layouts with a good amount of success. Deviations in the measured transmittance of a sample from the ideal simulated spectrum can almost always be attributed to variation in the growth itself, rather than inaccuracies in the model. Using a simple transmittance measurement (which is fast, cheap, and completely non-destructive), general assertions can be made about a sample and its suitability for progression to the next phase of processing. Misaligned mirrors, poor cavity positioning, and weak/absent resonances are all able to be detected with this method. This allows optically poor samples to be rejected without the need to waste time, money, and resources processing them.

The transmission measurements themselves are a feature of the telecoms wavelength nature of the devices, as the shorter wavelength datacoms VCSELs are too absorbing for any transmission to be measurable. Reflectivity measurements are difficult to take with any accuracy, as the light must be incident on the sample, and measured from the same location (normal to the sample surface). Often requiring redirecting optics, such as mirrors or optical fibres, absolute reflectance measurements become increasingly difficult to achieve due to the difficulty in collecting the reflected light. Baseline calibration is also much easier with transmission, as a perfect transmitter (empty sample holder), and a perfect absorber (blocking the sample beam) are all that is required. Reflectance on the other hand needs a perfect reflector to calibrate, which is incredibly difficult to approximate across a range of wavelengths.

When looking at the transmission is not enough, utilising the in-house BEXP-AFM cross-sectioning technique can quickly find problems such as incorrect layer thicknesses, poor interfaces, and general material quality. BEXP-measured layer data has repeatedly proved to be accurate and reliable when compared to the measured transmittance of a device. Using these combined filters, processing huge numbers of devices simply is not necessary, and paves the way for higher-level production.

Positive steps were taken towards identifying the requirements for a good cavity resonance, with high-reflectivity mirrors serving to make the VCSEL extremely sensitive

to small changes in the structure. A sensitive device is not desirable, as a small variation in the layer thicknesses can completely destroy the resonance, and therefore the chances of a functioning laser. By reducing the overall reflectivity of the top and bottom mirrors, a more reliable resonance was achieved, displaying extremely consistent results through multiple growths. The IQE lower DBRs were of an extremely high quality, reducing the growth time in the MBE by a large margin. Having quality controlled mirrors meant that the focus could be on the cavity and upper layers, reducing the number of ways a growth could stray from the targets. Combining the MOVPE growth with an MBE overgrowth required some adjustments, but stable cavities were produced.

Working devices proved difficult to obtain, with samples struggling with high resistances and extremely low output powers. ECV measurement pointed to an issue with the doping in the upper DBR, and a number of other factors could be contributing to the high resistance. Fully MBE-grown devices offered little in the way of improvement, suggesting that the issue could be in the processing, or the upper DBR itself. Further assessment on the performance of these VCSELs could include contact resistance, doping profiles, $\text{Al}_x\text{Ga}_{1-x}\text{As}$ compositions, layer interface grading, active region carrier behaviour, cavity lengths, free carrier absorption due to layer doping, current confinement, and more. Being able to reject optically poor samples is of key importance, as all of those factors require processing, so any step that will reduce the cleanroom work needed will save time and money.

Light output has been demonstrated, however, suggesting that with refinement a telecoms wavelength VCSEL can be produced using the $\text{GaAs-Al}_x\text{Ga}_{1-x}\text{As}$ material system. It has been shown that with calibration, a MOVPE lower mirror can be combined with a quantum ring active region and MBE upper mirror to produce resonant devices. Once issues with resistance and processing have been identified and addressed, it appears likely that a cheap telecoms VCSEL can be mass produced on a large scale.

Potential next steps for this work are wide-ranging, with the main areas including electrical properties, processing considerations, and characterisation. A first step would be to determine the cause of the device's high electrical resistance, focusing on the DBR doping levels and grading structure. The diffusion of the beryllium dopant would need to be addressed, to ensure that each layer has the doping as specified by the design. P-down devices, whereby the structure is 'flipped' to have the p-DBR on the bottom, could avoid the beryllium issue by having a carbon-doped lower DBR grown at IQE via MOVPE, providing a much more consistent doping profile. The flipped structure may

also increase output intensity due to having the highly absorbing p-doped layers away from the emitted light. However, the accurate and versatile transmittance measurements used in this work may no longer be possible, as a thick p-type substrate would absorb the sample beam.

Testing and refining the contacts used, particularly the composition and deposition, will also ensure that the potential for any rogue resistance be greatly reduced, as contact resistance will often mask the underlying behaviour of the devices. Current confinement, such as wet oxidation, will be required to improve efficiency and reduce carrier loss, and will need extensive calibration to ensure optimum efficiency. Once device performance is improved, the effect of mesa size would also need to be investigated for this material system, to assess the effect on device output. This could coincide with testing the speed of the lasers, to determine how the quantum ring active region performs in a data transmission capacity. The work can also be extended to array systems, allowing for higher powers, novel emitter layouts, and sensing applications. All of these next steps would need to be combined with the various methods of characterisation described in this work, to ensure resources are not spent investigating poor quality material, and to prove that the structures are scalable to mass production levels.

List of Figures

1.1	Sketch of attenuation over distance for a standard optical fibre showing the short-wavelength datacoms region (850 nm), and the longer-wavelength telecoms bands.[3]	2
2.1	A typical interface between two layers of complex refractive index n_m explaining the electric field propagation notation in this work.	7
2.2	Propagation of the electric field components through a full system of N layers and $N + 1$ interfaces.	11
2.3	Top: The simulated transmittance of a transparent 350 μm GaAs substrate in air with no corrections for incoherence. Bottom: The same substrate corrected for incoherent reflections inside the thick material.	15
2.4	(a) The simulated reflectance of an example GaAs/AlAs 1550 nm resonator with an estimated AlAs cavity thickness of 200 nm showing the Fabry-Perot dip at 1498 nm. (b) The simulated reflectance of the same resonator after the TFCalc optimisation of the cavity thickness, with the Fabry-Perot dip now at the correct (1550 nm) wavelength.	17
2.5	TFCalc window for assigning the sensitivity parameters to the model. Both layer thickness and refractive index can be varied, with distribution type determining whether the values are varied depending on a fixed uniform value, or by a normal distribution of thicknesses within the range set by the user. The type of variation can be a relative percentage, or by a fixed thickness. The number of trials can be set, as well as the type of Monte Carlo analysis to run. A worst-possible analysis will set all parameters as far from specification as possible within the set parameters to determine the outcome.	18

2.6	(a:)The simulated reflectance from figure 2.4(b) after 1000 randomised thickness variation trials using a uniform distribution of $\pm 5\%$. The red lines show the superposition of every trial. (b:) An identical trial performed on a design with a much stronger resonance due to a larger number of DBR repeats on either side of the cavity.	19
2.7	Schematic showing the primary components of a GaAs - $\text{Al}_x\text{Ga}_{1-x}\text{As}$ VCSEL	20
2.8	Schematic showing paths <i>a</i> and <i>b</i> travelling through a structure with two layers on a substrate, where $n_1 = n_s > n_2 > n_0$. All interfaces produce a reflected and transmitted component, so other paths through the structure are neglected for this example. Additionally, the paths are drawn at an angle for clarity, all paths are normal to the surface of the structure. . . .	21
2.9	Calculated peak reflectance of a GaAs - $\text{Al}_{0.9}\text{Ga}_{0.1}\text{As}$ DBR with an increasing number of quarter-wave pairs. The inset shows a zoomed view of the high (greater than 99%) reflectivity behaviour as the number of repeats increases.	24
2.10	Simulated reflectance spectra of a GaAs - $\text{Al}_{0.9}\text{Ga}_{0.1}\text{As}$ DBR with an increasing number of quarter-wave pairs.	25
2.11	Digital-monolayer approximation of the graded interface for a $\text{Al}_{0.12}\text{Ga}_{0.88}\text{As}$ - $\text{Al}_{0.9}\text{Ga}_{0.1}\text{As}$ DBR showing the changes in composition and refractive index.[30, 31, 32]	26
2.12	(a:) A schematic of the type-II GaAs - GaSb - GaAs structure showing the confined holes and unconfined electrons. (b:) Typical room-temperature LED emission from a QR active region measured by P. Hodgson.	27
2.13	Left: Overlay of the normalised electric field profile and the refractive index profile of the cavity inside a simulated VCSEL at a target wavelength of 1270 nm. Right: The modelled transmittance spectrum of the VCSEL containing the optimised cavity.	28
3.1	Schematic of a spectrophotometer.	31
3.2	Left: Cary 500 sample chamber showing the parallel sample and reference beam paths. Right: Sample chamber with solid state sample holder fitted. a: Sample holder arm. b: Sample beam aperture plate. c: Reference beam aperture plate. d: Adjustable mount for sample arm (with optional motorisation).	32

- 3.3 An integrating sphere collecting reflected light from a sample with **a**: all components included and **b**: the specular component removed thus collecting only the diffuse reflections. 33
- 3.4 **Left**: the integrating sphere with cover removed, showing the reflective coating and access ports. **Right**: The sphere with cover in place, showing the port used for measurements. 34
- 3.5 **(a)**: The flat calibration standard used to calibrate for diffuse samples. **(b)**: The protruding calibration standard used to emulate highly specular samples. **(c)**: The flat calibration standard in position showing how high-angle reflections are lost to the sample port wall. **(d)**: The protruding standard allows all of the reflected light to be collected, thus behaving more as a specular surface. 35
- 3.6 Automated sample mapper compatible with the Cary 5000's rail mounting system produced in-house at Lancaster University. The sample arm mount (circled), allows for the use of machined or 3D printed parts to suit the sample being measured. 36
- 3.7 **(a)**: An example peak detection from a calibration sample showing the maximum value of the transmittance. **(b)**: A rejected scan from the same wafer map, due to the range being smaller than some pre-set value. In this case the low amplitude is due to the sample beam clipping the edge of the wafer. 37
- 3.8 An example wafer map of the sample in figure 3.7 37
- 3.9 **Top**: An example VCSEL transmission spectrum with easily visible stop-band and cavity resonance. **Bottom**: The derivative of the same spectrum, showing the section of near-zero differential 38
- 3.10 **Top**: An example VCSEL transmission spectrum with misaligned stop-bands. **Bottom**: The derivative of the same spectrum, showing two sections of near-zero differential, with multiple peaks between them. . . . 39
- 3.11 A basic process monitoring setup utilizing a viewport on the chamber to measure the interference generated by the sample. 40
- 3.12 An example of the ICP reflection intensity vs time measurement showing the periodic nature of the DBR sample being etched. 40
- 3.13 A screen shot of the implemented etch simulation software showing an example DBR structure similar to the one in figure 3.12. 42

- 4.1 Diagram of the BEXP process showing the angled sample, mechanically polished to some shallow angle θ , serving to broaden the cross-section and distance the layers of interest from the effects of the mask during Ar-ion milling. 45
- 4.2 Composite AFM image of a cross-sectioned VCSEL prepared using BEXP clearly showing the upper DBR, cavity region, and lower DBR. 45
- 4.3 A schematic of the propagation of light within a thick substrate. With incident light of intensity I_0 , reflected and transmitted components R_i and T_i , respectively, and the upwards and downwards internally propagating components P_{U_i} and P_{D_i} , respectively. (Paths are angled for clarity, all components are normal to the surface.) 47
- 4.4 A simplified schematic of the MS-SIMS tool's energy and mass selectors. **(a)** is the electrostatic sector, where the radius of curvature r_a depends on the ion kinetic energy E_I and the electric field $|\vec{E}|$. **(b)** is the magnetic sector, where ions enter with selected energy E_I , so that the radius of curvature becomes dependant on the mass m and magnetic field strength B 50
- 4.5 A simplified schematic of an example ToF-SIMS mass spectrometer section. The ejected ions are accelerated by an electric field into the flight region. The ions are then redirected and energy-separated by a reflectron before hitting the detector. 52
- 4.6 A simplified schematic of an example XPS system. The energy of the ejected photoelectrons is dependent on the element and orbital they were released from. The ion beam sputters the surface while the X-ray beam is focused at the bottom of the etch crater to create a depth-based measurement. 53
- 5.1 A schematic of the structure of the DBR, where layers A are GaAs with a target thickness of 115.0 nm and layers B nominally consist of $\text{Al}_{0.9}\text{Ga}_{0.1}\text{As}$ with a target thickness of 130.7 nm. 57
- 5.2 Measured and simulated (designed) transmission of the calibration sample incorporating a transparent substrate and backside reflection. 57
- 5.3 AFM image of the cross-sectioned sample showing clear layers and interfaces. 58

5.4	Updated model using the layer thicknesses from table 5.1 compared to the measured transmission. The shaded area marks the uncertainty in the model.	58
5.5	(a) Measured transmittance of three GaAs substrates with different doping types. (b) Calculated extinction coefficients of the GaAs wafers as a function of wavelength.	60
5.6	The shaded areas indicate the range of possible k values for: (a) n doped (Si), (b) undoped, and (c) p doped (Zn).	61
5.7	An up-to-date model of the short-period characterisation sample showing clear agreement with the measured transmission. The shaded region represents the cumulative error in the model.	62
5.8	Depth profile performed using magnetic-sector SIMS with the top layer on the left and the substrate on the right.	63
5.9	Top: An example transmission spectrum from the centre of the sample wafer showing the transmission peak at around 1395 nm. Bottom A map of the transmission peak's wavelength in respect to the position on the sample wafer.	66
5.10	MS-SIMS alloy percentage for aluminium and gallium against the sputtering time. Actual depth in the device is not stated as the sputtering rate varies by material and is not accurately known.	67
5.11	Sputter time for each layer of the staircase sample analysed using MS-SIMS, with the surface on the left and the substrate on the right.	69
5.12	ToF-SIMS alloy percentage for aluminium and gallium against the sputtering time. Actual depth in the device is not stated as the sputtering rate varies by material and is not accurately known.	70
5.13	Sputter time for each layer of the staircase sample analysed using ToF-SIMS, with the surface on the left and the substrate on the right.	71
5.14	XPS alloy percentage for aluminium and gallium against the etch time. Actual depth in the device is not stated as the sputtering rate varies by material and is not accurately known.	72
5.15	Top: The atomic percentages of gallium, aluminium, and arsenic for the first 12 $\text{Al}_x\text{Ga}_{1-x}\text{As}$ layers in the sample with empty symbols showing the desired percentage. Bottom: SEM image and 2D maps of some of the sample's upper layers showing elemental concentration	74

5.16	Top: 2D elemental maps showing lower layers in the device, as well as contamination due to sputtered copper. Bottom: graph of atomic percentages showing the copper contamination and corresponding variation in arsenic concentration.	75
5.17	Direct comparison of the measured aluminium content of each of the $\text{Al}_x\text{Ga}_{1-x}\text{As}$ layers, by all four different techniques.	76
6.1	A diagram of the first version of the SPLED active region (not to scale) showing the GaSb quantum ring layer embedded within the GaAs structure	80
6.2	A diagram of the second version of the SPLED active region (not to scale) showing the quantum dot layer embedded within the $\text{Al}_{0.6}\text{Ga}_{0.4}\text{As}$ structure below the GaSb quantum ring light-generating layer.	81
6.3	(a): Design 1 band diagram showing the triangle well confined state and carrier tunnelling. (b): Design 2 band diagram showing dual barrier structure and GaAs quantum dot. The light emitting region is still a GaSb QR structure to the right of the barrier structure, and is not shown.	81
6.4	Top: Refractive index profile of the Design 1 cavity region with simulated electric field profile centred on the quantum ring region. Bottom: Simulated transmittance spectrum of the Design 1 SPLED with stop-band and resonance both centred on 1550 nm.	83
6.5	Top: An example refractive Index profile of the Design 2.1 cavity region with simulated electric field profile centred on the quantum rings. Bottom: Example simulated transmittance spectrum of the Design 2.1 SPLED with stop-band and resonance both centred on 1550 nm.	85
6.6	The measured transmission spectra of the three samples compared to the ideal (simulated) transmission, a: sample 1.1 ($d = 15$ nm), b: sample 1.2 ($d = 20$ nm), c: sample 1.3 ($d = 25$ nm).	86
6.7	Transmission model of sample 1.2 updated with BEXP layer thicknesses from table 6.4 compared to the measurement.	87
6.8	Low-resolution wafer map of a fragment (1/8th of a wafer) of sample 1.2 showing cavity peak wavelength across the sample.	88
6.9	Top: Aluminium depth profile of a SPLED showing the target Al fraction. Bottom: Zoomed view of the upper DBR and cavity region.	89
6.10	Top: Transmission spectrum of sample 2.1. Bottom: Transmission spectrum of sample 2.2.	90

6.11	Top: Transmission spectrum of sample 2.3. Bottom: Transmission spectrum of sample 2.4.	91
6.12	Comparison of the measured vs the simulated transmission incorporating the measured cross-section data.	92
6.13	Wavelength of cavity resonance map of sample 2.4 on a quarter wafer of unprocessed material.	93
6.14	I-V profile of a processed device from sample 1.2, with a turn-on voltage of around 2 V.	93
6.15	The room-temperature emission of one of the sample 1.2 SPLEDs compared to the reflectance spectrum. Inset: An optical microscope image of a typical processed device, with a mesa diameter of 200 μm	94
6.16	(a): The I-V characteristics of one of the sample 2.3 SPLEDs. (b): The emission of the same sample 2.3 device at room temperature, with a bias voltage of 8.2 V.	95
7.1	Upper: The simulated electric field profile overlaid with the refractive index at the target wavelength of 1350 nm. Lower: The simulated transmittance spectrum of the target structure, showing the cavity resonance at the target wavelength.	99
7.2	Upper: The measured transmittance of piece 1 of the VCSEL compared to the modelled spectrum of the ideal structure showing a shift to shorter wavelengths. Lower: Zoomed cavity transmittance of various small pieces of sample (1-5), where the position on the original wafer is unknown.	100
7.3	A composite AFM image showing a cross-section of the full device. The dark layers are the $\text{Al}_x\text{Ga}_{1-x}\text{As}$ with the darkest layers inside the cavity being $\text{Al}_{0.9}\text{Ga}_{0.1}\text{As}$ oxidation candidate layers.	100
7.4	The updated model comprised of the full BEXP data compared to the measured transmittance.	101
7.5	An XPS depth profile of the VCSEL structure shown in figure 7.3. The profile stops partway into the lower DBR due to time constraints and layer mixing.	102
7.6	An example I-V curve from a 200 μm diameter device, showing clear diode behaviour and a knee voltage of 2.3 V.	103

7.7	Room temperature 30 mA emission of a 200 μm diameter VCSEL device showing resonance at 1330 nm and a side emission around 1230 nm. The device was operated at 100 Hz with a 10 % duty cycle.	104
7.8	Simulated transmittances of the proposed lower DBR designs with the aim of covering the majority of the telecoms region.	106
7.9	Electric field simulation centred around the active region, with the graded lower DBR on the right and the square upper DBR on the left. (a) has a buffer optical thickness equivalent to a quarter wavelength and (b) has a buffer optical thickness equivalent to a half wavelength.	107
7.10	Optical transmittance simulation of the design in table 7.4 showing a strong resonance at the target wavelength.	108
7.11	Measured transmittance of a sample 1270 nm DBR grown at IQE compared to the simulated transmittance of the design.	109
7.12	Top: Transmittance spectrum of the test growth compared to the modelled transmittance of the ideal structure. Bottom: Zoomed view of the cavity peak showing good positioning but poor resonance strength.	110
7.13	Transmittance spectrum of the growth incorporating quantum rings compared to the modelled transmittance of the ideal structure. No cavity resonance is distinguishable from the noise floor.	111
7.14	Transmittance spectrum of the growth incorporating quantum rings compared to the modelled transmittance of the ideal structure using BEXP measured layer thicknesses.	111
7.15	Top: Transmittance spectrum of the growth with 24 upper DBR repeats compared to the modelled transmittance of the ideal structure. Bottom: Zoomed view of the stop-band showing a small transmittance peak roughly aligned with the edge of the modelled stop-band.	112
7.16	The thickness of each layer of the upper DBR of the device in figure 7.15 showing the layer variation over the duration of the growth. The repeats are in order of growth, i.e. layer 1 is next to the active region and 24 is at the surface.	114
7.17	Updated modelled transmittance of the structure using BEXP individual layer thicknesses alongside the measured transmittance of the sample.	114

- 7.18 **Top:** Transmittance spectrum of the growth with 20 upper DBR repeats compared to the modelled transmittance of the ideal structure. **Bottom:** Zoomed view of the stop-band showing a small transmittance peak at around 1250 nm. 115
- 7.19 Transmittance of samples a-c compared to the simulated structure from table 7.7. 117
- 7.20 A zoomed view of the transmittance of samples a-c compared to the simulated structure from table 7.7. Sample a has an elevated baseline, likely due to a calibration issue with the spectrophotometer. 118
- 7.21 Optical microscope images of the processed VCSEL devices with mesa sizes of 29 μm (**left**) and 90 μm (**right**). 118
- 7.22 An example I-V curve from a 90 μm diameter device with extremely high resistance. Reverse breakdown begins to occur at -20 V 119
- 7.23 **Top:** 1 mA emission of a 90 μm diameter device operating around 1260 nm. **Bottom:** 6 mA emission from the same device, showing increased intensity, particularly outside the stop-band region. 120
- 7.24 ECV depth profile of the sample as measured by IQE showing the carrier concentration through the upper DBR. The GaAs layers, **a**, have a target doping of $2.00 \times 10^{18} \text{ cm}^{-3}$, and the $\text{Al}_{0.9}\text{Ga}_{0.1}\text{As}$, **b**, have a target doping of $4.00 \times 10^{18} \text{ cm}^{-3}$ 121
- 7.25 Measured transmittance of the VCSEL structure with 30 lower DBR repeats and 15 upper repeats compared to the simulated design. 121
- 7.26 Measured transmittance of the repeated VCSEL structure with 30 lower DBR repeats and 15 upper repeats compared to the simulated design. The specification is identical to the sample in figure 7.25. 122
- 7.27 An example I-V curve from a 90 μm diameter device, with a generally low resistance. 122
- 7.28 The emission of a processed Mk 3 device with a drive current of 50 mA. The device failed after the measurement was taken. 123
- 7.29 Schematic of the proposed mesa definition for the Mk 4 devices. The first 5 DBR repeats after the cavity are doped, providing the upper contacting site. The rest of the upper DBR is undoped, providing a low-absorption section of the device. 123

7.30	Simulated electric field profile of the design outlined in table 7.8 showing clear symmetry and alignment with the quantum ring layers.	124
7.31	Top: Transmittance spectrum of the growth from table 7.8 with 24 upper repeats compared to the modelled transmittance of the ideal structure. Bottom: Zoomed view of the stop-band showing a transmittance peak at around 1270 nm.	125
7.32	Cavity peak amplitude with respect to position across the wafer showing up a 15 nm variation towards the edge of the wafer.	126
7.33	Transmittance spectrum of the growth from table 7.8 with 15 upper repeats compared to the modelled transmittance of the ideal structure. . . .	126
7.34	An example I-V curve from a 200 μm diameter device.	127

List of Tables

5.1	Table comparing target layer thicknesses to those acquired using BEXP.	58
5.2	Stated batch specifications of the wafers used in this calibration as provided by Wafer Technologies Ltd.	59
5.3	Batch thickness uncertainty (table 5.2) and the corresponding average uncertainty in the extinction coefficient for each wafer as calculated from the data in figure 5.6. Percentage error uses the average k value and uncertainty for each substrate.	61
5.4	The target structure to be used in comparing the methods of compositional characterisation. GaAs layers between the $\text{Al}_x\text{Ga}_{1-x}\text{As}$ layers provide a buffer to prevent mixing, as well as make it easier to view the layers of interest in a depth profile.	65
5.5	Averaged MS-SIMS results compared to target values.	68
5.6	Averaged ToF-SIMS results compared to target values.	68
5.7	Averaged XPS results compared to target values.	73
5.8	Table of measured aluminium fraction for each method of analysis.	73
6.1	Initial resonant-cavity SPLED structure for Design 1 with variable lower i-n barrier region.	82
6.2	The Design 2 resonant-cavity SPLED design with quantum dot-based electron generation region.	84
6.3	The parameters for each of the 4 Design 2 devices.	84
6.4	The thicknesses of sample 1.2 as measured using BEXP. For layers with multiple repeats, thicknesses shown are the average of every repeated layer.	87
6.5	The averaged thicknesses of sample 2.2 as measured using BEXP. For layers with multiple repeats, thicknesses shown are the average of every repeated layer.	92

7.1	VCSEL structure for the Mk1 design grown entirely at Lancaster.	98
7.2	The averaged thicknesses of the Mk1 VCSEL as measured using BEXP.	101
7.3	One of the lower DBR designs to be grown by MOVPE with graded interfaces and a half layer GaAs cap. The target centre wavelength for this structure was 1270 nm.	105
7.4	Design of the MBE section of the VCSEL growth, with 29 upper repeats, a half-wavelength cavity, and 5 sets of quantum rings. A 30 nm $\text{Al}_{0.97}\text{Ga}_{0.03}\text{As}$ layer is included so that an oxide aperture may be incorporated when processed.	108
7.5	The averaged thicknesses of the sample in figure 7.13 as measured using BEXP.	109
7.6	The averaged thicknesses of the sample in figure 7.15 as measured using BEXP.	113
7.7	Design of the MBE section of the 1270 nm VCSEL growth, with 20 upper repeats, a half-wavelength cavity, and 5 sets of quantum rings. The upper spacer has been replaced with a solid $\text{Al}_{0.97}\text{Ga}_{0.03}\text{As}$ layer and a thin marker layer has been added to allow for the start of the growth to be identified in a cross-section.	116
7.8	VCSEL structure for the Mk4 design to be produced entirely at Lancaster. 30 lower DBR repeats is combined with either 24 or 15 upper repeats to assess both a high and low reflectivity design. * To reduce the resistance and optical absorption of the upper DBR, the goal is to etch the upper DBR mesa so that only the ten layers closest to the cavity are contacted. These ten layers will be doped, while the rest remain intrinsic.	124

Bibliography

- [1] Haruhisa Soda, Kenichi Iga, Chiyuki Kitahara, and Yasuharu Suematsu. GaInAsP/InP surface emitting injection lasers. *Japanese Journal of Applied Physics*, 18(12):2329–2330, December 1979. doi: 10.1143/jjap.18.2329. URL <https://doi.org/10.1143/jjap.18.2329>.
- [2] Preeti Wadhvani and Yadav Shubhangi. Vertical-cavity surface-emitting lasers (VCSEL) market size. Technical Report GMI4920, Global Market Insights, Jan 2021.
- [3] Marie Wandel. Attenuation in silica-based optical fibers. *Dept. Photon. Eng., Ph. D. thesis, Tech. Univ. Denmark, Denmark*, 2005.
- [4] Building digital UK, 2020. URL <https://www.gov.uk/guidance/building-digital-uk>.
- [5] ITU recommendation G.9807.1, 10-Gigabit capable symmetric passive optical network (XGS-PON), 2016. URL <https://www.itu.int/rec/T-REC-G.9807.1-202010-P!Amd2>.
- [6] K. Iga, F. Koyama, and S. Kinoshita. Surface emitting semiconductor lasers. *IEEE Journal of Quantum Electronics*, 24(9):1845–1855, September 1988. doi: 10.1109/3.7126. URL <https://doi.org/10.1109/3.7126>.
- [7] Y. Hayashi, T. Mukaiharu, N. Hatori, N. Ohnoki, A. Matsutani, F. Koyama, and K. Iga. Lasing characteristics of low-threshold oxide confinement InGaAs-GaAlAs vertical-cavity surface-emitting lasers. *IEEE Photonics Technology Letters*, 7(11):1234–1236, November 1995. doi: 10.1109/68.473456. URL <https://doi.org/10.1109/68.473456>.
- [8] D.L. Huffaker, D.G. Deppe, and J. Shin. Low threshold half-wave vertical-cavity lasers. *Electronics Letters*, 30(23):1946–1947, November 1994. doi: 10.1049/el:19941348. URL <https://doi.org/10.1049/el:19941348>.

- [9] G.M. Yang, M.H. MacDougal, and P.D. Dapkus. Ultralow threshold current vertical-cavity surface-emitting lasers obtained with selective oxidation. *Electronics Letters*, 31(11):886–888, May 1995. doi: 10.1049/el:19950610. URL <https://doi.org/10.1049/el:19950610>.
- [10] M.H. MacDougal, P.D. Dapkus, V. Pudikov, Hanmin Zhao, and Gye Mo Yang. Ultralow threshold current vertical-cavity surface-emitting lasers with AlAs oxide-GaAs distributed Bragg reflectors. *IEEE Photonics Technology Letters*, 7(3):229–231, March 1995. doi: 10.1109/68.372729. URL <https://doi.org/10.1109/68.372729>.
- [11] Jonghyun Park, Taeyong Kim, Sung-Han Kim, and Sang-Bae Kim. A passively aligned VCSEL transmitter operating at fixed current over a wide temperature range. *Opt. Express*, 17(7):5147–5152, Mar 2009. doi: 10.1364/OE.17.005147. URL <http://www.opticsexpress.org/abstract.cfm?URI=oe-17-7-5147>.
- [12] K.L. Lear, K.D. Choquette, R.P. Schneider, S.P. Kilcoyne, and K.M. Geib. Selectively oxidised vertical cavity surface emitting lasers with 50% power conversion efficiency. *Electronics Letters*, 31(3):208–209, February 1995. doi: 10.1049/el:19950125. URL <https://doi.org/10.1049/el:19950125>.
- [13] Ewa Simpanen, Johan S. Gustavsson, Anders Larsson, Magnus Karlsson, Wayne V. Sorin, Sagi Mathai, Michael R. Tan, and Scott R. Bickham. 1060 nm single-mode VCSEL and single-mode fiber links for long-reach optical interconnects. *Journal of Lightwave Technology*, 37(13):2963–2969, July 2019. doi: 10.1109/jlt.2019.2908249. URL <https://doi.org/10.1109/jlt.2019.2908249>.
- [14] W. Hofmann, P. Moser, P. Wolf, A. Mutig, M. Kroh, and D. Bimberg. 44 Gbs⁻¹ VCSEL for optical interconnects. In *Optical Fiber Communication Conference/National Fiber Optic Engineers Conference 2011*. OSA, 2011. doi: 10.1364/nfoec.2011.pdpc5. URL <https://doi.org/10.1364/nfoec.2011.pdpc5>.
- [15] Alex Mutig and Dieter Bimberg. Progress on high-speed 980 nm VCSELs for short-reach optical interconnects. *Advances in Optical Technologies*, 2011:1–15, September 2011. doi: 10.1155/2011/290508. URL <https://doi.org/10.1155/2011/290508>.
- [16] H. E. Li and Kenichi Iga. *Vertical-cavity surface-emitting laser devices*. Springer, 2011.

- [17] C Jung, R King, R Jäger, M Grabherr, F Eberhard, R Michalzik, and K J Ebeling. Highly efficient oxide-confined VCSEL arrays for parallel optical interconnects. *Journal of Optics A: Pure and Applied Optics*, 1(2):272–275, January 1999. doi: 10.1088/1464-4258/1/2/030. URL <https://doi.org/10.1088/1464-4258/1/2/030>.
- [18] Anjin Liu, Philip Wolf, James A. Lott, and Dieter Bimberg. Vertical-cavity surface-emitting lasers for data communication and sensing. *Photonics Research*, 7(2):121, January 2019. doi: 10.1364/prj.7.000121. URL <https://doi.org/10.1364/prj.7.000121>.
- [19] K. Nakahara, T. Tsuchiya, T. Kitatani, K. Shinoda, T. Taniguchi, T. Kikawa, M. Aoki, and M. Mukaikubo. 40 Gbs⁻¹ direct modulation with high extinction ratio operation of 1.3 μm InGaAlAs multiquantum well ridge waveguide distributed feedback lasers. *IEEE Photonics Technology Letters*, 19(19):1436–1438, October 2007. doi: 10.1109/lpt.2007.903530. URL <https://doi.org/10.1109/lpt.2007.903530>.
- [20] Koichiro Adachi, Kazunori Shinoda, Takeshi Kitatani, Toshihiko Fukamachi, Yasunobu Matsuoka, Toshiki Sugawara, and Shinji Tsuji. 25 Gbs⁻¹ multichannel 1.3 μm surface-emitting lens-integrated DFB laser arrays. *Journal of Lightwave Technology*, 29(19):2899–2905, October 2011. doi: 10.1109/jlt.2011.2163814. URL <https://doi.org/10.1109/jlt.2011.2163814>.
- [21] R. Jager, M. Grabherr, C. Jung, R. Michalzik, G. Reiner, B. Weigl, and K.J. Ebeling. 57% wallplug efficiency oxide-confined 850 nm wavelength GaAs VCSELs. *Electronics Letters*, 33(4):330, 1997. doi: 10.1049/el:19970193. URL <https://doi.org/10.1049/el:19970193>.
- [22] C.C. Wu, K. Tai, T.C. Huang, and K.F. Huang. Reliability studies of gain-guided 0.85 μm GaAs/AlGaAs quantum well surface emitting lasers. *IEEE Photonics Technology Letters*, 6(1):37–39, January 1994. doi: 10.1109/68.265882. URL <https://doi.org/10.1109/68.265882>.
- [23] Y.H. Chang, P.C. Peng, W.K. Tsai, G. Lin, FangI Lai, R.S. Hsiao, H.P. Yang, H.C. Yu, K.F. Lin, J.Y. Chi, S.C. Wang, and H.C. Kuo. Single-mode monolithic quantum-dot VCSEL in 1.3 μm with sidemode suppression ratio over 30 dB. *IEEE Photonics Technology Letters*, 18(7):847–849, April 2006. doi: 10.1109/lpt.2006.871831. URL <https://doi.org/10.1109/lpt.2006.871831>.

- [24] P. D. Hodgson, M. Hayne, A. J. Robson, Q. D. Zhuang, and L. Danos. GaSb quantum rings in GaAs/Al_xGa_{1-x}As quantum wells. *Journal of Applied Physics*, 119(4):044305, January 2016. doi: 10.1063/1.4940880. URL <https://doi.org/10.1063/1.4940880>.
- [25] Max Born. *Principles of optics; electromagnetic theory of propagation, interference, and diffraction of light*,. Pergamon Press, Oxford, New York, 5th ed. edition, 1975. ISBN 0080180183.
- [26] O. S. Heavens. *Optical Properties of Thin Solid Films (Dover Books on Physics)*. Dover Publications, feb 2011. ISBN 0486669246.
- [27] P. Yeh. *Optical Waves in Layered Media*. Wiley-Interscience, mar 2005. ISBN 0471731927.
- [28] C. L. Mitsas and D. I. Siapkas. Generalized matrix method for analysis of coherent and incoherent reflectance and transmittance of multilayer structures with rough surfaces, interfaces, and finite substrates. *Applied Optics*, 34(10):1678, April 1995. doi: 10.1364/ao.34.001678. URL <https://doi.org/10.1364/ao.34.001678>.
- [29] Charalambos C. Katsidis and Dimitrios I. Siapkas. General transfer-matrix method for optical multilayer systems with coherent, partially coherent, and incoherent interference. *Appl. Opt.*, 41(19):3978–3987, Jul 2002. doi: 10.1364/AO.41.003978. URL <http://ao.osa.org/abstract.cfm?URI=ao-41-19-3978>.
- [30] S. Adachi. GaAs, AlAs, and Al_xGa_{1-x}As: Material parameters for use in research and device applications. *Journal of Applied Physics*, 58(3):R1–R29, 1985. doi: 10.1063/1.336070. URL <https://doi.org/10.1063/1.336070>.
- [31] S. Adachi. Optical properties of Al_xGa_{1-x}As alloys. *Phys. Rev. B*, 38:12345–12352, Dec 1988. doi: 10.1103/PhysRevB.38.12345. URL <https://link.aps.org/doi/10.1103/PhysRevB.38.12345>.
- [32] D. E. Aspnes, S. M. Kelso, R. A. Logan, and R. Bhat. Optical properties of Al_xGa_{1-x}As. *Journal of Applied Physics*, 60(2):754–767, 1986. doi: 10.1063/1.337426. URL <https://doi.org/10.1063/1.337426>.
- [33] J.A. Lott, N.N. Ledentsov, V.M. Ustinov, N.A. Maleev, A.E. Zhukov, A.R. Kovsh, M.V. Maximov, B.V. Volovik, Zh.I. Alferov, and D. Bimberg. InAs-InGaAs quantum dot VCSELs on GaAs substrates emitting at 1.3 μm. *Electronics Letters*, 36

- (16):1384, 2000. doi: 10.1049/el:20000988. URL <https://doi.org/10.1049/el:20000988>.
- [34] M.C. Larson, M. Kondow, T. Kitatani, K. Nakahara, K. Tamura, H. Inoue, and K. Uomi. GaInNAs-GaAs long-wavelength vertical-cavity surface-emitting laser diodes. *IEEE Photonics Technology Letters*, 10(2):188–190, February 1998. doi: 10.1109/68.655353. URL <https://doi.org/10.1109/68.655353>.
- [35] R. A. Mair, J. Y. Lin, H. X. Jiang, E. D. Jones, A. A. Allerman, and S. R. Kurtz. Time-resolved photoluminescence studies of $\text{In}_x\text{Ga}_{1-x}\text{As}_{1-y}\text{N}_y$. *Applied Physics Letters*, 76(2):188–190, January 2000. doi: 10.1063/1.125698. URL <https://doi.org/10.1063/1.125698>.
- [36] M. Ahmad Kamarudin, M. Hayne, R. J. Young, Q. D. Zhuang, T. Ben, and S. I. Molina. Tuning the properties of exciton complexes in self-assembled GaSb/GaAs quantum rings. *Phys. Rev. B*, 83:115311, Mar 2011. doi: 10.1103/PhysRevB.83.115311. URL <https://link.aps.org/doi/10.1103/PhysRevB.83.115311>.
- [37] O Madelung. *Semiconductors : Data Handbook*. Springer Berlin Heidelberg, Berlin, Heidelberg, 2004. ISBN 978-3-642-18865-7.
- [38] Shigeki Kobayashi, Chao Jiang, Takuya Kawazu, and Hiroyuki Sakaki. Self-assembled growth of GaSb type II quantum ring structures. *Japanese Journal of Applied Physics*, 43(No. 5B):L662–L664, apr 2004. doi: 10.1143/jjap.43.l662. URL <https://doi.org/10.1143%2Fjjap.43.l662>.
- [39] R. Timm, H. Eisele, A. Lenz, L. Ivanova, G. Balakrishnan, D. L. Huffaker, and M. Dähne. Self-organized formation of GaSb/GaAs quantum rings. *Phys. Rev. Lett.*, 101:256101, Dec 2008. doi: 10.1103/PhysRevLett.101.256101. URL <https://link.aps.org/doi/10.1103/PhysRevLett.101.256101>.
- [40] E. P. Smakman, J. K. Garleff, R. J. Young, M. Hayne, P. Rambabu, and P. M. Koenraad. GaSb/GaAs quantum dot formation and demolition studied with cross-sectional scanning tunneling microscopy. *Applied Physics Letters*, 100(14):142116, 2012. doi: 10.1063/1.3701614. URL <https://doi.org/10.1063/1.3701614>.
- [41] T. Nowozin, L. Bonato, A. Högnér, A. Wiengarten, D. Bimberg, Wei-Hsun Lin, Shih-Yen Lin, C. J. Reyner, Baolai L. Liang, and D. L. Huffaker. 800 meV localization energy in GaSb/GaAs/ $\text{Al}_{0.3}\text{Ga}_{0.7}\text{As}$ quantum dots. *Applied Physics*

- Letters*, 102(5):052115, February 2013. doi: 10.1063/1.4791678. URL <https://doi.org/10.1063/1.4791678>.
- [42] R. J. Young, E. P. Smakman, A. M. Sanchez, P. Hodgson, P. M. Koenraad, and M. Hayne. Optical observation of single-carrier charging in type-II quantum ring ensembles. *Applied Physics Letters*, 100(8):082104, February 2012. doi: 10.1063/1.3688037. URL <https://doi.org/10.1063/1.3688037>.
- [43] D. M. Thomas, R. J. Hunt, N. D. Drummond, and M. Hayne. Binding energies of excitonic complexes in type-II quantum rings from diffusion quantum Monte Carlo calculations. *Physical Review B*, 99(11), March 2019. doi: 10.1103/physrevb.99.115306. URL <https://doi.org/10.1103/physrevb.99.115306>.
- [44] P. D. Hodgson, T. J. Wilson, A. J. Robson, Q. Zhuang, K. Kennedy, S. Kumar, S. McDougall, and Manus Hayne. Self-assembled GaSb quantum rings for >1200 nm light-emitting diodes and vertical-cavity surface-emitting lasers on GaAs substrates. *Light: Science and Applications*, February 2021.
- [45] Chih-Hsien Cheng, Chih-Chiang Shen, Hsuan-Yun Kao, Dan-Hua Hsieh, Huai-Yung Wang, Yen-Wei Yeh, Yun-Ting Lu, Sung-Wen Huang Chen, Cheng-Ting Tsai, Yu-Chieh Chi, Tsung Sheng Kao, Chao-Hsin Wu, Hao-Chung Kuo, Po-Tsung Lee, and Gong-Ru Lin. 850/940 nm VCSEL for optical communication and 3D sensing. *Opto-Electronic Advances*, 1(3):18000501–18000511, 2018. doi: 10.29026/oea.2018.180005. URL <https://doi.org/10.29026/oea.2018.180005>.
- [46] Rainer Michalzik. *VCSELs fundamentals, technology and applications of vertical-cavity surface-emitting lasers*. Springer, 2013.
- [47] Y. Ohiso, T. Sato, T. Shindo, and H. Matsuzaki. 1.3 μm buried-heterostructure VCSELs with GaAs/algaas metamorphic DBRs grown by MOCVD. *Electronics Letters*, 56(2):95–97, 2020. ISSN 0013-5194. doi: 10.1049/el.2019.2958.
- [48] J. B. Héroux, X. Yang, and W. I. Wang. GaInNAs resonant-cavity-enhanced photodetector operating at 1.3 μm . *Applied Physics Letters*, 75(18):2716–2718, November 1999. doi: 10.1063/1.125126. URL <https://doi.org/10.1063/1.125126>.
- [49] P. Moser, J. A. Lott, P. Wolf, G. Larisch, A. Payusov, N. N. Ledentsov, and D. Bimberg. Energy-efficient oxide-confined 850 nm VCSELs for long-distance

- multimode fiber optical interconnects. *IEEE Journal of Selected Topics in Quantum Electronics*, 19(2):7900406–7900406, March 2013. ISSN 1558-4542. doi: 10.1109/JSTQE.2012.2218795.
- [50] N. Haghighi, P. Moser, and J. A. Lott. Power, bandwidth, and efficiency of single VCSELs and small VCSEL arrays. *IEEE Journal of Selected Topics in Quantum Electronics*, 25(6):1–15, Nov 2019. ISSN 1558-4542. doi: 10.1109/JSTQE.2019.2922843.
- [51] S. Jette-Charbonneau, N. Lahoud, R. Charbonneau, G. Mattiussi, and P. Berini. End-facet polishing of surface plasmon waveguides in lithium niobate. *IEEE Transactions on Advanced Packaging*, 31(3):479–483, 2008.
- [52] P Mogilevsky. Preparation of thin ceramic monofilaments for characterization by TEM. *Ultramicroscopy*, 92(3-4):159–164, August 2002. doi: 10.1016/s0304-3991(02)00129-8. URL [https://doi.org/10.1016/s0304-3991\(02\)00129-8](https://doi.org/10.1016/s0304-3991(02)00129-8).
- [53] S Rubanov and P.R Munroe. The application of FIB milling for specimen preparation from crystalline germanium. *Micron*, 35(7):549–556, October 2004. doi: 10.1016/j.micron.2004.03.004. URL <https://doi.org/10.1016/j.micron.2004.03.004>.
- [54] Y. Androussi, T. Benabbas, and A. Lefebvre. Moiré-like fringes in transmission electron microscopy images of coherently strained semiconductor islands. *Ultramicroscopy*, 93(2):161–167, November 2002. doi: 10.1016/s0304-3991(02)00156-0. URL [https://doi.org/10.1016/s0304-3991\(02\)00156-0](https://doi.org/10.1016/s0304-3991(02)00156-0).
- [55] Hideyuki Takahashi, Ayako Sato, Masaru Takakura, Norihisa Mori, Juergen Boerder, Walter Knoll, and John Critchell. A new method of surface preparation for high spatial resolution EPMA/SEM with an argon ion beam. *Microchimica Acta*, 155(1-2):295–300, May 2006. doi: 10.1007/s00604-006-0559-0. URL <https://doi.org/10.1007/s00604-006-0559-0>.
- [56] Omid Mokhtari Amirmajdi, Roya Ashyer-Soltani, Michael Paul Clode, Samjid H. Mannan, Yunqi Wang, Enric Cabruja, and Giulio Pellegrini. Cross-section preparation for solder joints and MEMS device using argon ion beam milling. *IEEE Transactions on Electronics Packaging Manufacturing*, 32(4):265–271, October 2009. doi: 10.1109/tepm.2009.2029344. URL <https://doi.org/10.1109/tepm.2009.2029344>.

- [57] Oleg V. Kolosov and Ilya Grishin. Method for ion beam polishing and polished sample, European Patent EP2537017, 2012.
- [58] O V Kolosov, I Grishin, and R Jones. Material sensitive scanning probe microscopy of subsurface semiconductor nanostructures via beam exit Ar ion polishing. *Nanotechnology*, 22(18):185702, March 2011. doi: 10.1088/0957-4484/22/18/185702. URL <https://doi.org/10.1088/0957-4484/22/18/185702>.
- [59] Alexander J. Robson, Ilya Grishin, Robert J. Young, Ana M. Sanchez, Oleg V. Kolosov, and Manus Hayne. High-accuracy analysis of nanoscale semiconductor layers using beam-exit Ar-ion polishing and scanning probe microscopy. *ACS Applied Materials & Interfaces*, 5(8):3241–3245, April 2013. doi: 10.1021/am400270w. URL <https://doi.org/10.1021/am400270w>.
- [60] Aleksandar D. Rakić and Marian L. Majewski. Modeling the optical dielectric function of GaAs and AlAs: Extension of Adachi’s model. *Journal of Applied Physics*, 80(10):5909–5914, November 1996. doi: 10.1063/1.363586. URL <https://doi.org/10.1063/1.363586>.
- [61] Ralph Stair, William E. Schneider, and John K. Jackson. A new standard of spectral irradiance. *Applied Optics*, 2(11):1151, November 1963. doi: 10.1364/ao.2.001151. URL <https://doi.org/10.1364/ao.2.001151>.
- [62] Axel Donges. The coherence length of black-body radiation. *European Journal of Physics*, 19(3):245–249, May 1998. doi: 10.1088/0143-0807/19/3/006. URL <https://doi.org/10.1088/0143-0807/19/3/006>.
- [63] Olaf Stenzel. *The physics of thin film optical spectra: an introduction*. Number volume 44 in Springer series in surface sciences. Springer, Cham Heidelberg New York Dordrecht London, second edition edition, 2016. ISBN 9783319216027 9783319216010. OCLC: 927525691.
- [64] D. D. Sell, H. C. Casey, and K. W. Wecht. Concentration dependence of the refractive index for n - and p -type GaAs between 1.2 and 1.8 eV. *Journal of Applied Physics*, 45(6):2650–2657, June 1974. doi: 10.1063/1.1663645. URL <https://doi.org/10.1063/1.1663645>.
- [65] K. H. Chang, C. P. Lee, J. S. Wu, D. G. Liu, D. C. Liou, M. H. Wang, L. J. Chen, and Mario A. Marais. Precise determination of aluminum content in AlGaAs.

- Journal of Applied Physics*, 70(9):4877–4882, 1991. doi: 10.1063/1.349030. URL <https://doi.org/10.1063/1.349030>.
- [66] Z. R. Wasilewski, M. M. Dion, D. J. Lockwood, P. Poole, R. W. Streater, and A. J. SpringThorpe. Composition of algaas. *Journal of Applied Physics*, 81(4):1683–1694, 1997. doi: 10.1063/1.364012. URL <https://doi.org/10.1063/1.364012>.
- [67] G. S. Solomon, D. Kirillov, H. C. Chui, and J. S. Harris Jr. Determination of AlAs mole fraction in $\text{Al}_x\text{Ga}_{1-x}\text{As}$ using Raman spectroscopy and x-ray diffraction. *Journal of Vacuum Science & Technology B: Microelectronics and Nanometer Structures Processing, Measurement, and Phenomena*, 12(2):1078–1081, 1994. doi: 10.1116/1.587092. URL <http://avs.scitation.org/doi/abs/10.1116/1.587092>.
- [68] R. Kumar, P. Mukhopadhyay, S. K. Jana, A. Bag, S. Ghosh, S. Das, M. K. Mahata, and D. Biswas. Comprehensive study of AlGaAs/GaAs heterostructures grown by MBE: Structural and compositional analysis. In *2014 IEEE 2nd International Conference on Emerging Electronics (ICEE)*, pages 1–4, Dec 2014. doi: 10.1109/ICEmElec.2014.7151137.
- [69] Bin Gong and Christopher E. Marjo. Quantitative ToF-SIMS depth profiling of a multi-phased III–V semiconductor matrix via the analysis of secondary cluster ions. *Surface and Interface Analysis*, 48(7):422–427, 2016. doi: 10.1002/sia.5928. URL <https://onlinelibrary.wiley.com/doi/abs/10.1002/sia.5928>.
- [70] K. Iltgen, C. Bendel, A. Benninghoven, and E. Niehuis. Optimized time-of-flight secondary ion mass spectroscopy depth profiling with a dual beam technique. *Journal of Vacuum Science & Technology A*, 15(3):460–464, 1997. doi: 10.1116/1.580874. URL <https://doi.org/10.1116/1.580874>.
- [71] S. J. Pearton, U. K. Chakrabarti, W. S. Hobson, and A. P. Kinsella. Reactive ion etching of GaAs, AlGaAs, and GaSb in Cl_2 and SiCl_4 . *Journal of Vacuum Science & Technology B: Microelectronics Processing and Phenomena*, 8(4):607–617, 1990. doi: 10.1116/1.585027. URL <https://avs.scitation.org/doi/abs/10.1116/1.585027>.
- [72] A. Benninghoven. Surface investigation of solids by the statical method of secondary ion mass spectroscopy (SIMS). *Surface Science*, 35:427–457, March 1973. doi: 10.1016/0039-6028(73)90232-x. URL [https://doi.org/10.1016/0039-6028\(73\)90232-x](https://doi.org/10.1016/0039-6028(73)90232-x).

- [73] Y. Gao. A new secondary ion mass spectrometry technique for III-V semiconductor compounds using the molecular ions CsM^+ . *Journal of Applied Physics*, 64(7):3760–3762, 1988. doi: 10.1063/1.341381. URL <https://doi.org/10.1063/1.341381>.
- [74] Agnieszka Priebe, Tianle Xie, Gerhard Bürki, Laszlo Pethö, and Johann Michler. The matrix effect in TOF-SIMS analysis of two-element inorganic thin films. *J. Anal. At. Spectrom.*, 35:1156–1166, 2020. doi: 10.1039/C9JA00428A. URL <http://dx.doi.org/10.1039/C9JA00428A>.
- [75] Bin Gong and Christopher E. Marjo. Quantitative ToF-SIMS depth profiling of a multi-phased III-V semiconductor matrix via the analysis of secondary cluster ions. *Surface and Interface Analysis*, 48(7):422–427, January 2016. doi: 10.1002/sia.5928. URL <https://doi.org/10.1002/sia.5928>.
- [76] John Moulder. *Handbook of x-ray photoelectron spectroscopy : a reference book of standard spectra for identification and interpretation of XPS data*. Physical Electronics Division, Perkin-Elmer Corp, Eden Prairie, Minn, 1992. ISBN 0962702625.
- [77] R. F. Egerton. *Electron energy-loss spectroscopy in the electron microscope*. Springer, New York, 2011. ISBN 978-1-4419-9583-4.
- [78] Jucheol Park, Sung Heo, Jae-Gwan Chung, Heekoo Kim, HyungIk Lee, Kihong Kim, and Gyeong-Su Park. Bandgap measurement of thin dielectric films using monochromated STEM-EELS. *Ultramicroscopy*, 109(9):1183–1188, August 2009. doi: 10.1016/j.ultramic.2009.04.005. URL <https://doi.org/10.1016/j.ultramic.2009.04.005>.
- [79] Charles Cherqui, Niket Thakkar, Guoliang Li, Jon P. Camden, and David J. Masiello. Characterizing localized surface plasmons using electron energy-loss spectroscopy. *Annual Review of Physical Chemistry*, 67(1):331–357, 2016. doi: 10.1146/annurev-physchem-040214-121612. URL <https://doi.org/10.1146/annurev-physchem-040214-121612>. PMID: 27215817.
- [80] Y. F. Lao, A. G. U. Perera, H. L. Wang, J. H. Zhao, Y. J. Jin, and D. H. Zhang. Optical characteristics of p-type GaAs-based semiconductors towards applications in photoemission infrared detectors. *Journal of Applied Physics*, 119(10):105304, March 2016. doi: 10.1063/1.4943591. URL <https://doi.org/10.1063/1.4943591>.
- [81] Alberto Boretti, Lorenzo Rosa, Andrew Mackie, and Stefania Castelletto. Electrically driven quantum light sources. *Advanced Optical Materials*, 3(8):1012–1033,

- March 2015. doi: 10.1002/adom.201500022. URL <https://doi.org/10.1002/adom.201500022>.
- [82] Xing Ding, Yu He, Z.-C. Duan, Niels Gregersen, M.-C. Chen, S. Unsleber, S. Maier, Christian Schneider, Martin Kamp, Sven Höfling, Chao-Yang Lu, and Jian-Wei Pan. On-demand single photons with high extraction efficiency and near-unity indistinguishability from a resonantly driven quantum dot in a micropillar. *Physical Review Letters*, 116(2), January 2016. doi: 10.1103/physrevlett.116.020401. URL <https://doi.org/10.1103/physrevlett.116.020401>.
- [83] Xing Lin, Xingliang Dai, Chaodan Pu, Yunzhou Deng, Yuan Niu, Limin Tong, Wei Fang, Yizheng Jin, and Xiaogang Peng. Electrically-driven single-photon sources based on colloidal quantum dots with near-optimal antibunching at room temperature. *Nature Communications*, 8(1), October 2017. doi: 10.1038/s41467-017-01379-6. URL <https://doi.org/10.1038/s41467-017-01379-6>.
- [84] L. Turyanska, A. Baumgartner, A. Chaggar, A. Patanè, L. Eaves, and M. Henini. Sharp-line electroluminescence from individual quantum dots by resonant tunneling injection of carriers. *Applied Physics Letters*, 89(9):092106, 2006. doi: 10.1063/1.2337540. URL <https://doi.org/10.1063/1.2337540>.
- [85] M. J. Conterio, N. Sköld, D. J. P. Ellis, I. Farrer, D. A. Ritchie, and A. J. Shields. A quantum dot single photon source driven by resonant electrical injection. *Applied Physics Letters*, 103(16):162108, October 2013. doi: 10.1063/1.4825208. URL <https://doi.org/10.1063/1.4825208>.
- [86] T J Wilson, P D Hodgson, A J Robson, C Jackson, B Grew, and M Hayne. A detailed comparison of measured and simulated optical properties of a short-period GaAs/Al_xGa_{1-x}As distributed Bragg reflector. *Semiconductor Science and Technology*, 35(5):055003, March 2020. doi: 10.1088/1361-6641/ab76af. URL <https://doi.org/10.1088/1361-6641/ab76af>.
- [87] M. Grabherr, R. Jager, R. Michalzik, B. Weigl, G. Reiner, and K.J. Ebeling. Efficient single-mode oxide-confined GaAs VCSELs emitting in the 850 nm wavelength regime. *IEEE Photonics Technology Letters*, 9(10):1304–1306, October 1997. doi: 10.1109/68.623244. URL <https://doi.org/10.1109/68.623244>.
- [88] P. Zhou, J. Cheng, C. F. Schaus, S. Z. Sun, K. Zheng, E. Armour, C. Hains, W. Hsin, D. R. Myers, and G. A. Vawter. Low series resistance high-efficiency GaAs/AlGaAs

- vertical-cavity surface-emitting lasers with continuously graded mirrors grown by mocvd. *IEEE Photonics Technology Letters*, 3(7):591–593, 1991. doi: 10.1109/68.87923.
- [89] M.G. Peters, D.B. Young, F.H. Peters, J.W. Scott, B.J. Thibeault, and L.A. Coldren. 17.3% peak wall plug efficiency vertical-cavity surface-emitting lasers using lower barrier mirrors. *IEEE Photonics Technology Letters*, 6(1):31–33, January 1994. doi: 10.1109/68.265880. URL <https://doi.org/10.1109/68.265880>.
- [90] P Blood. Capacitance-voltage profiling and the characterisation of III-V semiconductors using electrolyte barriers. *Semiconductor Science and Technology*, 1(1):7–27, July 1986. doi: 10.1088/0268-1242/1/1/002. URL <https://doi.org/10.1088/0268-1242/1/1/002>.
- [91] G. E. Kohnke, M. W. Koch, C. E. C. Wood, and G. W. Wicks. Beryllium diffusion in GaAs/AlGaAs single quantum well separate confinement heterostructure laser active regions. *Applied Physics Letters*, 66(21):2786–2788, May 1995. doi: 10.1063/1.113475. URL <https://doi.org/10.1063/1.113475>.
- [92] D. L. Miller and P. M. Asbeck. Be redistribution during growth of GaAs and AlGaAs by molecular beam epitaxy. *Journal of Applied Physics*, 57(6):1816–1822, March 1985. doi: 10.1063/1.334409. URL <https://doi.org/10.1063/1.334409>.

Appendices

Appendix A: Transfer Matrix Method

MATLAB Script

```

% Written in MATLAB by T.Wilson. Final Version 20/01/2021
% Using https://doi.org/10.1364/A0.34.001678 and https://doi.org/10.1364/A0.41.003978
%
% This function takes an array of complex layer refractive indices (N+iK)
% and an array of thicknesses (Array lengths must match). Lambda is the
% focus wavelength. All paramters must have the same units, but can have
% the units the user chooses (eg nm, um etc) as long as the refractive
% index data matches.
%
% The function is designed to be called by another script, and will return
% the total reflectance and transmittance of the stack at the chosen
% wavelength.

function [R,T] = TMM_Extended(N, D, Lambda)

    n0 = 1; %Refractive index in incident medium (Air/Vacuum)
    S = Interface(n0,N(1)); %First layer

    for i = 1:length(N)-1 %All layers except substrate
        P = Prop(N(i), D(i), Lambda);
        T = Interface(N(i), N(i+1));
        S = S*P*T;
    end

    if D(end) < 20000 %Check for substrate thickness, coherence length set at 20um
        Ps = Prop(N(end), D(end), Lambda);
        Tb = Interface(N(end), n0);
        S = S*Ps*Tb;
        r_TMM = S(2,1)/S(1,1);
        t_TMM = 1/S(1,1);
        R = abs(r_TMM)^2; %Total reflection from all layers
        T = abs(t_TMM)^2; %Total transmission through all layers assuming n0 = nExit
        return;
    else %Use incoherent correction for substrate
        T_f = T_Int(S);
        Tmn = Interface(N(end),n0);
        T_b = T_Int(Tmn);
        P = P_Int(N(end), D(end), Lambda);
        S = T_f*P*T_b;
        R = S(2,1)/S(1,1); %Total reflection from all layers
        T = 1/S(1,1); %Total transmission through all layers assuming n0 = nExit
    end

```

```

    end
end

function [r,t] = Fresnel(n1,n2) %Fresnel coefficients at interface n1|n2
    n1 = real(n1);
    n2 = real(n2);
    r = (n1-n2)/(n1+n2);
    t = (2*n1)/(n1+n2);
end

function T = Interface(n1,n2) %Interface Matrix
    [r,t] = Fresnel(n1,n2);
    T(1,1) = 1;
    T(1,2) = r;
    T(2,1) = r;
    T(2,2) = 1;
    T = (1/t)*T;
end

function P = Prop(n, d, Lambda) %Layer propagation Matrix
    k = 2*pi*n/Lambda;
    P(1,1) = exp(k*d*-1i);
    P(1,2) = 0;
    P(2,1) = 0;
    P(2,2) = exp(k*d*1i);
end

function [rf, rb, tf, tb] = C_Fresnel(M) %Complex Fresnel coefficients from system matrix M
    rf = M(2,1)/M(1,1);
    rb = -M(1,2)/M(1,1);
    tf = 1/M(1,1);
    tb = det(M)/M(1,1);
end

function T = T_Int(M) %Incoherent interface matrix for epilayer|substrate boundary
    [rf, rb, tf, tb] = C_Fresnel(M);
    T(1,1) = 1;
    T(1,2) = -abs(rb)^2;
    T(2,1) = abs(rf)^2;
    T(2,2) = abs(tf*tb)^2 - abs(rf*rb)^2;
    T = (1/(abs(tf)^2))*T;
end

```

```
function P = P_Int(n, d, Lambda) %Incoherent propagaion matrix for substrate
    k = 2*pi*n/Lambda;
    P(1,1) = abs(exp(-k*d*1i))^2;
    P(1,2) = 0;
    P(2,1) = 0;
    P(2,2) = abs(exp(k*d*1i))^2;
end
```